

https://dspace.org/

A novel peptide-enhanced drug delivery system for squamous cell oesophageal carcinoma

Adeyemi, Samson Adebowale

2017

https://hdl.handle.net/10539/25547

Adeyemi, Samson Adebowale, (2017) A novel peptide-enhanced drug delivery system for squamous cell oesophageal carcinoma, University of the Witwatersrand, Johannesburg, https://hdl.handle.net/10539/25547

Downloaded from a DSpace repository. https://dspace.org/

A Novel Peptide-Enhanced Drug Delivery System for Squamous Cell Oesophageal Carcinoma

SAMSON ADEBOWALE ADEYEMI

A thesis submitted to the Faculty of Health Sciences, University of the Witwatersrand

in fulfilment of the requirements for the degree of Doctor of Philosophy

Supervisor:

Professor Viness Pillay

University of the Witwatersrand, Department of Pharmacy and Pharmacology,

Johannesburg, South Africa

Co-Supervisor:

Professor Yahya Essop Choonara

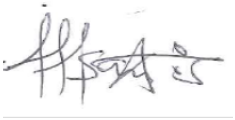
University of the Witwatersrand, Department of Pharmacy and Pharmacology,

Johannesburg, South Africa

Johannesburg, 2017

DECLARATION

I, Samson Adebowale Adeyemi, declare that this thesis is my own work. It has been submitted for the degree of Doctor of Philosophy in the Faculty of Health Sciences in the University of the Witwatersrand, Johannesburg. It has not been submitted before for any degree or examination at this or any other University.



……

This …21st. day of ……September…….. 2017

PUBLICATIONS

1. Functionalized Nanocarriers for Enhanced Bioactive Delivery to Squamous Cell Carcinomas: Targeting Approaches and Related Biopharmaceutical Aspects: A.S. Adebowale, Y.E. Choonara, P. Kumar, L.C. du Toit, V. Pillay. Current Pharmaceutical Design, 21 (2015) 3167–3180.

2. Synthesis and *In vitro* Characterization of a pH-sensitive Chitosan-Polyethylenimine Nanosystem for the Potential Delivery of Therapeutic Proteins: Samson A. Adeyemi, Yahya E. Choonara, Pradeep Kumar, Lisa C. du Toit and Viness Pillay. Journal of Drug Delivery Science and Technology, 39 (2017) 266 – 276.

3. Design and Characterization of Endostatin Loaded Nanoparticles for *In Vitro* Anti-angiogenesis in Squamous Cell Carcinoma: Samson A. Adeyemi, Yahya E. Choonara, Pradeep Kumar, Lisa C. du Toit and Viness Pillay. Journal of Nanomaterials, DOI: 10.1155/2017/2539065.

4. Anti-proliferative Activities of Folate-targeted Endostatin-loaded Nanoparticles on Oesophageal Squamous Cell Carcinoma: Samson A. Adeyemi, Yahya E. Choonara, Pradeep Kumar, Lisa C. du Toit, Thashree Marimuthu and Viness Pillay. Submitted to International Journal of Nanomedicines, February, 2017.

5. A Novel Dual Peptide-Enhanced Endostatin-Loaded Nano-construct for Targeted Anti-Angiogenic Effects in Squamous Cell Carcinoma: Samson A. Adeyemi, Yahya E. Choonara,

Pradeep Kumar, Lisa C. du Toit, Thashree Marimuthu and Viness Pillay. Submitted to journal of Nanomedicine: Nanotechnology, Biology and Medicine, March, 2017.

RESEARCH OUTPUTS AT CONFERENCE PROCEEDINGS

1. Samson Adebowale Adeyemi, Yahya Essop Choonara, Lisa Claire Du Toit, Pradeep Kumar, and Viness Pillay. A Novel Chitosan-based Nano-construct for Targeted Subcutaneous Delivery of Proteins via the Lymphatic System in Squamous Cell Carcinoma. ***(Podium Presentation).*** *6th Cross-Faculty Graduate Symposium*, University of the Witwatersrand, Johannesburg, South Africa, October 27 - 31, 2014.

2. Samson Adebowale Adeyemi, Yahya Essop Choonara, Lisa Claire Du Toit, Pradeep Kumar, and Viness Pillay. Preparation and Characterization of Novel PEGylated Chitosan-grafted-Polyethylineimine Nanospheres for Targeted Subcutaneous Delivery of Proteins via the Lymphatic System in Squamous Cell Carcinoma. ***(Podium Presentation)***. *Academy of Pharmaceutical Sciences of South Africa*, Johannesburg, South Africa, September 17 - 19, 2015.

3. Samson Adebowale Adeyemi, Yahya Essop Choonara, Lisa Claire Du Toit, Pradeep Kumar, and Viness Pillay. A Novel Functionalized Chitosan-based Nanoconstruct for Targeted Subcutaneous Delivery of Protein therapeutics in Squamous Cell Carcinoma. *(**Poster Presentation**)*. *10th World Biomaterials Congress*, Montreal, Canada , 17 – 22 May, 2016.

4. Samson Adebowale Adeyemi, Yahya Essop Choonara, Lisa Claire Du Toit, Pradeep Kumar, and Viness Pillay. A Novel Peptide-Enhanced Endostatin-Loaded Nano-construct for Targeted Anti-Angiogenic Effect in Squamous Cell Carcinoma. (***Podium Presentation***). *Faculty of Health Sciences Research Day*, University of the Witwatersrand, Johannesburg, South Africa, September 1, 2016.

5. Samson Adebowale Adeyemi, Yahya Essop Choonara, Lisa Claire Du Toit, Pradeep Kumar, and Viness Pillay. A Novel Folate-Decorated Nano-Cargo for Targeted Endostatin Delivery in Squamous Cell Carcinoma. (***Podium Presentation***). *APA International Conference on Advanced Polymers, Biomaterials, Bioengineering & Nano Drug Delivery*, Flic-En-Flac, Mauritius, September 5 - 7 , 2016.

ABSTRACT

Cancer has been described as one of the major and leading causes of death worldwide. By the year 2030, it has been postulated that over 21.4 million new cases of cancer are anticipated, with 17 million cancer deaths annually and a total of 75 million people living with cancer within five years of diagnosis. Chemotherapy is the main therapeutic intervention for treating people living with oesophageal squamous cell carcinoma (OSCC). However, drug resistance, non-targeted delivery, sub-optimal dosage at disease sites and side effects on healthy cells have rendered it inefficient and ineffective in combating the disease even after combination chemotherapy. The paradigm shift in cancer nanomedicine employs the use of short functional peptides and ligands, conjugated to the surfaces of nanoparticles, for direct and active drug delivery systems in *in vitro* and *in vivo* assays. Smart and intelligent nanosystems remain a proactive and promising treatment alternative to circumvent the anomalies of current convectional cancer chemotherapeutics and enhance their delivery for optimal anti-tumoral effects. Based on these modalities, the conceptualization, design, optimization and characterization of a smart peptide-enhanced ligand-functionalized nano-construct – referred to herein as a *PEL nanosystem* – capable of encapsulating, targeting and controlling the release of endostatin (ENT), was fabricated in this study.

Physicochemical parameters that characterized the design of a smart nano-construct in cancer therapy including satisfactory size, shape and surface properties, cellular uptake and internalization by tumor cells, low cellular toxicity to healthy cells and enhanced anti-tumoral activity of the encapsulated drug informed the fabrication of the PEL nanosystem. An optimized PEG-PEI-CHT nano-conjugate was developed as predicted by the Box–Behnken design model and surface-functionalized with Ly-P-1, PENT and FA as targeting moieties. Fourier Transform Infrared (FTIR) spectroscopy and Nuclear Magnetic Resonance (NMR) analysis confirmed the successful grafting of the nano-conjugates while Transmission Electron Microscopy (TEM) and Dynamic Light Scathering (DLS) analyses confirmed the synthesis of PEL nanoparticles with an average size less than 100nm. Scanning Electron Microscopy (SEM) results confirmed the morphology of the PEL nanosystem to be spherical with rough surfaces due to the attachments of the functionalized moieties. The release profile of the PEL nanosystem showed increased release of ENT at the acidic tumor micro-environment than observed at the physiological pH of healthy cells. Interestingly, the smart PEL nanosystem exhibited an enhanced targeted release of ENT for anti-tumoral effects on KYSE-30 cells relative to the unmodified nanosystem. The PEL nanosystem loaded with ENT showed a pragmatic inhibition of potent angiogenic factors including cell proliferation, nuclear apoptosis and necrosis, cell migration and invasion, as well as reduced expressions of both VEGF-C and MMP2 proteins as molecular makers for anti-angiogenesis. Athymic nude mice induced with OSSC xenografts showed a dramatic reduction in tumor volume with increased necrotic arears after treatment with the PEL ENT-loaded nanoparticles relative to the control.

Overall, detailed *in vitro, ex vivo* cellular and *in vivo* experiments validated the fabricated PEL nanoparticulate systems as efficient delivery vehicles of ENT for enhancing its anti-tumoral activity by targeting the angiogenic pathway in KYSE-30 cells as presented in this study. While ENT was selected as a peptide-based anti-cancer model drug in this study due to its broad spectrum anti-angiogenic activities and limitations, the novel PEL nanosystem can be employed to incorporate alternative cancer chemotherapeutics for enhanced on-site delivery for an optimum therapeutic response in cancer therapy.

RESEARCH ACCOLADES

1. National Research Foundation (NRF) supervisor-linked Scholarship, South Africa, 2013 - 2015
2. Technology Innovation Agency (TIS) Doctoral Scholarship Grant Holder, South Africa, 2016 and 2017
3. Wits University Postgraduate Merit Award (PMA) Doctoral Scholarship, South Africa, 2014 – 2016
4. Wits University Postgraduate International Conference Travel Grant to attend the 10th World Biomaterials Congress, Montreal, Canada, 17 – 22 May, 2016.
5. National Research Foundation Knowledge, Interchange and Collaboration (KIC) International Travel Grant, 2016 to attend the 10th World Biomaterials Congress, Montreal, Canada , 17 – 22 May, 2016.

ACKNOWLEDGEMENTS

*My hope is built on nothing else than **JESUS Blood and RIGHTEOUSNESS**…."Seest thou a man diligent in his business? He shall stand before kings; he shall not stand before mean men"*

- Proverb 22:29

"Indolence is a delightful but distressing state; we must be doing something to be happy. Action is no less necessary than thought to be instinctive tendencies of the human frame"

- Mahatma Gandhi

The above thoughts aptly describe the cascade mechanism of events that made this study a reality. Although it has been a herculean task, this research study is a product of meticulous research, painstaking planning, brainstorming sessions and punctilious editing through the synergistic effort of some of the most brilliant minds I ever come across.

My sincere and profound gratitude goes to my supervisor, Professor Viness Pillay. His mentorship, supervision, relentless guidance, supports and attention to detail contributes immensely to the successful completion of this study. I am most grateful for giving me the platform to explore my undying quest for excellence which WADDP represents. I cannot but say thank you to my co-supervisor - Professor Yahya Essop Choonara for his constructive and meticulous advice, research planning and editing of research outputs during the course of this study. A hearty thanks to Professor Lisa du Toit and Dr Pradeep Kumar. Your immense contributions to the successful completion of this study are greatly appreciated from conceptualisation to design, and from analyses to editing of research reports.

Special thanks to the National Research Foundation and the University of the Witwatersrand for the bursary and postgraduate merit award given to me during the period of this study. To my

colleagues at WITS Advance Drug Delivery Platform (WADDP), thanks for the harmonious working relationship we had together, for all our constructive arguments and intellectual disputes which have positively impacted the quality of this study. My gratitude knows no bounds.

This research work is the product of a dream. To those who nurtured the dream from conception to birth: my mum, my siblings, nuclear family and family friends, you are highly appreciated for always being there for me. To you I say – I can't thank myself. Special thanks to Prof. Kennedy Erlwanger, Dr Olufemi David Akilo, Dr.Thashree Marimuthu, members of the school of therapeutic science and faculty of health sciences - Grace Maubane, Palesa Khumalo, Anna Moronga, and Owen Naiker. Your selfless and sacrificial assistance at different time points is highly appreciated. Special thanks to the technical staff of the Department of Pharmacy and Pharmacology, Mr. Sello Ramarumo, Ms. Nompumelelo Damane, Mr. Kleinbooi Mohlabi, Mr. Bafana Themba and Phumzile Madodo. I also thank the staff of the CAS at Wits, Sr. Mary-Ann Costello, Patrick Selahle, Sr. Ammelia Rammekwa, Kershneee Chetty, Lorrraine Setimo and Nico Douths.

To my ever loving wife, Ooreofe Adeyemi, thank you for your tender and loving care, patience, trust, determination and encouragement without which the completion of this research would not have been possible. You ever remain dear to my heart. To my adorable daughter - Nanette and loving son – Nathan, I say thank you for believing in your daddy in the pursuit of academic excellence.

Above all, to God be the Glory for the strength and grace to pull through this study

DEDICATION

With gratitude to God, this research work is whole-heartedly dedicated to my grandmother: Mrs Morenike Christianah Adebisi, who crafted in me the quest for and pursuit of academic excellence.

ANIMAL ETHICS DECLARATION

I, Samson Adebowale Adeyemi confirm that the study entitled "*In vivo* subcutaneous delivery os an injectable peptide-enhanced endostatin loaded nanosystem for Oesophageal Squamous Cell Carcinoma treatment in an Athymic nude mice model" received the approval from the Animal Ethics Committee of the University of the Witwatersrand with ethics clearance number **2016/01/04/D** (see Appendix D)

TABLE OF CONTENTS

DECLARATION i

PUBLICATIONS ii

RESEARCH OUTPUTS AT CONFERENCE PROCEEDINGS iv

ABSTRACT vi

RESEARCH ACCOLADES vii

ACKNOWLEDGEMENTS viii

DEDICATION x

ANIMAL ETHICS DECLARATION xi

TABLE OF CONTENTS xii

LIST OF FIGURES xxvii

LIST OF TABLES xxxiii

LIST OF EQUATIONS xxxiv

LIST OF ABBREVIATIONS xxxv

CHAPTER 1

INTRODUCTION

1.1 Background of the study 1

1.2. Rationale for this Study 4

1.3. Aim and Objectives 6

1.4. Novelty of this Study 7

1.5. Overview of the Thesis 7

1.6. Concluding Remarks 10

1.7. References 10

CHAPTER 2

FUNCTIONALIZED NANOCARRIERS FOR ENHANCED BIOACTIVE DELIVERY TO SQUAMOUS CELL CARCINOMAS: AND RELATED BIOPHARMACEUTICAL ASPECTS

2.1. Introduction....14

2.2. Current Conventional Chemotherapy in Squamous Cell Carcinoma....17

2.3. Application of Polymeric Materials and their Limiting Factors in Cancer Nanomedicine..20

2.4. Targeted Delivery Systems in Squamous Cell Carcinoma....26

2.4.1. Exploring the Enhanced Permeability and Retention (EPR) Effect for Passive Targeting....27

2.5. Targeted-Ligand Nanotechnology for an Enhanced Therapeutic Response in Squamous Cell Carcinoma: A Way Forward....30

2.5.1. Folate receptors: Strategic ligands for targeted nanoconstructs for squamous cell carcinoma....32

2.5.2. Transferrin receptors....33

2.5.3. Homing peptides....34

2.5.3.1. LyP-1: A dual-effect homing peptide for targeting tumor cells and vasculature..39

2.5.3.2. CGKRK – A pentapeptide with a penetrative homing signature....41

2.6. Concluding Remarks....42

2.8. References....43

CHAPTER 3

SYNTHESIS AND IN VITRO CHARACTERIZATION OF A pH-SENSITIVE CHITOSAN-POLYETHYLENIMINE NANOSYSTEM FOR THE POTENTIAL DELIVERY OF THERAPEUTIC PROTEINS

3.1. Introduction....59

3.2. Materials and Methods....61

3.2.1. Materials....61

3.2.2. Synthesis of the Chitosan-g-Polyethylene imine (CHT-g-PEI) Complex....62

3.2.3. Synthesis of Chitosan-g-Polyethylene imine (CHT-g-PEI) grafted bi-functional Polyethylene Glycol (NH_2-PEG-CHT-g-PEI) Complex....62

3.2.4. Nanoparticle Synthesis and BSA Entrapment into the Nanoparticles from Preformed Polymer Complex....63

3.2.5. Determination of Nanoparticle Recovery and Drying....64

3.2.6. Characterization of the Synthesized Co-Polymer Complex and BSA Loaded Nanoparticles....64

3.2.6.1. Confirmation of structural transformation and formation of the grafted co-polymer complex....64

3.2.6.2. Elucidation of nanoparticle size, surface charge and morphology....65

3.2.6.3. Thermodynamic event mapping of the native and grafted co-polymer and the BSA loaded nanoparticles....66

3.2.6.4. BSA loading efficiency and *in vitro* release studies....66

3.3. Results and Discussion....67

3.3.1. Confirmation of the Synthesis of the Grafted Copolymer Complex and BSA Loaded Nanoparticles....67

3.3.2. Evaluation of the Thermal Stability of the Native Polymers, Co-polymer Complex and Synthesized Nanoparticles....73

3.3.3. Assessment of the Nanoparticle Size, Surface Charge and Morphology....76

3.3.4. Assessment of BSA encapsulation and *in vitro* release kinetics....79

3.4. Concluding remarks.....84
3.7. References.....85

CHAPTER 4

DESIGN AND CHARACTERIZATION OF ENDOSTATIN-LOADED NANOPARTICLES FOR *IN VITRO* ANTI-ANGIOGENESIS IN SQUAMOUS CELL CARCINOMA

4.1. Introduction....91

4.2. Materials and Methods 93

4.2.1. Materials 93

4.2.2 Methods 94

4.2.2.1. Preparation of [CHI-g-PEI-PEG-NH_2]-Endostatin-loaded nanoparticles 94

4.2.2.1.1. Synthesis of the CHI-g-PEI conjugate 94

4.2.2.1.2. Synthesis of CHI-g-PEI-PEG-NH_2 Conjugate....94

4.2.2.1.3. Bovine Serum Albumin/ Endostatin Entrapment and Nanoparticle Synthesis 95

4.2.2.2. Analysis of Chemical and Functional Transformations via Fourier Transform Infrared Spectroscopy 95

4.2.2.3. Evaluation of Structural Modifications via Nuclear Magnetic Resonance Spectroscopy....96

4.2.2.4. Particle size, Surface charge, Conductivity and Structural Morphology measurement 96

4.2.2.5. Determination of the Drug Loading Capacity and Entrapment Efficiency of the Nanoparticles 97

4.2.2.6. Determination of the Degree of Swelling of the Nanoparticles 98

4.2.2.7. *In vitro* Drug Release and Chromatographic Apparatus/Condition for Reverse Phase HPLC 98

4.2.2.8. Optimization of the Formulatory Components using Box-Behnken Experimental Design....99

4.2.2.9. Nanoparticle Cyto-compactibility and Cell Proliferation Assay 99

4.3. Results and Discussion 100

4.3.1. Polymer grafting, nanoparticle synthesis and characterization 100

4.3.2. Confirmation of the Physicochemical Properties and Morphology of Endostatin-loaded Nanoparticles 105

4.3.3. Confirmation of BSA/Endostatin Loading Capacity and Entrapment Efficiency of Nanoparticles 111

4.3.4. Nanoparticle Swelling Behaviour and *in vitro* Drug Release 113

4.3.4.1. Effects of chitosan and TPP concentrations on swelling and release kinetics ..114

4.3.4.2. Effects of pH on nanoparticle swelling and BSA/endostatin release..... 115

4.3.4.3. Effects of PEI and PEGylation on swelling and drug release 116

4.3.5. Optimization of the experimentally-derived Box–Behnken formulations..... 119

4.3.6. Confirmation of Cytocompatibility and Anti-angiogenic effect of endostatin-loaded nanoparticles 123

4.4. Concluding remarks..... 126

4.7. References 127

CHAPTER 5

ANTI-PROLIFERATIVE ACTIVITIES OF FOLATE-TARGETED ENDOSTATIN-LOADED NANOPARTICLES ON OESOPHAGEAL SQUAMOUS CELL CARCINOMA

5.1. Introduction....134

5.2. Materials and Methods....136

5.2.1. Materials....136

5.2.2. Methods....137

5.2.2.1. Preparation of FA-PEG-PEI-g-CHT Endostatin loaded nanoparticles....137

5.2.2.1.1. Synthesis of CHI-g-PEI FITC labelled conjugates....137

5.2.2.1.2. Synthesis of Folate-decorated PEG-PEI-CHT FITC labelled conjugates....138

5.2.2.1.3. Endostatin Entrapment and synthesis of FA decorated nanoparticles....138

5.2.2.2. Characterization of Conjugated FA-PEG-PEI-CHT Nanoparticles....139

5.2.2.2.1. Determination of Chemical and Functional Transformations using Fourier Transform Infrared Spectroscopy....139

5.2.2.2.2. Structural Modifications using Nuclear Magnetic Resonance Spectroscopy....139

5.2.2.2.3. Size, Zeta potential and Structural Morphology ENT-loaded Nanoparticles....139

5.2.2.2.4. *In vitro* Endostatin Release....140

5.2.2.3. Analysis of the Endostatin-loaded Nanoparticles is an OSCC Cell Line....140

5.2.2.3.1. Polymer Cyto-compatibility and Cell Proliferation Assay....141

5.2.2.3.2. Cellular uptake, internalization and sub-cellular localization of nanoparticles....141

5.2.2.3.3. Endothelial cell migration assay using a modified Boyden Chamber....142

5.3. Results and Discussion....143

5.3.1. Biofunctionalization of Polymer Conjugates and ENT-loaded Nanoparticles....143

5.3.2. *In vitro* Release Kinetics of ENT from FA-decorated Nanoparticles....148

5.3.3. *In vitro* Cellular Uptake and Intracellular Trafficking of Nanoparticles....150

5.3.4. Polymer Cyto-compactibility and Anti-proliferation Effects of FA-linked Nanoparticles 157

5.3.5. FA-decorated ENT-loaded Nanoparticles Inhibit KYSE-30 Cells' Motility *In vitro* 160

5.4. Concluding remarks.....162

5.7. References 163

CHAPTER 6

A NOVEL DUAL PEPTIDE-ENHANCED ENDOSTATIN-LOADED NANO-CONSTRUCT FOR TARGETED ANTI-ANGIOGENIC EFFECTS IN SQUAMOUS CELL CARCINOMA

6.1. Introduction....170

6.2. Materials and Methods....172

6.2.1. Materials....172

6.2.2. Methods....173

6.2.2.1. Preparation of Peptide-PEG-PEI-g-CHT Endostatin loaded nanoparticles....173

6.2.2.1.1. Synthesis of CHI-g-PEI conjugates....173

6.2.2.1.2. Synthesis of Peptide-Enhanced PEG-PEI-CHT FITC labelled conjugates....174

6.2.2.1.2.1. Cyclization of conjugated LyP-1-PEG-NH_2 conjugates....174

6.2.2.1.2.2. Preparation of FITC labelled LyP-1/PENT-PEG-NH_2 conjugates....175

6.2.2.1.2.3. Preparation of FITC labelled Peptide Enhanced PEG-PEI-CHT conjugates....175

6.2.2.2. Endostatin Entrapment and synthesis of Peptide Enhanced ENT-loaded nanoparticles....175

6.2.2.3. Characterization of Conjugated Peptide-Enhanced PEG-PEI-CHT Nanoparticles....176

6.2.2.3.1. Determination of Chemical and Functional Transformations using Fourier Transform Infrared Spectroscopy....176

6.2.2.3.2. Structural Modifications using Nuclear Magnetic Resonance Spectroscopy....176

6.2.2.3.3. Size, Zeta potential and Structural Morphology Peptide-Enhanced ENT-loaded Nanoparticles....176

6.2.2.4. *In vitro* Endostatin Release....177

6.2.2.5. Cell Culture Experiments....178

6.2.2.5.1. Polymer Cyto-compatibility and Cell Proliferation Assay....178

6.2.2.5.2. Cellular uptake, Internalization and sub-cellular localization of nanoparticles....179

6.2.2.5.3. Endothelial Cell Migration Assay using Modified Boyden Chamber....180

6.2.2.5.4. Anti-VEGF and Anti-MMP2 ELISA assay 180
6.3. Results and Discussion 181
6.3.1. Structural and functional modifications of peptide functionalized nano-conjugates .181
6.3.2. *In vitro* ENT release from modified ENT-loaded nanoparticles 187
6.3.3. Effects of physicochemical properties of peptide functionalized ENT-loaded nanoparticles on cellular uptake, internalization and sub-cellular colocalization 189
6.3.4. Specific binding and cytotoxic effects of peptide-enhanced ENT-loaded nanoparticles 194
6.3.5. Reduced migration and anti-proliferative effects of LyP-1/PENT functionalized nanosystem on KYSE-30 cells 196
6.3.6. Enzyme linked immunosorbent assay (ELISA) for VEGF-C and MMP2 199
6.4. Concluding remarks.....202
6.7. References 203

CHAPTER 7

IN VIVO SUBCUTANEOUS DELIVERY OF AN INJECTABLE PEPTIDE-ENHANCED ENDOSTATIN LOADED NANO-SYSTEM FOR OESOPHAGEAL SQUAMOUS CELL CARCINOMA TREATMENT IN ATHYMIC MICE MODEL

7.1 Introduction 211

7.2. Materials and Methods 213

7.2.1. Cell lines and establishment of xenografts 213

7.2.2. Animal welfare, housing and habituation prior to drug study experiment 213

7.2.3. Administration of KYSE-30 cells and development of tumor xenograft in mice 214

7.2.4. Preparation of endostatin-loaded PEL nanosystem components 216

7.2.5. Administration of the PEL nanosystem loaded with endostatin 216

7.2.6. *In vivo* study design 217

7.2.7. Ultrasound imaging of solid tumor in athymic nude mice 221

7.2.7.1. Protocol for microultrasound imaging 221

7.2.8. Blood collection and tissue sampling for histological analyses 222

7.2.9. Preparation of calibration standards and generation of corresponding *in vivo* and *in vitro* endostatin release samples 224

7.2.10. Quantification of *in vivo* endostatin concentrations released from the PEL nanosystem into the plasma of nude mice with solid tumor 224

7.3. Results and Discussions 226

7.3.1. Effects of ENT-loaded PEL nanosystems on tumor volume and mice weight 226

7.3.2. *In vivo* quantification of plasma concentration of endostatin released from the PEL nanosystem in mice bearing KYSE-30 cells xenograft 230

7.3.3. Necrotic and anti-angiogenic effects of endostatin-loaded PEL nanosystem in KYSE-30 xenografts 234

7.4. Concluding remarks 236

7.5. References 237

CHAPTER 8

CONCLUSIONS AND RECOMMENDATIONS

8.1. Conclusions.....242

8.2. Recommendations.....244

APPENDICES

9.1. APPENDIX A 246

9.1.1. Research Publications 246

9.1.1.1. Review paper 246

9.1.1.2. Research paper I 246

9.1.1.3. Research paper II 247

9.1.1.4. Research paper III 248

9.1.1.5. Research paper IV 250

9.2. APPENDIX B 251

9.2.1. Abstracts of Research Outputs at Conference Proceedings 251

9.2.1.1. 6th Cross-Faculty Graduate Symposium, University of the Witwatersrand, Johannesburg, South Africa, October 27th-31st, 2014. 251

9.2.1.2. Academy of Pharmaceutical Sciences of South Africa, Johannesburg, South Africa, September 17th -19th, 2015. 252

9.2.1.3. 10th World Biomaterials Congress, Montreal, Canada , 17th – 22nd May, 2016. 253

9.2.1.4. Faculty of Health Sciences Research Day, University of the Witwatersrand, Johannesburg, South Africa, September 1, 2016 254

9.2.1.5. APA International Conference on Advanced Polymers, Biomaterials, Bioengineering & Nano Drug Delivery, Flic-En-Flac, Mauritius, September 5th -7th , 2016. 255

9.3.1. APPENDIX C 257

9.3.2. Certificate of research presentation 257

9.3.3. Certificate of research presentation 258

9.3.4. Certificate of research presentation 259

9.4. APPENDIX D 260

9.4.1. Animal ethics approval 260

LIST OF FIGURES

Figure 1.1: Schematic conceptual flow diagram for a novel peptide-enhanced ligand (PEL) functionalized drug delivery system for OSCC management. 6

Figure 2.1: Nanoparticle designs, in terms of size, shape, modulus, charge, material, surface, and cargo, as well as their interactions in the body, determines their individual behaviour. Reprinted under the permission of (Hauert and Bhatia, 2014), (Copyright Elsevier Publishers, 2014). 23

Figure 2.2: Schematic representation of nanoparticle internalization in cells (Danhier et al., 2012) (Copyright Elsevier Publishers, 2011) 28

Figure 2.3: Passive and active targeting of nanocarriers. Nanocarriers can reach tumors selectively through the leaky vasculature surrounding the tumors. Ligands grafted at the surface of nanocarriers bind to receptors (over)-expressed by cancer cells (green) or angiogenic endothelial cells (pink) (Danhier et al., 2012) (Copyright Elsevier Publishers, 2011). 30

Figure 2.4: Different possible approaches of peptides in cancer nanomedicine. Peptides can be used as anticancer drug, cytotoxic drug carrier, vaccine, hormones, and radionuclide carrier. Figure adapted from (Thundimadathil, 2012). 35

Figure 2.5: Principle of cell-selective peptide targeting and delivery. (a) A homing peptide (HP) has no inherent internalization properties and only delivers its cargo to specific cell-surface receptors. (b) A HP conjugated to a cell-penetrating peptide (HP-CPP) undergoes receptor binding and then typically undergoes cargo internalization via endocytosis or pore formation. (c) A cell-penetrating homing peptide (CPHP) has the ability to internalize without the aid of external agents. Reprinted with permission from (Svensen et al., 2012) (Copyright Elsevier Publishers, 2012). 36

Figure 3.1: Schematic showing the mechanism of synthesis of the NH_2-PEG-CHT-g-PEI complex (A) Addition of PEI to CHT molecules increases its internalization efficiency and buffering capacity while (B) the introduction of the PEG component unto the CHT-g-PEI copolymer reduces the cytotoxic effect of PEI and also protects the encapsulated BSA molecules within the CHT nanoparticles.....68

Figure 3.2: Proton NMR spectra of the synthesized copolymer complex in a solution of 5:1 concentration of D_2O and CD_3COOD respectively. (a) Represents the conjugation of CHT and PEI with their corresponding peaks, (b) the grafting of PEG to preformed CHT-g-PEI copolymer. 70

Figure 3.3: FTIR spectra showing the various peaks in the grafted, un-grafted biodegradable polymers and synthesized nanoparticles. 72

Figure 3.4: Thermogravimetric graph showing the thermal stability of the biodegradable polymers and the nanoparticles from the co-polymer complex. 74

Figure 3.5: Superimposed DSC thermograms showing the thermal analysis of grafted/un-grafted

polymers and BSA-loaded/BSA-free nanoparticles. (a) Thermograms of native and grafted copolymers, (b) thermograms of BSA-loaded and unloaded nanoparticles 75

Figure 3.6: TEM micrograph of the BSA loaded nanoparticles. Nanoparticles showed spherical shape with an average size < 100 nm. 76

Figure 3.7: Nanoparticles size intensity profile for BSA loaded nanoparticles using Dynamic Light Scattering. Nanoparticles were dispersed in distilled H_20 prior to measurement. 77

Figure 3.8: Gold-platinum sputtered SEM Micrograph of BSA loaded nanoparticles. Magnification = 50.00 KX; Voltage = 10.00 kV. 78

Figure 3.9: Nanoparticle Zeta potential measurement profile. Nanoparticles sample was dispersed in distilled H20. 79

Figure 3.10: Release Profile of BSA loaded nanosystem prepared at conditions: CHT concentration = 2mg/mL, CHT-based complex/TPP mass ratio = 2:1, BSA concentration = 1mg/mL. Released medium = PBS, Temperature = 37 ± 1 oC, pH = 7.4 and 6.8. Samples were analysed in triplicates (n=3). 84

Figure 4.1: Proposed reaction scheme for the preparation of grafted polymers. 101

Figure 4.2: ^{1}H NMR spectra showing the grafting of polymer conjugates in D_2O:CD_3COOD (5:1). a) CHT-g-PEI and, b) CHT-g-PEI-PEG-NH_2 102

Figure 4.3: FTIR Spectra for native polymers, grafted polymer conjugates, and the endostatin-loaded nanoparticle system. 105

Figure 4.4: Hydrodynamic size and surface charge of optimized Endostatin-loaded nanoparticle. (a) Average nanoparticle size is 100.6 nm with PDI value of 0.274 and (b) surface zeta potential of nanoparticles is +7.95 mV. 109

Figure 4.5: TEM images of optimized Endostatin-loaded nanoparticles 110

Figure 4.6: Gold-platinum sputtered SEM micrographs of the optimized ENT-loaded nanoparticles. (a) Magnification = 8.36 KX; (b) Magnification = 50.00 KX 111

Figure 4.7: Swelling behaviour of drug-loaded nanoparticles. a) Effect of varying CHT concentrations on swelling behaviour of nanoparticles b) effect of varying pH conditions on the swelling behaviour nanoparticles at pH 6.8 and 7.4 respectively c) effect of PEI and PEG grafting on the swelling behaviour of nanoparticles. 114

Figure 4.8: Reverse Phase HPLC chromatogram of BSA. Retention time of BSA as a model for endostatin is 2.216 minutes and run time is 6 minutes. No interference was observed for RP-HPLC for blank sample. Elusion was monitored at wavelength of 280 nm to detect BSA as previously reported (Mukhopadhyay, 2013). 117

Figure 4.9: Cumulative drug release of the 15 experimental design formulations at pH 6.8 (left panel) and 7.4 (right panel). BSA release is higher at acidic pH of 6.8 than at physiological pH of 7.4 for each corresponding formulation. 118

Figure 4.10: Surface plots showing the effects of polymer, TPP and surfactant concentrations on

(a) nanoparticle size, (b) surface charge and (c) ENT release.....120

Figure 4.11: Response Optimization plot showing the desirability value, the values of independent variables and predicted values of the optimized nanoparticles.....122

Figure 4.12: *In vitro* drug release kinetics of the optimized endostatin-loaded nanoparticle system at changing pH conditions of 6.8 and 7.4. 123

Figure 4.13: Cell viability/proliferation of treated and untreated oesophageal squamous cell carcinoma (KYSE-30) after 24 hour exposure to the nano-formulations at varying polymer concentrations.....126

Figure 5.1: Schematic diagram showing the preparation of Folate decorated nanoparticulate system. 144

Figure 5.2: FTIR spectra showing conjugation of native polymers and FA decorated nanoparticles. 146

Figure 5.3: ^{1}H NMR of grafted copolymers in D_2O:CH_3COOD (5:1) a) PEG-PEI-g-CHT conjugate b) FA-PEG-PEI-g-CHT conjugate c) FA-PEG-COOH.....148

Figure 5.4: *In vitro* release of ENT from FA-functionalized nanoparticles. The release profile was in two phase, with an initial burst release followed by continuous release. Release was higher and more rapid at acidic endosomal and cancer microenvironment pH (4.6 and 6.8 respectively) than at physiological pH of 7.4 of healthy cells. 149

Figure 5.5: TEM micrograph of the FA-decorated endostatin-loaded nanoparticles. Nanoparticles showed spherical shape with an average size < 200 nm with a hollow centre pore assumed to be encapsulated particles of ENT within the nanoparticle matrix. 151

Figure 5.6: Gold-platinum sputtered SEM Micrograph of FA-decorated ENT-loaded nanoparticles. Magnification = 10.07 KX; Voltage = 10.00 kV. Particle showed spherical shape morphology with rough surfaces at high magnification assumed to be folate particles attached to the nanoparticles' surfaces. To check the surface morphology of the particles, SEM was conducted on larger sized particles. 151

Figure 5.7: Average zeta size of FA decorated ENT-loaded nanoparticle using dynamic light scattering. Average hydrodynamic size of nanoparticles was recorded was less than 250 nm in line with both the TEM and SEM average sizes. 152

Figure 5.8: Average zeta surface potential of FA decorated endostatin-loaded nanoparticles. An average positively charged surface was recorded at 12.9 mV. 153

Figure 5.9: Cellular uptake and internalization of FA-decorated endostatin-loaded nanoparticles in KYSE-30 cells. This is after the incubation with FITC labelled endostatin-loaded FA-PEG-PEI-g-CHT nanoparticles; (i) from transmitted light channel, (ii) from FITC channel, (iii) from overlaid channel upon staining the nucleus with DAPI (blue). 154

Figure 5.10: Proposed mechanisms for the cellular uptake and internalization of Folate-decorated endostatin-loaded nanoparticles. 155

Figure 5.11: Sub-cellular Colocalization of FA decorated nanoparticles. (i) KYSE-30 cells treated

with nanoformulation and stained with mitochondrial specific dye rhodamine 123 (ii) treated cells stained with FITC-labelled FA-decorated nanoparticles (iii) treated cells' nucleus stained with DAPI and (iv) merged confocal image of i – iii showing co-localization of the FA-decorated nanoparticles in both the nucleus and the mitochondrial in KYSE-30 cells. 157

Figure 5.12: Cell viability/proliferation of treated and untreated oesophageal squamous cell carcinoma (KYSE-30) after exposure to 24 hours of the nanoformulations at varying concentrations. (i) Red column is the control without treatment (ii) pink column are cells treated with the native polymer conjugate (iii) the blue column represents cells treated with ENT-loaded nanoparticles and (iv) cyan column represents FA-decorated ENT-loaded nanoparticles. 159

Figure 5.13: Confocal microscopic image of KYSE-30 nucleus. (i) Untreated KYSE-30 nucleus showing the intact morphology and chromatin materials within the nucleus. (ii) Necrotic and apoptotic effects of FA decorated nanoparticles on the nucleus of KYSE-30 cells. Apoptotic nuclei were swollen while necrotic nuclei were condensed and lysed with leaky nuclear materials. 160

Figure 5.14: The result of migration assay of KYSE-30 cells with 1000 ug/mL pre-incubation with native ENT-loaded nanoparticles and Folate-decorated ENT-loaded nanoparticles. Untreated KYSE-30 cells containing FBS free culture media only serve as the control. (a) Both treatments showed inhibition to KYSE-30 migration at about 74.12% and 71.72% for FA-decorated nanoparticles and unfunctionalized ENT-loaded nanoparticles respectively. (b) migrated KYSE-30 cells were fixed with 4% paraformaldehyde and stained with trypan blue and then imaged using fluorescent microscope. 162

Figure 6.1: Reaction scheme for the synthesis of peptide-enhanced nanoparticulate system. 182

Figure 6.2: ^{1}HNMR of grafted copolymers in D_2O:CH_3COOD (5:1) a) PEI-CHT conjugate b) Linear LyP-1-PEG-NH_2 conjugate c) Cyclic LyP-1-PEG-NH_2 conjugate (d) Cyclic LyP-1-PEG-PEI-CHT conjugate. 183

Figure 6.3: FTIR spectra of native and peptide-enhanced nanosystems. (a) spectra of the native polymers including CHT, PEI and PEG (b) spectra showing peaks for CHT, PEI and CHT-g-PEI nano-conjugate (c) spectra of PEG and peptide-PEG conjugates (d) spectra of CHT-g-PEI, LyP-1-PEG and LyP-1-PEG-PEI-CHT nano-conjugates. 185

Figure 6.4: *In vitro* ENT release peptide-enhanced ENT-loaded nanoparticles (a) LyP-1 functionalized ENT-loaded nanoparticles (b) PENT functionalized ENT-loaded nanoparticles. 188

Figure 6.5: Physicochemical characterization of peptide-functionalized ENT-loaded nanoparticles. (a) TEM micrographs of peptide-enhanced ENT-loaded nanoparticles (b) SEM micrographs of peptide-enhanced ENT-loaded nanoparticles (c) Hydrodynamic zeta size of peptide-enhanced ENT-loaded nanoparticles (d) Zeta surface charge of peptide-enhanced ENT-loaded nanoparticles. 190

Figure 6.6: CLSM micrograph showing cellular uptake and internalization of peptide-enhanced ENT-loaded nanoparticles. Nanoparticles were labelled with FITC. 192

Figure 6.7: DIC micrographs showing subcellular colocalization of peptide-enhanced ENT-loaded nanoparticles in the nucleuses of KYSE-30 cells stained with DAPI. (a) LyP-1 functionalized targeted ENT-loaded nanoparticles (b) PENT functionalized targeted ENT-loaded

nanoparticles. 192

Figure 6.8: CLSM images of the nucleus of KYSE-30 cells stained with DAPI (a) untreated KYSE-30 cells (b) KYSE-30 cells pre-incubated with peptide-functionalized ENT-loaded nanoparticles. Shrank and depleted nuclear membrane showed signs of apoptosis and necrosis. 193

Figure 6.9: CLSM images of mitochondrial stained with rhodamine 123 in live KYSE-30 cells. Altered-configuration of the mitochondrial morphology and disrupted mitochondrial membrane showed apoptosis (Johnson et al., 1980). 195

Figure 6.10: KYSE-30 cells viability after pre-incubation with nanoformulations at varying concentrations for 24 hours. 197

Figure 6.11: Transwell migration assay of KYSE-30 cells pre-treated with native, ENT-loaded and Peptide-functionalized nanoformulations (a) Representative microscopic images of the transwell inserts of KYSE-30 cells after pre-incubation with different nanoformulations (i) control, (ii) native polymer conjugates, (iii) ENT-loaded nanoparticles (iv) LyP-1 functionalized ENT-loaded nanoparticles, (v) PENT functionalized ENT-loaded nanoparticles. The inserts show the macroscopic images of transwell inserts stained by trypan violet. Pores of the membranes could also be observed as the numerous small, round and dark colored dots in the picture. (b) Histogram showing the quantification of the relative migration of KYSE-30 cells toward the chemo-attractant. Relative cell migration was expressed as the percentage of migrated cells with treatment compared to those without treatment (control). 198

Figure 6.12: VEGF-C expression in Oesophageal squamous cell carcinoma KYSE-30 cells under cell culture conditions. KYSE-30 cells in culture conditions were washed with PBS and cultured in fresh medium without FBS as control. LyP-1 and PENT functionalized ENT-loaded nanoparticles were dissolved in free FBS culture media (2.5 mg/mL) as treatment groups. Culture supernatants were harvested at 12, 24 and 48 hours post-treatment by ELISA assay. Concentration of VEGF in supernatants was represented as pg/mL in duplicates according to the manufacturer's protocol. 200

Figure 6.13: Effects of ENT on MMP-2 production by KYSE-30 squamous carcinoma cells. KYSE-30 cells (80% confluent, in a 75 cm^2 flask) were incubated with both LyP-1/PENT functionalized ENT-loaded nanoparticles for 48 hours (each at 2.5 mg/mL). Untreated KYSE-30 cells were used as control. Cell supernatants were harvested for MMP2 assay by ELISA. Samples were prepared in duplicates according to the manufacturer's manual.....202

Figure 7.1: Photographic evidence of (a) Housing of the nude mice (b) daily routine animal investigation (c) - (d) daily measurement of mice weight using the weighing balance.....214.

Figure 7.2: Graphical image of solid tumor. Mice developed tumor after 35 days post-KYSE-30 cells inoculation.....215.

Figure 7.3: Representative images showing excised tumor measurement using a digital caliper from an infested mouse among the control group. .....216.

Figure 7.4: Schematic showing the *in vivo* studies model for the PEL nanosystem containing peptide/ligand-PEG-CHI-PEI nanoparticles loaded with/without endostatin as preclinical studies for targeting OSCC. .....220.

Figure 7.5: Ultrasound imaging experiment using vevo imager. (a) Mice were anaesthezied with isofuran (b) ultrasound imaging gel was applied onto the tumor visualized with a vevo imager transducer (c) – (d) ultrasound images of solid tumor.....222.

Figure 7.6: Blood collection from anaesthetised mouse using cardiac puncture. Blood were collected into heparin-free 1 mL minicollect serum tubes (Grainer Bio-One GMbH, Kremsmunster, Austria) on ice and centrifuged to separate plasma from the whole blood sample. Plasma for each sample was stored in -80 ^{0}C freezer until further analyses. .....223.

Figure 7.7: Tissue sample collection. Solid tumor, the heart, lung, kidney, liver, spleen, and the oesophagus were surgically collected and stored in 10%v/v neutral buffered formaldehyde. .223.

Figure 7.8: Therapeutic effects of PEL nanosystem treatment in KYSE-30 xenografts. (a) Kinetics of tumor growth. Athymic nude mice were implanted with KYSE-30 cells (n=3 mice/group) and treated or not treated with native ENT, ENT-loaded nanoparticles, FA-functionalized ENT-loaded nanoparticles and peptide-enhanced ENT-loaded nanoparticles (20 mg/kg/d). Mice were sacrificed on the 25 days post-treatment (b) selected macroscopic images of excised solid tumors. Group 1 = Control, group 2 = ENT treated, group 3 = ENT-loaded nanoparticles, group 4 = FA-ENT-loaded nanoparticles, and group 5 = peptide-ENT-loaded nanoparticles. .....228.

Figure 7.9: Change in body mass of athymic mass for the control and treatment groups over the study period. Human OSCC cells (KYSE-30) (5 × 106) were implanted in the right flank of athymic mice (n = 3). Equimolar injections were administered every day (for a total of 5 times) of Control (PBS), ENT (4mg/kg), ENT-Nano (20mg/kg), FA-ENT-Nano (20mg/kg), and Peptide-ENT-Nano (20mg/kg). No significant difference was observed in the body weight of treated mice. Meanwhile, there is a dramtic reduction in mice body weight of control (untreated) from 29g – 22.96g before termination. Error bars indicate ± SD. .....230.

Figure 7.10: Typical chromatogram depicting a) ENT and b) the separation of both ENT and diclofenac sodium after spiking. 10 µL 0.00625 mg/mL solution of diclofenac sodium was used as internal standard to spike extracted plasma samples of ENT and *in vitro* ENT release samples from the nanoparticles. .....232.

Figure 7.11: Calibration curves generated for endostatin at 280 nm, SD ≤ 0.02049, N = 5.....233.

Figure 7.12: Plasma endostatin concentration profile depicting the release behaviour over 8 hours of native endostatin relative to encapsulated endostatin nanoparticles, and functionalized endostatin-loaded nanoparticles. SD = 0.021. .....234.

Figure 7.13: Representative cross-sectional images of tumor samples showing the necrotic areas after treatments or no treatment with PEL nanosystem. Images were viewed and captured under a light microscopy at high magnification 100x. .....236.

LIST OF TABLES

Table 2.1: Examples of some current convectional drugs for cancer therapy 19

Table 2.2: Examples of nanoparticles employed in cancer nanomedicine obtained from biodegradable polymers, encapsulants and their methods of preparation 24

Table 2.3: Examples of nanoparticles produced from Poly (lactic acid) and its conjugates in cancer nanomedicine 25

Table 2.4: Homing peptides employed in cancer nanomedicine 38

Table 4.1: Box-Behnken experimental design for formulation variables and responses at pH 7.4 and 6.8 respectively 108

Table 4.2: Drug loading capacity and entrapment efficiency.....112

Table 6.1: Assignment of FTIR spectra of native polymers, polymer and peptide conjugates presented in Figure 6.3. 186

Table 7.1: Drugs and recommended dosages as administered to mice .....219.

Table 7.2: UPLC parameters employed for the determination of ENT concentration in vitro and in vivo .....225.

LIST OF EQUATIONS

Equation 3.1:.....67

Equation 3.2:.....69

Equation 4.1:.....97

Equation 4.2:.....97

Equation 4.3:.....100

Equation 4.4:.....103

Equation 4.5:.....103

Equation 4.6:.....103

Equation 4.7:.....103

Equation 5.1:.....143

Equation 6.1:.....180

LIST OF ABBREVIATIONS

AESC	Animal Ethics Screening Committee
BSA	Bovine Serum Albumin
CAS	Central Animal Service
CDI	Carbonyldiimidazole
CHT	Chitosan
CHT-PEI	Chitosan grafted Polyethylene imine conjugate
PEG-PEI-CHT	Polyethylene glycol-polyethylene grated chitosan nano-conjugate
DA	Degree of Deacetylation
EDC	1-Ethyl-3-(3-dimethylaminopropyl)-carbodiimide
EE	Entrapment Efficiency
ENT	Endostatin
ELISA	Enzyme-Linked Immunosorbent Assay
FTIR	Fourier Transform Infrared Spectroscopy
FITC	FIuorecein isothiocyanate
HPLC	High Performance Liquid Chromatographic
NHS	N-hydroxysuccinimide
Pdi	Polydisperity index
PEI	Polyethyleneimine
PENT	Pentapeptide
PEL	Peptide Enhanced Ligand
PEG	Polyethylene glycol
PCD	Programmed Cell Death

PVA	Polyvinyl alcohol
RPMI	Roswell Park Memorial Institute
SEM	Scanning Electron Microscopy
sc	Subcutaneous
TEM	Transmission Electron Microscopy
TGA	Thermogravimetric Analysis
DSC	Differential scanning calorimetry
NMR	Nuclear Magnetic Resonance
TPP	Tripolyphosphate
UPLC	Ultra Performance Liquid Chromatographic
VEGF	Vascular Endothelial Growth Factor
MMP2	MMP2 matrix metallopeptidase 2

CHAPTER 1

INTRODUCTION

1.1 Background of the study

The global burden of cancer as reported by the International Agency for Research on Cancer (IARC) showed that cancer incidence has increased to twice its previous occurrence in the past 30 years (American Cancer Society, 2011). Their findings showed that in 2008 there were more than 12 million new cases of cancer diagnosed out of which 7.6 million deaths were recorded and 25 million persons living with cancer worldwide (American Cancer Society, 2011). Meanwhile, by the year 2030, it has been postulated that over 21.4 million new cases of cancer could be expected, with 17 million cancer deaths yearly and a total of 75 million people living with cancer within five years of diagnosis (Biemar and Foti, 2013).

Squamous cell oesophageal cancer, also known as Oesophageal Squamous Cell Cancer (OSCC), is ranked 8th as the most common cancer and 6th major cause of cancer death worldwide (Higuchi et al., 2009). Reports have shown that about 462,000 people are diagnosed with oesophageal cancer worldwide yearly and 386,000 people of this populace die from this pandemic disease (Cancer Research UK, 2005). The incidence rate varies between different geographical regions accounting for an eighteen-fold variation in male, and approximately forty-fold variation, in female rates. Meanwhile, variation in mortality rates is also similar (Cancer Research UK, 2005).

While the knowledge of the aetiology of OSCC remains obscure, tobacco smoking and excessive alcohol consumption, especially those brewed at home and concoction drinking have

consistently been shown to be important risk factors (GLOBOCAN, 2008; Hendricks and Parker, 2002). *N*-nitrosamine compounds are one among the different types of known carcinogens in cigarette smoke which react with DNA to form DNA adducts and affect the helical structure of DNA, leading to defective DNA pairing and synthesis. DNA adducts are known to be elevated in smokers and increase the risk for the development of OSCC. Similarly, ingestion of nitrosamines may also be involved in OSCC. High concentration of nitrosamines in food and tobacco is considered to be of a great risk factor, especially where certain dietary habits, combined with nutritional deficiencies, exist. Humans are exposed to a wide range of N-nitroso-compounds (NOCS) ranging from diet, tobacco smoking and drinking water (Gangolli et al., 1994). Exogenously, preformed nitrosamines are found most often in cured meat products, foods that are preserved through smoking and addition of additives for drying them and other salted preserved foods. Conversely, nitrosamines are formed in the body from the catalyzed reaction between nitrate and nitrite (Gangolli et al., 1994; Lin, 1990).

Chemotherapy is the main therapeutic intervention for treating people living with OSCC. However, drug resistance has rendered it inefficient and ineffective in combating the disease even after combination chemotherapy (Wang et al., 2016). Thus, a major step in improving drug sensitivity is crucial towards improved treatment of OSCC patients (Wang et al., 2010). The distribution of conventional chemotherapeutic agents is not specific within the body where they affect both cancerous and normal cells (Nguyen, 2011). Due to this limitation, the amount of active drug available to the tumor is reduced and results in suboptimal treatment owing to an increase in toxic effects. The advent of molecular therapy as a potent method for targeted therapy in order to overcome the lack of specificity of conventional chemotherapeutic agents has been well documented. Meanwhile, the development of resistance in OSCC cells can by-pass cytotoxicity both in conventional chemotherapeutics and the use of newly improved molecular targeted therapeutics (Cho et al., 2008). Endostatin (ENT) is a naturally occurring, 20-

kDa C-terminal fragment derived from type XVIII collagen. ENT specifically inhibits endothelial cell proliferation and is a potent angiogenesis inhibitor with potent anti-tumoral activity (O'Reilly et al., 1997). Meanwhile, like every other peptide therapeutics, the circulation half-life of ENT is short with rapid renal clearance, in vivo instability and sub-optimal dosage at disease sites (Abdollahi et al., 2004; Zheng, 2009). Therefore, novel strategy designed to ameliorates these limitations and maximize the unique potential of ENT in targeting the angiogenic pathways could be a promising intervention in OSCC management.

Many peptides and proteins have been investigated to possess biological activities that mark them as potential anti-cancer agents. Peptide inhibitors of angiogenesis such as endostatin, are under various stages of clinical trials and development with promising prospective as anti-cancer drugs (Torchilin and Lukyanov, 2003). Peptides as targeting ligands of nanoparticles are becoming even more relevant in cancer research and many are developed from different larger proteins or ligands (Zhang et al., 2012).

Most often, targeting peptides are conjugated with other functional peptides or conjugated with other nanoparticles to augment drug delivery both *in vitro* and *in vivo* (Zhang et al., 2012). The current identification of tumor homing peptides through phage display technology has opened a new strategy for targeted therapy of OSCC diseases. The use of homing peptides in targeted OSCC therapy is due to the fact that their properties are readily combined with that of a toxin or a pro-drug molecule. Targeted therapy restricts the toxic effects of a drug to the malignant tissues, thereby increasing its efficacy and decreasing the undesired side-effects of the drug to normal cells or tissues (Laakkonen, 2007). Both LyP-1, a nine-amino acid-cyclic peptide, and CGKRK (abbreviated as PENT in this study), among other homing peptide types, have been shown to inhibit tumor growth in a tumor-bearing mice when conjugated with fluorescein and doxorubicin as well as serve as tumor imaging tools (Laakkonen, 2007). These two peptides

coupled with other ligands such as folate whose receptors have been shown to be highly expressed in tumor cells were employed in this study to formulate a novel targeted ternary drug delivery system referred to henceforth as the PEL nanosystem, as a potential treatment alternative for OSCC.

1.2. Rationale for this Study

A major challenge in cancer nanomedicine is the issue of non-targeted delivery of conventional cancer therapeutics (Zugazagoitia et al., 2016). Different strategies to circumvent this hurdle are in high demand for the design of potent alternatives including surface modification of smart nanosystems for direct targeting and delivery of their payloads at the disease sites (Malinowsky, 2011). The advent and development of nanoparticles, by employing both passive and active targeting strategies, has been shown to aggravate the intracellular concentration of drugs in cancer cells without its harmful effect in normal cells (Cho et al., 2008). Also, the binding of nanoparticles to targeted receptors allow it an easy entrance into the cell as they are usually engulfed by endosomes through receptor-mediated endocytosis. As such, they can easily escape the recognition by P-glycoprotein and other macrophages from the reticuloendothelial system which are the main drug resistance mechanisms (Nguyen, 2011; Wang and Thanou, 2010). Biodegradable and Food and Drug Administration (FDA) approved polymers including chitosan (CHT) (Sabnis and Block, 2000), polyethylene imine (PEI) (Gordon et al., 2016) and polyethylene glycol (PEG) (Malek et al., 2008) were employed for the synthesis of a novel nano-construct in which ENT was encapsulated.

The use of protein and peptides as efficient cancer therapeutics is limited owing to their rapid elimination from the circulating system as a result of renal filtration, enzymatic degradation, uptake by the reticuloendothelial system and their toxic effects in non-targeted organs or tissues as well as low permeability across cellular membranes (Torchilin and Lukyanov, 2003).

Meanwhile, the effect of enhanced permeability and retention as well as the drainage of macromolecules through the lymphatic system could be averted by incorporating proteins/peptides into polymeric nanoparticles (Wang and Thanou, 2010). Similarly, the use of short homing peptides as molecular targets in cancer nanomedicines has gained enormous considerations over the past decades (Pearce et al., 2012; Svensen et al., 2012). Surface functionalization of the synthesized nanoparticles in this study was achieved using both LyP-1 and PENT as homing peptides.

Furthermore, ligand-targeted delivery system using folate receptors as molecular signature on tumor cells have been well documented (Hilgenbrink and Low, 2005; Leamon and Reddy, 2004; Lu and Low, 2002; Wang and Low, 1998). Thus, folate-decorated nanoparticles as well as both LyP-1 and PENT modified nanoparticulate systems could be promising formulation strategies with specific capabilities for overcoming drug resistance in OSCC therapy since these ligands are usually internalized through receptor-mediated endocytosis.

Angiogenesis, as the process by which new blood vessels are formed, remains a unique mechanism by which tumor vasculatures are developed, sustained, and metastasize in living systems (Folkman, 2006). Targeting the angiogenic pathway has been reported as a promising strategy in cancer nanomedicine, including OSCC (Barzi and Lenz, 2012; Chang et al., 2009). Interestingly, ENT inhibits angiogenesis (Abdollahi et al., 2004) and serve a model drug that inhibits many angiogenic factors within the tumor microenvironments (Hutchinson, 2002; Wan et al., 2013). Therefore, in this study, a novel PEL nanosystem loaded with ENT as treatment modality for anti-angiogenic targets in OSCC was formulated as shown in the schematic depicted in Figure 1.1.

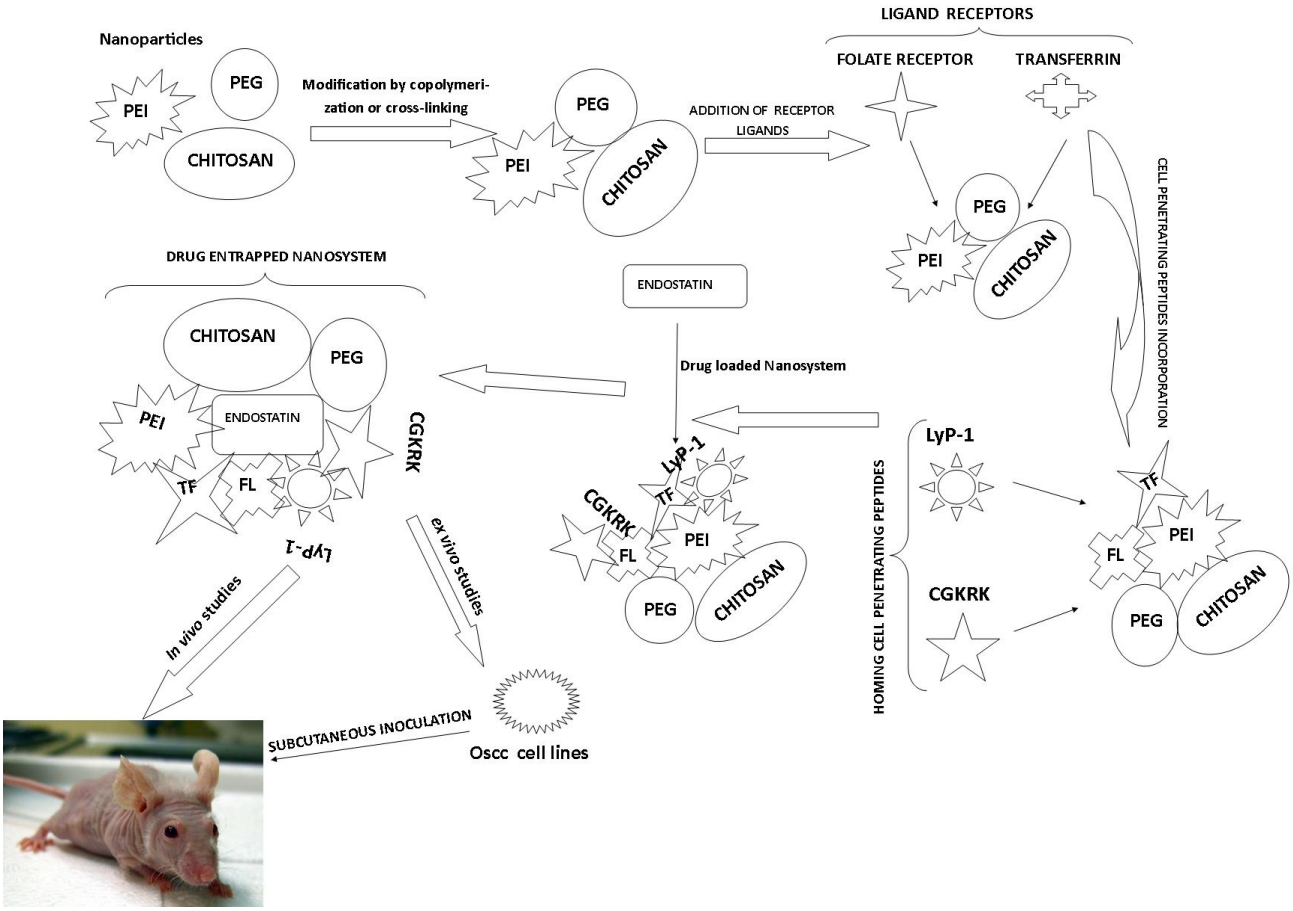


Figure 1.1: Schematic conceptual flow diagram for a novel peptide-enhanced ligand (PEL) functionalized drug delivery system for OSCC management.

1.3. Aim and Objectives

The aim of this study is to carry out comprehensive *in vitro*, *ex vivo* and *in vivo* of PEL nanosystem on OSCC cell lines as a novel ternary drug delivery system comprising of a peptide/ligand/nanoparticle/endostatin conjugates as potential anti-angiogenic treatment strategies. In order to achieve this aim pragmatically, the following specific objectives were performed:

1. Synthesize novel PEG-PEI-CHT nano-conjugates as vector for ENT delivery in OSCC therapy

2. Optimize the synthesized ENT-loaded PEG-PEI-CHT nanoparticles with maximum ENT release for anti-angiogenic effects in OSCC management

3. Design and functionalize the formulated PEG-PEI-CHT ENT-loaded nanoparticles with folic acid for targeted anti-proliferative activity in OSCC treatment

4. Develop a novel LyP-1/PENT functionalized delivery system as a potential targeted therapeutic option for anti-angiogenic effects in OSSC therapy

5. Perform an *in-depth in vitro* cellular characterization of the novel PEL nanosystems as targeted delivery cargoes for enhanced ENT delivery in OSCC cells

6. Evaluate the anti-tumoral efficacy of the ligand and peptide functionalized ENT-loaded nanoparticles on OSCC cells in athymic nude mice model inoculated with KYSE-30 cells.

1.4. Novelty of this Study

The following strategies highlight the novelty of this research:

1. Design and characterization of PEG-PEI-CHT nano-constructs as targeted delivery cargo for endostatin delivery in OSCC management

2. Design, formulation and functionalization of smart folate-decorated PEG-PEI-CHT endostatin-loaded nanoparticles labelled with fluorescein isothiocyanate (FITC) for targeted folate-receptor mediated anti-proliferative effects in OSCC therapy

3. Design and fabrication of an intelligent LyP-1/PENT functionalized PEG-PEI-CHT endostatin-loaded nano-conjugates labelled with FITC with unique homing potentials to nuclear and mitochondrial proteins as molecular signatures on OSCC cells

1.5. Overview of the Thesis

In order to provide a detailed insight into the study, the thesis is sectioned into interwoven chapters that provide a logical and holistic understanding of the strategies employed in the design and characterization of the PEL nanoparticulate system in OSCC management.

Chapter 1 contextualizes the global burden and treatment alternatives for the cancer pandemic, the rationale and motivation for this research, the novelty, as well as the aim and specific objectives of this study.

Chapter 2 reviews the challenges encountered in cancer nanomedicines, the unique influence of nanoparticulate systems for enhanced drug delivery, and possible smart delivery options using ligands and short homing peptides as drivers of drug-loaded nano-constructs to facilitate the targeted delivery of their payloads at disease sites with optimal dosage, increased therapeutic effects, and prolonged circulation half-life without harm to healthy cells.

Having contextualized the theoretical basis for the design of a smart PEL nanosystem for the delivery of potent cancer therapeutics, **chapter 3** ushers in the preliminary design, formulation and characterization of endostatin-loaded nanoparticles for anti-angiogenic effects in OSCC management. The novel methodology employed in grafting the biodegradable PEG-PEI-CHT polymer conjugates was affirmed while the response of the nanoparticulate system to changing pH environments was evaluated. *In-depth* physicochemical properties of the PEG-PEI-CHT conjugates were examined using various conventional techniques to validate the successful conjugation of the native polymers.

Chapter 4 discusses the detailed parameters that influenced the optimization of the PEG-PEI-CHT polymer conjugates including the concentration of the chitosan backbone, Sodium triphosphate (TPP) concentration as a polyanionic agent using Box-Behnken Design. The surface desolvation of PEG on ENT loading and release as well as the protonating influence of PEI for enhance binding of the synthesized nanoparticles to the negatively charged surfaces of KYSE-30 cells, as model cells for OSCC, were investigated.

The successful design and optimization of the nanoparticulate system led to the surface functionalization of the ENT-loaded nanoparticles using folic acid as presented in **chapter 5**. Folate directed endostatin-loaded nanoparticles showed higher anti-proliferation against OSCC cells *in vitro.* The migratory response of KYSE-30 cells was inhibited while the anti-tumoral efficacy of endostatin was improved upon encapsulated with the Folate functionalized nano-constructs.

Chapter 6 highlights the specific targeting of nuclear and mitochondrial proteins using both LyP-1 and PENT as molecular drivers of endostatin-loaded nanoparticles to OSCC cells. LyP-1 and PENT functionalized nanoformulations exhibited increased anti-angiogenic properties on KYSE-30 cells. KYSE-30 cell migration was impeded while both metallomembrane protease 2 (MMP2) and vascular endothelial growth factor C (VEGF-C), as potent angiogenic factors, were significantly reduced when quantified using ELISA assays.

After a thorough *in vitro* characterization of the PEL nanosystems in Chapters 4, 5 and 6, the *in vivo* performance of the PEL endostatin-loaded nanoparticle was evaluated in **Chapter 7** to further ascertained its anti-tumoral efficacy. More so, the correlation between the *in vitro* and *in vivo* release behaviors of endostatin within the PEL nanoparticles was investigated. Histological assessment and marked reduction in solid tumor size are key indices to predicting significant anti-tumoral changes in cancer nanomedicines.

Chapter 8 provides the summary of the overall findings of this research, followed by proactive recommendations for the PEL nanosystem and prospective outlooks for efficient utilization of this current design in OSCC management.

1.6. Concluding Remarks

Overcoming drug resistance is the hallmark of cancer nanomedicine. Design of smart and intelligent nanoparticulate systems that can facilitate direct and specific targeting of cancer therapeutics are gold standards for enhanced management OSCC. The novel PEL nanosystem can be considered an alternative strategy for targeted delivery of endostatin for anti-angiogenic activity in OSCC therapy by by-passing the reticulo-endothelial system and resistance from glycoproteins inherent within biological systems. Interestingly, this novel development has the capacity to improve the bioavailability and sustained release of ENT specifically to the tumor sites for enhanced anti-tumoral effect. The next chapter reviews the role of nanotechnology in the design of smart nanosystems for targeted delivery of cancer chemotherapeutics in OSCC.

1.7. References

Abdollahi, A., Hahnfeldt, P., Maercker, C., Gröne, H.-J., Debus, J., Ansorge, W., Folkman, J., Hlatky, L., Huber, P.E., 2004. Endostatin's antiangiogenic signaling network. Mol. Cell 13, 649–663.

American Cancer Society, 2011. Global Cancer Facts & Figures 2nd Edition.

Barzi, A., Lenz, H.-J., 2012. Angiogenesis-related agents in esophageal cancer. Expert Opin. Biol. Ther. 12, 1335–1345.

Biemar, F., Foti, M., 2013. Global progress against cancer—challenges and opportunities. Cancer Biol. Med. 10, 183–186.

Cancer Research UK, 2005. CancerStats Worldwide Cancer.

Chang, D.-K., Chiu, C.-Y., Kuo, S.-Y., Lin, W.-C., Lo, A., Wang, Y.-P., Li, P.-C., Wu, H.-C., 2009. Antiangiogenic Targeting Liposomes Increase Therapeutic Efficacy for Solid Tumors. J. Biol. Chem. 284, 12905–12916.

Cho, K., Wang, X., Nie, S., Chen, Z.G., Shin, D.M., 2008. Therapeutic nanoparticles for drug delivery in cancer. Clin. Cancer Res. Off. J. Am. Assoc. Cancer Res. 14, 1310–1316.

Folkman, J., 2006. Antiangiogenesis in cancer therapy--endostatin and its mechanisms of action. Exp. Cell Res. 312, 594–607.

Gangolli, S.D., van den Brandt, P.A., Feron, V.J., Janzowsky, C., Koeman, J.H., Speijers, G.J., Spiegelhalder, B., Walker, R., Wisnok, J.S., 1994. Nitrate, nitrite and N-nitroso compounds. Eur. J. Pharmacol. 292, 1–38.

GLOBOCAN, 2008. Oesophageal cancer risk in South Africa WCRF. http://globocan.iarc.fr/

Gordon J. Lutz, Shashank R. Sirsi, Jason H. Williams., 2016. PEG–PEI Copolymers for Oligonucleotide Delivery to Cells and Tissues. Gene Therapy Protocols, Volume 433 of the series Methods in Molecular Biology™ pp 141-150.

Hendricks, D., Parker, M.I., 2002. Oesophageal Cancer in Africa 263–268.

Higuchi, K., Koizumi, W., Tanabe, S., Sasaki, T., Katada, C., Azuma, M., Nakatani, K., Ishido, K., Naruke, A., Ryu, T., 2009. Current Management of Esophageal Squamous-Cell Carcinoma in Japan and Other Countries. Gastrointest. Cancer Res. 3, 153–161.

Hilgenbrink, A.R., Low, P.S., 2005. Folate receptor-mediated drug targeting: From therapeutics to diagnostics. J. Pharm. Sci. 94, 2135–2146.

Hutchinson, E., 2002. Angiogenesis: Endostatin and Wnt signalling. Nat. Rev. Cancer 2, 643–643.

Laakkonen, P., 2007. Tumour-homing peptides : tools for targeting , imaging and destruction 35, 780–783.

Leamon, C.P., Reddy, J.A., 2004. Folate-targeted chemotherapy. Adv. Drug Deliv. Rev. 56, 1127–1141.

Lin, J.K., 1990. Nitrosamines as potential environmental carcinogens in man. Clin. Biochem. 23, 67–71.

Lu, Y., Low, P.S., 2002. Folate-mediated delivery of macromolecular anticancer therapeutic agents. Adv. Drug Deliv. Rev., Polymer Conjugates for Cancer Therapy 54, 675–693.

Malek, A., Czubayko, F., Aigner, A., 2008. PEG grafting of polyethylenimine (PEI) exerts

different effects on DNA transfection and siRNA-induced gene targeting efficacy. J. Drug Target. 16, 124–139.

Malinowsky, K., 2011. Targeted therapies in cancer - challenges and chances offered by newly developed techniques for protein analysis in clinical tissues. J. Cancer 26.

Nguyen, K.T., 2011. Targeted Nanoparticles for Cancer Therapy: Promises and Challenges. J. Nanomedicine Nanotechnol. 2.

O'Reilly, M.S., Boehm, T., Shing, Y., Fukai, N., Vasios, G., Lane, W.S., Flynn, E., Birkhead, J.R., Olsen, B.R., Folkman, J., 1997. Endostatin: an endogenous inhibitor of angiogenesis and tumor growth. Cell 88, 277–285.

Pearce, T.R., Shroff, K., Kokkoli, E., 2012. Peptide Targeted Lipid Nanoparticles for Anticancer Drug Delivery. Adv. Mater. 24, 3803–3822.

PEG–PEI Copolymers for Oligonucleotide Delivery to Cells and Tissues - Springer, 2008. . In: Methods in Molecular Biology™. Humana Press.

Sabnis, S., Block, L.H., 2000. Chitosan as an enabling excipient for drug delivery systems. I. Molecular modifications. Int. J. Biol. Macromol. 27, 181–186.

Svensen, N., Walton, J.G.A., Bradley, M., 2012. Peptides for cell-selective drug delivery. Trends Pharmacol. Sci. 33, 186–192.

Torchilin, V.P., Lukyanov, A.N., 2003. Peptide and protein drug delivery to and into tumors : challenges and solutions 8, 259–266.

Wan, Y.-Y., Tian, G.-Y., Guo, H.-S., Kang, Y.-M., Yao, Z.-H., Li, X.-L., Liu, Q.-H., Lin, D.-J., 2013. Endostatin, an angiogenesis inhibitor, ameliorates bleomycin-induced pulmonary fibrosis in rats. Respir. Res. 14, 56.

Wang, H., Yao, Z., Tang, H., Zhao, Y., Zhang, X., Yao, S., Yang, S., Liu, Y., 2016. Weekly nanoparticle albumin-bound paclitaxel in combination with cisplatin versus weekly solvent-based paclitaxel plus cisplatin as first-line therapy in Chinese patients with advanced esophageal squamous cell carcinoma. OncoTargets Ther. 9, 5663–5669.

Wang, M., Thanou, M., 2010. Targeting nanoparticles to cancer. Pharmacol. Res., Towards clinical applications of nanoscale medicines 62, 90–99.

Wang, S., Low, P.S., 1998. Folate-mediated targeting of antineoplastic drugs, imaging agents, and nucleic acids to cancer cells. J. Controlled Release 53, 39–48.

Wang, Z., Li, Y., Ahmad, A., Azmi, A.S., Kong, D., Banerjee, S., Sarkar, F.H., 2010. Targeting miRNAs involved in cancer stem cell and EMT regulation: An emerging concept in overcoming drug resistance. Drug Resist. Updat. 13, 109–118.

Zhang, X., Eden, H.S., Chen, X., 2012. Peptides in cancer nanomedicine : Drug carriers , targeting ligands and protease substrates. J. Controlled Release 159, 2–13.

Zheng, M., 2009. Endostatin derivative angiogenesis inhibitors. Chin. Med. J. (Engl.) 122, 1947–1951.

Zugazagoitia, J., Guedes, C., Ponce, S., Ferrer, I., Molina-Pinelo, S., Paz-Ares, L., 2016. Current Challenges in Cancer Treatment. Clin. Ther. 38, 1551–1566.

CHAPTER 2

FUNCTIONALIZED NANOCARRIERS FOR ENHANCED BIOACTIVE DELIVERY TO SQUAMOUS CELL CARCINOMAS: TARGETING APPROACHES AND RELATED BIOPHARMACEUTICAL ASPECTS

2.1. Introduction

Cancer has been described as one of the major and leading causes of death worldwide (Hauert and Bhatia, 2014). The global burden of cancer as reported by the International Agency for Research on Cancer (IARC) showed that cancer incidence has increased to twice its previous occurrence in the past 30 years. By the year 2030, it has been postulated that over 21.4 million new cases of cancer could be expected, with 17 million cancer deaths annually, and a total of 75 million people living with cancer within five years of diagnosis. The World Health Organization report showed that in 2012, 8.2 million people died from cancer globally of which 60% of the new cases reported annually were from Africa, Asia, Central and South America and only 30% of cancers could be prevented (WHO, 2014).

Squamous-cell carcinoma (SCC) is a type of cancer that originates from a type of epithelial cell known as the squamous cell. Squamous cells are the main portion of the epidermis of the skin, and this cancer type accounts for the major forms of skin cancer. Squamous cells also occur in the lining of the upper respiratory and digestive tracts, and other areas of the body. SCC thus occurs as a form of cancer in diverse tissues, including the lips, mouth, oesophagus, head and neck, urinary bladder, prostate, lung, vagina, and cervix (Kato and Torigoe, 1977; Gurudutt and Genden, 2011; Zakkouri et al., 2011; Markopoulos, 2012;). Despite sharing the same classification, the SCC of different body sites can show tremendous differences in their

prevalence, presenting symptoms, natural history, prognosis, and response to treatment. An estimated 700,000 cases of SCC are diagnosed each year in the US, resulting in approximately 2,500 deaths. Of these, however, oral cancer accounts for 2-4 % of all cancer cases (Markopoulos, 2012), while squamous cell oesophageal cancer is ranked 8th as the most common cancer type and 6th major cause of cancer death worldwide (Hendricks and Parker, 2002).

While the knowledge of the etiology of SCC remains obscure, tobacco smoking and excessive alcohol consumption, especially those brewed at home and concoction drinking have consistently been shown to be important risk factors (Hendricks and Parker, 2002). N-nitrosamine compounds are one among different types of known carcinogens in cigarette smoke which react with DNA or RNA molecules to form DNA adducts and affect the helical structure of DNA, leading to defective DNA pairing and synthesis (Lin, 1990). DNA adducts are known to be elevated in smokers and increase the risk for the development of SCC (Jakszyn and Gonzalez, 2006). Human papillomavirus (HPV) has also been identified as a causative agent for different cancer types due to SCC (Fakhry et al., 2008). Additionally, the most significant contribution to skin cancer due to SCC is a result of ultraviolet radiation (UVR) exposure (Bickers et al., 2006)

Chemotherapy is the main therapeutic intervention for treating people living with SCC. However, drug resistance has rendered it inefficient and ineffective in combating the disease even after combination chemotherapy. Thus, a major step in improving drug efficacy is crucial towards improved treatment of SCC patients (Wang and Thanou, 2010).

The recent advent of nanoparticles a few decades ago has shown great potential in overcoming the barriers to the delivery of several traditional pharmaceuticals. This has led to the emergence of different drug delivery platforms into clinical treatments of cancer diseases. Until now, the

huge success achieved through the development of liposomal anthracycline drug doxobubicin, as nano-therapeutics by exploiting the leaky vasculature of the tumor microenvironment has been globally accepted and approved by Food and Drug Administration (FDA) for clinical use as a nanoparticle-based drug therapy for cancer. This formulation was coated with polyethylene glycol (PEG) with an average size of 100 nm to minimized the clearance of the liposome from the blood and increase the half-life of the drug (Pearce et al., 2012).

Numerous peptides and proteins have been investigated that possess biological activities that mark them as potential anti-cancer agents. Peptide inhibitors of angiogenesis such as endostatin, are under various stages of clinical trials and development with promising prospective as anti-cancer drugs (Torchilin and Lukyanov, 2003). Peptides as targeting ligands of nanoparticles are becoming even more relevant in cancer research and many are developed from different larger proteins or ligands. Most often, targeting peptides are conjugated with other functional peptides or conjugated with other nanoparticles to augment drug delivery both *in vitro* and *in vivo* (Zhang et al., 2012). The current identification of tumor homing peptides through phage display technology has opened a new strategy for targeted therapy of SCC diseases. The use of homing peptides in targeted SCC therapy is due to the fact that their properties are readily combined with that of a toxin or a pro-drug molecule. Targeted therapy restricts the toxic effects of a drug to the malignant tissues, thereby increasing its efficacy and decreasing the undesired side-effects of the drug to normal cells or tissues (Enbäck and Laakkonen, 2007).

Despite the advances in cancer nanomedicine, targeted approaches in the delivery of therapeutics for the treatment of squamous cell carcinoma related tumours have not been well established. Many of the research and review documents on cancer nanomedicine are focused on other cancer types with little reference to targeted approaches in SCC. Thus, our focus in this chapter is to highlight and explore some of the current convectional drugs in cancer

nanomedicine, cutting edge nanotechnologies for nanoparticle synthesis, possible targeted formulations for squamous cell carcinomas with focus on folate and transferrin receptors as ligand receptors, and the potential application of homing peptides as specific targeting moieties on nano-constructs for the destruction of cancer cells and vasculature with respect to SCC.

2.2. Current Conventional Chemotherapy in Squamous Cell Carcinoma

While chemotherapy still remains an important therapeutic strategy for cancer treatment, its inability to completely remove all tumor cells due to intrinsic or acquired drug resistance, which is the most common cause of tumor recurrence, has been a major setback in its holistic application (Kibria et al., 2013). Conventional chemotherapy employs the use of drugs whose bioavailability and absorption depends of several factors such as solubility, molecular weight, pKa, number of hydrogen bonds attached to each atom of the molecule and chemical stability, which all limit the achievement of an effective therapeutic response of the drug (He and Shi, 2014; Vilar et al., 2012a) . Meanwhile, the low molecular weight of conventional chemotherapeutics account for their rapid renal clearance which results in frequent administration and/or high dosage to achieve a therapeutic effect (Vilar et al., 2012b). Thus, the use of combinational chemotherapeutics approach has been employed in cancer therapy. The distribution of conventional chemotherapeutic agents is not specific within the body where they affect both cancerous and normal cells. Due to this limitation, the amount of active drug available to the tumor is reduced and results in suboptimal treatment owing to an increase in toxic effects. The advent of molecular therapy as a potent method for targeted therapy in order to overcome the lack of specificity of conventional chemotherapeutic agents has been well documented. Meanwhile, the development of resistance in cancer cells can by-pass cytotoxicity both in conventional chemotherapeutics and the use of newly improved molecular targeted therapeutics (Cho et al., 2008b). Therefore, research into drug delivery systems aim to improve both the pharmacokinetic and pharmacodynamics properties of chemotherapeutic agents

including absorption, distribution, metabolism, excretion, mechanism of action, pharmacological response and affinity to the site of action.

Various Food and Drug Agency (FDA) approved chemotherapeutic agents including paclitaxel, doxorubicin, 5-fluorouracil, irinotecan (camptosar), topotecan (hycamptin) and cisplastin have been investigated as anticancer agents as listed in Table 2.1. Several other antiangiogenic drugs are in clinical trials for cancer therapy. Bandyopadhyay and co-workers investigated the potential synergistic anti-tumor activity of doxorubicin in combination with TbR1-KI in animal models of metastatic breast cancer (Bandyopadhyay et al., 2010). Their results showed that combination of Doxorubicin and TbRI-KI enhanced the efficacy of doxorubicin in reducing tumor growth and lung metastasis in the 4T1 orthotopic xenograft model in comparison to single treatments. Irinotecan (CPT-11), a water soluble derivative of camptothecin, was pegylated (NKTR-102) in a preclinical model. Its accumulation in the tumor was found to be 300-fold increase compared to that of topo 1 inhibitor (Li et al., 2013). The result showed that NKTR-102 had a wider range of activity in a broad spectrum of tumors. NKTR-102 is currently in phase II of clinical studies for patients with metastatic breast cancer as well as in phase III for patients with solid malignant tumors including ovarian cancer (Hoch et al., 2009). Paclitaxel as strong anti-cancer drug is currently limited in its administration due to its adverse side effect and hydrophobicity. Meanwhile, Zhang and his co-workers conjugated paclitaxel in a covalent reaction with monomethoxy-poly(ethylene glycol)-b-poly(lactide) (MPEG-PLA) block copolymer. The antitumoral effect of the conjugated paclitaxel against human liver cancer H7402 cell lines using the MTT assay was found to be cytotoxic against H7402 cells (Zhang et al., 2005). The use of cis-dichlorodiamminoplatinum (Cisplatin) in the treatment of varieties of cancers including lymphoma, testicular cancer, and glioma has been well documented (X. Li et al., 2008). However, its short blood circulation time and grave cytotoxic effect have limited its full application as a chemotherapeutic agent. Aronov and colleagues conjugated the platinum group

of cisplatin to folate-targeted PEG as a carrier. The nano system was able to explore the folate receptor-mediated endocytosis (FRME) framework, thus increasing its circulation time in the blood (Aronov et al., 2003).

Table 2.1: Examples of some current conventional drugs for cancer therapy

Convectional chemotherapeutics	**Target tumour cell or tissue**	**Molecular targets**	**References**
Doxorubicin	Human and murine breast cancer cells	TGFβ type I receptor kinase inhibitor (TβRI-KI)	(Bandyopadhyay et al., 2010)
Paclitaxel	Ovarian carcinoma cells	c-Jun N-terminal kinase/stress-activated protein kinase (INK/SAPK), cyclin-dependent kinases	(Kajiyama et al., 2007)
Cetuximab	Human hepatoma cells	Epidermal growth factor receptor (EGFR)	(Fuchs et al., 2008)
Tamoxifen	Breast cancer cells	tyrosine-phosphorylated β-catenin	(Kim et al., 2009)
Erlotinib	Human hepatoma cells; lung cancer	Epidermal growth factor receptor (EGFR)	(Yauch et al., 2005)
Gefitinib	Head and neck squamous cell carcinoma; non-small-cell lung carcinoma	Epithelial growth factor receptor tyrosine kinase (EGFR-TK)	(Frederick et al., 2007)
Cisplatin	Pancreatic cancer cells	Zeb-1: (transcriptional suppressor of E-cadherin)	(Arumugam et al., 2009)
Lapatinib	Breast cancer	EGFR and HER2 tyrosine kinases	(Konecny et al., 2008)
5-fluorouracil	Pancreatic cancer cells	Zeb-1: (transcriptional suppressor of E-cadherin)	(Arumugam et al., 2009)
Gemcitabine	Pancreatic cancer cells	Notch-2, Jagged-1,	(Z. Wang et

		vimentin, ZEB1, Slug, Snail, nuclear factor- κI5, and β-catenin	al., 2009)
Oxaliplatin	Colorectal cancer cells	E-cadherin, beta-catenin, plakoglobin, Snail, and kappaB	(Yang et al., 2006)

2.3. Application of Polymeric Materials and their Limiting Factors in Cancer Nanomedicine

The use of polymeric materials for the delivery of chemotherapeutic agents has contributed immensely to circumventing some of the challenges faced by current conventional chemotherapeutics in cancer management. Polymeric materials are often used for controlled drug release systems in which specific chemotherapeutic agents are either embedded into or conjugated to the polymeric matrices thereby increases the bioavailability of the drug, by-pass the resistance due to the reticuloendothelial system (RES) as well as enhances the chances of reaching its exact target with optimal therapeutic effect having the correct dosage. Polymers used in controlled drug release systems are usually referred to as therapeutic polymers and possess distinct physicochemical properties. Thus, the formulation strategy for the design of an effective drug release system takes into consideration the size, shape, the surface composition in term of charge and coating, and the material make-up of the polymer (Vilar et al., 2012a; Wang et al., 2011). These combinations influence its mobility and its interaction with the environment (Figure 2.1). Examples of frequently used biodegradable polymeric materials for the preparation of nanoparticles, their methods of preparation, as well as the encapsulated therapeutics are presented in Table 2.2 and 2.3.

The size of a nanoparticle has been well documented to affect its time of circulation, extravasation, its diffusion rate and internalization into the cellular compartments (Dreaden et

al., 2012). Meanwhile, nanoparticles which are less than 5nm have a shorter circulation time with swift entrance into tumor cells and diffuse across the tumor tissue (Soo Choi et al., 2007); thus making their retention within the tumor cell more challenging since they are rapidly filtered by the kidney and rapid renal clearance in the urine. However, nanoparticles with larger size ranging between 5nm and 500nm have a higher circulatory retention time and aggregate in solid tumors by passing through the enlarged pores in angiogenic vessels by the enhanced permeability and retention (EPR) effect (Maeda et al., 2013). Nanoparticle size also affects its cellular internalization since different nanoparticle sizes are transported through diverse endocytic channels (Wang et al., 2011). For instance, Nagayama and co-workers reported that the biodistribution of polystyrene nanoparticles with thesame composition and different particle sizes of 50 and 500nm respectively displayed a higher level of agglomeration of the larger nanoparticles in the liver cell (Nagayama et al., 2007). Meanwhile, the uptake of the 50 nm size polystyrene nanoparticle in the hepatic cell was much faster at the lower temperature of 4^0C against 37^0C. It was suggested that the possible mechanism of hepatic uptake was mediated by surface absorption of proteins leading to opsonisation. In the same vein, pegylated PHDCA nanoparticles of varying size range of small (<100 nm), medium (100-200 nm) and large (>200 nm), were shown to influence protein absorption when incubated with serum protein for 2 hours (Fang et al., 2006). A significant correlation between particle size and protein absorption was observed among the different nanoparticle sizes having the same formulation. Small nanoparticle (80 nm) showed protein absorption of 6% as opposed to 23% and 34% serum protein quantified with large nanoparticle sizes of 171 and 243 nm respectively.

The shape of a nanoparticle also has a pertinent effect on its cellular update. Spherical nanoparticles have been shown to exhibit high cellular uptake especially in situations such as tumor environments (GENG et al., 2007). Nanoparticles with high aspect ratios with rigid morphology have been reported to aggregate more slowly in macrophages than those with both

a small and flexible morphology, which increases their retention time within the blood and subsequently reduces their clearance time from the blood stream (Hauert and Bhatia, 2014; Venkataraman et al., 2011). Different toxicities of materials with similar chemical composition (silica), but different shape (nanowire vs nanoparticle), has been reported (Adili et al., 2008). It was mainly observed that silica nanoparticles exhibited very little cytotoxicity even at the highest concentrations as opposed to silica nanowires when tested *in vivo* using two different human epithelial cell lines. These results showed that structural differences in term of shape between silica nanomaterials have commensurate effects on interaction of these nanomaterials with cells.

The circulation time of a nanoparticle is also affected by its charge. The opsonisation of charged particles is high and they are rapidly cleared by the immune system (Owens III and Peppas, 2006). Charged nanoparticles are preferentially engulfed by tumor cells than their uncharged counterparts once they are in a tumor environment. Various research has been conducted in constructing shielded nanoparticles that undergo removal of their neutral coatings once they enter a tumor environment, due to changes in pH or enzymatic activity, to release their charged interior (Romberg et al., 2008). As such, passive coating, using polyethylene glycol has been well employed in order to shield the charge of nanoparticles, increase their circulation time, as well as enhance their aggregation in tumor tissue (Petros and DeSimone, 2010). In the same vein, the challenges faced by the engulfment of nanoparticles by phagocytes can be reduced by coating it with “self-peptides” derived from the human “don’t eat me” receptor CD47 (Rodriguez et al., 2013). In an experiment conducted by Kommareddy and colleagues, the *in vivo* long time circulating potential, biodistribution and passive tumor targeting of PEG-modified thiolated gelatin nanoparticles (~250 nm; ca. -5 mV) were evaluated by injecting indium-111 (111In)-labeled nanoparticles into breast tumor (MDA-MB-435)-bearing nude mice (Kommareddy and Amiji, 2007). PEGylated thiolated nanoparticles were found to have longer circulation times, with

the plasma and tumor half-life of 15.3 and 37.8 hours, respectively than nonthiolated nanoparticles with very short half-life of ~3 hours. The results also showed preferential localization of thiolated nanoparticles in the tumor mass. The reason for such an effect induced by the thiolated functional group on the surface of the nanoparticles is not yet well established. However, it could be as a result of aggregation of nanoparticles through the disulfide bond formation or reaction with thiolated molecules circulating in the blood. Meanwhile, it has been established that neutral or negatively charged surface nanoparticles possessed a reduced plasma protein adsorption and low rate of nonspecific cellular uptake (Alexis et al., 2008).

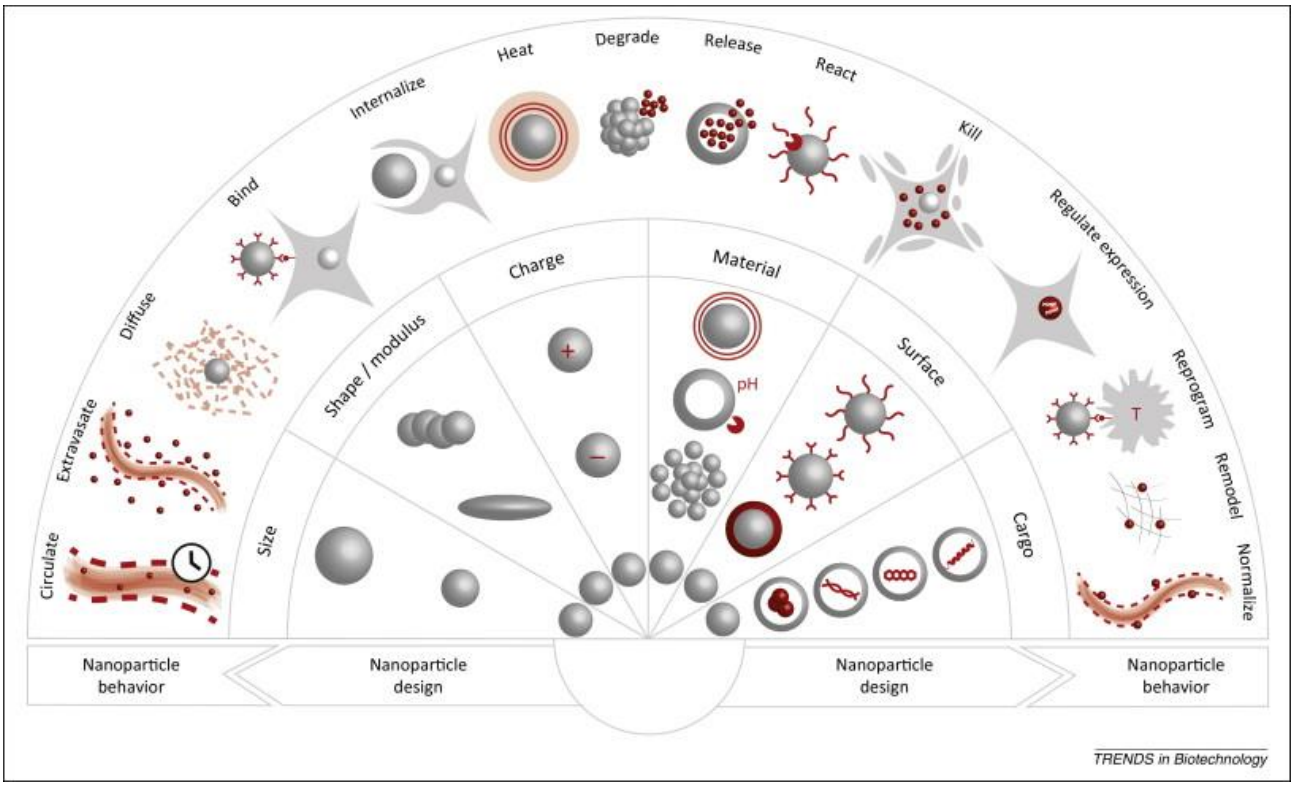


Figure 2.1: Nanoparticle designs, in terms of size, shape, modulus, charge, material, surface, and cargo, as well as their interactions in the body, determines their individual behaviour. Reprinted under the permission of (Hauert and Bhatia, 2014), (Copyright Elsevier Publishers, 2014).

Table 2.2: Examples of nanoparticles employed in cancer nanomedicine obtained from biodegradable polymers, encapsulants and their methods of preparation

Polymer	Method of preparation	Encapsulant	Size (nm)	References
Alginate/poly-l-lysine	Ionic gelation	Doxorubicin	250-850	(Rajaonarivony et al., 1993)
Chitosan	Ionic gelation	Doxorubicin	213±3	(Janes et al., 2001)
Chitosan	Emulsion-droplet coalescence	Gadopentetic acid	452	(Tokumitsu et al., 1999)
Alginate/chitosan copolymer	Electrostatic interactions	Cisplatin	180-350	(Cafaggi et al., 2007)
Polyethylene oxide-Poly-L-caprolactone. (PEO-PCL) copolymer	Solvent displacement	Tamoxifen	187-207	(Shenoy and Amiji, 2005)
Polyethylene glycol- Poly-L-caprolactone (mPEG-PCL)	Ring-opening polymerization	Taxol	>100	(Kim and Lee, 2001)
Gelatin	Desolvation	Paclitaxel	600-1000	(Lu et al., 2004)
Poly-butyl-cyanoacrylate (PBC)	Emulsion polymerization	Ftorafur	90±15	(Arias et al., 2007)
Poly(ethyl-2-cyanoacrylate)	Emulsion polymerization	Ftorafur	80±30	(Arias et al., 2007)

Table 2.3: Examples of nanoparticles produced from Poly (lactic acid) and its conjugates in cancer nanomedicine

Polymer	Method of preparation	Encapsulant	Size (nm)	References
Poly(lactic acid)	Solvent displacement	Doxorubicin	270	(Némati et al., 1996)
Poly(lactic acid) - poly(glycolic acid) copolymer	Solvent displacement	Doxorubicin	274	(Némati et al., 1996)
Poly(lactic acid) - poly(glycolic acid) copolymer	Emulsion/solvent diffusion	Doxorubicin	<1000	(Yoo et al., 1999)
Poly(lactic acid)	Emulsion/solvent diffusion	DNA	<300	
Poly (D,L-lactic-co-glycolic acid)	Solvent evaporation (single emulsion)	Curcumin & Fluorouracil	5-150	(Balasubramanian et al., 2014)
Poly (D,L-lactic-co-glycolic acid)	Nanoprecipitation	9-Nitrocamptothecin	207 ± 26	(Derakhshandeh et al., 2007)
Poly (D,L-lactic-co-glycolic acid)	Interfacial deposition(nanoprecipitation)	Paclitaxel	<200	(Fonseca et al., 2002)
Poly (D,L-lactic-co-glycolic acid) - mPEG	Double emulsion	Cisplatin		(Avgoustakis et al., 2002)
Poly(lactic acid)	Emulsion/solvent diffusion	DNA	<300	
Poly (D,L-lactic-co-glycolic acid)	Solvent evaporation	Dexamethasone	230	(Gómez-Gaete et al., 2007)
Poly (D, lactic acid)	Emulsion/solvent diffusion	Oridonin	137.3	(Xing et al., 2007)
Poly (D,L-lactic-co-glycolic acid)	Solvent displacement	Xanthones	<300	(Teixeira et al., 2005)

Poly (D,L-lactic-co-glycolic acid)	Interfacial deposition	Rose Bengal	150	(Redhead et al., 2001)
Poly (D,L-lactic-co-glycolic acid)	Solvent evaporation (double emulsion)	Triptorelin	400-600	(Nicoli et al., 2001)
Poly(ethylene glycol)-poly(lactide) copolymer	Solvent evaporation (single emulsion)	Paclitaxel	80	(Yu et al., 2010)

2.4. Targeted Delivery Systems in Squamous Cell Carcinoma

Various cargos such as chemotherapeutics (Wang et al., 2012); small interfering RNA (siRNA) (Kanasty et al., 2013) for the knockdown of genes in tumor cells; antiangiogenic agents (Bocci et al., 2013); agents that disrupt the extracellular matrix (Goodman et al., 2007); imaging agents (Bao et al., 2013) as well as adjuvants that activate the immune system (Moon et al., 2012); are transported by nanoparticles. The main critical objective to be achieved in drug delivery formulation is the efficient and specific delivery of chemotherapeutic agents or the aforementioned cargos to their desired target sites. While a large number of non-viral vectors with variable efficiency are available and are being employed in drug delivery systems, a major setback of most carriers is the lack of specificity to their target sites *in vivo*. Over expression of some receptors at high levels on certain tumor cells can be explored as potential targets that facilitate the binding and delivery of functionalized nanoparticles into the intracellular matrix (Ruoslahti et al., 2010).

The complete sequencing of the human genome and the subsequent delineation of their functions, have provided a rapid identification of a large number of enzymes as novel cancer antigen targets as the expression of all the genes in cancer cells have been identified (Sznol and Davis, 2002). Tumor antigens are useful tumor biomarkers in identifying tumor cells with

diagnostic tests and are potential candidates for use in cancer therapy. Tumor antigens can either be specific or associated. Upon its determination as specific expression in tumor, the antigen can either be used to induce antitumor immune responses or employed as targets for antibody-based therapeutics. Different modern molecular procedures are now being used to discover molecules that are specific to certain tissues or are overexpressed in certain tumors with minimal expression in normal tissues. Some molecules are found to contain certain mutations that are unique to tumor cells. As such, the tumor antigen will usually be specific to a patient and therefore requires the identification of the mutation in the individual patient, as well as designing a vaccine suitable exclusively for said patient. Meanwhile, several other tumor specific antigens are expressed in many patients therefore allowing for the development of an "off-the-shelf vaccine" (Sznol and Davis, 2002).

2.4.1. Exploring the Enhanced Permeability and Retention (EPR) Effect for Passive Targeting

To circumvent the current drawbacks in current convectional cancer chemotherapeutics such as damage to normal and healthy tissues leading to systemic cytotoxicity and sub-optimal dosage which limits their therapeutic efficacy, the use of various nanotechnologies have been employed in cancer therapy (Danhier et al., 2012). The advent and development of nanoparticles, by employing both passive and active targeting strategies, has been shown to aggravate the intracellular concentration of drugs in cancer cells without its harmful effect in normal cells (Cho et al., 2008a). Furthermore, the binding of nanoparticles to targeted receptors allow it an easy entrance into the cell as they are usually engulfed by endosomes through receptor-mediated endocytosis (Figure 2.2). Thus, they can easily escape the recognition by P-glycoprotein and other macrophages from the reticuloendothelial system which is the main drug resistance mechanisms (Cho et al., 2008a).

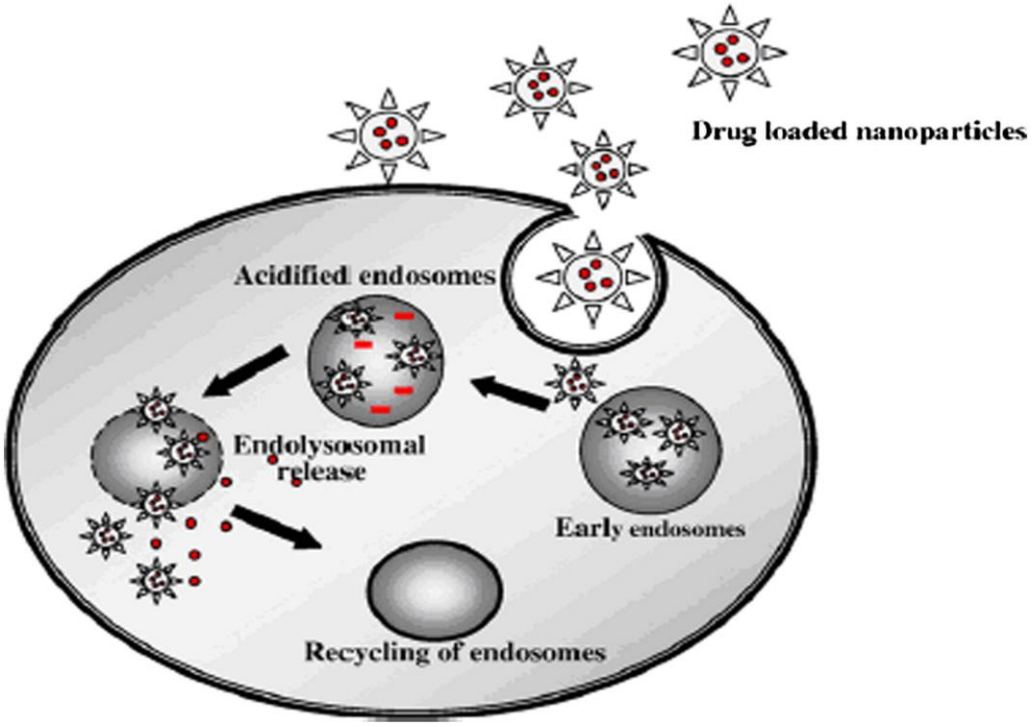


Figure 2.2: Schematic representation of nanoparticle internalization in cells (Danhier et al., 2012) (Copyright Elsevier Publishers, 2011)

Chemotherapeutic agents aimed at solid tumours are encapsulated within nanoparticles in order to alter both their pharmacokinetic and pharmacodynamic profiles. Once a drug is encapsulated, the fate of the drug is no longer dictated by its own intrinsic properties but is instead controlled by the pharmacokinetics of its carriers (Pearce et al., 2012).

Usually, fabricated nanoparticles employ two main strategies to advance tumor cells viz (i) Passive targeting and (ii) Active targeting. The strategy of passive targeting involves the manipulation of the nanoparticle size to exploit the unique anatomical and pathological abnormalities of the tumor vasculature. As such, the smaller size of nanoparticles allow their easy passage into and accumulation inside the interstitial space due to an enhance permeability effect. Meanwhile, the lymphatic vessels are not present in tumour cells or rather ineffective which contribute to the inefficient drainage of the tumor tissue, a phenomenon described as

"enhanced retention" (Danhier et al., 2012; Matsumura and Maeda, 1986). As shown in Figure 2.3, the surface of nanoparticles are functionalized with targeting ligands (Danhier et al., 2010) which are chosen to selectively target and bind specific receptors that are over-expressed by tumor cells or tumor vasculature but are not expressed by healthy cells. The receptor of these ligands has to be homogeneously expressed on all the cells targeted. However, this important factor is a major problem in the choice of targeted ligands to date.

Two cellular targets are often exploited in cancer nanomedicine including (i) the cancer cells and (ii) the endothelial cells of the tumor. A number of over-expressed receptors have been investigated in order to target the cancer cells. These include the transferrin receptors, the epidermal growth factor receptors (EGFR) or integrins, the folate receptors, and the glycoproteins. Specific receptors identified for targeting the endothelial cells of the tumor that have been researched to date are the vascular endothelial growth factor receptors (VEGFR 1 & 2), the integrins ($\alpha_4\beta_3$, $\alpha_5\beta_1$), the vascular cell adhension molecule-1 (VCAM-1), and the matrix metalloproteinase (MMPs). Using these strategies, targeted nanosystems are designed to specifically target and eliminate angiogenic blood vessels and thereby kill tumor cells indirectly (Danhier et al., 2012, 2010).

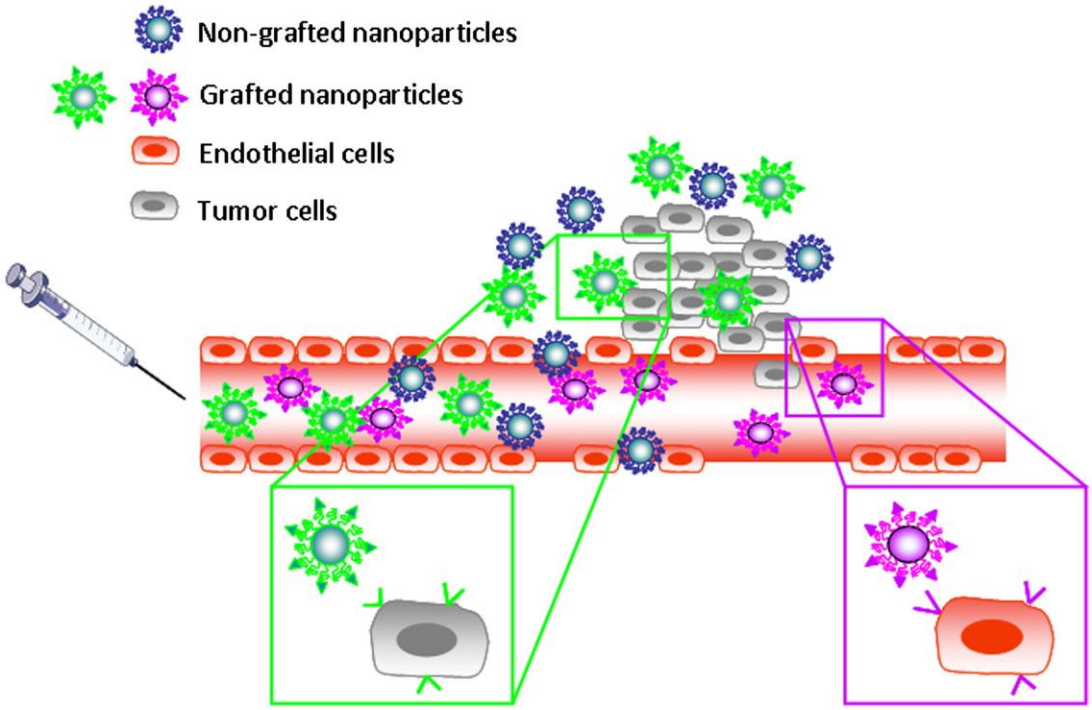


Figure 2.3: Passive and active targeting of nanocarriers. Nanocarriers can reach tumors selectively through the leaky vasculature surrounding the tumors. Ligands grafted at the surface of nanocarriers bind to receptors (over)-expressed by cancer cells (green) or angiogenic endothelial cells (pink) (Danhier et al., 2012) (Copyright Elsevier Publishers, 2011).

2.5. Targeted-Ligand Nanotechnology for an Enhanced Therapeutic Response in Squamous Cell Carcinoma: A Way Forward

In order to specifically target a drug to tumour cells, the discovery and identification of suitable ligands that bind to the cancer cells is necessary in drug delivery research. Meanwhile, natural ligands have been shown to possess strong mitogenic and neoangiogenic activities (Pan et al., 2013). Common ligands such as proteins and peptides, carbohydrates, vitamins, antibodies and aptamers have been applied in different drug delivery systems to increase the specificity of targeting systems (Zhang et al., 2012). Whereas monoclonal antibodies and antibody fragments that serve as ligands have been shown to have specific targets, a major limitation in their application is their immunogenicity (Nechansky and Kircheis, 2010). Conversely, the use of small peptides as targeting moieties, has gained enormous considerations due to their smaller size than antibodies, low immunogenicity, their large scale synthesis by chemical methods,

ability to be incorporated into certain delivery cargos and their ability to achieve high specificity (Chen et al., 2012).

A major aim of attaching a targeted moiety onto the surface of nanoparticles is to promote its selective binding into the cell and internalization into the biological systems. Meanwhile, when targeting ligands are not incorporated unto nanoparticle surface, their interactions with the cell membranes are non-specific and lower even upon their PEGylation (Wang and Thanou, 2010). A number of parameters have been shown to contribute toward the effective targeting of the attached surface ligands aside the nature of the ligand itself. These include (i) the method of ligand loading (Kirpotin et al., 1997) (ii) degree of PEGylation, (Fens et al., 2008) and (iii) ligand density (Shmeeda et al., 2009). Detailed information about the effects of these factors on the effect of the targeting ligand can be found in another review (Wang and Thanou, 2010). On a general note, it is believed that the inclusion of targeted ligands onto nanoparticles does not facilitate their accumulation into tumours. Instead, it shows higher efficacy by increasing the internalization of these functionalized nanoparticles into the tumor cells (Wang and Thanou, 2010) though with some exceptions where both folate and antibody targeted nanoparticles accumulate into the tumors much faster than compared to non-targeted nanoparticles (Song et al., 2009).

A novel urokinase plasminogen activator receptor (uPAR) targeting ligand consisting of an 11-amino-acid sequence named U11 peptide modified with an alkyl chain to form an U11 peptide-lipid amphiphile, targeting the urokinase plasminogen activator receptor was synthesized by Wang and co-workers (M. Wang et al., 2009) to target breast and prostate cancers. RGD peptide, synthesised by phage display technology, has also been shown to have high affinity to $\alpha_5\beta_3$ integrin receptors overexpressed on angiogenic vasculatures (Schiffelers et al., 2003). Many other examples of shorter ligands as targeting moieties for nanoparticle-targeting include

small molecules such as anisamide, a ligand for sigma receptors over-expressed on lung cancer cells (S.-D. Li et al., 2008), and folic acid, specific for the folate receptors on ovarian cells (Pan and Lee, 2004; Zhao et al., 2008) have been well investigated.

2.5.1. Folate receptors: Strategic ligands for targeted nanoconstructs for squamous cell carcinoma

The folate receptor is a 38 kDa glycosylphosphatidylinositol-anchored glycoprotein which binds folic acid at a very low nanomolar affinity (Kamen and Caston, 1986). Once the vitamin is captured, it is transported into the cell via receptor-mediated endocytosis (Antony, 1996). Owing to the overexpression of folate receptors at the endothelial surface of different cancer cell types including ovarian, lung, brain, head and neck, renal cells and breast (Shmeeda et al., 2006), it is often utilized for the specific delivery of folate-linked drugs into cancer cells (Weitman et al., 1992). Indeed, the application of folate-decorated nanoconstructs has been widely explored to deliver various proteins, chemotherapeutic agents, gene therapy vectors, immunogenic haptens, imaging agents, and liposomes into cancer cells by receptor-mediated internalization (Lu and Low, 2002). For instance, recent studies have shown that folate-targeted liposomes containing doxorubicin are more potent than non-targeted liposomes in treating FR-expressing murine leukemias (Pan et al., 2002). In another related experiment, folate-conjugation of liposomes was reported to significantly enhance their uptake to about tenfold into ovarian cancer cells and tumor-associated macrophages within tumor ascites fluid in comparison to ovarian cancer cells devoid of folate attachment (Turk et al., 2004). As opposed to malignant cells, normal healthy cells transport a reduced folate across their membranes but do not transport folate-conjugates of any type (Byrne et al., 2008). There are two general strategies that have been exploited for the targeted delivery of drugs to tumor cells in which folate receptors are fully expressed. These strategies include (i) coupling folate receptor to a monoclonal antibody, and (ii) coupling the folate receptor to a high affinity ligand, folic acid.

Using the first strategy, antibodies including their fragments and derivatives, against the folate receptor have been evaluated for tumor imaging and immunotherapy in clinical investigations. These have shown significant targeting efficacy in ovarian cancer patients (Campbell et al., 1991). Subsequently, folic acid, which is a high affinity ligand of the folate receptor, maintains its receptor binding properties when coupled via its γ-carboxyl group. Thus, conjugating the receptor to folic acid presents an alternative method of targeting the folate receptor for functioning. This strategy has been successfully applied to liposomal drug carriers, *in vitro* receptor-specific delivery of protein toxins, anti-T-cell receptor antibodies, interleukin-2, chemotherapy agents, γ-emitting radiopharmaceuticals, magnetic resonance imaging contrast agents, and gene transfer vectors (Luhrs et al., 1992). Folate receptors have gained enormous application in targeted ligand therapy due to the fact that they are inexpensive, non-toxic, non-immunogenic, easy to conjugate to carriers, retain high binding affinity, and are stable in storage and in circulation (Low and Antony, 2004).

2.5.2. Transferrin receptors

Transferrin is a serum iron-binding glycoprotein devoid of the heme component and function as an iron-transporter to proliferating cells (Singh, 1999). Transferrin has recently gained recognition and application as an important target for cancer therapeutics owing to the increased presence of transferrin receptor at the surface of both metastatic and drug resistant cells as opposed to normal healthy cells (Singh, 1999). Once transferrin binds to its receptors at the cellular surface, transferrin is endocytosed into the acidic compartments of the cell where its iron component is dissociated. Meanwhile, transferrin receptor is abundantly expressed in tumour cells due to the increased demand for iron (Gatter et al., 1983). A number of experiments have been performed in which the transferrin receptor has been explored as targeted ligand for cancer therapeutics in human clinical trials including adriamycin (Faulk et al., 1990), cisplatin (Head et al., 1997), and diphtheria toxin (Rainov and Söling, 2005). The iron-

binding efficiency of the transferrin ligand is a major characteristic for targeting the transferrin receptor since a decrease iron-binding affinity by the ligand resulted in a lower binding efficiency to the transferrin receptor (Bellocq et al., 2003). Davis and his colleagues have recently synthesized transferrin-polymer-drug conjugates (transferrin-PEG-admantane (Tf-PEG-AD) which was used to target malignant tumors including Ewing's sarcoma (Bellocq et al., 2003; Hu-Lieskovan et al., 2005). In another related experiment, the same authors carried out a novel study using transferrin-conjugated liposomes as carriers to deliver small interfering RNA (siRNA) cargo in non-human primates (Heidel et al., 2007). It was further found that these transferrin-conjugated liposomes were efficient in reducing the tumor size in a metastatic mouse model of Edwin's sarcoma. Meanwhile, the safety of the administration of these particles in non-human primates was established (Hu-Lieskovan et al., 2005; Pun et al., 2004). Transferrin has also been conjugated with liposomes to co-encapsulate both doxorubicin and verapamil (Tf-L-DOX/VER) which proved to be effective in overcoming multi-drug resistance (Wu et al., 2007). The cellular uptake of the functionalized cargos was 5.2 and 2.8 times more cytotoxic than the non-targeted liposomes for both doxorubicin and verapamil, respectively. Also, it was reported that there was a reduction in the cytotoxic difference between the targeted and non-targeted liposomes with the incorporation of 2 mg/ml free transferrin. Thus, the importance of transferrin as an effective moiety in targeted therapy for cellular uptake and cytotoxicity of chemotherapeutics was elucidated (Wu et al., 2007).

2.5.3. Homing peptides

Many peptides and proteins have been investigated to possess biological activities that mark them as potential anti-cancer agents. Different approaches for the application of peptides in cancer nanomedicine are presented in Figure 2.4. Peptide inhibitors of angiogenesis such as endostatin are under various stages of clinical trials and development with promising prospective as anti-cancer drugs (Torchilin and Lukyanov, 2003). Peptides as targeting ligands

of nanoparticles are becoming even more relevant in cancer research and many are developed from different larger proteins or ligands. Homing peptides are short peptides of about 3 – 15 amino acids, that specifically recognize, bind and home to either normal tissues or pathological conditions after they are delivered into the system. In this chapter, our focus is on LyP-1 and a lysine rich pentapeptide, CGKRK, as homing peptides that specifically home to tumor cells or vasculature. A list of peptides homing to tumors are presented in Table 2.4 and detailed information about these peptides is available in the literature (Laakkonen and Vuorinen, 2010; Svensen et al., 2012).

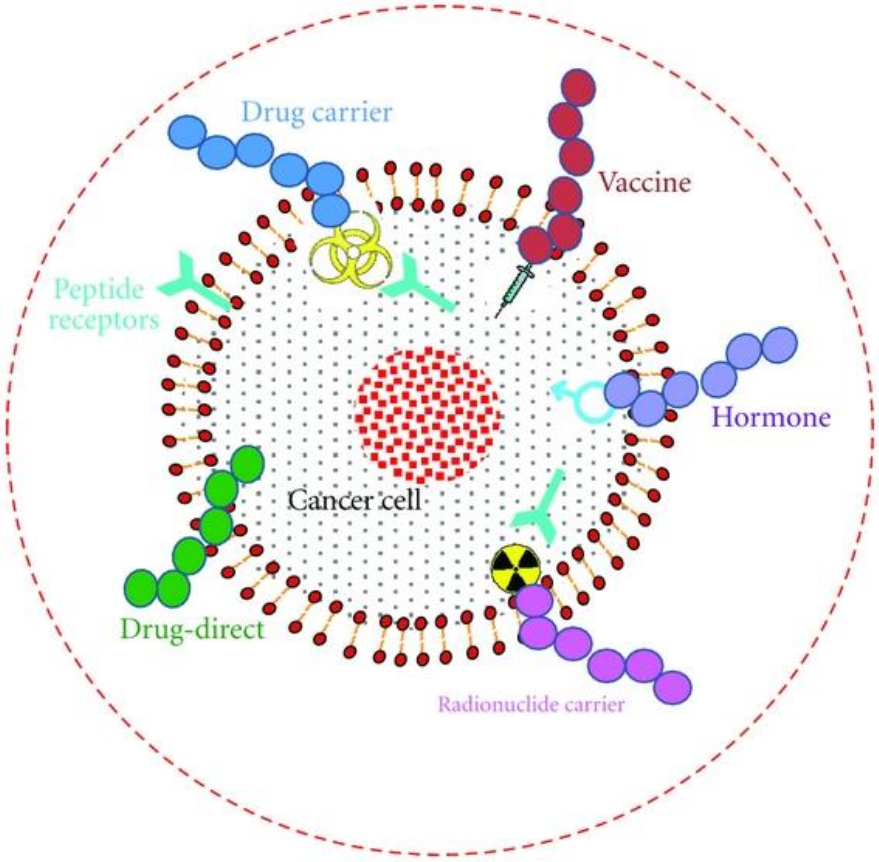


Figure 2.4: Different possible approaches of peptides in cancer nanomedicine. Peptides can be used as anticancer drug, cytotoxic drug carrier, vaccine, hormones, and radionuclide carrier. Figure adapted from (Thundimadathil, 2012).

Peptides that mediate the delivery of therapeutics can been classified into three different groups including (i) Homing peptides which only deliver their cargo to the surface of cells because they do not possess internalization properties (HPs) (Figure 2.5a) (ii) peptides that are coupled to a cell-penetrating peptide (CPP), which facilitates the internalization of their cargo via cell mediated endocytosis or pore formation (Figure 2.5b) and (iii) cell-penetrating homing peptides (CPHPs), which have the ability to internalize without any assistance from external agents (Figure 2.5c) (Svensen et al., 2012).

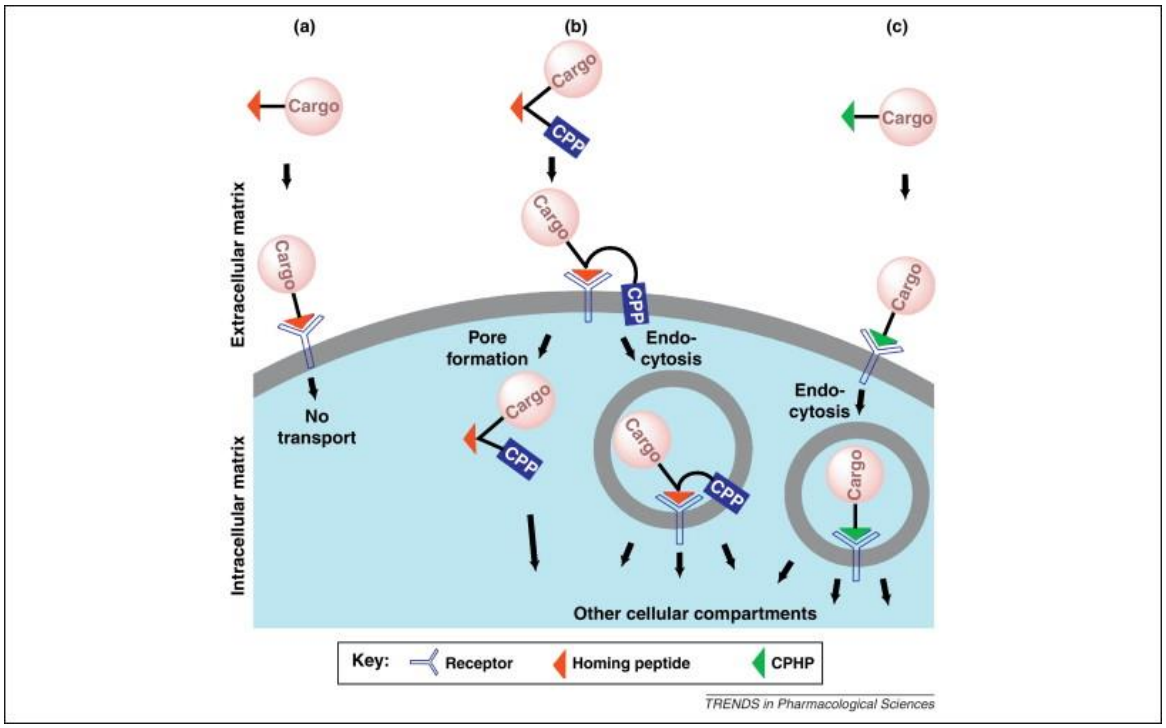


Figure 2.5: Principle of cell-selective peptide targeting and delivery. (a) A homing peptide (HP) has no inherent internalization properties and only delivers its cargo to specific cell-surface receptors. (b) A HP conjugated to a cell-penetrating peptide (HP-CPP) undergoes receptor binding and then typically undergoes cargo internalization via endocytosis or pore formation. (c) A cell-penetrating homing peptide (CPHP) has the ability to internalize without the aid of external agents. Reprinted with permission from (Svensen et al., 2012) (Copyright Elsevier Publishers, 2012).

Different approaches for generating homing peptides with affinity for tissue-specific markers have been identified. Upon the introduction of the concept homing tumour in 1998, a number of

homing peptides have been discovered by both *in vitro* and *in vivo* phage display technology (Svensen et al., 2012). The RDG (Arg-Gly-Asp) (Renata Pasqualini et al., 1997) and NGR (Asn-Gly-Arg) (Arap et al., 1998) peptides were the first two homing peptides that were discovered. Meanwhile, tumor homing of these peptides seem to be independent of the type of tumor, which showed that the receptors of these peptides are upregulated during angiogenesis (Laakkonen and Vuorinen, 2010).

Most often, targeting peptides are conjugated with other functional peptides or conjugated with other nanoparticles to augment drug delivery both *in vitro* and *in vivo* (Zhang et al., 2012). The current identification of tumor homing peptides through phage display technology has opened a new strategy for targeted therapy of SCC diseases. The use of homing peptides in targeted SCC therapy is due to the fact that their properties are readily combined with that of a toxin or a pro-drug molecule. Targeted therapy restricts the toxic effects of a drug to the malignant tissues, thereby increasing its efficacy and decreasing the undesired side-effects of the drug to normal cells or tissues (Enbäck and Laakkonen, 2007). Quite often, the EPR effect is explored in order to improve the aggregation of homing peptide nanoparticle-based delivery systems to tumors. This has helped to channel imaging and therapeutic agents to the primary tumor site. The ability of peptides to bind to various cellular targets with strong affinity and simultaneously attach to the nanoparticles without losing their binding ability accounts for their efficient application as targeting ligands (Pearce et al., 2012). Both LyP-1 and CGKRK; a nine-amino acid-cyclic peptide and a pentapeptide, respectively, among other homing peptide types, have been shown to inhibit tumor growth in a tumor-bearing mouse when conjugated with fluorescein and doxorubicin as well as serve as tumor imaging tools (Enbäck and Laakkonen, 2007). These two peptides coupled with other receptors which have been shown to be highly expressed in tumor cells can be potential targets in SCC therapy and are explored further in this chapter.

Table 2.4: Homing peptides employed in cancer nanomedicine

Sequence (no of amino acids)	Name	Mode of action	Target tumor	Target cell	Receptor	Identification method	Reference
CGKRK (5) CDTRL (5) CGTKRKC (7)	KRK	CPP	Skin carcinoma and dysplastic skin, breast carcinoma	Angiogenic blood vessels and tumor cells	NR	Phage display	(Hoffman et al., 2003)
CRSRKG (6) CRGRRST (7) CKAAKNK (7)	RSR RGR KAA	CPP	Angiogenic islets and Pancreatic tumor	Pericycytes and endothelial cells	NR and PDGFR-beta	Phage display	(Joyce et al., 2003)
CRGDKGPD (8)	Irgd	CPP	Several types of tumor	Angiogenic blood vasculature	Integrin alpha$_v$		(Sugahara et al., 2009)
CGNKRTRGC (9)	LyP-1	CPP	Breast tumor and Osteosarcoma	Tumor cells, lymphatic endothelium	P32/gCIqR	Phage display	(Fogal et al., 2008)
CNRRTKAGC (9)	LyP-2	CPP	Cervical tumor, dysplasia and squamous cell carcinoma of the skin	Lymphatic vessels	NR		(Zhang et al., 2006)
CREAGRKAC (9)	REA		Prostate cancers, breast tumors, cervical cancer, xenografts	Lymphatic vessels	NR	Phage display	(Zhang et al., 2006)
CLSDGKRKC (9)	LSD		Human melanoma and Osteosarcoma xenografts	Lymphatic vessels	NR	Phage display	(Zhang et al., 2006)
CSRPRRSEC (9)			Dysplastic skin	Blood vessels	NR		(Hoffman et al., 2003)
CAGRRSAYC (9)	AGR		Prostate intraepithelial neoplasia	Lymphatic vessels	NR	Phage display	(Zhang et al., 2006)

CDCRGDCFC (9)	RGD-4C		Several types of tumor	Angiogenic blood vasculature	Integrin alpha$_v$		(R. Pasqualini et al., 1997)
TAASGVRSMH (10) LTLRWVGLMS (10)			B16 melanoma	NG2-positive pericytes	NG2	Phage display	(Burg et al., 1999)
SNPFSKPYGLTV (12) YPHYSLPGSSTL (12)	PIVO-8 PIVO-24		Several types of human cancer xenografts	Tumor angiogenesis	VEGF	Phage display	(Chang et al., 2009)
CNGRCVSGCAGRC (13)	NGR		Several types of tumor	Angiogenic blood vasculature	Aminopeptidase N(CD13)	Phage display	(Pasqualini et al., 2000)
HMGN2-NF3 (31)	F3	CPHPs	MDA-MB-435, HL-60	Angiogenic blood vessels and tumor cells	Nucleolin	Phage display	(Christian et al., 2003)

2.5.3.1. LyP-1: A dual-effect homing peptide for targeting tumor cells and vasculature

The lymphatic system has been described as an important route of tumor metastasis. Many cancer types selectively spread through the lymphatics. Recent investigations and findings of growth factors and molecular markers for lymphatic endothelial cells have shown the relationship between tumor cells and the lymphatic vasculature of tumors. Marker proteins such as LYVE-1 (Banerji et al., 1999), podoplanin (Breiteneder-Geleff et al., 1999), and Prox-1 (Wigle et al., 2002) have been widely explored and showed that lymphatic vessels are readily available in the tumor environments and that several tumors also contain lymphatics within the tumor mass (Laakkonen et al., 2002). Meanwhile, the intratumoral lymphatic vessels are usually not functionally involved in transporting tissue fluid (Leu et al., 2000) and are usually filled with tumor cells (Laakkonen et al., 2004a). A number of currently available experimental and clinical data strongly suggest that important factors that possibly determine the ability of a tumor to

metastasize could be attributed to the number of lymphatics in a tumor, the size of the lymphatics as well as the expression of lymphangiogenic growth factors (Pepper, 2001). As such, reducing metastasis by specifically targeting tumor lymphatics as well as the tumor tissue adjacent to these vessels for destruction becomes realistic (Laakkonen et al., 2004b).

LyP-1 is a nine-amino-acid cyclic peptide (CGNKRTRGC) and was identified and isolated from human MDA-MB-435 breast cancer xenografts using the phage display biopanning technique (Laakkonen et al., 2002). Aside from the recognition of tumour-associated lymphatic vessels, LyP-1 identifies a marker that is shared by both the tumour cells and the tumour endothelial cells like other vascular homing peptides (Enbäck and Laakkonen, 2007; Laakkonen et al., 2002). It is often found to accumulate in the nucleus of both the primary tumor cell as well as their metastatic lesions after intravenous injection. LyP-1, binds specifically to the lymphatic vessels in certain tumors, but not to the lymphatics of normal tissues (Laakkonen et al., 2002). Its uniqueness as a homing peptide lies in its ability to cause the apoptosis of the cells to which it binds in addition to its homing and internalization by the lymphatic endothelial cells and tumour cells. The LyP-1 binds to a cell surface form of mitochondrial protein, p32 which serves as its receptor (Fogal et al., 2008). The cytotoxic anti-tumor effect of LyP-1 was seen upon its systemic delivery to tumour-bearing mice as it inhibits the growth of the tumour (Laakkonen et al., 2004b). The Specific homing of the LyP-1 peptide to the tumour- associated lymphatic vessels of certain tumours was the first demonstration that tumour lymphatic vessels can differ from normal lymphatic vessels. LyP-1 has also been successfully employed as tumor imaging tool. Laakkonen and co-workers (Laakkonen et al., 2004b, 2002) investigated the systemic delivery of fluorescein-conjugated LyP-1 to tumor-bearing mice. It was found that LyP-1 was efficiently internalized and accumulated and thereby concentrates the fluorescein to the nuclei of the targeted cells, allowing imaging of the tumours. The homing properties of LyP-1 have also been exploited in the intravenous administration of qdots (nanocrystals that are fluorophores i.e,

substances that absorb photons of light, and subsequently re-emit photons at a different wavelength) in a targeted delivery to tumour cells. LyP-1 coated qdots displayed an outstanding homing specificity for the relevant vascular target site in accordance to previous reports (Laakkonen et al., 2002). In another experiment, LyP-1 was conjugated to a PEGylated liposomes loaded with fluorescein or doxorubicin (Yan et al., 2012). This group of researchers found that LyP-1-conjugated PEGylated liposomes could be targeted to metastatic lymph nodes based on their specific binding to tumor cells, tumor lymphatics and tumor-associated macrophages. Meanwhile, they also found it to be a safe and effective drug delivery system of antineoplastic agents for targeted therapy of lymphatic metastatic tumors. Wang et al (Z. Wang et al., 2012) investigated (LyP-1) conjugated PEG-PCL micelles (LyP-1-PM) micelles loaded with Artemisinin using highly metastatic breast cancer MDA-MB-435S cells and lymphatic endothelial cells (LEC) model cells. It was discovered that LyP-1 functionalized PEG-PCL system might be promising in terms of specific delivery of therapeutic or imaging agents to both highly metastatic breast tumor and its lymphatics. Thus, LyP-1, which binds specifically to tumor lymphatics, can provide a potential platform for developing tumour targeted systems that can specifically destroy tumor lymphatics.

2.5.3.2. CGKRK – A pentapeptide with a penetrative homing signature

The screening of all peptides homing to a mouse model of SCC resulted in the identification of CGKRK. It is a pentapeptide that can home to all types of tumor tested during the experiment and it is capable of penetrating the nucleus of the targeted cell. Its internalization has been proposed to be as a result of its binding to heparan sulfates at the surface of the cell (Pepper, 2001). In comparison to LyP-1, is also basic in nature and resembles other cell penetrating peptides (CPPs) like Tat and penetratin (Langel, 2006). However, both LyP-1 and CGKRK differ from other CPPs in that their cellular uptake requires energy and is cell-type specific for the

lymphatic endothelial and tumor cells in tumors that display the receptor for these peptides (Enbäck and Laakkonen, 2007; Laakkonen et al., 2004b).

In summary, the inclusion of ligand as targeting moieties either in an *in vitro* or *in vivo* experiments has demonstrated that targeted nanoparticles agglomerate in specific tissues to enhance therapeutic efficacy. Meanwhile, a large numbers of literatures are available in this area of strategic nanoparticles targeting.

2.6. Concluding Remarks

In this review, we have focused on the current cutting edge convectional technologies for the design of functionalized nanoconstructs for targeted delivery of therapeutics for SCC. Conventional chemotherapeutic agents still remain a potent treatment for patients with squamous cell carcinoma though limited in its efficacy due to sub-optimal dosage and multi-drug resistance through the reticuloendothelial system. Meanwhile, the advent of novel nanotechnologies in designing and fabricating nanoparticles as carriers for chemotherapeutic cargos has enhanced the successful delivery of convectional chemotherapeutics through passive transport into the cellular system. Advances in technological approaches leading to the complete sequence of the human genome has allowed for the screening and identification of several molecular makers that could serve as molecular zip codes for targeted cancer drug delivery. The discovery of phage technology for the discovery of several peptides has stimulated intensive research using these peptides as targeting moieties for homing various therapeutics to both tumor cells and its vasculature. Targeted ligands such as folate and transferrin receptors are efficient in the design of cargos that specifically target tumour cells as opposed to normal cells since these receptors are uniquely up-regulated across various tumor types. Furthermore, the incorporation of Lyp-1 as homing moiety to nanoconstructs for targeted delivery in cancer nanomedicine can yield an efficient result leading to the destruction of both the cancer cells and

its vasculature. The combinatorial strategy of attaching both homing peptides and ligands as dual moieties on nano-cargos should further strengthen the advantages of each technology in cancer targeted therapy. The future holds many promises and possibilities in this concept of cancer nanomedicine particularly in the treatment of cancer diseases emanating from SCC. More significantly, both targeted and non-targeted polymeric nanoparticles are now in different preclinical and clinical stages. Emerging nano-strategies to control their sizes and multifunctionality are the main factors for their increasing applications as anticancer agents.

2.8. References

Adili, A., Crowe, S., Beaux, M.F., Cantrell, T., Shapiro, P.J., McIlroy, D.N., Gustin, K.E., 2008. Differential cytotoxicity exhibited by silica nanowires and nanoparticles. Nanotoxicology 2, 1–8.

Alexis, F., Pridgen, E., Molnar, L.K., Farokhzad, O.C., 2008. Factors Affecting the Clearance and Biodistribution of Polymeric Nanoparticles. Mol. Pharm. 5, 505–515.

Antony, A.C., 1996. Folate Receptors. Annu. Rev. Nutr. 16, 501–521.

Arap, W., Pasqualini, R., Ruoslahti, E., 1998. Cancer treatment by targeted drug delivery to tumor vasculature in a mouse model. Science 279, 377–380.

Arias, J.L., Gallardo, V., Ruiz, M.A., Delgado, A.V., 2007. Ftorafur loading and controlled release from poly(ethyl-2-cyanoacrylate) and poly(butylcyanoacrylate) nanospheres. Int. J. Pharm. 337, 282–290.

Aronov, O., Horowitz, A.T., Gabizon, A., Gibson, D., 2003. Folate-targeted PEG as a potential carrier for carboplatin analogs. Synthesis and in vitro studies. Bioconjug. Chem. 14, 563–574.

Arumugam, T., Ramachandran, V., Fournier, K.F., Wang, H., Marquis, L., Abbruzzese, J.L., Gallick, G.E., Logsdon, C.D., McConkey, D.J., Choi, W., 2009. Epithelial to mesenchymal transition contributes to drug resistance in pancreatic cancer. Cancer Res.

69, 5820–5828.

Avgoustakis, K., Beletsi, A., Panagi, Z., Klepetsanis, P., Karydas, A.G., Ithakissios, D.S., 2002. PLGA–mPEG nanoparticles of cisplatin: in vitro nanoparticle degradation, in vitro drug release and in vivo drug residence in blood properties. J. Controlled Release 79, 123–135.

Balasubramanian, S., Girija, A.R., Nagaoka, Y., Iwai, S., Suzuki, M., Kizhikkilot, V., Yoshida, Y., Maekawa, T., Nair, S.D., 2014. Curcumin and 5-fluorouracil-loaded, folate- and transferrin-decorated polymeric magnetic nanoformulation: a synergistic cancer therapeutic approach, accelerated by magnetic hyperthermia. Int. J. Nanomedicine 9, 437–459.

Bandyopadhyay, A., Wang, L., Agyin, J., Tang, Y., Lin, S., Yeh, I.-T., De, K., Sun, L.-Z., 2010. Doxorubicin in Combination with a Small TGFβ Inhibitor: A Potential Novel Therapy for Metastatic Breast Cancer in Mouse Models. PLoS ONE 5, e10365.

Banerji, S., Ni, J., Wang, S.X., Clasper, S., Su, J., Tammi, R., Jones, M., Jackson, D.G., 1999. LYVE-1, a new homologue of the CD44 glycoprotein, is a lymph-specific receptor for hyaluronan. J. Cell Biol. 144, 789–801.

Bao, G., Mitragotri, S., Tong, S., 2013. Multifunctional Nanoparticles for Drug Delivery and Molecular Imaging. Annu. Rev. Biomed. Eng. 15, 253–282.

Bellocq, N.C., Pun, S.H., Jensen, G.S., Davis, M.E., 2003. Transferrin-Containing, Cyclodextrin Polymer-Based Particles for Tumor-Targeted Gene Delivery. Bioconjug. Chem. 14, 1122–1132.

Bickers, D.R., Lim, H.W., Margolis, D., Weinstock, M.A., Goodman, C., Faulkner, E., Gould, C., Gemmen, E., Dall, T., 2006. The burden of skin diseases: 2004. A joint project of the American Academy of Dermatology Association and the Society for Investigative Dermatology. J. Am. Acad. Dermatol. 55, 490–500.

Bocci, G., Paolo, A.D., Danesi, R., 2013. The pharmacological bases of the antiangiogenic

activity of paclitaxel. Angiogenesis 16, 481–492.

Breiteneder-Geleff, S., Soleiman, A., Kowalski, H., Horvat, R., Amann, G., Kriehuber, E., Diem, K., Weninger, W., Tschachler, E., Alitalo, K., Kerjaschki, D., 1999. Angiosarcomas express mixed endothelial phenotypes of blood and lymphatic capillaries: podoplanin as a specific marker for lymphatic endothelium. Am. J. Pathol. 154, 385–394.

Burg, M.A., Pasqualini, R., Arap, W., Ruoslahti, E., Stallcup, W.B., 1999. NG2 proteoglycan-binding peptides target tumor neovasculature. Cancer Res. 59, 2869–2874.

Byrne, J.D., Betancourt, T., Brannon-Peppas, L., 2008. Active targeting schemes for nanoparticle systems in cancer therapeutics. Adv. Drug Deliv. Rev., 60, 1615–1626.

Cafaggi, S., Russo, E., Stefani, R., Leardi, R., Caviglioli, G., Parodi, B., Bignardi, G., De Totero, D., Aiello, C., Viale, M., 2007. Preparation and evaluation of nanoparticles made of chitosan or N-trimethyl chitosan and a cisplatin–alginate complex. J. Controlled Release, 121, 110–123.

Campbell, I.G., Jones, T.A., Foulkes, W.D., Trowsdale, J., 1991. Folate-binding protein is a marker for ovarian cancer. Cancer Res. 51, 5329–5338.

Chang, D.-K., Chiu, C.-Y., Kuo, S.-Y., Lin, W.-C., Lo, A., Wang, Y.-P., Li, P.-C., Wu, H.-C., 2009. Antiangiogenic Targeting Liposomes Increase Therapeutic Efficacy for Solid Tumors. J. Biol. Chem. 284, 12905–12916.

Chen, Z., Deng, J., Zhao, Y., Tao, T., 2012. Cyclic RGD peptide-modified liposomal drug delivery system: enhanced cellular uptake in vitro and improved pharmacokinetics in rats. Int. J. Nanomedicine 7, 3803–3811.

Cho, K., Wang, X., Nie, S., Chen, Z., Shin, D.M., 2008. Therapeutic Nanoparticles for Drug Delivery in Cancer. Clin. Cancer Res. 14, 1310–1316.

Christian, S., Pilch, J., Akerman, M.E., Porkka, K., Laakkonen, P., Ruoslahti, E., 2003. Nucleolin expressed at the cell surface is a marker of endothelial cells in angiogenic blood vessels. J. Cell Biol. 163, 871–878.

Danhier, F., Ansorena, E., Silva, J.M., Coco, R., Le Breton, A., Préat, V., 2012. PLGA-based nanoparticles: An overview of biomedical applications. J. Controlled Release, Drug Delivery Research in Europe 161, 505–522.

Danhier, F., Feron, O., Préat, V., 2010. To exploit the tumor microenvironment: Passive and active tumor targeting of nanocarriers for anti-cancer drug delivery. J. Controlled Release 148, 135–146.

Derakhshandeh, K., Erfan, M., Dadashzadeh, S., 2007. Encapsulation of 9-nitrocamptothecin, a novel anticancer drug, in biodegradable nanoparticles: factorial design, characterization and release kinetics. Eur. J. Pharm. Biopharm. 66, 34–41.

Dreaden, E.C., Austin, L.A., Mackey, M.A., El-Sayed, M.A., 2012. Size matters: gold nanoparticles in targeted cancer drug delivery. Ther. Deliv. 3, 457–478.

Enbäck, J., Laakkonen, P., 2007. Tumour-homing peptides: tools for targeting, imaging and destruction. Biochem. Soc. Trans. 35, 780–783.

Fakhry, C., Westra, W.H., Li, S., Cmelak, A., Ridge, J.A., Pinto, H., Forastiere, A., Gillison, M.L., 2008. Improved Survival of Patients With Human Papillomavirus–Positive Head and Neck Squamous Cell Carcinoma in a Prospective Clinical Trial. J. Natl. Cancer Inst. 100, 261–269.

Fang, C., Shi, B., Pei, Y.-Y., Hong, M.-H., Wu, J., Chen, H.-Z., 2006. In vivo tumor targeting of tumor necrosis factor-alpha-loaded stealth nanoparticles: effect of MePEG molecular weight and particle size. Eur. J. Pharm. Sci. 27, 27–36.

Faulk, W.P., Taylor, C.G., Yeh, C.J., McIntyre, J.A., 1990. Preliminary clinical study of transferrin-adriamycin conjugate for drug delivery to acute leukemia patients. Mol. Biother. 2, 57–60.

Fens, M.H. a. M., Hill, K.J., Issa, J., Ashton, S.E., Westwood, F.R., Blakey, D.C., Storm, G., Ryan, A.J., Schiffelers, R.M., 2008. Liposomal encapsulation enhances the antitumour efficacy of the vascular disrupting agent ZD6126 in murine B16.F10 melanoma. Br. J.

Cancer 99, 1256–1264.

Fogal, V., Zhang, L., Krajewski, S., Ruoslahti, E., 2008. Mitochondrial/cell surface protein p32/gC1qR as a molecular target in tumor cells and tumor stroma. Cancer Res. 68, 7210–7218.

Fonseca, C., Simões, S., Gaspar, R., 2002. Paclitaxel-loaded PLGA nanoparticles: preparation, physicochemical characterization and in vitro anti-tumoral activity. J. Controlled Release 83, 273–286.

Frederick, B.A., Helfrich, B.A., Coldren, C.D., Zheng, D., Chan, D., Bunn Jr., P.A., Raben, D., 2007. Epithelial to mesenchymal transition predicts gefitinib resistance in cell lines of head and neck squamous cell carcinoma and non-small cell lung carcinoma. Mol. Cancer Ther. 6, 1683–1691.

Fuchs, B.C., Fujii, T., Dorfman, J.D., Goodwin, J.M., Zhu, A.X., Lanuti, M., Tanabe, K.K., 2008. Epithelial-to-mesenchymal transition and integrin-linked kinase mediate sensitivity to epidermal growth factor receptor inhibition in human hepatoma cells. Cancer Res. 68, 2391–2399.

Gatter, K.C., Brown, G., Trowbridge, I.S., Woolston, R.E., Mason, D.Y., 1983. Transferrin receptors in human tissues: their distribution and possible clinical relevance. J. Clin. Pathol. 36, 539–545.

GENG, Y., DALHAIMER, P., CAI, S., TSAI, R., TEWARI, M., MINKO, T., DISCHER, D.E., 2007. Shape effects of filaments versus spherical particles in flow and drug delivery. Nat. Nanotechnol. 2, 249–255.

Gómez-Gaete, C., Tsapis, N., Besnard, M., Bochot, A., Fattal, E., 2007. Encapsulation of dexamethasone into biodegradable polymeric nanoparticles. Int. J. Pharm., 331, 153–159.

Goodman, T.T., Olive, P.L., Pun, S.H., 2007. Increased nanoparticle penetration in collagenase-treated multicellular spheroids. Int J Nanomed 2, 265–274.

Gurudutt, V.V., Genden, E.M., 2011. Cutaneous Squamous Cell Carcinoma of the Head and Neck. J. Skin Cancer 2011, e502723.

Hauert, S., Bhatia, S.N., 2014. Mechanisms of cooperation in cancer nanomedicine: towards systems nanotechnology. Trends Biotechnol., Special Issue: Next Generation Therapeutics 32, 448–455.

He, Q., Shi, J., 2014. MSN Anti-Cancer Nanomedicines: Chemotherapy Enhancement, Overcoming of Drug Resistance, and Metastasis Inhibition. Adv. Mater. 26, 391–411.

Head, J.F., Wang, F., Elliott, R.L., 1997. Antineoplastic drugs that interfere with iron metabolism in cancer cells. Adv. Enzyme Regul., Proceedings of the Thirty-seventh Symposium on Regulation of Enzyme Activity and Synthesis in Normal and Neoplastic Tissues held at Indiana University School of Medicine 37, 147–169.

Heidel, J.D., Yu, Z., Liu, J.Y.-C., Rele, S.M., Liang, Y., Zeidan, R.K., Kornbrust, D.J., Davis, M.E., 2007. Administration in non-human primates of escalating intravenous doses of targeted nanoparticles containing ribonucleotide reductase subunit M2 siRNA. Proc. Natl. Acad. Sci. 104, 5715–5721.

Hendricks, D., Parker, M.I., 2002. Oesophageal cancer in Africa. IUBMB Life 53, 263–268.

Hoch, U., Masuoka, L., Maslyar, D., Von Hoff, D., 2009. 8015 NKTR-102 demonstrates nonclinical and phase 1 clinical anti-tumor activity in ovarian cancer. Eur. J. Cancer Suppl., Joint ECCO 15 – 34th ESMO Multidisciplinary Congress BERLIN, 20–24 SEPTEMBER 2009 Abstract Book 7, 454.

Hoffman, J.A., Giraudo, E., Singh, M., Zhang, L., Inoue, M., Porkka, K., Hanahan, D., Ruoslahti, E., 2003. Progressive vascular changes in a transgenic mouse model of squamous cell carcinoma. Cancer Cell 4, 383–391.

Hu-Lieskovan, S., Heidel, J.D., Bartlett, D.W., Davis, M.E., Triche, T.J., 2005. Sequence-Specific Knockdown of EWS-FLI1 by Targeted, Nonviral Delivery of Small Interfering RNA Inhibits Tumor Growth in a Murine Model of Metastatic Ewing's Sarcoma. Cancer

Res. 65, 8984–8992.

Jakszyn, P., Gonzalez, C.-A., 2006. Nitrosamine and related food intake and gastric and oesophageal cancer risk: a systematic review of the epidemiological evidence. World J. Gastroenterol. WJG 12, 4296–4303.

Janes, K.A., Fresneau, M.P., Marazuela, A., Fabra, A., Alonso, M.J., 2001. Chitosan nanoparticles as delivery systems for doxorubicin. J. Controlled Release 73, 255–267.

Joyce, J.A., Laakkonen, P., Bernasconi, M., Bergers, G., Ruoslahti, E., Hanahan, D., 2003. Stage-specific vascular markers revealed by phage display in a mouse model of pancreatic islet tumorigenesis. Cancer Cell 4, 393–403.

Kajiyama, H., Shibata, K., Terauchi, M., Yamashita, M., Ino, K., Nawa, A., Kikkawa, F., 2007. Chemoresistance to paclitaxel induces epithelial-mesenchymal transition and enhances metastatic potential for epithelial ovarian carcinoma cells. Int. J. Oncol. 31, 277–283.

Kamen, B.A., Caston, J.D., 1986. Properties of a Folate Binding Protein (FBP) isolated from porcine kidney. Biochem. Pharmacol. 35, 2323–2329.

Kanasty, R., Dorkin, J.R., Vegas, A., Anderson, D., 2013. Delivery materials for siRNA therapeutics. Nat. Mater. 12, 967–977.

Kato, H., Torigoe, T., 1977. Radioimmunoassay for tumor antigen of human cervical squamous cell carcinoma. Cancer 40, 1621–1628.

Kibria, G., Hatakeyama, H., Harashima, H., 2013. Cancer multidrug resistance: mechanisms involved and strategies for circumvention using a drug delivery system. Arch. Pharm. Res. 37, 4–15.

Kim, M.R., Choi, H., Cho, K.B., Kim, H.S., Kang, K.W., 2009. Involvement of Pin1 induction in epithelial-mesenchymal transition of tamoxifen-resistant breast cancer cells. Cancer Sci. 100, 1834–1841.

Kim, S.Y., Lee, Y.M., 2001. Taxol-loaded block copolymer nanospheres composed of methoxy poly(ethylene glycol) and poly(ε-caprolactone) as novel anticancer drug carriers.

Biomaterials 22, 1697–1704.

Kirpotin, D., Park, J.W., Hong, K., Zalipsky, S., Li, W.-L., Carter, P., Benz, C.C., Papahadjopoulos, D., 1997. Sterically Stabilized Anti-HER2 Immunoliposomes: Design and Targeting to Human Breast Cancer Cells in Vitro†. Biochemistry (Mosc.) 36, 66–75.

Kommareddy, S., Amiji, M., 2007. Biodistribution and pharmacokinetic analysis of long-circulating thiolated gelatin nanoparticles following systemic administration in breast cancer-bearing mice. J. Pharm. Sci. 96, 397–407.

Konecny, G.E., Venkatesan, N., Yang, G., Dering, J., Ginther, C., Finn, R., Rahmeh, M., Fejzo, M.S., Toft, D., Jiang, S.-W., Slamon, D.J., Podratz, K.C., 2008. Activity of lapatinib a novel HER2 and EGFR dual kinase inhibitor in human endometrial cancer cells. Br. J. Cancer 98, 1076–1084.

Laakkonen, P., Åkerman, M.E., Biliran, H., Yang, M., Ferrer, F., Karpanen, T., Hoffman, R.M., Ruoslahti, E., 2004a. Antitumor activity of a homing peptide that targets tumor lymphatics and tumor cells. Proc. Natl. Acad. Sci. U. S. A. 101, 9381–9386.

Laakkonen, P., Akerman, M.E., Biliran, H., Yang, M., Ferrer, F., Karpanen, T., Hoffman, R.M., Ruoslahti, E., 2004b. Antitumor activity of a homing peptide that targets tumor lymphatics and tumor cells. Proc. Natl. Acad. Sci. U. S. A. 101, 9381–9386.

Laakkonen, P., Porkka, K., Hoffman, J.A., Ruoslahti, E., 2002. A tumor-homing peptide with a targeting specificity related to lymphatic vessels. Nat. Med. 8, 751–755.

Laakkonen, P., Vuorinen, K., 2010. Homing peptides as targeted delivery vehicles. Integr. Biol. 2, 326–337.

Langel, √úlo (Ed.), 2006. Handbook of Cell-Penetrating Peptides, Second Edition, Pharmacology and Toxicology: Basic and Clinical Aspects. CRC Press.

Leu, A.J., Berk, D.A., Lymboussaki, A., Alitalo, K., Jain, R.K., 2000. Absence of functional lymphatics within a murine sarcoma: a molecular and functional evaluation. Cancer Res. 60, 4324–4327.

Li, S.-D., Chono, S., Huang, L., 2008. Efficient Oncogene Silencing and Metastasis Inhibition via Systemic Delivery of siRNA. Mol. Ther. 16, 942–946.

Li, W., Zhan, P., De Clercq, E., Lou, H., Liu, X., 2013. Current drug research on PEGylation with small molecular agents. Prog. Polym. Sci., Topical Issue on Biorelevant Polymers 38, 421–444.

Li, X., Li, R., Qian, X., Ding, Y., Tu, Y., Guo, R., Hu, Y., Jiang, X., Guo, W., Liu, B., 2008. Superior antitumor efficiency of cisplatin-loaded nanoparticles by intratumoral delivery with decreased tumor metabolism rate. Eur. J. Pharm. Biopharm. 70, 726–734.

Lin, J.K., 1990. Nitrosamines as potential environmental carcinogens in man. Clin. Biochem. 23, 67–71.

Low, P.S., Antony, A.C., 2004. Folate receptor-targeted drugs for cancer and inflammatory diseases. Adv. Drug Deliv. Rev., Folate Receptor-Targeted Drugs for Cancer and Inflammatory Diseases 56, 1055–1058.

Lu, Y., Low, P.S., 2002. Folate-mediated delivery of macromolecular anticancer therapeutic agents. Adv. Drug Deliv. Rev., Polymer Conjugates for Cancer Therapy 54, 675–693.

Lu, Z., Yeh, T.-K., Tsai, M., Au, J.L.-S., Wientjes, M.G., 2004. Paclitaxel-loaded gelatin nanoparticles for intravesical bladder cancer therapy. Clin. Cancer Res. 10, 7677–7684.

Luhrs, C.A., Raskin, C.A., Durbin, R., Wu, B., Sadasivan, E., McAllister, W., Rothenberg, S.P., 1992. Transfection of a glycosylated phosphatidylinositol-anchored folate-binding protein complementary DNA provides cells with the ability to survive in low folate medium. J. Clin. Invest. 90, 840–847.

Maeda, H., Nakamura, H., Fang, J., 2013. The EPR effect for macromolecular drug delivery to solid tumors: Improvement of tumor uptake, lowering of systemic toxicity, and distinct tumor imaging in vivo. Adv. Drug Deliv. Rev. 65, 71–79.

Markopoulos, A.K., 2012. Current Aspects on Oral Squamous Cell Carcinoma. Open Dent. J. 6, 126–130.

Matsumura, Y., Maeda, H., 1986. A new concept for macromolecular therapeutics in cancer chemotherapy: Mechanism of tumoritropic accumulation of proteins and the antitumor agent smancs. Cancer Res. 46, 6387–6392.

Moon, J.J., Huang, B., Irvine, D.J., 2012. Engineering Nano- and Microparticles to Tune Immunity. Adv. Mater. 24, 3724–3746.

Nagayama, S., Ogawara, K., Fukuoka, Y., Higaki, K., Kimura, T., 2007. Time-dependent changes in opsonin amount associated on nanoparticles alter their hepatic uptake characteristics. Int. J. Pharm. 342, 215–221.

Nechansky, A., Kircheis, R., 2010. Immunogenicity of therapeutics: a matter of efficacy and safety. Expert Opin. Drug Discov. 5, 1067–1079.

Némati, F., Dubernet, C., Fessi, H., Colin de Verdière, A., Poupon, M.F., Puisieux, F., Couvreur, P., 1996. Reversion of multidrug resistance using nanoparticles in vitro: Influence of the nature of the polymer. Int. J. Pharm. 138, 237–246.

Nicoli, S., Santi, P., Couvreur, P., Couarraze, G., Colombo, P., Fattal, E., 2001. Design of triptorelin loaded nanospheres for transdermal iontophoretic administration. Int. J. Pharm. 214, 31–35.

Owens III, D.E., Peppas, N.A., 2006. Opsonization, biodistribution, and pharmacokinetics of polymeric nanoparticles. Int. J. Pharm. 307, 93–102.

Pan, W.-S., Han, C., Yue, L., Tai, L., Li Zhou, Li, X., Xing, G., Yang, X., Sun, 2013. A novel small peptide as an epidermal growth factor receptor targeting ligand for nanodelivery in vitro. Int. J. Nanomedicine 1541.

Pan, X., Lee, R.J., 2004. Tumour-selective drug delivery via folate receptor-targeted liposomes. Expert Opin. Drug Deliv. 1, 7–17.

Pan, X.Q., Zheng, X., Shi, G., Wang, H., Ratnam, M., Lee, R.J., 2002. Strategy for the treatment of acute myelogenous leukemia based on folate receptor β–targeted liposomal doxorubicin combined with receptor induction using all-trans retinoic acid. Blood 100,

594–602.

Pasqualini, R., Koivunen, E., Kain, R., Lahdenranta, J., Sakamoto, M., Stryhn, A., Ashmun, R.A., Shapiro, L.H., Arap, W., Ruoslahti, E., 2000. Aminopeptidase N is a receptor for tumor-homing peptides and a target for inhibiting angiogenesis. Cancer Res. 60, 722–727.

Pasqualini, R., Koivunen, E., Ruoslahti, E., 1997. αv Integrins as receptors for tumor targeting by circulating ligands. Nat. Biotechnol. 15, 542–546.

Pasqualini, R., Koivunen, E., Ruoslahti, E., 1997. Alpha v integrins as receptors for tumor targeting by circulating ligands. Nat. Biotechnol. 15, 542–546.

Pearce, T.R., Shroff, K., Kokkoli, E., 2012. Peptide Targeted Lipid Nanoparticles for Anticancer Drug Delivery. Adv. Mater. 24, 3803–3822.

Pepper, M.S., 2001. Lymphangiogenesis and tumor metastasis: myth or reality? Clin. Cancer Res. Off. J. Am. Assoc. Cancer Res. 7, 462–468.

Petros, R.A., DeSimone, J.M., 2010. Strategies in the design of nanoparticles for therapeutic applications. Nat. Rev. Drug Discov. 9, 615–627.

Pun, S.H., Tack, F., Bellocq, N.C., Cheng, J., Grubbs, B.H., Jensen, G.S., Davis, M.E., Brewster, M., Janicot, M., Janssens, B., Floren, W., Bakker, A., 2004. Targeted delivery of RNA-cleaving DNA enzyme (DNAzyme) to tumor tissue by transferrin-modified, cyclodextrin-based particles. Cancer Biol. Ther. 3, 641–650.

Rainov, N.G., Söling, A., 2005. Technology evaluation: TransMID, KS Biomedix/Nycomed/Sosei/PharmaEngine. Curr. Opin. Mol. Ther. 7, 483–492.

Rajaonarivony, M., Vauthier, C., Couarraze, G., Puisieux, F., Couvreur, P., 1993. Development of a new drug carrier made from alginate. J. Pharm. Sci. 82, 912–917.

Redhead, H.M., Davis, S.S., Illum, L., 2001. Drug delivery in poly(lactide-co-glycolide) nanoparticles surface modified with poloxamer 407 and poloxamine 908: in vitro characterisation and in vivo evaluation. J. Controlled Release 70, 353–363.

Rodriguez, P.L., Harada, T., Christian, D.A., Pantano, D.A., Tsai, R.K., Discher, D.E., 2013. Minimal “self” peptides that inhibit phagocytic clearance and enhance delivery of nanoparticles. Science 339, 971–975.

Romberg, B., Hennink, W.E., Storm, G., 2008. Sheddable Coatings for Long-Circulating Nanoparticles. Pharm. Res. 25, 55–71.

Ruoslahti, E., Bhatia, S.N., Sailor, M.J., 2010. Targeting of drugs and nanoparticles to tumors. J. Cell Biol. 188, 759–768.

Schiffelers, R.M., Koning, G.A., ten Hagen, T.L.M., Fens, M.H.A.M., Schraa, A.J., Janssen, A.P.C.A., Kok, R.J., Molema, G., Storm, G., 2003. Anti-tumor efficacy of tumor vasculature-targeted liposomal doxorubicin. J. Control. Release Off. J. Control. Release Soc. 91, 115–122.

Shenoy, D.B., Amiji, M.M., 2005. Poly(ethylene oxide)-modified poly(ε-caprolactone) nanoparticles for targeted delivery of tamoxifen in breast cancer. Int. J. Pharm. 293, 261–270.

Shmeeda, H., Mak, L., Tzemach, D., Astrahan, P., Tarshish, M., Gabizon, A., 2006. Intracellular uptake and intracavitary targeting of folate-conjugated liposomes in a mouse lymphoma model with up-regulated folate receptors. Mol. Cancer Ther. 5, 818–824.

Shmeeda, H., Tzemach, D., Mak, L., Gabizon, A., 2009. Her2-targeted pegylated liposomal doxorubicin: Retention of target-specific binding and cytotoxicity after in vivo passage. J. Controlled Release 136, 155–160.

Singh, M., 1999. Transferrin as a targeting ligand for liposomes and anticancer drugs. Curr. Pharm. Des. 5, 443–451.

Song, S., Liu, D., Peng, J., Deng, H., Guo, Y., Xu, L.X., Miller, A.D., Xu, Y., 2009. Novel peptide ligand directs liposomes toward EGF-R high-expressing cancer cells in vitro and in vivo. FASEB J. 23, 1396–1404.

Soo Choi, H., Liu, W., Misra, P., Tanaka, E., Zimmer, J.P., Itty Ipe, B., Bawendi, M.G.,

Frangioni, J.V., 2007. Renal clearance of quantum dots. Nat. Biotechnol. 25, 1165–1170.

Sugahara, K.N., Teesalu, T., Karmali, P.P., Kotamraju, V.R., Agemy, L., Girard, O.M., Hanahan, D., Mattrey, R.F., Ruoslahti, E., 2009. Tissue-penetrating delivery of compounds and nanoparticles into tumors. Cancer Cell 16, 510–520.

Svensen, N., Walton, J.G.A., Bradley, M., 2012. Peptides for cell-selective drug delivery. Trends Pharmacol. Sci. 33, 186–192.

Sznol, M., Davis, T., 2002. Tumor antigens as targets for anticancer drug development. In: Kerr, B.C.B.J. (Ed.), Anticancer Drug Development. Academic Press, San Diego, pp. 157–170.

Teixeira, M., Alonso, M.J., Pinto, M.M.M., Barbosa, C.M., 2005. Development and characterization of PLGA nanospheres and nanocapsules containing xanthone and 3-methoxyxanthone. Eur. J. Pharm. Biopharm. Off. J. Arbeitsgemeinschaft Für Pharm. Verfahrenstechnik EV 59, 491–500.

Thundimadathil, J., 2012. Cancer Treatment Using Peptides: Current Therapies and Future Prospects. J. Amino Acids 2012, e967347.

Tokumitsu, H., Ichikawa, H., Fukumori, Y., 1999. Chitosan-gadopentetic acid complex nanoparticles for gadolinium neutron-capture therapy of cancer: preparation by novel emulsion-droplet coalescence technique and characterization. Pharm. Res. 16, 1830–1835.

Torchilin, V.P., Lukyanov, A.N., 2003. Peptide and protein drug delivery to and into tumors: challenges and solutions. Drug Discov. Today 8, 259–266.

Turk, M.J., Waters, D.J., Low, P.S., 2004. Folate-conjugated liposomes preferentially target macrophages associated with ovarian carcinoma. Cancer Lett. 213, 165–172.

Venkataraman, S., Hedrick, J.L., Ong, Z.Y., Yang, C., Ee, P.L.R., Hammond, P.T., Yang, Y.Y., 2011. The effects of polymeric nanostructure shape on drug delivery. Adv. Drug Deliv.

Rev., Hybrid nanostructures for diagnostics and therapeutics 63, 1228–1246.

Vilar, G., Tulla-Puche, J., Albericio, F., 2012. Polymers and drug delivery systems. Curr. Drug Deliv. 9, 367–394.

Wang, A.Z., Langer, R., Farokhzad, O.C., 2012. Nanoparticle Delivery of Cancer Drugs. Annu. Rev. Med. 63, 185–198.

Wang, J., Byrne, J.D., Napier, M.E., DeSimone, J.M., 2011. More Effective Nanomedicines through Particle Design. Small 7, 1919–1931.

Wang, M., Löwik, D.W.P.M., Miller, A.D., Thanou, M., 2009. Targeting the urokinase plasminogen activator receptor with synthetic self-assembly nanoparticles. Bioconjug. Chem. 20, 32–40.

Wang, M., Thanou, M., 2010. Targeting nanoparticles to cancer. Pharmacol. Res., Towards clinical applications of nanoscale medicines 62, 90–99.

Wang, Z., Li, Y., Kong, D., Banerjee, S., Ahmad, A., Azmi, A.S., Ali, S., Abbruzzese, J.L., Gallick, G.E., Sarkarr, F.H., 2009. Acquisition of epithelial-mesenchymal transition phenotype of gemcitabine-resistant pancreatic cancer cells is linked with activation of the notch signaling pathway. Cancer Res. 69, 2400–2407.

Wang, Z., Yu, Y., Ma, J., Zhang, H., Zhang, H., Wang, X., Wang, J., Zhang, X., Zhang, Q., 2012. LyP-1 Modification To Enhance Delivery of Artemisinin or Fluorescent Probe Loaded Polymeric Micelles to Highly Metastatic Tumor and Its Lymphatics. Mol. Pharm. 9, 2646–2657.

Weitman, S.D., Lark, R.H., Coney, L.R., Fort, D.W., Frasca, V., Zurawski Jr., V.R., Kamen, B.A., 1992. Distribution of the folate receptor GP38 in normal and malignant cell lines and tissues. Cancer Res. 52, 3396–3401.

WHO 2014. http://www.who.int/cancer/en/ (accessed 11.24.14).

Wigle, J.T., Harvey, N., Detmar, M., Lagutina, I., Grosveld, G., Gunn, M.D., Jackson, D.G., Oliver, G., 2002. An essential role for Prox1 in the induction of the lymphatic endothelial

cell phenotype. EMBO J. 21, 1505–1513.

Wu, J., Lu, Y., Lee, A., Pan, X., Yang, X., Zhao, X., Lee, R.J., 2007. Reversal of multidrug resistance by transferrin-conjugated liposomes co-encapsulating doxorubicin and verapamil. J. Pharm. Pharm. Sci. 10, 350–357.

Xing, J., Zhang, D., Tan, T., 2007. Studies on the oridonin-loaded poly(d,l-lactic acid) nanoparticles in vitro and in vivo. Int. J. Biol. Macromol. 40, 153–158.

Yan, Z., Wang, F., Wen, Z., Zhan, C., Feng, L., Liu, Y., Wei, X., Xie, C., Lu, W., 2012. LyP-1-conjugated PEGylated liposomes: A carrier system for targeted therapy of lymphatic metastatic tumor. J. Controlled Release 157, 118–125.

Yang, A.D., Fan, F., Camp, E.R., van Buren, G., Liu, W., Somcio, R., Gray, M.J., Cheng, H., Hoff, P.M., Ellis, L.M., 2006. Chronic oxaliplatin resistance induces epithelial-to-mesenchymal transition in colorectal cancer cell lines. Clin. Cancer Res. Off. J. Am. Assoc. Cancer Res. 12, 4147–4153.

Yauch, R.L., Januario, T., Eberhard, D.A., Cavet, G., Zhu, W., Fu, L., Pham, T.Q., Soriano, R., Stinson, J., Seshagiri, S., Modrusan, Z., Lin, C.-Y., O'Neill, V., Amler, L.C., 2005. Epithelial versus mesenchymal phenotype determines in vitro sensitivity and predicts clinical activity of erlotinib in lung cancer patients. Clin. Cancer Res. 11, 8686–8698.

Yoo, H.S., Oh, J.E., Lee, K.H., Park, T.G., 1999. Biodegradable nanoparticles containing doxorubicin-PLGA conjugate for sustained release. Pharm. Res. 16, 1114–1118.

Yu, D.-H., Lu, Q., Xie, J., Fang, C., Chen, H.-Z., 2010. Peptide-conjugated biodegradable nanoparticles as a carrier to target paclitaxel to tumor neovasculature. Biomaterials 31, 2278–2292.

Zakkouri, F.A., Ouaouch, S., Boutayeb, S., Rimani, M., Gamra, L., Mrabti, H., Errihani, H., 2011. Squamous cell carcinoma in situ arising in mature cystic teratoma of the ovary: a case report. J. Ovarian Res. 4, 5.

Zhang, L., Giraudo, E., Hoffman, J.A., Hanahan, D., Ruoslahti, E., 2006. Lymphatic zip codes in

premalignant lesions and tumors. Cancer Res. 66, 5696–5706.

Zhang, X., Li, Y., Chen, X., Wang, X., Xu, X., Liang, Q., Hu, J., Jing, X., 2005. Synthesis and characterization of the paclitaxel/MPEG-PLA block copolymer conjugate. Biomaterials 26, 2121–2128.

Zhang, X.-X., Eden, H.S., Chen, X., 2012. Peptides in cancer nanomedicine: Drug carriers, targeting ligands and protease substrates. J. Controlled Release 159, 2–13.

Zhao, X., Li, H., Lee, R.J., 2008. Targeted drug delivery via folate receptors. Expert Opin. Drug Deliv. 5, 309–319.

CHAPTER 3

SYNTHESIS AND IN VITRO CHARACTERIZATION OF A pH-SENSITIVE CHITOSAN-POLYETHYLENIMINE NANOSYSTEM FOR THE POTENTIAL DELIVERY OF THERAPEUTIC PROTEINS

3.1. Introduction

The use of peptides and proteins as potent chemotherapeutic agents has increased due to advances in novel biotechnological techniques that have allowed for the availability of large quantities of biopharmaceutical products over the last decades (Adebowale et al., 2015; Bürki et al., 2011; Fosgerau and Hoffmann, 2015). The majority of protein- and peptide-based chemotherapeutic formulations are currently administered through the parenteral route and approximately 75% are administered as injectables (Fosgerau and Hoffmann, 2015; Sollohub and Cal, 2010).

Polysaccharides such as chitosan (CHT), has been extensively researched in recent years as a carrier for the delivery of therapeutic peptides and proteins aside being employed in the design of non-viral gene vectors (Dang and Leong, 2006; Gan and Wang, 2007; George and Abraham, 2006). Chitosan is a cationic biocompatible and biodegradable linear binary polysaccharide derived from chitin. Upon deacetylation, the glucosamine backbone of chitosan has a high density of amine groups that can allow for strong electrostatic interaction with proteins that display an overall negative charge at neutral pH. (Gao et al., 2010a; Mao et al., 2004). However, cellular internalization of chitosan is significantly low. This is a noteworthy limitation to its application for the delivery of proteins and peptides (Kim et al., 2005). To circumvent this limitation, several attempts have been explored based on reactions with free amino groups

particularly when combined with anionic or cationic biopolymers such as polyethyleimine (PEI) (Jiang et al., 2007; Lu et al., 2014; Tripathi et al., 2012; Zhao et al., 2009).

PEI is regarded as the most effective cationic synthetic polymer used in gene delivery due to its high proton-buffering capacity (Gao et al., 2010b). However, it is seldom employed in protein delivery (Didenko et al., 2005). The pKa values of PEI amines exceed the physiological pH range, thereby accounting for its buffering capacity (Neu et al., 2005). Concerns have been raised regarding the toxicity of PEI which is linked to its molecular weight. It has been shown that low molecular weight PEI reduced cytotoxicity though with less transfection potential than high molecular weight PEI due to lack of degradable linkages which makes it toxic for therapeutic application (Fischer et al., 1999; Jiang et al., 2007; Kunath et al., 2003). In order to overcome this challenge, a rational approach is to combine low molecular weight PEI using degradable linkages to form copolymers with suitable high molecular weight via covalent modification of PEI onto chain transfer carriers such as Poly (ethylene glycol) (PEG) (Jia et al., 2013; Malek et al., 2008; Roberts et al., 2002; Sirsi et al., 2005). Various studies have shown that PEGYlation, the introduction of PEG and its derivatives onto other polymers, has improved the colloidal stability as well as reduced the toxicity of polymers such as PEI (Jia et al., 2013). In addition, PEGYlated surfaces can protect peptide or protein carriers from uptake by the Reticuloendothelial System (RES) and effectively increase the *in vivo* circulation time of therapeutic peptide/protein carriers (Kaul and Amiji, 2004; Lohcharoenkal et al., 2014; Young Lee et al., 2006). While few reports are available on the use of CHT, PEI and PEG with their derivatives as carriers for protein/peptide therapeutics, most copolymer complexes documented from these polymers explored the transport of genes in the form of a polyplex (Holzerny et al., 2012; Merkel et al., 2009; Ulasov et al., 2011).

Therefore, the aim of this chapter is to discuss the development of a PEGYlated chitosan-based polyethyleneimine nanosystem loaded with Bovine Serum Albumin (BSA) as a model protein for targeted delivery of therapeutic peptides. While Zhang et al. (2010) reported the synthesis of grafted co-polymer of PEG-CHT-PEI, it was employed to transfect DNA in gene delivery and not proteins. Meanwhile, our intention is to use this conjugated nano-cargo for the delivery of peptide-based cancer therapeutics which are challenged with degradation by the reticuloendothelial system and short circulation period within the biological systems. To the best of our knowledge, no current studies have employed this tri-block conjugates for such purpose in cancer nanomedicines. Furthermore, a novel unilateral approach employing tripolyphosphate (TPP) as a polyanionic agent for the formation of amino group terminal PEGYlated chitosan-grafted polyethyleimine (NH_2-PEG-CHT-g-PEI) nanoparticles was employed. As such, the distal amino group on the polyethylene glycol moiety could be explored for functionalization with specialized ligands for targeted therapy. Also, the increased overall amines present in the nanosystem could increase its buffering capacity and thus enhance its cellular internalization (Liu and Reineke, 2007).

3.2. Materials and Methods

3.2.1. Materials

Low molecular weight chitosan (DA=75-85%, MW=50-190kDa), branched polyethylenimine (PEI) (Molecular weight Mw=25KDa), functionalized poly (ethylene) glycol (NH_2-PEG-COOH, Mw=2100g/mol), Bovine Serum Albumin (BSA) (M_W=66kDa), 1-ethyl-3-(3-dimethylaminopropyl) carbodiimide hydrochloride (EDC), N-hydroxysuccinimide (NHS), Sodium tripolyphosphate (TPP) (M_W=367.86g/mol), poly(vinyl alcohol) (PVA) (M_W=85,000g/mol) were purchased from Sigma-Adrich Co., Ltd. (St. Louis, MO, USA). All other reagents were analytical grade unless stated otherwise.

3.2.2. Synthesis of the Chitosan-g-Polyethylene imine (CHT-g-PEI) Complex

A copolymer of Chitosan-g-Polyethylene imine, denoted as (CHT-g-PEI), was synthesized using a modified method described by (Gao et al., 2010c) (Figure 3.1(A)). Briefly, 0.5g of chitosan was dissolved in 20mL of 0.5% acetic acid and the pH was adjusted to 7.0. The reaction mixture was stirred (at 100 rpm) overnight. Thereafter, 20mL of 0.000834M 1, 1-Carbonyldiimidazole (CDI) was added to the chitosan solution and agitated for 1 hour at 25^0C to activate the amine group in the chitosan solution. 20mL of 0.00056M PEI was then added to the activated chitosan mixture in a molar ratio of 2:1 and the polymerization process was left to proceed at 25^0C. The final product was then purified by dialysis against water for 72 hours using a dialysis membrane (M_W=12,000 kDa). The CHT-g-PEI co-polymer powder was then collected through lyophilization over 24 hours. The final product was then stored until further characterization using Fourier Transformed Infrared (FT-IR) spectroscopy and Nuclear Magnetic Resonance (NMR) to confirm the synthesis of the co-polymer as well as Differential Scanning Calorimetry (DSC) to ascertain the thermodynamic behaviour of the newly synthesized co-polymer.

3.2.3. Synthesis of Chitosan-g-Polyethylene imine (CHT-g-PEI) grafted bi-functional Polyethylene Glycol (NH_2-PEG-CHT-g-PEI) Complex

A copolymer synthesis procedure described by Jiang et al. (2008) with modifications was employed in the synthesis of the amino terminal copolymer complex (NH_2-PEG-CHT-g-PEI) following an amide formation reaction between the activated carboxyl groups of NH_2-PEG-COOH and the amine groups of CHT-g-PEI as shown in Figure 3.1(B). Briefly, 10mL of 0.1mmol of PEG was dissolved in 10mL of 0.1M MES buffer at pH 6.5. 1.2mg of NHS and 2mg of EDC were added to the mixture to activate the carboxyl groups of PEG for 15 minutes. 1.15mg of CHT-g-PEI (0.001mmol) was then added to the mixture and the reaction was allowed to proceed for 12 hours on ice and an additional 12 hours at 25^0C. The reaction mixture was then purified using a dialysis membrane ($M_{W=}$12 000kDa) against distilled water for 72 hours. The

synthesized complex was then lyophilized for 24 hours and the dried product was collected. The final product was then characterized using FTIR and NMR to ascertain the formation of the complex as well as DSC analysis to verify the thermodynamic behaviour.

3.2.4. Nanoparticle Synthesis and BSA Entrapment into the Nanoparticles from Preformed Polymer Complex

An ionic gelation technique was used to prepare NH_2-PEG-CHT-g-PEI nanoparticles using Sodium Tripolyphosphate (TPP) as a polyionic cross linker as shown in Figure 3.1. 2mg/mL of chitosan was prepared by dissolving 200mg in 100mL 0.5% acetic acid and the pH adjusted to 5.51. The reaction mixture was left overnight on a magnetic stirrer. The resultant mixture was filtered through a 0.2µm Millipore filter. 20mL of 0.000834M N,N'-Carbonyldiimidazole (CDI) solution was then added to 85mL of the filtered chitosan solution and agitated on a magnetic stirrer for 1 hour to activate the amine group. Thereafter, 40mL 0.25% branched PEI solution (filtered), was added drop-wisely under rigorous stirring using a magnetic stirrer to the activated CHT solution. The reaction mixture was then sonicated for 30 minutes under ice and allowed to polymerize for 24 hours on a magnetic stirrer. The grafted CHT-g-PEI complex was purified using a dialysis membrane (M_W=12 000kDa) against distilled water for 2 days. Subsequently, 50mL 1mg/mL solution of PEG was filtered and added drop-wise to 100mL of CHT-g-PEI solution complex under high-speed agitation. 11.9mg EDC and 10.5mg NHS were then added to the reaction mixture to activate the amine group of the CHT-g-PEI co-polymer and sonicated under ice for 30 minutes. An amide bond formed between the carboxylic acid group in PEG and the amine group of the CHT-g-PEI co-polymer complex as previously explained. The resultant mixture was then polymerized for 12 hours at 4^{o}C and another 12 hours at 25°C. The resultant complex (NH_2-PEG-CHT-g-PEI) was then purified using a dialysis membrane (M_W=12 000kDa) against distilled water for 48 hours.

Protein-loaded nanoparticles using BSA as a model protein was prepared as follows: 40mL of 1mg/mL solution of BSA prepared in Phosphate Buffer Saline, pH 7.4, was added to 80mL of purified NH_2-PEG-CHT-g-PEI solution and gently stirred for 10 minutes. To 75mL of the reaction mixture, 40mL of 0.2% TPP solution was added dropwise as a cross linking agent under high speed stirring and sonicated for 14 minutes on ice and allowed to homogenously gelate. 20mL 1% PVA solution was then added to the reaction mixture as a surfactant. The resultant gel was centrifuged at 5000rpm for 1 hour. The clear supernatant was discarded and the nanoparticles re-suspended in double deionized water until further analysis

3.2.5. Determination of Nanoparticle Recovery and Drying

The re-suspended nanoparticle containing pellet in double distilled water was filtered using a 0.2µm Millipore filter paper and dried nanoparticles were collected using a Nano-Spray Dryer B-90 (Buchi, Switzerland). The Nano-Spray conditions were set as follows: inlet temperature = 45^oC, drying air flow rate = 100L/min, spray = 100%, pump rate = 2, pressure = 33mbar and temperature humidity = 43%. A spray dry cap size of 4µm was employed.

3.2.6. Characterization of the Synthesized Co-Polymer Complex and BSA Loaded Nanoparticles

3.2.6.1. Confirmation of structural transformation and formation of the grafted co-polymer complex

FT-IR spectra with wave number ranging between 650–4000cm^{-1} with a resolution of 4cm^{-1} and 64 scans per spectrum were recorded on both the lyophilized and spray dried samples of the native polymers, the grafted complex and the synthesized NH_2-PEG-CHT-g-PEI nanoparticles. The FT-IR spectra was used to evaluate, confirm and compare structural transformations in terms of the disappearance and formation of chemical bonds by characteristic functional groups as measured on a PerkinElmer Spectrum 2000 FTIR spectrometer, employing a single-

reflection diamond MIRTGS detector (PerkinElmer Spectrum 100, Llantrisant, Wales, UK), with an ATR-FTIR cell, having a diamond crystal internal reflection element using a constant pressure of 120psi. The structures of the prepared CHT-g-PEI copolymer as well as the NH_2-PEG-CHT-g-PEI complex were also characterised by proton Nuclear Magnetic Resonance (^{1}H NMR). ^{1}H NMR measurements were performed at 300K and the solvents comprised D_2O doped with CD_3COOD in a ratio of 5:1 on a Bruker 500MHz (NMR spectrometer Billerica, MA, USA).

3.2.6.2. Elucidation of nanoparticle size, surface charge and morphology

The size and surface charge of the nanoparticles were evaluated using a Malvern Zetasizer Nano ZS (Malvern Instruments, Worcestershire, UK). Diluted samples of nanoparticles in deionized water were sonicated for 30 seconds (SONICS Vibra CellTM, Newtown, CT, USA), placed in disposable polystyrene cuvettes and the dynamic scatter intensity was recorded at 25^{o}C. The average size and the polydispersity index (PDI) were recorded. The Zeta average potential and the conductivity of the nanoparticles were also measured. Transmission Electron Microscopy (TEM) (FEI Tecnai T12 TEM, 60-120kV, Hillsboro, OR, USA), was also employed to confirm the size of the nanoparticles. TEM samples were prepared by dispersing a small quantity of the samples in distil water, ultra-sonicated for 15 minutess and allowed a single drop of the nanoparticle suspension to dry overnight at 25^{0}C on a Form Var® coated 200-mesh copper grip (TAAB Laboratories Equipment Ltd., Aldermaston, England).

In order to investigate the morphology of the nanoparticles, spray-dried NH_2-PEG-CHT-g-PEI powder was placed onto an aluminium specimen stub covered with a double-sided carbon adhesive disc and sputter-coated with both palladium and gold for 4 minutes at 20KV. NH_2-PEG-CHT-g-PEI nanoparticles were then viewed by a Scanning Electron Microscope (SEM) (SIGMA VP, ZEISS Electron Microscopy, Carl Zeiss Microscopy Ltd; Cambridge, UK).

3.2.6.3. Thermodynamic event mapping of the native and grafted co-polymer and the BSA loaded nanoparticles

The thermal stability and the decomposition temperature of the native polymers, their complex and the synthesized nanoparticles were evaluated using thermal gravimetric analysis (TGA) (PerkinElmer, TGA 4000, Llantrisant, Wales, UK). Thermogravimetric measurements were recorded and analysed using Pyris™ software (PerkinElmer, Llantrisant, Wales, UK) as percentage weight against temperature. The temperature range was set at 30–900^{0}C at a heating rate of 10^{0}C/min under a continuous N_2 flow. The thermal behaviour of the native CHT, CHT-g-PEI and NH_2-PEG-CHT-g-PEI as well as the BSA loaded nanoparticles was determined by Differential Scanning Calorimeter (DSC; Mettler Toledo, DSC1, STARe System, Schwerzenback, Switzerland). Samples ranging from 3-5.2mg, depending on sample type, were placed into 40µL aluminium pans and heated from 15-380^{o}C with a heating rate of 10^{o}C/min under a N_2 atmosphere.

3.2.6.4. BSA loading efficiency and *in vitro* release studies

The loading efficiency of BSA in the nanoparticles was analyzed by determining the concentration of BSA in the supernatant using the Bradford colorimeter assay (Sigma-Aldrich Co., Ltd. St. Louis, MO, USA). The concentration of BSA in solution based on the formation of a complex between a dye, (Coomassie Briliant Blue G250), and BSA in solution was employed. The linear concentration range between 0.1–1.4mg/mL of BSA as the standard protein molecule was employed.

The quantity of BSA loaded into the nanoparticles was calculated as the difference between the target loading and the BSA recovered in the supernatant. The supernatant of the BSA loaded nanoparticle solution was collected by decantation after centrifugation at 5000rpm for 1 hour. The BSA content in the supernatant was quantified by UV spectrophotometry at 595nm using

the Bradford protein assay. Samples were analyzed in triplicate and the protein loading efficiency (PLE) was calculated using Equation 3.1.

$$PLE = \frac{(\text{Total quantity of loaded BSA} - \text{quantity of BSA in the supernatant})}{\text{Total quantity of loaded BSA}} \times 100 \ldots\ldots Eq.3.1$$

To determine the *in vitro* release profile of BSA, the nanoparticle sediment at the bottom of the 15mL centrifuge tube was diluted with 5mL PBS (pH7.4) and incubated at 37^{o}C in a water bath. At specific time intervals, 3mL sample of the nanoparticle suspension was removed, centrifuged and analyzed for BSA quantity using the Bradford reagent. Samples in the 15mL tube were replenished with 3mL fresh PBS solution to maintain sink condition at 370C. Samples were taken in triplicate and analyzed.

3.3. Results and Discussion

3.3.1. Confirmation of the Synthesis of the Grafted Copolymer Complex and BSA Loaded Nanoparticles

We have successfully synthesized a grafted NH_2-PEG-CHT-g-PEI complex in a two-step procedure through amide formation reactions as shown in Figure 3.1. In the first reaction, CHT-g-PEI copolymer was synthesized. CDI as a cross linker was employed using one of its imidazolyl group to couple an amino group of chitosan and its other imidazolyl to linked the amino group of PEI. The molar ratio of CDI to the amine of chitosan was kept at 2:1. Meanwhile, the feed molar ratio of PEI to amine of chitosan was 3:1. In the second reaction step, an amide bond was formed between the amino group of the amine in the CHT-g-PEI copolymer and the carboxylic group in PEG using both EDC and NHS to immobilize the carboxylic group of the later.

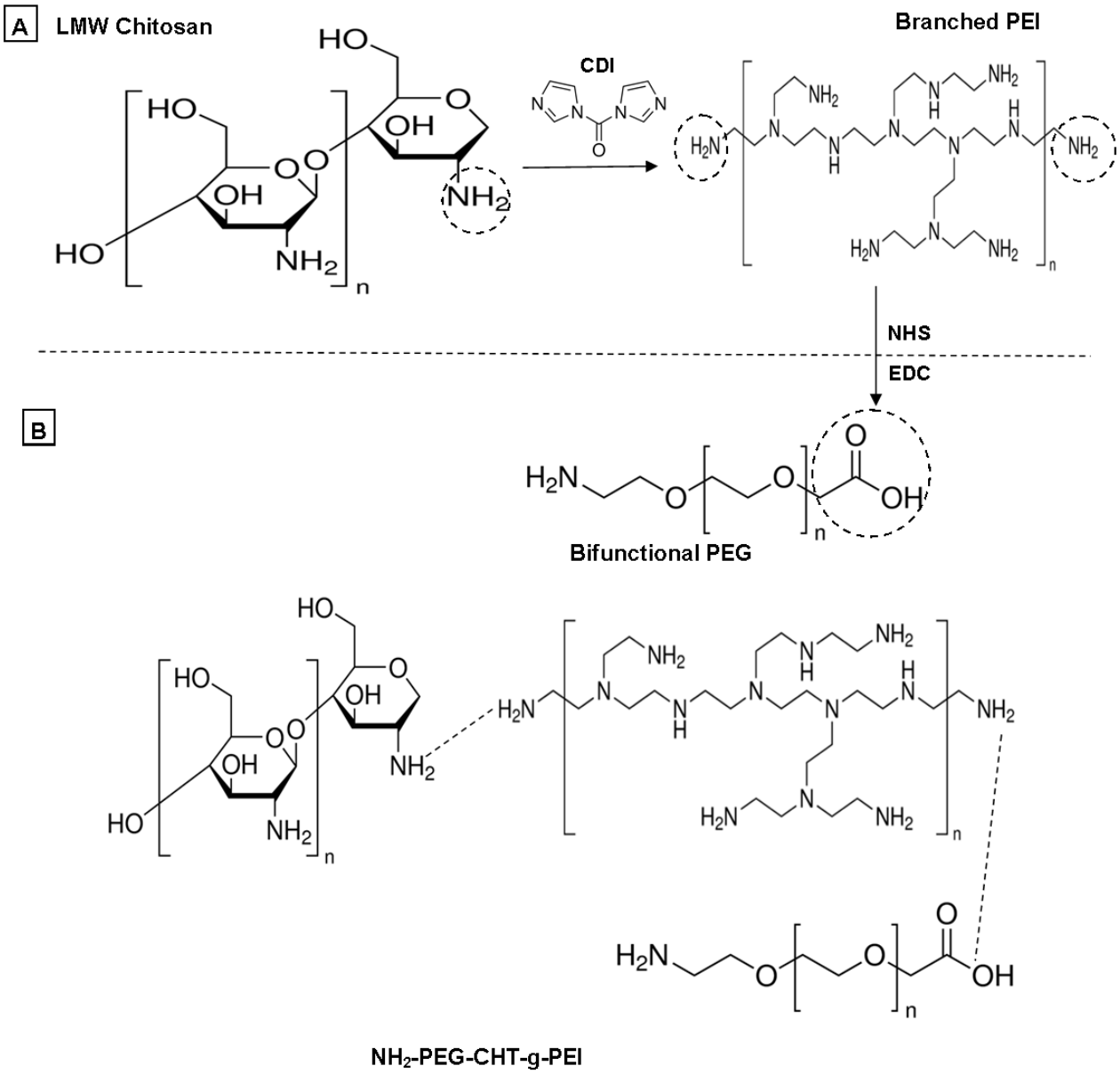


Figure 3.1: Schematic showing the mechanism of synthesis of the NH_2-PEG-CHT-g-PEI complex (A) Addition of PEI to CHT molecules increases its internalization efficiency and buffering capacity while (B) the introduction of the PEG component unto the CHT-g-PEI copolymer reduces the cytotoxic effect of PEI and also protects the encapsulated BSA molecules within the CHT nanoparticles.

FT-IR spectroscopy and ^{1}H NMR experiments were employed to determine the composition as well as validate the structural transformations of the synthesized copolymer complexes as shown in Figures 3.2 and 3.3 respectively. As presented in Figure 3.2 (a), proton peaks area

between the of range 2.6–3.3 ppm were assigned to the (-$NHCH_2CH_2$-) of PEI and that of the (-$OCCH_3$-) in Chitosan was shown at 1.9ppm indicating that the PEI was grafted to Chitosan (Jiang et al., 2008). Similarly, the proton peaks of PEG was shown between 3.4–3.7ppm (-CH_2CH_2O-) while that PEI was represented between 3.1–3.3ppm (-$NHCH_2CH_2$-) in Figure 2 (b) (Jia et al., 2013). Meanwhile, the characteristic peak of CHT was represented at 1.9ppm (-$OCCH_3$-) which also confirmed the successful grafting of the polymers.

The degree of grafted (DG) of PEI onto CHT was calculated by the following formula.

$$DG = \frac{W_2}{W_1} \times 100\% = \frac{24.25}{214.25} \times 100\% = 11.3\ \% \quad Eq \ldots 3.2$$

$where \quad W_1 = mass\ of\ pure\ graft\ co-polymer$

$W_2 = mass\ of\ graft\ chains$

$$W_1 = MW_{CHT} + (MW_{PEI} \times DS) = 190kDa + (25kDa \times 0.97) = 214.25\ kDa$$

$$W_2 = n(MW_{PEI} \times DS) = (25kDa \times 0.97) = 24.25\ kDa$$

$MW_{PEI} = molecular\ weight\ of\ PEI$

$MW_{CHT} = molecular\ wight\ of\ CHT$

By comparing the integration of proton signals at δ = 2.5–3.2 ppm and δ = 2.9–3.7 ppm, the degrees of substitution of PEI per CHT D-glucosamine unit was calculated:

$$Degree\ of\ substitution\ (DS) = \frac{I_{PEI,\ CH_2\ CH_2NH}}{I_{CHT,H2,H3-H6}} = \frac{4.04/4}{6.24/6} = 0.97$$

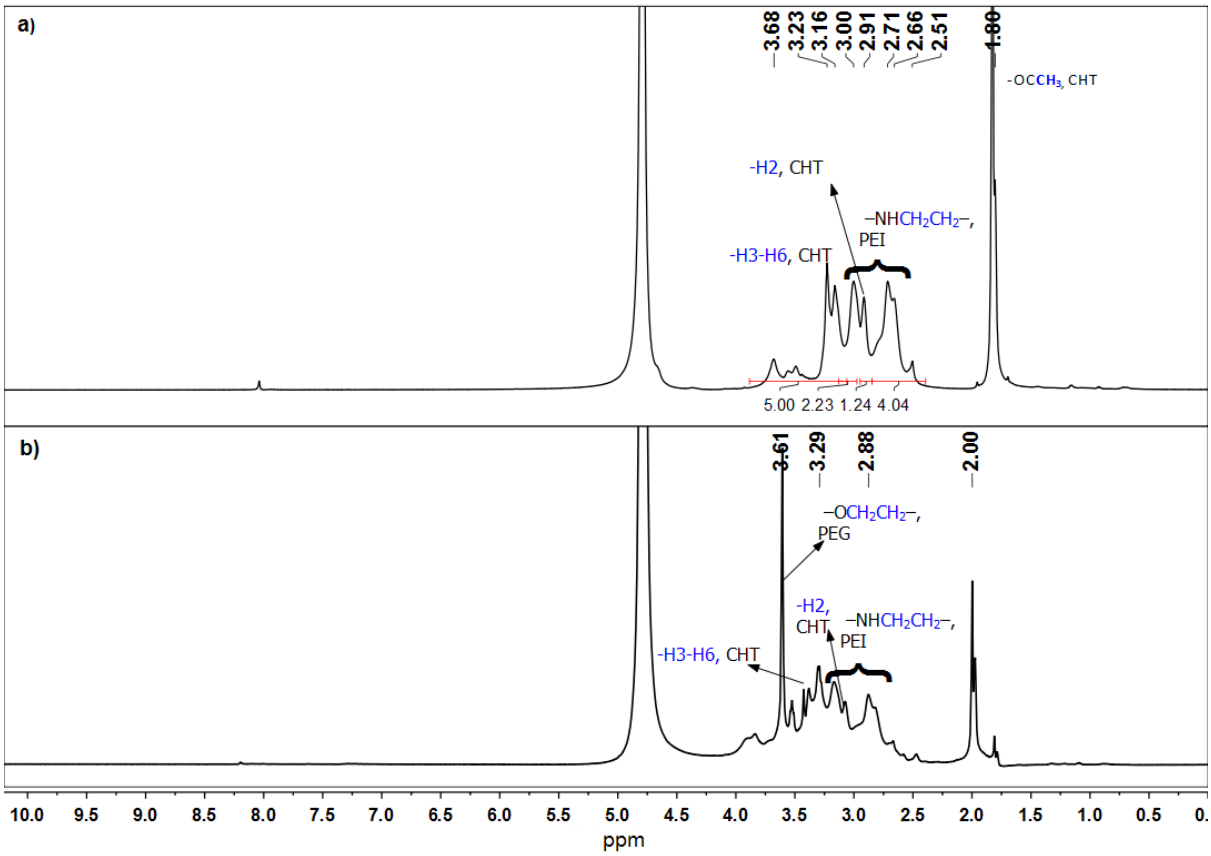


Figure 3.2: Proton NMR spectra of the synthesized copolymer complex in a solution of 5:1 concentration of D_2O and CD_3COOD respectively. (a) Represents the conjugation of CHT and PEI with their corresponding peaks, (b) the grafting of PEG to preformed CHT-g-PEI copolymer.

The FT-IR spectrum of the native and grafted polymers was shown in Figure 3.3. C-H and N-H stretching of the imidazole bonds between the amines of CHT and PEI in the grafted polymer conjugate (CHT-g-PEI) were assigned at 3312 and 3376 cm^{-1} (Ramasamy, 2015), respectively, as presented in Figure 3.3(iii). When the bi-functional PEG (NH_2-PEG-COOH) was conjugated to the CHT-g-PEI polymer conjugate, the FT-IR spectra of the NH_2-PEG-CHT-g-PEI grafted polymer (Figure 3.3(v)) showed a peak at 871.15cm^{-1} in the fingerprint region which was from the ^{V}C-O in the pyranose ring of chitosan thereby indicating the presence of chitosan as the core polymer framework in the synthesized NH_2-PEG-CHT-g-PEI trilayered complex. Also, the appearance of peaks at 1450.58 and 822.14cm^{-1} were attributed to the absorption of -$NHCH_2CH_2$- moieties which is from the branched PEI. The formation of an amide bond between

the carboxylic group of PEG, and the amine group of CHT-g-PEI copolymer was vividly noted in the NH_2-PEG-CHT-g-PEI complex. The characteristics peak at 1696.52cm^{-1} was assigned to the absorption from the C=O stretch in amide bond I, 1463.73 and 1496.4cm^{-1} were peaks attributed to the absorptions from both the N-H bend and C-N stretch in amine bond II while the tripartite absorption peaks at 1310.03, 1279.60 and 1251.85cm^{-1} were attributed to the N-H bend in plane and C-N stretch in amide bond III. Meanwhile, an absorption peak at 3389.35cm^{-1} was attributed to the N-H stretch from the free primary amine group attached to the PEG in the complex (NH_2-PEG-CHT-g-PEI) in Figure 3.3(v). Similarly, the characteristic peak of PEI was represented at an absorption peak of 822.14cm^{-1} while that the peak at 871.15cm^{-1} was assigned to CHT. Further, the characteristic peaks at 2978.23, 2853.50 and 2828.52cm^{-1} were attributed to the asymmetric stretching of CH_3 and CH_2 of chitosan polymer in the complex (AbdElhady, 2012). Upon the encapsulation of BSA within the grafted polymer matrix and nanoparticle formation, due to interactions between negative ions of TPP and the positively charged amines in the polymer complex, some of the peaks disappeared as seen in Figure 3(vi). Thus, ^{1}H NMR and FT-IR spectra results suggested that the NH_2-PEG-CHT-g-PEI copolymer were successfully synthesized, and BSA encapsulated.

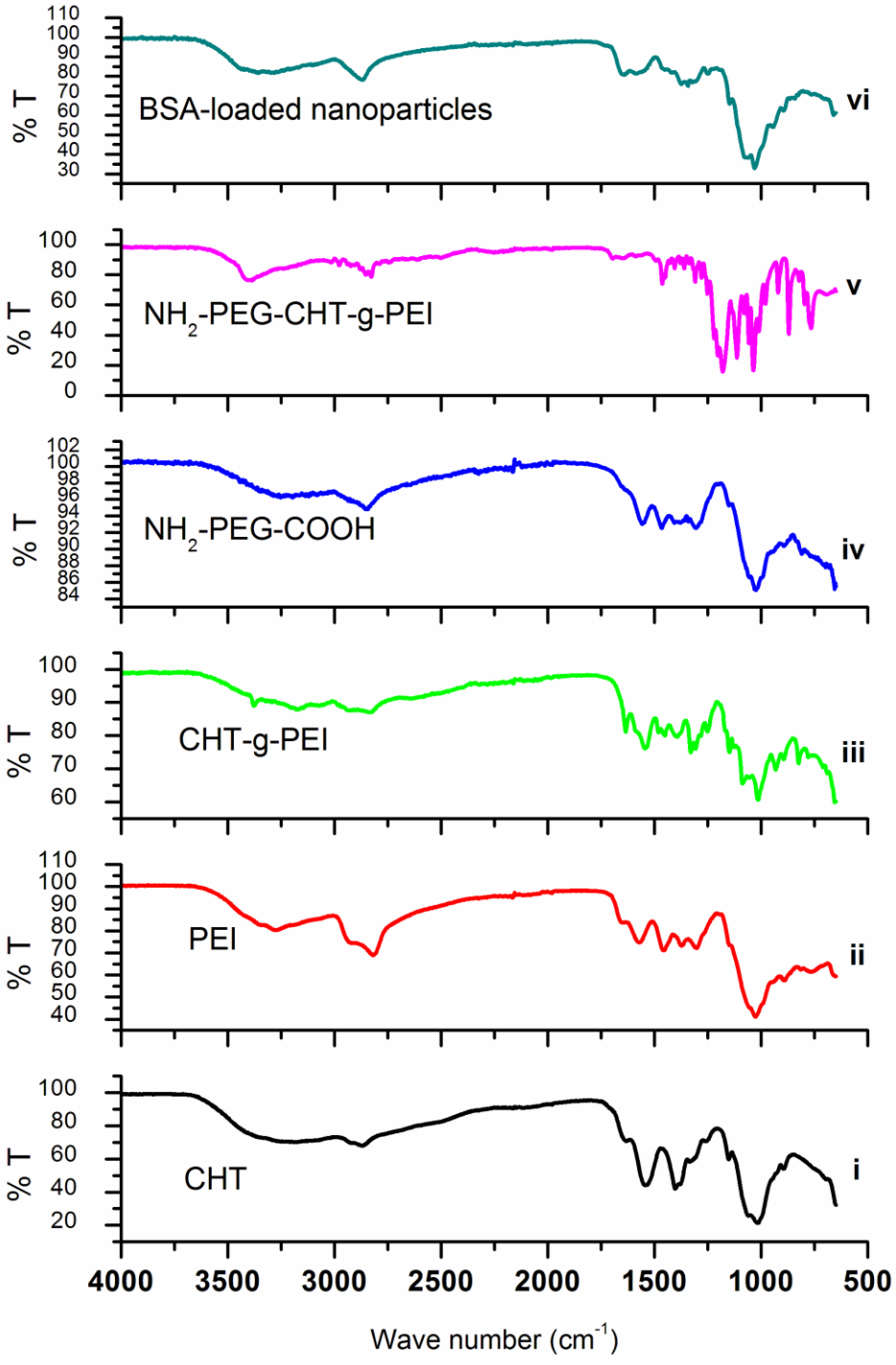


Figure 3.3: FTIR spectra showing the various peaks in the grafted, un-grafted biodegradable polymers and synthesized nanoparticles.

3.3.2. Evaluation of the Thermal Stability of the Native Polymers, Co-polymer Complex and Synthesized Nanoparticles

In order to investigate the transitions in the thermo-physical properties of the synthesized nanoparticles as well as the native polymers with respect to both temperature and time, Thermogravimetric Analysis (TGA) and Differential Scanning Calorimetry (DSC) experiments were performed. As shown in Figure 3.4(i), there were four distinct degradation events observed in the TGA thermogram of the synthesized nanoparticles (NH_2-PEG-CHT-g-PEI) from the grafted complex. The initial weight loss region begins from 50-100°C, accounting for 5% weight loss due to H_2O evaporation from the nanoparticles. The second degradation event was observed at 260°C with 10% weight loss, corresponding to the first degradation curve for the native chitosan (Figure 3.4(iv)) and is attributed to the decomposition of the chitosan main chain (Elhefian et al., 2012). Similarly, the third degradation event observed for the nanoparticles at 380°C (60% weight loss), corresponds to the second steep degradation pattern observed at 390°C for the branched PEI (Figure 3.4(ii)). The fourth degradation event observed from the nanoparticle thermogram is at about ~550°C (88% weight loss) and close to the third degradation pattern at 600°C in the PEG TGA curve (Figure 3.4(iv)). Compared to the native CHT, PEI and PEG, the TGA thermogram of the nanoparticles from the grafted copolymers showed that the thermal stability of the nanoparticle was comparatively high (Figure 3.4). Furthermore, from this analysis, the TGA thermogram of the nanoparticles further confirmed the successful grafting of the three biodegradable polymers within the nanosystem.

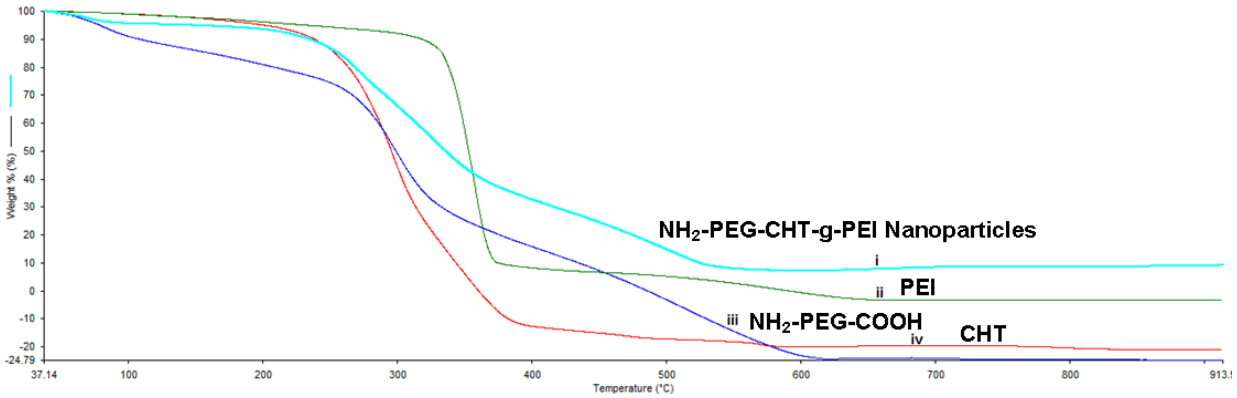


Figure 3.4: Thermogravimetric graph showing the thermal stability of the biodegradable polymers and the nanoparticles formed from the co-polymer complex.

Meanwhile, the thermal behaviour of the native polymers as well as both the BSA-loaded and free nanoparticles were analyzed by DSC and shown in Figure 3.5. As observed, the melting point (T_m) in the grafted CHT-g-PEI copolymer at 320°C (Figure 3.5a (i)) was higher than in native CHT (300°C) (Figure 3.5a (ii)). This change in the melting temperature is attributed to the increased heat energy required in terms of the transitions in the heat flow rate (more endothermic: from 4-6mW) due to bond breaking between the NH_2 groups in the two polymers during synthesis. Thus, the CHT-g-PEI copolymer complex was more thermally stable than the native chitosan. Upon the addition of PEG to the grafted CHT-g-PEI copolymer complex (Figure 3.5a (iii), the shifts observed in both the glass transition (T_g) and the crystallization (T_c) temperatures of the CHT-g-PEI and NH_2-PEG-CHT-g-PEI grafted copolymers (Figure 3.5a) suggest that the CHT-g-PEI copolymer complex (Figure 3.5a (i)) was more crystalline than the NH_2-PEG-CHT-g-PEI copolymer complex. Meanwhile, the BSA-loaded nanoparticles (Figure 3.5b (i)) were less stable in comparison to the BSA-free nanoparticles (Figure 3.5b (ii)).

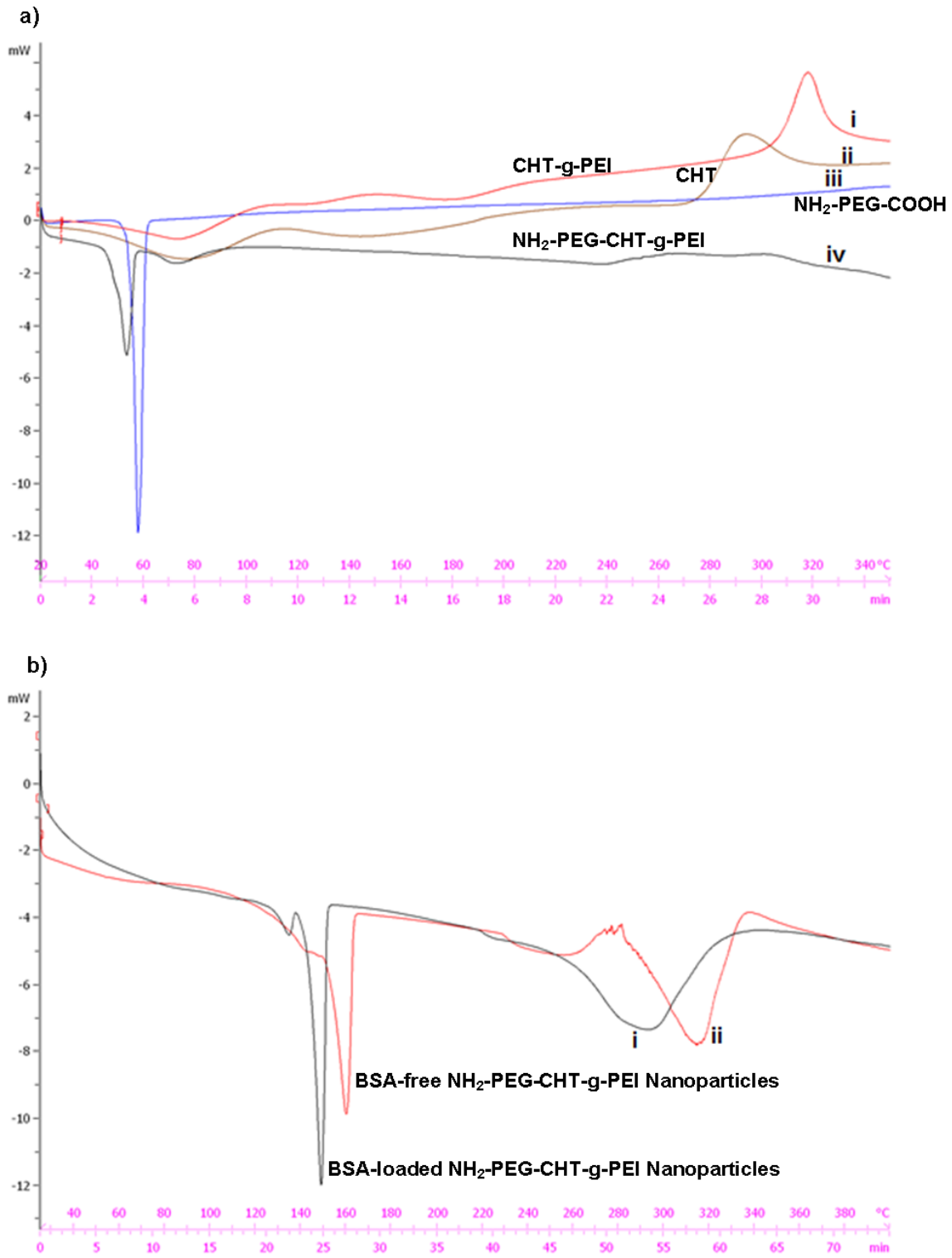


Figure 3.5: Superimposed DSC thermograms showing the thermal analysis of grafted/un-grafted polymers and BSA-loaded/BSA-free nanoparticles. (a) Thermograms of native and grafted copolymers, (b) thermograms of BSA-loaded and unloaded nanoparticles

3.3.3. Assessment of the Nanoparticle Size, Surface Charge and Morphology

The size and surface properties of nanoparticles are crucial parameters to ensure cellular uptake in SCC. More importantly, the particle size determines the accessibility and efficient passage of the nanoparticles to the target site (Jiang et al., 2007). Particle size and surface-dependent colloids <520nm have been shown to be taken up from subcutaneous tissue to the lymphatics (Ikomi et al., 2012, 1999). As shown in Figures 3.6 and 3.7, both TEM and Dynamic Light Scattering (DLS) results respectively revealed that the nanoparticles were spherically shaped and had a narrow particle size distribution with a polydispersity index (PDI) value of 0.232 and an average size of 63.14±31.31nm.

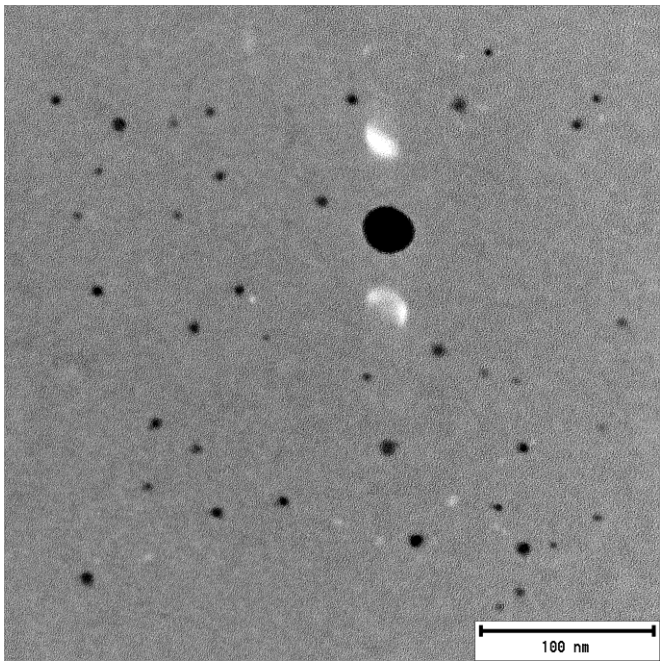


Figure 3.6: TEM micrograph of the BSA loaded nanoparticles. Nanoparticles possessed a spherical shape with an average size < 100 nm.

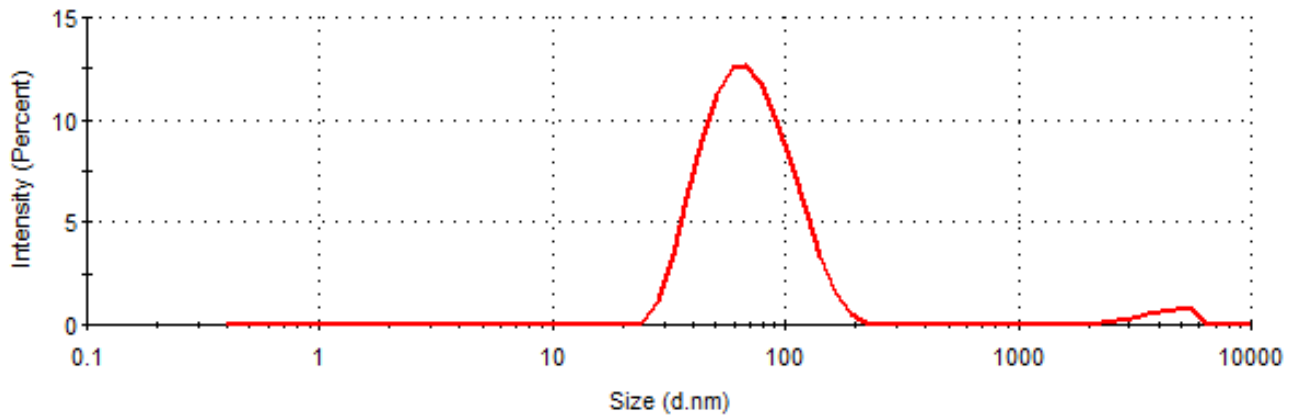


Figure 3.7: Nanoparticles size intensity profile for BSA loaded nanoparticles using Dynamic Light Scattering. Nanoparticles were dispersed in distilled H_20 prior to measurement.

Furthermore, the spherical shape of the nanoparticles was confirmed by SEM micrographs (Figure 3.8). The variance in the size of the nanoparticles between the DLS, TEM and SEM results was due to the fact that chitosan nanoparticles swell in aqueous media and possible agglomeration of smaller particles to form large size particles. DLS provides the hydrodynamic diameter of nanoparticles and TEM samples were prepared in aqueous solution though transiently. Particle size distribution by microscopy is considered as an absolute measurement of particle size and it can differentiate between single particles and aggregates (Jia et al., 2013). Thus, both TEM and SEM provide the actual diameter of nanoparticles in a dry state. However, some of the larger particles displayed in the SEM micrographs was be due to aggregation of the chitosan-based complex/TPP nanoparticles since the hydrogen bonding interactions between the chitosan-based nanoparticles became dominant during the drying process (Fan et al., 2012). As such, the dry sample measurement using SEM accounts for the increase in size as opposed to the TEM and DLS results.

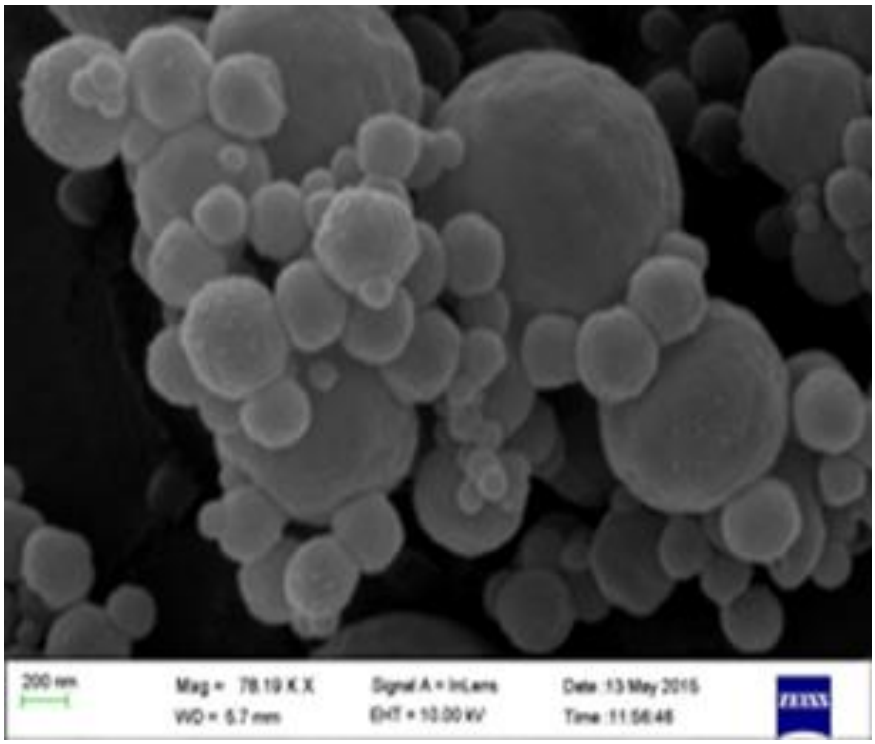


Figure 3.8: Gold-platinum sputtered SEM Micrograph of BSA loaded nanoparticles. Magnification = 50.00 KX; Voltage = 10.00 kV.

The surface charge of aqueous nanoparticles determines the stability as it is measured by electrophoresis and expressed as the electrophoretic mobility or converted to the zeta potential (mV). Nanoparticles having zeta potential values that are > +25mV or < -25mV usually have high degrees of stability. Colloidal dispersions with a low zeta potential value eventually aggregate due to Van der Waal interparticle attractions. As presented in Figure 3.9, a positive zeta potential value of 19.8mV was recorded for the chitosan-based nanoparticles having a conductivity of 0.0319mS/cm and viscosity (Cp) of 0.8872. The Refractive Index (RI) of the dispersant was 1.330. Since the nanoparticles were formed by interactions between the protonized $–NH^+$ in the PEG component of the grafted copolymer complex (NH_2-PEG-CHT-g-PEI) and the polyanionic phosphate groups in TPP, the zeta potential of nanoparticles increased as a result of an increase in the available protonized $–NH_3^+$ on the surface of the synthesized nanoparticles. Since many research studies have documented that protonated chitosan-based

nanoparticles displayed mucoadhesive characteristics, the synthesized nanoparticles may also possess mucoadhesive properties due to the molecular force of attraction generated by an electrostatic interaction between the positively charge ions on the nanoparticle surface and the negatively charge ions on mucosal surfaces in SCC. It is however of interest to note that the surface charge of most tumor cell membranes are negatively charged (Szachowicz-Petelska et al., 2012). Thus, the nanosystem could be an efficient delivery strategy for targeted transport of protein therapeutics in cancer therapy. Similarly, the positively charged surface of the nanoparticle accounts for the formation of larger particles as shown in the SEM micrograph due to agglomeration as discussed earlier (Figure 3.8).

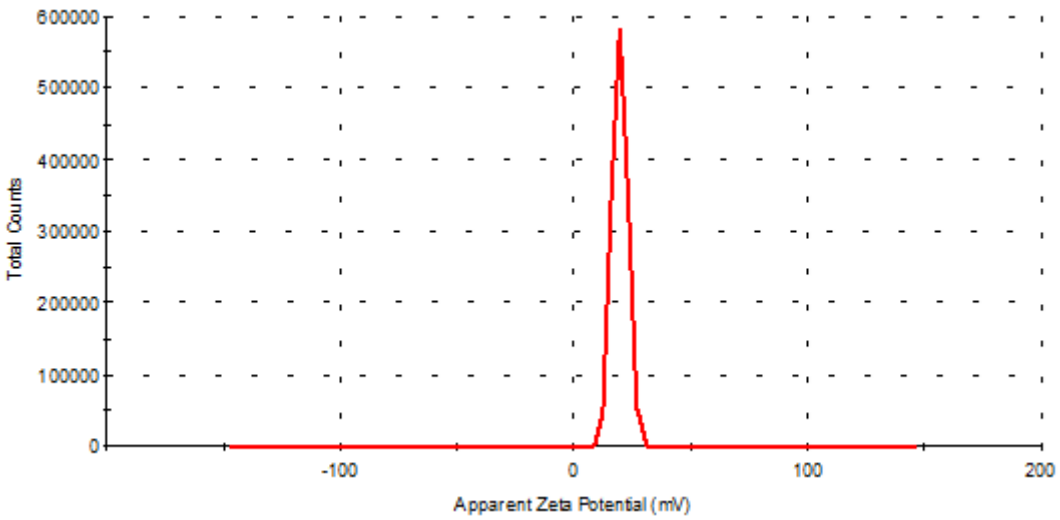


Figure 3.9: Nanoparticle Zeta potential measurement profile. Nanoparticles sample was dispersed in deionized water.

3.3.4. Assessment of BSA encapsulation and *in vitro* release kinetics

Through interpolation from the standard curve using Equation 3.1, the BSA-loading efficiency was computed to be 77.2±0.0095%. This result corroborates with both the findings of (Gan and Wang, 2007) and (Vila et al., 2004) with BSA-loading efficiencies of 61.1% and 50-60%

respectively for chitosan nanoparticles. The higher encapsulation obtained in this study was due to the higher degree of deacetylation (80-85%) of the chitosan component within the nanosystem and the influence of the cationic PEI moiety. This accounted for intermolecular interactions between the chitosan-based nanoparticles and the negatively charged functional group of the polypeptide chains within BSA. The degree of encapsulation of chitosan nanoparticles depended largely on how the cationic chains in chitosan interacted with the BSA molecules with complex 3-D structures having hydrophobic regions that folded within the 3-D matrix in an aqueous environment. It should be noted that BSA polypeptide chains have both positive and negative charges either of which influenced its interactions depending on the pH of the aqueous environment (Gan and Wang, 2007). The chitosan molecular chain was expected to be fully extended in solution at a pH of 5.5 since the electrostatic repulsion between the amine groups were present along the molecular chain. This therefore allowed BSA molecules to interact with the NH_2 group of chitosan without any major steric hindrance. Interestingly, studies have shown that BSA molecules only exhibit molecular reversible expansion at pH values < 4.5 or > 10.5 as the physical property of BSA remains virtually unchanged and more compacted at pH values over the intermediate pH range around its isoelectric point (Malamud and Drysdale, 1978). Similarly, chitosan with a higher degree of deacetylation contains more functional groups that can interact with the -COOH groups of BSA and subsequently gelate with polyanionic TPP groups (Sabnis and Block, 2000) thereby increasing BSA entrapment efficiency within the nanoparticles.

The addition of PEG onto chitosan nanoparticles has been reported to lower the encapsulation efficiency of BSA into the chitosan matrix (Kim et al., 1995). This is due to the formation of an intermolecular hydrogen bonding between the negatively charged oxygen atom on the convectional PEG backbone and the NH_2 groups of chitosan in gel system. There is a high possibility for the carboxylic group of BSA and the oxygen atom of PEG to compete in their

interaction with the NH_2 groups on chitosan thereby reducing the interaction between BSA and chitosan. As such, the PEG chains are entangled to the chitosan molecules thereby limiting the encapsulation of BSA into the chitosan nanoparticles. However, this assumption may not be applicable in our study since a bifunctional PEG with both amino and carboxylic terminals are employed. There is a high possibility that the excess amino groups in PEI increased the total available NH_2 in the nanosystem which interact with the carboxylic component of the PEG and not the negatively charged oxygen atom allowing for the encapsulation of the BSA molecules to the chitosan nanoparticles. It should also be noted that our strategy employed both NHS and EDC to immobilize both the COOH group of the bi-functional PEG and the NH_2 group of CHT-g-PEI copolymer to form the NH_2-PEG-CHT-g-PEI complex. Therefore, this novel combinatorial network of adding both PEI and bifunctional PEG unto chitosan nanoparticles provides a smart strategy for the encapsulation of protein therapeutics in cancer management.

Furthermore, the increased BSA encapsulation was also attributed to the influence of the CHT: TPP mass ratio in the nanosystem. A lower CHT:TPP mass ratio has been previously suggested to enhance BSA loading efficiency during the formation of CHT-BSA nanoparticles (Gan and Wang, 2007). High TPP concentration to fixed chitosan concentration may increase the solution pH value which consequently influences the overall negative charge at the surface of the BSA molecules. This enhances the electrostatic interactions between chitosan chains and BSA molecules (Alsarra et al., 2004). Another parameter that could justify the increased BSA encapsulation in this study was the effect of the BSA concentration as supported by the work of (Gan and Wang, 2007) though their report showed that the effect of BSA concentration and encapsulation were not conclusive and contradicting in some instances. For example, (Xu and Du, 2003) reported an inverse relationship between BSA encapsulation and the concentration effect. At a pH of 6, an increasing BSA concentration from 0.25-1.50mg/mL resulted in an increased encapsulation efficiency from 38.7-72.5% according to the findings of Gan and Wang

(2007). Meanwhile, a BSA concentration of 1mg/mL was employed as a model in this study with a PLE of 77.2%. In addition, the simultaneous interaction of TPP with both the BSA and chitosan moiety is suggested to influence an increase BSA encapsulation at higher concentrations. Thus, the results of this study showed an efficient entrapment of BSA within the chitosan chains of the chitosan-based nanoparticles.

As shown in Figure 3.10, the BSA release profile displayed an initial burst release phase, followed by prolonged gradual release kinetics that is expected with chitosan-based nanoparticles. There was a dramatic reduction in BSA release after the first 8 hours since subsequent BSA release requires swelling and degradation of the compact nanoparticles. A rapid release of 17% and 12% at pH 6.8 and 7.4, respectively, over the first 2 hours was observed. Meanwhile, after 8 hours, the release pattern was lowered and prolonged for up to 30 hours with 48% and 38% of BSA released at pH 6.8 and 7.4, respectively. The results showed that BSA release was modulatable by the changing pH conditions of the release medium. Previous reports regarding microspheres have shown that two different mechanisms are involved in the release pattern of BSA molecules including the diffusion of molecules and the degradation of the polymer matrix. The burst release phase of BSA was due to molecules dispersed close to the surface of the microspheres which were easily diffused in the initial incubation time (Xu and Du, 2003). As can be seen in the SEM micrograph (Figure 3.8), some deposits of BSA particles exist on the surface of the nanoparticles which could be easily released into the release buffer. It is possible for the nanoparticles with a large unique surface area to adsorb BSA molecules on their surfaces which may account for the initial burst release observed in this study. Another parameter that explicates the high initial burst release before steady state after 8 hours could be the high BSA loading efficiency as the BSA-loading capacity, as release rate is usually facilitated by increased protein concentration (Xu and Du, 2003).

Changing pH conditions have been reported to facilitate the release of encapsulated drug in polymeric nanosystems. As presented in Figure 3.10, the designed BSA loaded nanosystem exhibited dual pH responses at pH 6.8 and 7.4 respectively. The release pattern at pH 6.8 is higher than that exhibited at pH 7.4. For instance, after 8 hours, 25% and 17% of the loaded BSA was released at pH 6.8 and 7.4 respectively. Similarly, about 48% and 38% of the loaded BSA was released after 30 hours at pH 6.8 and 7.4 respectively. This is because pH-responsive systems, such as chitosan, swell in acidic medium thereby triggering the release of the encapsulated drug (Makhlof et al., 2011; Upreti et al., 2013). It is interesting to note that this changing effect of our nanosystem could be explored for the delivery of cancer chemotherapeutics since tumor microenvironments exhibit a more lower acidic condition (6.7 – 6.9) as opposed to the physiological pH of healthy cells at 7.4 (Petros and DeSimone, 2010).

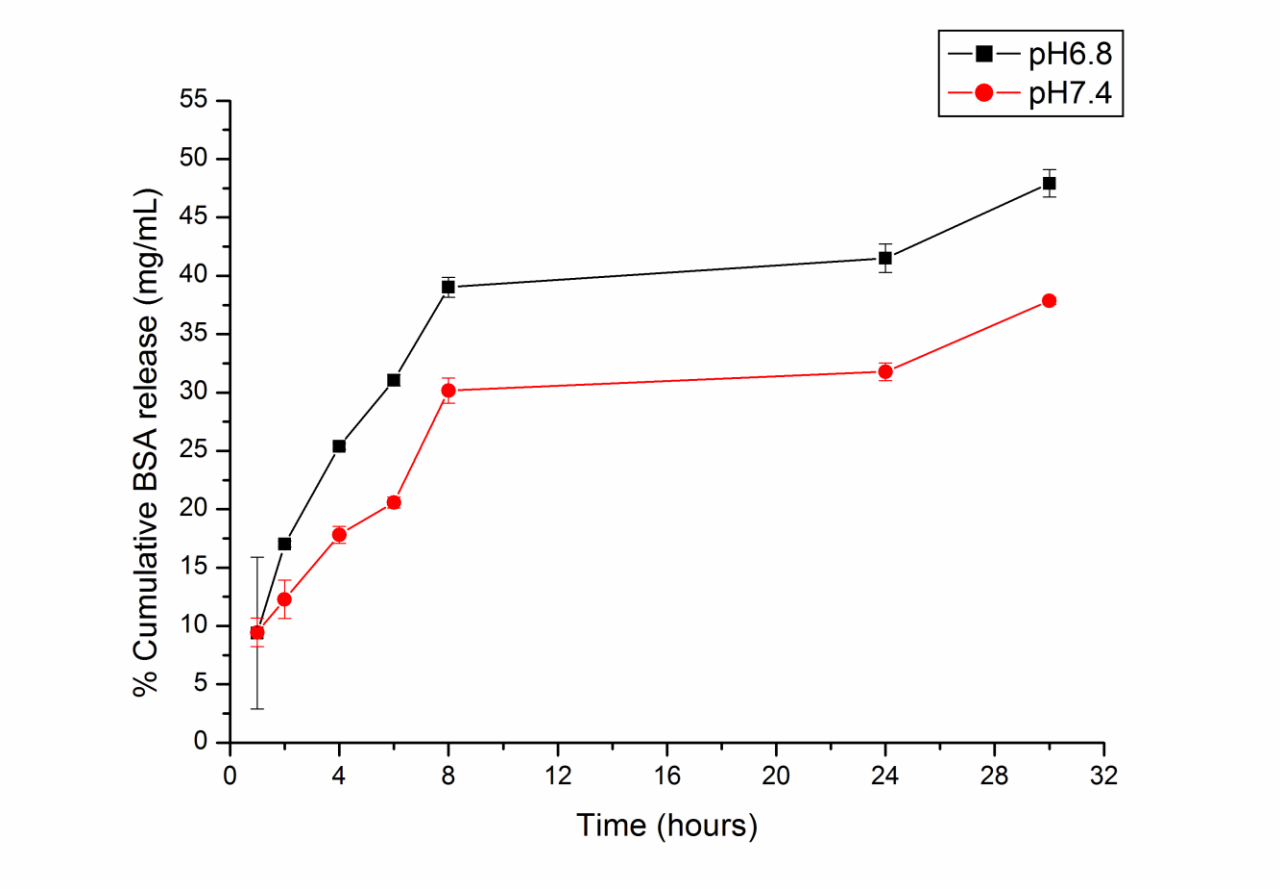


Figure 3.10: Release profiles of BSA-loaded nanosystems prepared at conditions: CHT concentration = 2mg/mL, CHT-based complex/TPP mass ratio = 2:1, BSA concentration = 1mg/mL. Released medium = PBS, Temperature = 37 ± 1°C, pH = 7.4 and 6.8. Samples were analyzed in triplicate (n=3).

3.4. Concluding remarks

Using BSA as a model protein, CHT-based BSA-loaded nanoparticles were synthesized and characterized. TGA and DSC results confirmed the thermal stability of the BSA-loaded nanoparticles compared with native polymers. BSA-loading efficiency was 77.2% with an initial burst release due to surface protein desorption and subsequent prolonged release through diffusion from sub-layers after 2 hours up to 30 hours at varying pH conditions. The release kinetics at pH 6.8 was higher than at pH 7.4. Conclusively, this nanosystem may be explored as a vehicle for pH-responsive targeting of therapeutic proteins in cancer nanomedicine as tumors are known to have acidic pH micro-environments.

3.7. References

AbdElhady, M.M., 2012. Preparation and Characterization of Chitosan/Zinc Oxide Nanoparticles for Imparting Antimicrobial and UV Protection to Cotton Fabric. Int. J. Carbohydr. Chem. 2012, e840591.

Adebowale, A.S., Choonara, Y.E., Kumar, P., du Toit, L.C., Pillay, V., 2015. Functionalized Nanocarriers for Enhanced Bioactive Delivery to Squamous Cell Carcinomas: Targeting Approaches and Related Biopharmaceutical Aspects. Curr. Pharm. Des. 21, 3167–3180.

Alsarra, I.A., Neau, S.H., Howard, M.A., 2004. Effects of preparative parameters on the properties of chitosan hydrogel beads containing Candida rugosa lipase. Biomaterials 25, 2645–2655.

Bürki, K., Jeon, I., Arpagaus, C., Betz, G., 2011. New insights into respirable protein powder preparation using a nano spray dryer. Int. J. Pharm. 408, 248–256.

Dang, J.M., Leong, K.W., 2006. Natural polymers for gene delivery and tissue engineering. Adv. Drug Deliv. Rev. 58, 487–499.

Didenko, V.V., Ngo, H., Baskin, D.S., 2005. Polyethyleneimine as a transmembrane carrier of fluorescently labeled proteins and antibodies. Anal. Biochem. 344, 168–173.

Elhefian, E.A., Nasef, M.M., Yahaya, A.H., 2012. Preparation and Characterization of Chitosan/Agar Blended Films: Part 2. Thermal, Mechanical, and Surface Properties. J. Chem. 9, 510–516.

Fan, W., Yan, W., Xu, Z., Ni, H., 2012. Formation mechanism of monodisperse, low molecular weight chitosan nanoparticles by ionic gelation technique. Colloids Surf. B Biointerfaces 90, 21–27.

Fischer, D., Bieber, T., Li, Y., Elsässer, H.-P., Kissel, T., 1999. A novel non-viral vector for DNA delivery based on low molecular weight, branched polyethylenimine: Effect of molecular weight on transfection efficiency and cytotoxicity. Pharm. Res. 16, 1273–1279.

Fosgerau, K., Hoffmann, T., 2015. Peptide therapeutics: current status and future directions. Drug Discov. Today 20, 122–128.

Gan, Q., Wang, T., 2007. Chitosan nanoparticle as protein delivery carrier—Systematic examination of fabrication conditions for efficient loading and release. Colloids Surf. B Biointerfaces 59, 24–34.

Gao, J.-Q., Zhao, Q.-Q., Lv, T.-F., Shuai, W.-P., Zhou, J., Tang, G.-P., Liang, W.-Q., Tabata, Y., Hu, Y.-L., 2010a. Gene-carried chitosan-linked-PEI induced high gene transfection efficiency with low toxicity and significant tumor-suppressive activity. Int. J. Pharm. 387, 286–294.

Gao, J.-Q., Zhao, Q.-Q., Lv, T.-F., Shuai, W.-P., Zhou, J., Tang, G.-P., Liang, W.-Q., Tabata, Y., Hu, Y.-L., 2010b. Gene-carried chitosan-linked-PEI induced high gene transfection efficiency with low toxicity and significant tumor-suppressive activity. Int. J. Pharm. 387, 286–294.

Gao, J.-Q., Zhao, Q.-Q., Lv, T.-F., Shuai, W.-P., Zhou, J., Tang, G.-P., Liang, W.-Q., Tabata, Y., Hu, Y.-L., 2010c. Gene-carried chitosan-linked-PEI induced high gene transfection efficiency with low toxicity and significant tumor-suppressive activity. Int. J. Pharm. 387, 286–294.

George, M., Abraham, T.E., 2006. Polyionic hydrocolloids for the intestinal delivery of protein drugs: Alginate and chitosan - a review. J. Controlled Release 114, 1–14.

Holzerny, P., Ajdini, B., Heusermann, W., Bruno, K., Schuleit, M., Meinel, L., Keller, M., 2012. Biophysical properties of chitosan/siRNA polyplexes: profiling the polymer/siRNA interactions and bioactivity. J. Control. Release Off. J. Control. Release Soc. 157, 297–304.

Ikomi, F., Hanna, G.K., Schmid-Schönbein, G.W., 1999. Size- and surface-dependent uptake of colloid particles into the lymphatic system. Lymphology 32, 90–102.

Ikomi, F., Kawai, Y., Ohhashi, T., 2012. Recent Advance in Lymph Dynamic Analysis in Lymphatics and Lymph Nodes. Ann. Vasc. Dis. 5, 258–268.

Jia, L., Li, Z., Zhang, D., Zhang, Q., Shen, J., Guo, H., Tian, X., Liu, G., Zheng, D., Qi, L., 2013. Redox-responsive catiomer based on PEG-ss-chitosan oligosaccharide-ss-polyethylenimine copolymer for effective gene delivery. Polym Chem 4, 156–165.

Jiang, H.-L., Kim, Y.-K., Arote, R., Nah, J.-W., Cho, M.-H., Choi, Y.-J., Akaike, T., Cho, C.-S., 2007. Chitosan-graft-polyethylenimine as a gene carrier. J. Controlled Release 117, 273–280.

Jiang, H.-L., Kwon, J.-T., Kim, E.-M., Kim, Y.-K., Arote, R., Jere, D., Jeong, H.-J., Jang, M.-K., Nah, J.-W., Xu, C.-X., Park, I.-K., Cho, M.-H., Cho, C.-S., 2008. Galactosylated poly(ethylene glycol)-chitosan-graft-polyethylenimine as a gene carrier for hepatocyte-targeting. J. Control. Release Off. J. Control. Release Soc. 131, 150–157.

Kaul, G., Amiji, M., 2004. Biodistribution and targeting potential of poly(ethylene glycol)-modified gelatin nanoparticles in subcutaneous murine tumor model. J. Drug Target. 12, 585–591.

Kim, T.H., Kim, S.I., Akaike, T., Cho, C.S., 2005. Synergistic effect of poly(ethylenimine) on the transfection efficiency of galactosylated chitosan/DNA complexes. J. Control. Release Off. J. Control. Release Soc. 105, 354–366.

Kunath, K., von Harpe, A., Fischer, D., Petersen, H., Bickel, U., Voigt, K., Kissel, T., 2003. Low-molecular-weight polyethylenimine as a non-viral vector for DNA delivery: comparison of physicochemical properties, transfection efficiency and in vivo distribution with high-molecular-weight polyethylenimine. J. Controlled Release 89, 113–125.

Liu, Y., Reineke, T.M., 2007. Poly(glycoamidoamine)s for gene delivery. structural effects on cellular internalization, buffering capacity, and gene expression. Bioconjug. Chem. 18, 19–30.

Lohcharoenkal, W., Wang, L., Chen, Y.C., Rojanasakul, Y., 2014. Protein Nanoparticles as Drug Delivery Carriers for Cancer Therapy. BioMed Res. Int. 2014, e180549.

Lu, H., Dai, Y., Lv, L., Zhao, H., 2014. Chitosan-Graft-Polyethylenimine/DNA Nanoparticles as Novel Non-Viral Gene Delivery Vectors Targeting Osteoarthritis. PLoS ONE 9.

Makhlof, A., Tozuka, Y., Takeuchi, H., 2011. Design and evaluation of novel pH-sensitive chitosan nanoparticles for oral insulin delivery. Eur. J. Pharm. Sci. 42, 445–451.

Malamud, D., Drysdale, J.W., 1978. Isoelectric points of proteins: a table. Anal. Biochem. 86, 620–647.

Malek, A., Czubayko, F., Aigner, A., 2008. PEG grafting of polyethylenimine (PEI) exerts different effects on DNA transfection and siRNA-induced gene targeting efficacy. J. Drug Target. 16, 124–139.

Mao, S., Shuai, X., Unger, F., Simon, M., Bi, D., Kissel, T., 2004. The depolymerization of chitosan: effects on physicochemical and biological properties. Int. J. Pharm. 281, 45–54.

Merkel, O.M., Librizzi, D., Pfestroff, A., Schurrat, T., Buyens, K., Sanders, N.N., De Smedt, S.C., Béhé, M., Kissel, T., 2009. Stability of siRNA polyplexes from poly(ethylenimine) and poly(ethylenimine)-g-poly(ethylene glycol) under in vivo conditions: Effects on pharmacokinetics and biodistribution measured by Fluorescence Fluctuation Spectroscopy and Single Photon Emission Computed Tomography (SPECT) imaging. J. Controlled Release 138, 148–159.

Neu, M., Fischer, D., Kissel, T., 2005. Recent advances in rational gene transfer vector design based on poly(ethylene imine) and its derivatives. J. Gene Med. 7, 992–1009.

Petros, R.A., DeSimone, J.M., 2010. Strategies in the design of nanoparticles for therapeutic applications. Nat. Rev. Drug Discov. 9, 615–627.

Ramasamy, R., 2015. Vibrational Spectroscopic Studies of Imidazole. Armen. J. Phys. 8, 51–55.

Roberts, M.J., Bentley, M.D., Harris, J.M., 2002. Chemistry for peptide and protein PEGylation. Adv. Drug Deliv. Rev. 54, 459–476.

Sabnis, S., Block, L.H., 2000. Chitosan as an enabling excipient for drug delivery systems. I. Molecular modifications. Int. J. Biol. Macromol. 27, 181–186.

Sirsi, S.R., Williams, J.H., Lutz, G.J., 2005. Poly(ethylene imine)-poly(ethylene glycol) copolymers facilitate efficient delivery of antisense oligonucleotides to nuclei of mature muscle cells of mdx mice. Hum. Gene Ther. 16, 1307–1317.

Sollohub, K., Cal, K., 2010. Spray drying technique: II. Current applications in pharmaceutical technology. J. Pharm. Sci. 99, 587–597.

Szachowicz-Petelska, B., Dobrzyska, I., Sulkowski, S., A., Z., 2012. Characterization of the Cell Membrane During Cancer Transformation. In: Ettarh, R. (Ed.), Colorectal Cancer Biology - From Genes to Tumor. InTech.

Tripathi, S.K., Goyal, R., Kumar, P., Gupta, K.C., 2012. Linear polyethylenimine-graft-chitosan copolymers as efficient DNA/siRNA delivery vectors in vitro and in vivo. Nanomedicine Nanotechnol. Biol. Med. 8, 337–345.

Ulasov, A.V., Khramtsov, Y.V., Trusov, G.A., Rosenkranz, A.A., Sverdlov, E.D., Sobolev, A.S., 2011. Properties of PEI-based Polyplex Nanoparticles That Correlate With Their Transfection Efficacy. Mol. Ther. 19, 103–112.

Upreti, M., Jyoti, A., Sethi, P., 2013. Tumor microenvironment and nanotherapeutics. Transl. Cancer Res. 2, 309–319.

Vila, A., Sánchez, A., Janes, K., Behrens, I., Kissel, T., Jato, J.L.V., Alonso, M.J., 2004. Low molecular weight chitosan nanoparticles as new carriers for nasal vaccine delivery in mice. Eur. J. Pharm. Biopharm., Chitosan 57, 123–131.

Xu, Y., Du, Y., 2003. Effect of molecular structure of chitosan on protein delivery properties of chitosan nanoparticles. Int. J. Pharm. 250, 215–226.

Young Lee, G., Park, K., Nam, J.H., Kim, S.Y., Byun, Y., 2006. Anti-tumor and anti-metastatic effects of gelatin-doxorubicin and PEGylated gelatin-doxorubicin nanoparticles in SCC7 bearing mice. J. Drug Target. 14, 707–716.

Zhang, W., Pan, S., Wen, Y., Luo, X., Zhang, X., 2010. Synthesis of poly(ethylene glycol)-g-chitosan-g-poly(ethylene imine) co-polymer and in vitro study of its suitability as a gene-delivery vector. J. Biomater. Sci. Polym. Ed. 21, 741–758.

Zhao, Q.-Q., Chen, J.-L., Lv, T.-F., He, C.-X., Tang, G.-P., Liang, W.-Q., Tabata, Y., Gao, J.-Q., 2009. N/P ratio significantly influences the transfection efficiency and cytotoxicity of a polyethylenimine/chitosan/DNA complex. Biol. Pharm. Bull. 32, 706–710.

CHAPTER 4

DESIGN AND CHARACTERIZATION OF ENDOSTATIN-LOADED NANOPARTICLES FOR *IN VITRO* ANTI-ANGIOGENESIS IN SQUAMOUS CELL CARCINOMA

4.1. Introduction

Squamous Cell Carcinoma (SCC), accounts for different cancer types emanating from various tissues of the body including the skin, oesophagus, head and neck, urinary bladder, prostate, lung, vagina, and cervix resulting in about 2,500 deaths annually in the United States (Adebowale et al., 2015). Over the years, chemo-radiation and surgery had been the prominent treatment options for patients diagnosed with SCC. Until recently, with the advent of cutting edge approaches using nanotechnology, chemotherapeutics employed in the management of SCC were hampered with diverse challenges such as sub-optimal dosage, cytotoxicity to normal cells due to non-targeted delivery, short circulation time as well as multiple resistances due to the Reticulo-Endothelial System (RES) (Adebowale et al., 2015).

To date, anti-cancer drugs have been encapsulated into diverse cargoes such as polymeric micelles, surface-modified particles, liposomes and nanoparticles as delivery vehicles in cancer nanomedicine (Hu and Zhang, 2010; Nishiyama and Kataoka, 2006; Torchilin, 2007) in an attempt to overcome these challenges. Nanoparticles, in contrast to other delivery vehicles, have a number of chemotherapeutic advantages including ease of injection, high drug-loading ratio, reduced toxicity to healthy cells/tissues and enhanced direct targeting effect in both primary and metastatic tumors (Hu and Zhang, 2010).

Angiogenesis, the formation of new blood vessels, is fundamental to the survival and growth of tumor cells (Folkman, 1990, 1971; Zheng, 2009). Recent focus has been on the use of natural and synthetic inhibitors of angiogenesis that can prevent or slow down the growth of tumor cells by blocking the formation of new blood vessels as a promising strategy for tumor therapy (Folkman, 2006a).

Endostatin is a proteolytic C-terminal fragment of collagen XVIII with a molecular weight of 20 kDa. Among other angiogenic inhibitors, endostatin has received the greatest attention for its broad-spectrum and low toxicity (Folkman, 2006b). These advantages speed up the investigation process of endostatin into the clinical trial (Herbst et al., 2001). Endostatin has been shown to inhibit endothelial cell proliferation, migration, and formation of new blood vessels (Kim et al., 2002; Zheng, 2009). However, as any other protein, endostatin has many clinical challenges in its application such as high dosage to maintain its efficacy, high price, short half-life and instability (Qiu et al., 2012). As such, incorporation into biodegradable polymers as delivery cargos could ameliorate these limitations.

Chitosan (CHT), as opposed to other naturally occurring polymers and CHT-based nanoparticles, have recently attracted much considerations in both pharmaceutical and biomedical applications due to its exceptional biological properties including biocompatibility, biodegradability and non-toxicity (Seda Tı˘glı Aydın and Pulat, 2012) but with low transfection efficiency. The high buffering potential and transfection efficiency of polyethylenimine (PEI) have been explored for the delivery of DNA and other anti-cancer therapeutics in the management of cancer diseases (Ip et al., 2015; Ogris et al., 2003; Zou et al., 2000). Meanwhile, covalent attachment of hydrophilic polyethylene glycol (PEG) onto the surfaces of nanoparticles prolongs the circulation half-life *in vivo* of encapsulated chemotherapeutics, shields the surface of

nanoparticles from uptake by the RES, and reduces carrier's cytotoxicity with improved colloidal stability (Jia et al., 2013).

In this study, we employed low molecular weight CHT grafted onto PEI as a cationic carrier for improved delivery of endostatin. Furthermore, the surfaces of these grated polymers were coated with PEG to improve endostatin encapsulation and prolong release *in vitro*. Surface PEGylation of the grafted polymer also enhances its stability in the extracellular matrix of oesophageal squamous cell carcinoma (OSCC) cells. Formulation parameters, optimisation and cyto-compatibility of the nanosystem were evaluated and the anti-angiogenic effect of endostatin-loaded nanoparticles was assessed in an OSCC cell line (KYSE-30).

4.2. Materials and Methods

4.2.1. Materials

Low molecular weight chitosan (DE=75-85%, MW=50-190kDa), branched polyethylenimine (PEI) (Molecular weight Mw=25KDa), Bovine Serum Albumin (BSA) (MW=66kDa), Human recombinant Endostatin (MW=22kDa), 1-ethyl-3-(3-dimethylaminopropyl) carbodiimide hydrochloride (EDC), N-hydroxysuccinimide (NHS), Sodium tripolyphosphate (TPP) (MW=367.86g/mol), poly(vinyl alcohol) (PVA) (MW=85,000g/mol), tricholroacetic acid (TCA) and acetonitrile (ACN) were purchased from Sigma-Adrich Co., Ltd. (St. Louis, MO, USA). Functionalized poly (ethylene) glycol (NH_2-PEG-COOH, Mw=2100g/mol) was from NANOCS (New York, NY, USA). Cell lines KYSE-30, RPMI, HAM's F12, Fetal Bovine Serum (FBS), and Pentamycin/streptomycin were from Life Bioscience (Oakleigh, VIC, Australia). All other solvents and reagents were of analytical grade unless stated otherwise.

4.2.2 Methods

4.2.2.1. Preparation of [CHI-g-PEI-PEG-NH_2]-Endostatin-loaded nanoparticles

4.2.2.1.1. Synthesis of the CHI-g-PEI conjugate

A Box-Behnken experimental design was employed to generate fifteen nanoformulations as presented in Table 4.1. A modified method described by Gao et al. (Gao et al., 2010) was employed to synthesize the CHT-g-PEI conjugate. Briefly, 0.5, 1.5 and 2.5mg/mL Chitosan (CHT) solutions were prepared in 0.5% acetic acid and left overnight (Table 4.1). 1, 1-Carbonyldiimidazole (CDI) was added to the CHT solutions and stirred for 1 hour at room temperature to activate the amine group in the CHT solution. Subsequently, 0.25%$^{v}/_{v}$ of branched Polyethylene imine (PEI) was gently added using a needle and syringe at a molar ratio of CHT amine: PEI concentration of 2:1. The reaction mixture was left to polymerize for 24 hours and dialyzed using a dialysis membrane (MW=12 000kDa) over double deonized water (DDW) for 24 hours. The final CHT-g-PEI powder was then collected by lyophilization over 24 hours (details of equipment used).

4.2.2.1.2. Synthesis of CHI-g-PEI-PEG-NH_2 Conjugate

Copolymer synthesis procedure described by Jiang et al. (Jiang et al., 2008) with modifications was employed in the synthesis of the amino terminal CHT-g-PEI-PEG-NH_2 copolymer conjugate following an amide formation reaction between the activated carboxyl groups of NH_2-PEG-COOH and the amine groups of CHT-g-PEI as previously described. Briefly, the carboxyl group of the bifunctional PEG (NH_2-PEG-COOH) was activated using NHS/EDC chemistry for 15 minutes. Furthermore, the CHT-g-PEI conjugate previously synthesized was gently added to the activated NH_2-PEG-COOH solution using a needle and syringe under stirring. The reaction was then allowed to polymerize at 4°C and 25°C for 12 hours respectively. The synthesized CHT-g-PEI-PEG-NH_2 conjugate was then dialyzed using a dialysis membrane (MW=12

000kDa) against DDW for 48 hours and the dried power was collected by lyophilization over 24 hours.

4.2.2.1.3. Bovine Serum Albumin/ Endostatin Entrapment and Nanoparticle Synthesis

An ionotropic gelation technique was employed for the synthesis of bovine serum albumin or Endostatin-loaded nanoparticles comprising the fifteen formulations and the optimized nanosystem, respectively. The fifteen formulations were prepared according to the formulation variables presented in Table 4.1. For the experimental design formulations, bovine serum albumin (BSA) was employed as a model drug for protein therapeutics for identification of the optimum nanoparticle system into which endostatin would ultimately be loaded. Briefly, 1mg/mL BSA solution was mixed with the solution mixture of CHT-g-PEI-PEG-NH_2 conjugate under mild stirring for 10 minutes. Varying concentrations of TPP as a cross linker was added drop-wise to the BSA-loaded mixture using a needle and syringe. The formation of an opaque and turbid solution confirmed the formation of the BSA-loaded nanoparticles. Varying concentrations of PVA were also added as surfactant during the nanoparticle synthesis as shown in Table 4.1. The synthesized nanoparticles were then allowed to undergo gelation for 1 hour under mild stirring and the resultant gel was centrifuged at 5000 rpm for 1 hour. The clear supernatant was discarded and the pellet was re-suspended in DDW and refrigerated at -80°C. The dried powder BSA/endostatin-loaded nanoparticles were then collected following lyophilization over 24 hours.

4.2.2.2. Analysis of Chemical and Functional Transformations via Fourier Transform Infrared Spectroscopy

The vibrational transitions in the chemical structures of CHT-g-PEI, CHT-g-PEI-PEG-NH_2 and Endostatin-loaded CHT-g-PEI-PEG-NH_2 were evaluated using Fourier transform infrared (FTIR) spectroscopy (PerkinElmer Inc., Waltham, Massachusetts, USA). Samples were placed on a single bounce diamond crystal and processed by a universal attenuated total reflectance (ATR)

polarization accessory, at a resolution of 4 cm^{-1}, with the spectrum ranging from 4000 to 650 cm^{-1}.

4.2.2.3. Evaluation of Structural Modifications via Nuclear Magnetic Resonance Spectroscopy

Nuclear Magnetic Resonance (NMR) spectra were recorded for CHT-g-PEI and CHT-g-PEI-PEG-NH_2 conjugates. Proton NMR chemical shifts, expressed in ppm and analyzed in deuterated water (D_2O) doped with deuterated acetic acid (CD_3COOD) in a ratio of 5:1 were recorded on a 500MHz Avance III spectrometer (Bruker BioSpin GmbH, Germany) at room temperature.

4.2.2.4. Particle size, Surface charge, Conductivity and Structural Morphology measurement

Malvern Zetasizer Nano ZS (Malvern Instruments, Worcestershire, UK) was employed to evaluate the size, zeta potential and the conductivity of the nanoparticles. Known sample weights were dispersed in DDW and sonicated for 30 seconds. 2 mL dispersed sample (2mL) was placed in disposable cuvettes and the dynamic scatter intensity was recorded at 25°C. The average zeta size, polydispersity index (PDI), zeta potential, and conductivity of the nanoparticles were recorded.

The size of the nanoparticles was also confirmed using Transmission Electron Microscopy (TEM) (FEI Tecnai T12 TEM, 60-120kV, Hillsboro, OR, USA). The nanoparticle system was dispersed in DDW, ultra-sonicated for 15 minutes and a single drop of the nanoparticle suspension was dropped on a Form Var® coated 200-mesh copper grip (TAAB Laboratories Equipment Ltd., Aldermaston, England), and allowed to air dry at 25°C prior to TEM analyses.

The morphology of the nanoparticles was examined using Scanning Electron Microscopy (SEM). Powdered sample of the nanoparticles was placed onto an aluminium specimen stub covered with a double-sided carbon adhesive disc and sputter-coated with both palladium and gold for 4 minutes at 20 kV. SEM images of Endostatin-loaded nanoparticles were then viewed by a Scanning Electron Microscope (SIGMA VP, ZEISS Electron Microscopy, Carl Zeiss Microscopy Ltd; Cambridge, UK).

4.2.2.5. Determination of the Drug Loading Capacity and Entrapment Efficiency of the Nanoparticles

Known amounts (3mg) of drug loaded nanoparticles of the 15 formulations and the optimized nanosystems were dispersed in 5mL DDW and shaken vigorously. The mixture was then centrifuged for 1 hour at 5000 rpm. The clear supernatant solution (2mL) was poured into the UV cuvette and the absorbance of the drug was read at 280nm for all samples using a NanoPhotometer. Measurements were performed in triplicate and the corresponding drug concentrations were computed from a standard calibration curve. The drug loading capacity (LC) and entrapment efficiency (EE) of the nanoparticles were calculated using Equation 4.1 and 4.2, respectively:

$$LC = \frac{Total\ amount\ of\ drug\ loaded - Unloaded\ drug\ in\ the\ supernatant}{Measured\ weight\ of\ drug\ loaded\ nanoparticles} \quad Eq..4.1$$

$$EE = \frac{Total\ amount\ of\ drug\ loaded - Unloaded\ drug\ in\ supernatant}{Total\ amount\ of\ drug\ loaded} \quad Eq\ ...4.2$$

4.2.2.6. Determination of the Degree of Swelling of the Nanoparticles

The swelling behaviour of the synthesized nanoparticles was determined at both pH 6.8 and 7.4 using the Malvern Zetasizer Nano ZS (Malvern Instruments, Worcestershire, UK). Known amounts of nanoparticles were incubated at 37°C in phosphate buffered saline (PBS, pH 6.8 and 7.4) over 4 hours. The average size of nanoparticles (nm) was recorded at 0, 1, 2, and 4 hours. Each sample was sonicated for 30 seconds (SONICS Vibra CellTM, Newtown, CT, USA), placed in disposable polystyrene cuvettes and the dynamic scatter intensity was recorded at 25°C for the corresponding pH at the specific time interval.

4.2.2.7. *In vitro* Drug Release and Chromatographic Apparatus/Condition for Reverse Phase HPLC

The drug release experiments were carried out at 37°C in an orbital shaker incubator (YIHDER, Taiwan) over 16 hours. Equivalent amounts of the BSA loaded and endostatin loaded nanoparticles were placed in a 15mL centrifuge tube with 5mL PBS buffer at both tumoral pH of 6.8 and physiological pH of 7.4. The release buffer medium (2mL aliquot) was removed at pre-determined time intervals (1, 2, 4, 6, 8 and 16 hours), filtered, and replaced with fresh amount of the buffer medium to maintain sink conditions. UV absorbance of the filtered samples were then measured at 280nm using the Alliance HPLC system, including Waters 2695 Separations module, Waters 996 PDA Detector; Millennium 32 chromatography analysis software, Waters Symmetry 300^{TM} C18 (4.6 mm × 250 mm, 5µm), Waters 1525 binary pump and Waters 2489 UV/visible detector, Superdex^{TM} 75Nhr 10/30 column. The fixed phase is Symmetry 300TM C18 (4.6 mm × 250 mm, 5µm). Mobile phases, solution A is 0.1% TCA-water (1:1000), solution B is 0.1% TCA-95% CAN (1:1000); flow rate is 1.0 mL/min. The temperature of the column or sample plate was set at 30°C and samples were quantified by the Lowry method. The cumulative BSA or Endostatin release was measured as a function of time.

4.2.2.8. Optimization of the Formulatory Components using Box-Behnken Experimental Design

Polynomial equations relating the dependent and independent variables using Minitab Statistical Software (MINITAB®, V15, Minitab, USA) were employed to calculate the optimized delivery system from the formulation process under constrained conditions for the measured responses. Using the optimization parameters, optimized endostatin-loaded nanoparticles were prepared following the same method employed for the 15 formulations. However, 0.5mg/mL human recombinant endostatin was loaded into the nanoparticles. For generation of the optimum formulation, the average nanoparticle size as well as the *in vitro* cumulative endostatin release from the loaded nanoparticles at pH 7.4 was minimized, while the release at tumor pH of 6.8 and the overall average surface charge of the nanoparticles was maximized. Response analysis was performed for all the variables tested. Surface and contour plots derived from the responses were used to authenticate the effects of the independent variables on the response factors.

4.2.2.9. Nanoparticle Cyto-compactibility and Cell Proliferation Assay

In vitro cell cytotoxicity was determined using Alamar blue assay. Human oesophageal Squamous Cell carcinoma cell line (KYSE-30) (Life Bioscience) were seeded in complete media comprising of RPMI and Ham's F12 (1:1), supplemented with 10% Fetal Bovine Serum, 2mM glutamine, sodium bicarbonate and 100µL penicillin/streptomycin (Sigma- Aldrich; St. Louise, MO, USA). The cells were maintained in an incubator (RS Biotech Galaxy, Irvine, UK), with a humidified atmosphere of 5% CO_2 at 37°C. KYSE-30 cells were diluted in a complete medium at a final concentration of 5×10^4 cells/mL and seeded (25µL/well) and incubated for 24 hours prior to cell proliferation evaluation using Alamar blue assay according to the manufacturer's procedures. Native nanoparticles and endostatin-loaded nanoparticles were dissolved in the serum free culture medium at varying concentrations of endostatin (125 µg/mL,

250 µg/mL, 500 µg/mL and 1000 µg/mL). Attached cells in the wells were treated with the various nano-formulations in triplicate for 24 hours and cell viability was quantified at maximum emission/excitation wavelengths of 535nm and 595nm, respectively, on a microplate reader (FilterMaxTM F5 Multi-Mode Microplate Reader, Molecular Devices, USA). Attached cells treated only with serum free media, without the nano-formulation, were used as a control. Results are presented as percentage cell viability (%CV±mean standard deviation), with the percentage of viable cells was calculated using the following Equation 4.3.

$$CV = \frac{Fluorescence\ reading\ in\ treated\ cells}{Fluorescence\ reading\ in\ control\ (untreated)\ cells} * 100 \ldots\ldots Eq\ 4.3$$

4.3. Results and Discussion

4.3.1. Polymer grafting, nanoparticle synthesis and characterization

As presented in the reaction schematics in Figure 4.1, the amine in acetylated low molecular weight CHT was grafted to the amine of 25KDa branch PEI through the CDI linkage chemistry. The two imidazolyl groups of CDI were used to couple the amines of both CHT and PEI. The feed molar ratio of PEI to amine of chitosan was 3:1 (based on our preliminary study). Similarly, amidation reaction between the carboxyl group on the bifunctional PEG and the free amine on the grafted CHT-g-PEI through NHS/EDC cross linkers was employed to synthesize the amino terminal CHT-PEI-PEG conjugate for Endostatin encapsulation. The structural and functional modification of both CHT-g-PEI and CHT-g-PEI-PEG-NH_2 conjugates were confirmed by both ^{1}H NMR and FTIR spectra as presented in Figure 2 and 3, respectively.

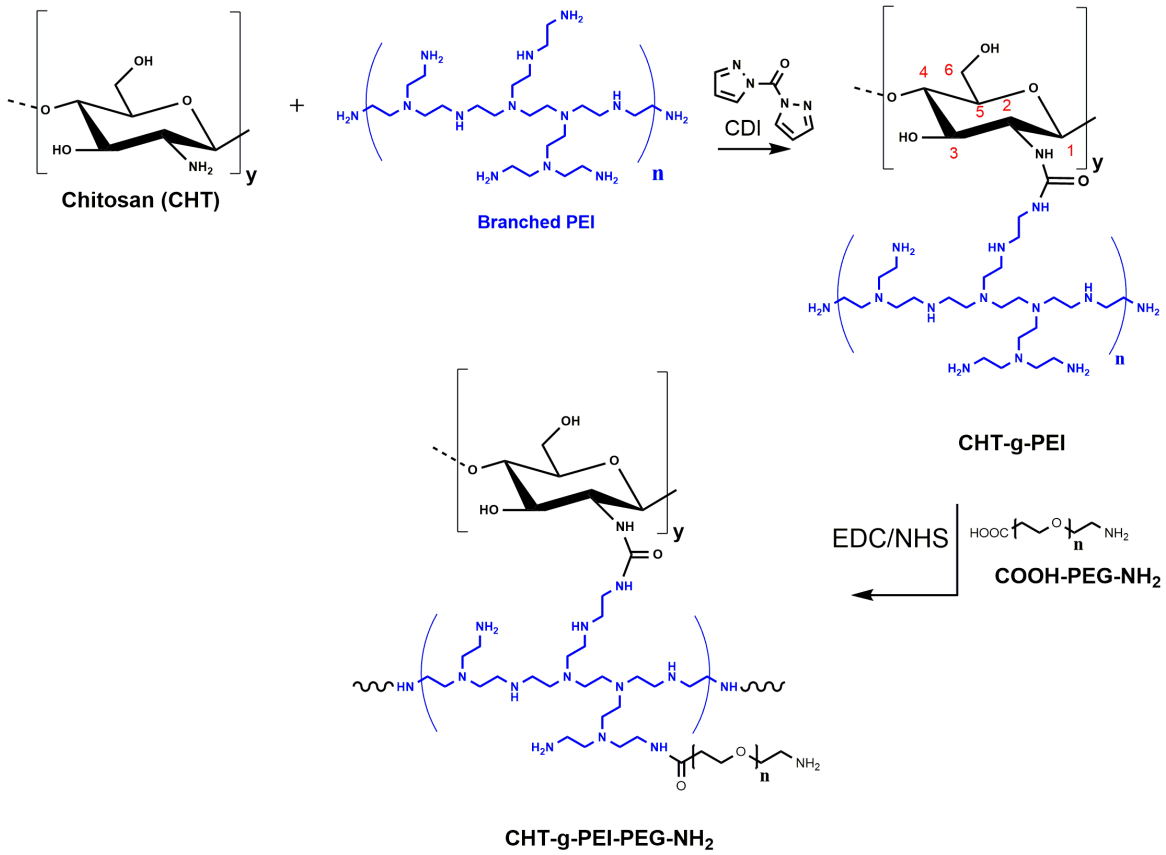


Figure 4.1: Proposed reaction scheme for the preparation of grafted polymers.

Figure 4.2 shows the ^{1}H NMR spectra of the grafted copolymers and PEG functionalized grafted polymer conjugate, respectively. From Figure 4.2a, characteristic peaks at δ = 2.9–3.7 ppm were assigned to D-glucosamine unit (H3, H4, H5, H6) of CHT, the peak at δ = 3.1 ppm is responsible for H2 and the peak at δ = 1.9 ppm is indicative of the methyl protons of N-acetyl group. The presence of peaks at δ = 2.5–3.2 ppm were assigned to methylene protons of PEI (–$NHCH_2CH_2$–), and confirmed that PEI was successfully grafted onto the CHT chain. Similar results were reported by Sarkar and co-workers (Sarkar et al., 2013) for the preparation of fluorescent chitosan-graft-polyethyleneimine and Lui and co-workers (Lu et al., 2014) for Chitosan-Graft-Polyethylenimine/DNA Nanoparticles. After the reaction between CHT-g-PEI and COOH-PEG-NH_2, there were new peaks in the ^{1}H spectrum at δ = 3.6 ppm which belonged to the methylene protons of PEG (–OCH_2CH_2–) (relative to Figure 4.2a). There was a slight

downfield shift of the signals of the characteristic protons of CHT and PEI (Figure 4.2b). This is possibly due to the deshielding of protons (CHT and PEI) as a result of addition of -OCH_2 of PEG moieties. Zhou and colleagues reported similar downfield shifts for the methylene proton signals of PEI after conjugation to PEG monomethyl ether with a carboxyl end group (mPEG–COOH) (Zhou et al., 2016).

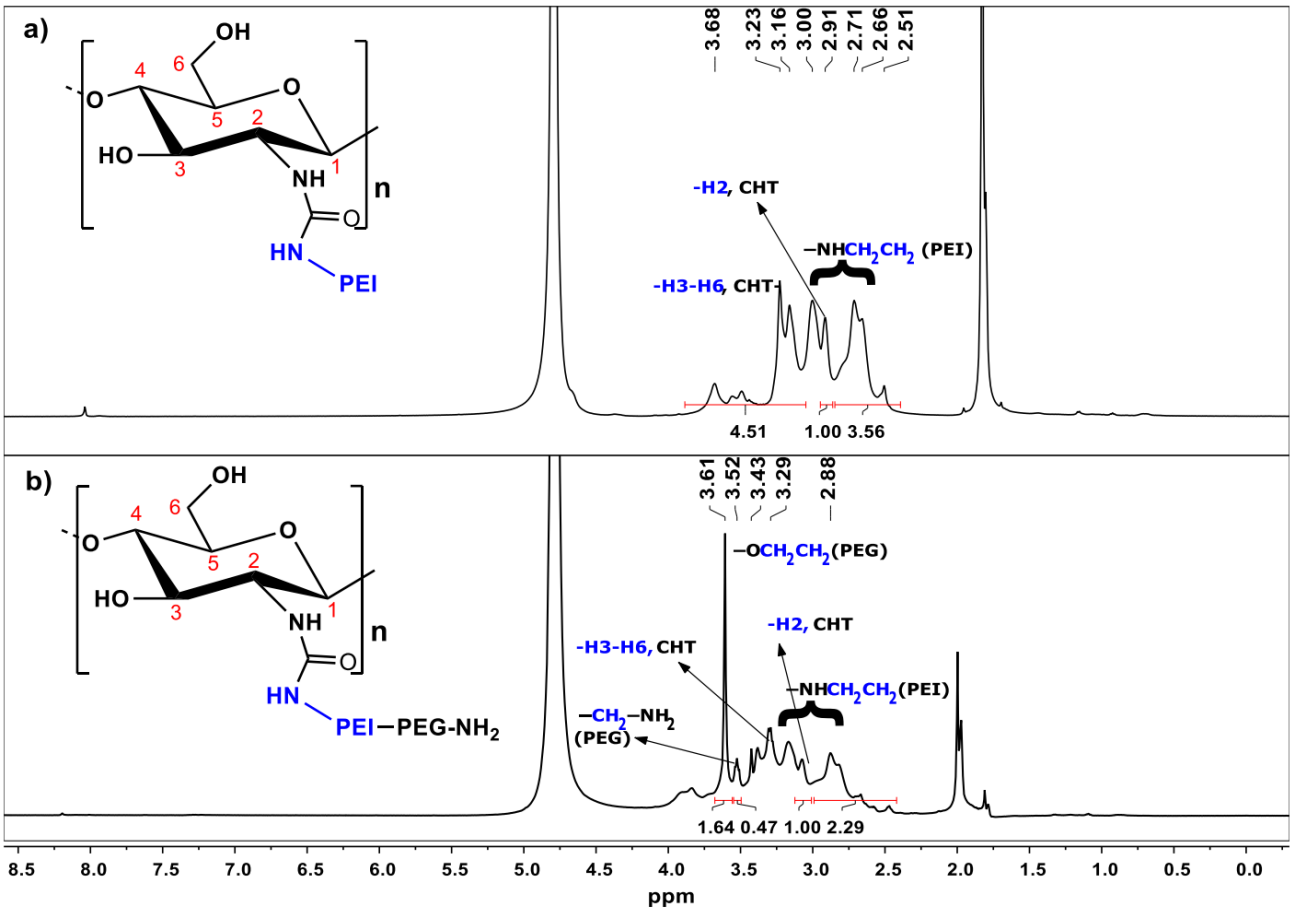


Figure 4.2: ^{1}H NMR spectra showing the grafting of polymer conjugates in D_2O:CD_3COOD (5:1). a) CHT-g-PEI and, b) CHT-g-PEI-PEG-NH_2

By comparing the integration of proton signals at δ = 2.5–3.2 ppm and δ = 2.9–3.7 ppm, the degree of substitution of PEI per CHT D-glucosamine unit was calculated (Equation 4.4). The integration values of H-2, was defined as 1 during the process of calculation.

$$Degree\ of\ substitution\ (DS) = \frac{\frac{[I_{PEI,\ CH_2\ CH_2NH}]}{4}}{\frac{[I_{CHT,H2,H3-H6}]}{6}} = \frac{3.56/4}{5.51/6} = 0.9 \ldots Eq \ldots 4.4$$

Thereafter degree of grafted (DG) of PEI onto CHT was calculated via Equation 4.5.

$$DG = \frac{W_2}{W_1} \times 100\% \ldots\ldots Eq \ldots 4.5$$

$$where \quad W_1 = mass\ of\ pure\ graft\ co-polymer$$

$$W_2 = mass\ of\ graft\ chains$$

$$DG = \frac{24.25}{214.3} kDa \times 100\% = 11.3\ \%$$

$$W_1 = MW_{CHT} + (MW_{PEI} \times DS) = 190\ kDa + (25kDa \times 0.97) = 214.3\ kDa$$

$$W_2 = = n(MW_{PEI} \times DS) = (25kDa \times 0.97) = 24.25\ kDa$$

The degree of grafting (DG) of PEG onto CHT-g-PEI was calculated based on the ^{1}H NMR using the integration of proton signals:

$$DS_{PEG} = \frac{\frac{[I_{PEG,\ CH_2\ CH_2\ NH_2}]}{2}}{\frac{[I_{CHT-g-PEI-PEG,\ CH_2\ CH_2NH_2}]}{4}} = \frac{0.47/2}{2.29/4} = 0.41 .. Eq \ldots . 4.6$$

$$DG = \frac{0.861}{215.2} kDa \times 100\% = 0.40\% \ldots Eq \ldots 4.7$$

$$W_1 = MW_{CHT-g-PEI} + (MW_{PEG} \times 0.41) = 214.3\ kDa + (2.1\ kDa \times 0.41) = 215.29\ kDa$$

$$W_2 = = n(MW_{PEG} \times DS) = (2.1 \times 0.41) = 0.861\ kDa$$

FT-IR spectra of the native and grafted polymers of CHT-g-PEI-PEG-NH_2 grafted copolymer are presented in Figure 4.3. The absorption of *v*(O-H) and *v*(N-H) at 3450–3200 cm^{-1}, *v*(C-H) at ~2930 and 2886 cm^{-1}, *v*(C = O NH_2) at 1656 and 1597 cm^{-1}, and *v*(C-O-C) at 1150 cm^{-1} in the FTIR spectra were assigned to CS D-glucosamine units thereby indicating the presence of chitosan as the core polymer framework in the synthesized CHT-g-PEI-PEG-NH_2 conjugate (Figure 4.3e). A new peak appeared at ~1590 cm^{-1}, which is indicative of the carboxyl in urea

group (Figure 4.3c). Further, the appearance of peaks at 1450.6 and 822.1 cm^{-1} were attributed to the absorption of -$NHCH_2CH_2$- moieties which is from the branched PEI, indicating that PEI was successfully grafted onto CHT (Chen et al., 2015).

The formation of an amide bond between the carboxylic group of PEG, and the amine group of CHT-g-PEI copolymer was noted in the CHT-g-PEI-PEG-NH_2 conjugate. As represented in the FT-IR spectrum in Figure 3(e), the characteristics peak at 1696.5 cm^{-1} was assigned to the absorption from the C=O stretch in amide bond I, 1463.7 and 1496.4 cm^{-1} were peaks attributed to the absorptions from both the N-H bend and C-N stretch in amine bond II while the tripartite absorption peaks at 1310.0, 1279.6 and 1251.9 cm^{-1} were attributed to the N-H bend in plane and C-N stretch in amide bond III. Meanwhile, an absorption peak at 3389.4 cm^{-1} was attributed to the N-H stretch from the free primary amine group attached to the PEG in the conjugate (CHT-g-PEI-PEG-NH_2). Similarly, the characteristic peak of PEI was represented as an absorption peak of 822.1cm^{-1} while the peak at 871.2 cm^{-1} was assigned to CHT (AbdElhady, 2012). Notably, the characteristic peak of PEG at 842 cm^{-1} contributing to the absorption of CH_2 from –$[CH_2CH_2O]_n$– was also found in the spectrum of the CHT-g-PEI-PEG-NH_2 polymer conjugate, which confirms its presence in the polymer construct (Zhou et al., 2016)

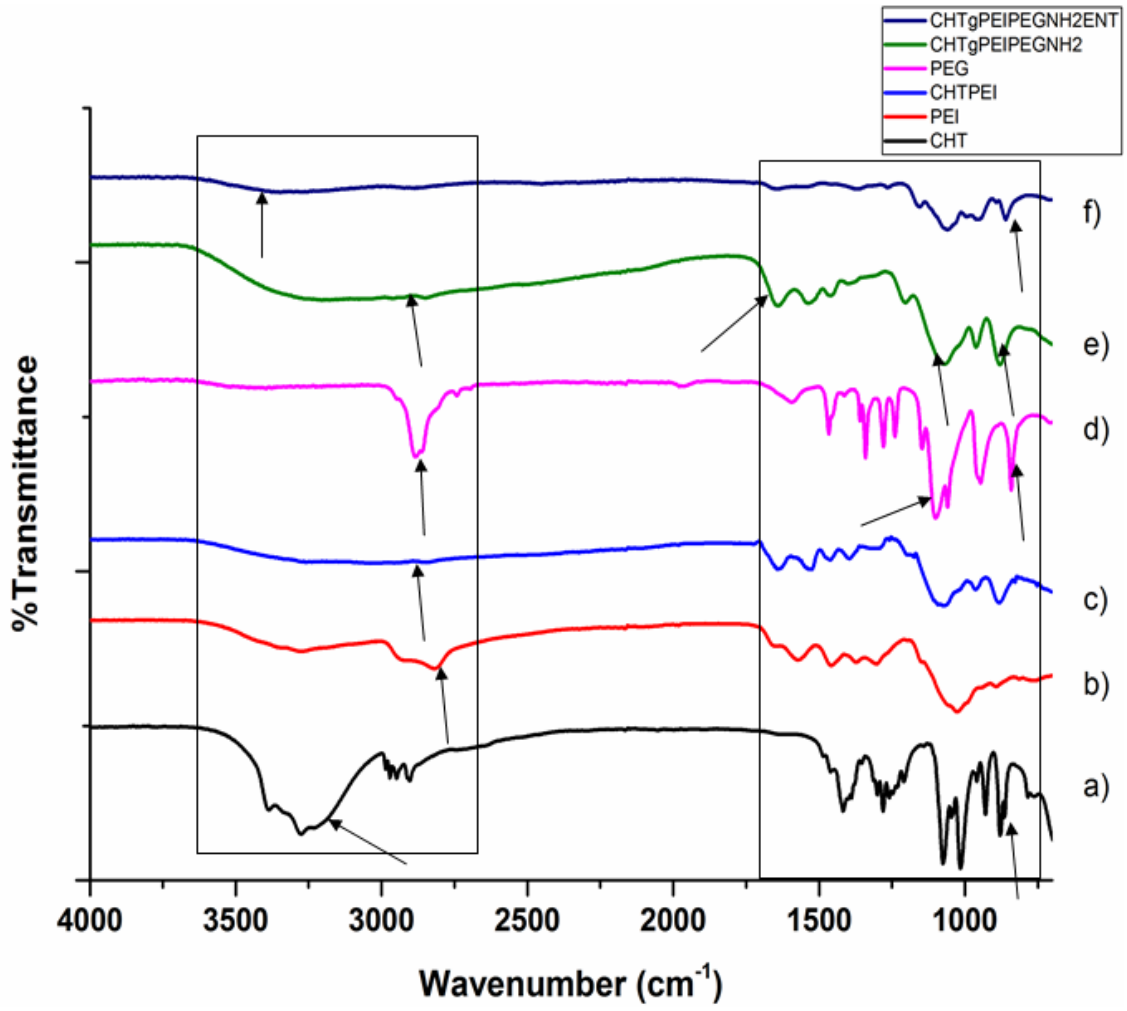


Figure 4.3: FTIR Spectra for native polymers, grafted polymer conjugates, and the endostatin-loaded nanoparticle system.

4.3.2. Confirmation of the Physicochemical Properties and Morphology of Endostatin-loaded Nanoparticles

Physicochemical properties, such as average particle size, surface zeta potential, conductivity and polydispersity index (PdI) of BSA/endostatin-loaded nanoparticles were measured using Dynamic Light Scattering (Zetasizer NanoZS, Melvern Instrument, UK). Table 4.1 shows the average particle size for the 15 formulations as influenced by the formulation variables. The average size of the nanoparticles ranged between 56.28nm (F11) and 363.10nm for F14.

Although formulations with similar concentration of the grafted polymer conjugates (CHT-g-PEI-PEG) seemed to have closely related average particle size (F2 = 84.22 nm and F4 = 97.38 nm), the surfactant concentration seemed to be a major determining factor for the average particle size distribution among the 15 formulations generated using the Box-Behnken design. For instance, the average particle sizes for F5, F6 and F15 with a polymer conjugate concentration (1.5mg/mL) were 300.10, 295.10 and 310.20nm, respectively, while F1 and F4 with the same polymer conjugate concentration (1.5mg/mL) had average particle sizes of 56.28 and 97.38nm, respectively, at a ratio of approximately 1:3, in comparison to F5, F6 and F15. Both F1 and F4 had a surfactant concentration of 1% PVA solution while F5, F6 and F15 had surfactant concentration of 0.55% PVA. Meanwhile, the concentration of TPP, as a polyionic agent, for the nanoparticle synthesis also influenced the average particle size of the nanoparticles among the 15 formulations. Formulations with the lowest TPP concentrations (F1 and F2 (0.1% TPP) had the lowest average particle size (F1 = 65.07nm, F2 = 84.22nm) compared to F14 = 363.10nm, 0.3% TPP as shown in Table 1. This is because crosslinking agents, such as TPP, harden the matrix of Chitosan nanoparticles leading to decreased water absorption (Mehrotra et al., 2011). However, higher PVA (1%, 0.55%) and TPP concentrations (0.3%), as seen in F4, F8 and F11, seemed to be favorable for the synthesis of moderately sized endostatin-loaded nanoparticles ranging between 56.28nm for F11 to 97.38nm for F4. In general, increased concentrations of the polymer conjugate (2.5mg/mL) and TPP (0.3%) with reduced PVA concentration (0.55%) lead to the synthesis of a reduced average particle size, F11 = 56.28nm). This could be as a result of strong electrostatic interactions between the BSA/endostatin molecules and the increased positively charged amino groups of CHT at higher concentration, as the main component in the grafted polymer conjugate (Zou et al., 2015). Furthermore, increased electrostatic interaction between the negative charge of TPP as a polyanionic agent at higher concentration and the positively charged amino group of CHT could possibly account for the reduction in nanoparticle size (Zou et al., 2015). Thus, the optimised endostatin-loaded

nanoparticles were prepared at CHT concentration of 2.5mg/mL and have an average hydrodynamic size of 100.6nm (Figure 4.4a). The PdI value of the nanoparticles from the 15 formulations ranged between 0.259 – 1.00. Interestingly, nanoparticles from most of the formulations had PdI value less than 1.00 showing their uniform disparity in solution. More importantly, the optimized nanoparticles have a PDI of 0.274.

The zeta potential values were positive for most of the formulations (Table 4.1). Overall, formulations with reduced chitosan concentration in the grafted polymer conjugate (0.5mg/mL) tend to have reduced zeta potential. The zeta potential decreased from a more positive charge towards negatively charge surfaces as the polymer conjugate concentration decreased from 2.5 – 0.5mg/mL (F3, F7, F11 compared to F9, F12 F13). Meanwhile, as the concentration of TPP, as the polyanionic agent decreased in the formulations, the PdI values increase across the formulations towards more positively charged surfaces with increasing chitosan concentration in the grafted polymer conjugate (F7 = +11.00 compared with F10 = +0.76; and F1 = +16.10, F2 = +19.80, compared with F4 = -1.87, F14 = -7.63). It is proposed that the overall positive charge on the surface of the nanoparticles originates from the protonation of the free amines on the Chitosan component of the grafted polymer conjugate (CHT-g-PEI-PEG-NH_2) as chitosan is the main polymer in the conjugate. Interactions between the negatively charged TPP solution and the positively charged chitosan-based polymer conjugate determined the overall surface charge of the synthesized nanoparticles. Thus, formulations with lower TPP concentration and higher concentration of the grafted polymer conjugate have more positively charged surfaces. Reports have shown that the surface of tumor cells is negatively charged (Chen et al., 2016; Dobrzyńska et al., 2013; Szachowicz-Petelska et al., 2012). Interestingly, the optimized endostatin-loaded nanoparticle has an average positive zeta potential value of 7.95mV (Figure 4.4b) which predisposed it for direct targeting in squamous cell carcinoma, as later presented in this study (Latha et al., 2012).

Table 4.1: Box-Behnken experimental design for formulation variables and responses at pH 7.4 and 6.8 respectively

	Variables			Responses			
Formulation	**Surfactant conc. (mg/mL)**	**TPP conc. (mg/mL)**	**Polymer conjugate conc. (mg/mL)**	**Size (nm)**	**Surface charge (mV)**	**Conductivity (mS/cm)**	**Polydispersity index**
F1	1.00	0.1	1.5	65.07	+16.10	0.054	0.259
F2	0.10	0.1	1.5	84.22	+19.80	0.079	0.367
F3	0.10	0.2	2.5	173.9	+10.40	0.056	0.689
F4	1.00	0.3	1.5	97.38	-1.87	0.048	0.302
F5	0.55	0.2	1.5	300.10	+11.92	0.053	0.529
F6	0.55	0.2	1.5	295.10	+9.05	0.053	0.715
F7	0.55	0.1	2.5	163.60	+11.00	0.038	0.268
F8	0.55	0.3	0.5	169.10	+8.95	0.062	0.731
F9	0.55	0.1	0.5	125.20	-6.11	0.067	0.403
F10	1.00	0.2	2.5	125.50	+0.76	0.049	1.000
F11	0.55	0.3	2.5	56.28	+9.08	0.055	1.000
F12	1.00	0.2	0.5	329.10	-12.30	0.052	0.788
F13	0.10	0.2	0.5	127.21	-8.94	0.057	1.000
F14	0.10	0.3	1.5	363.10	-7.63	0.062	0.408
F15	0.55	0.2	1.5	310.20	+13.10	0.048	0.550

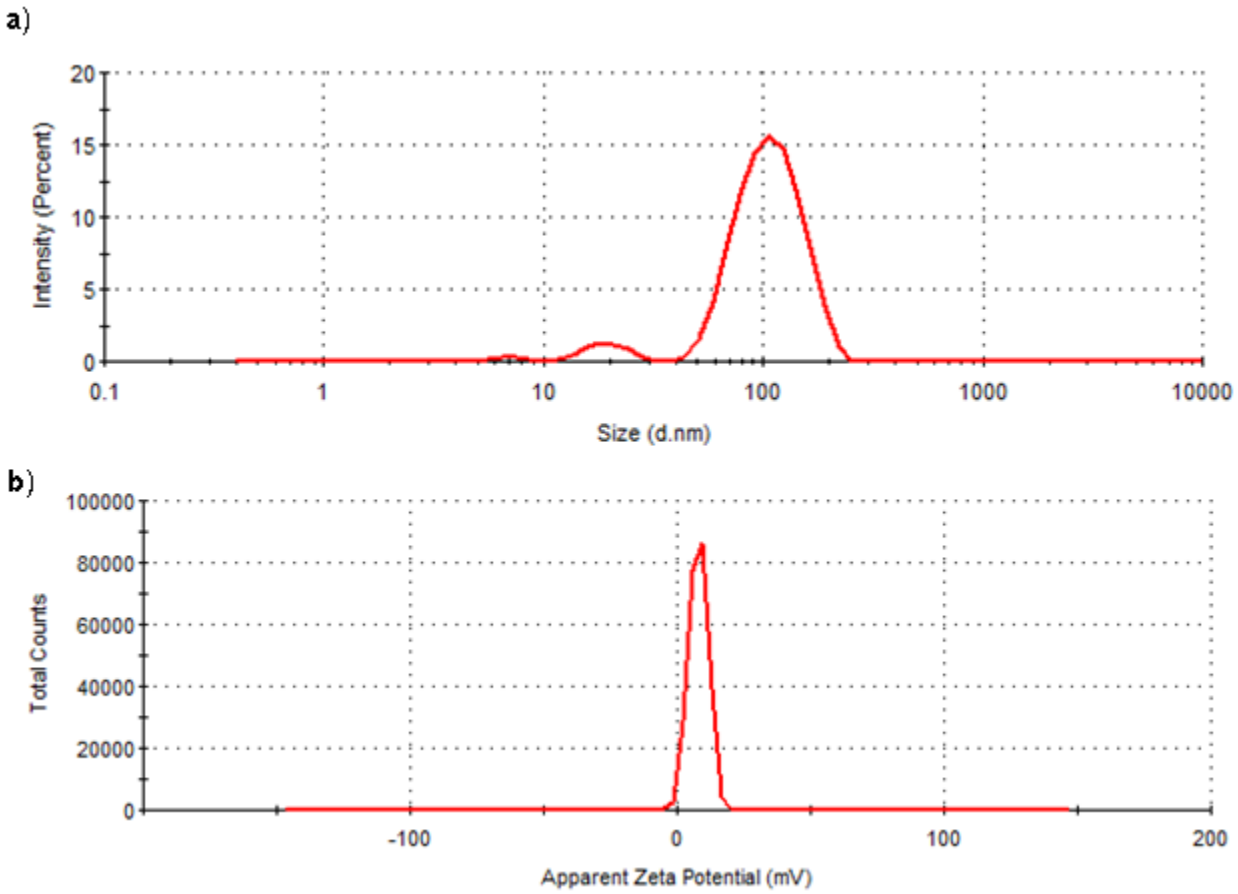


Figure 4.4: Hydrodynamic size and surface charge of the optimized Endostatin-loaded nanoparticle. (a) Average nanoparticle size is 100.6 nm with PDI value of 0.274 and (b) surface zeta potential of nanoparticles is +7.95 mV.

Both TEM and SEM micrographs (Figure 4.5 and 4.6 respectively) confirmed the morphology of endostatin-loaded nanoparticles to be spherical with transparent surfaces. Nanoparticle shape and size have been reported to influenced internal cellular binding and uptake of drug-loaded nanoparticles (He et al., 2010; Jiang et al., 2007; Sharma et al., 2010). Importantly, spherical shape nanoparticles possess enhanced cellular binding and internalization than nanoparticles with other shape configurations (Verma and Stellacci, 2010). The TEM images further confirmed that endostatin-loaded nanoparticles with an average size less than 100nm were successfully synthesized in agreement with the DLS average size measurement. The SEM micrograph also suggested that some of the smaller particles possibly agglomerate to form larger nanoparticles

(Sacchetti et al., 2002) ranging between 200 – 400nm. However, it should be noted that SEM images of the nanoparticles are acquired in their dried solid state as opposed to TEM and DLS average size measurements where the nanoparticles were dispersed in liquid. Interestingly, the average size of the optimized endostatin loaded nanoparticles are within the range for subcutaneous delivery intended for this study (Dreaden et al., 2012; Ikomi et al., 1999).

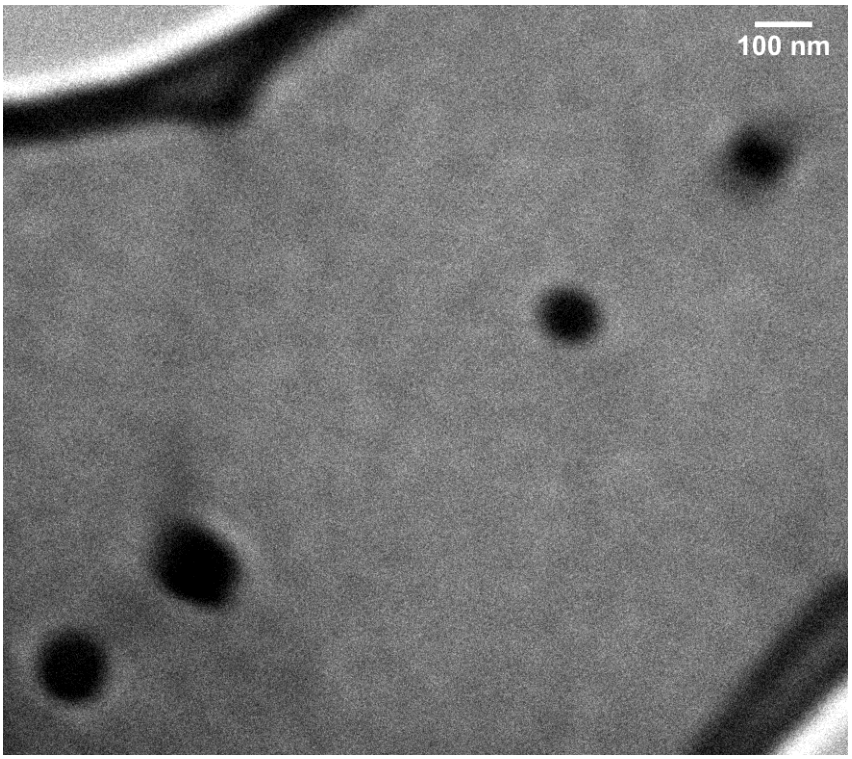


Figure 4.5: TEM images of optimized Endostatin-loaded nanoparticles

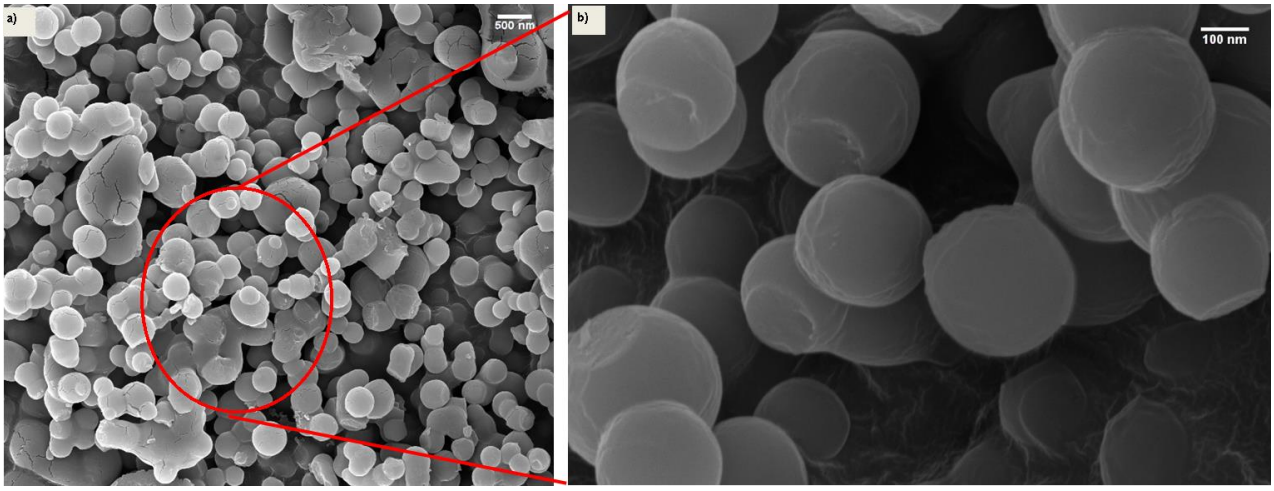


Figure 4.6: Gold-platinum sputtered SEM micrographs of the optimized ENT-loaded nanoparticles. (a) Magnification = 8.36 KX; (b) Magnification = 50.00 KX

4.3.3. Confirmation of BSA/Endostatin Loading Capacity and Entrapment Efficiency of Nanoparticles

As presented in Table 4.2, the drug loading capacity and entrapment efficiency of the 15 formulations showed that BSA, as a model drug, was successfully loaded and entrapped within the grafted CHT-based polymeric network, and ranged between 92.8% (F4) and 98.4% (F5). This could be attributed to the influence of PEG coating on the surface of the nanoparticle. PEG coating has been found to increase encapsulation efficiency as free dissolved drugs are captured within the matrix of nanoparticles during PEGylation (Mehrotra et al., 2011). In general, formulations with lower CHT concentrations (0.5mg/mL) showed higher loading and entrapment capacity (F8, F12, F13 compared to F7, F10, F11 with CHT concentration of 2.5mg/mL, Table 1). This could possibly be due to the lower viscosity that increases encapsulation of BSA or endostatin and possible promotion of gelation between CHT and TPP as the cross linking agent (Mehrotra et al., 2011). This corroborates the report of Vandenberg et al. (Vandenberg et al., 2001) that the viscous nature of the gelation medium affects the drug encapsulation during the synthesis of chitosan microspheres. More so, effective confinement of BSA/endostatin

molecules in the nanoparticles could be attributed to the electrostatic interaction between the proteins and the long chain of chitosan. Formulations (F8, F11 and F14 with higher TPP concentrations (0.3%) showed slightly higher encapsulation. This could be a result of increased crosslink density which possibly prevents the leaching away of entrapped BSA/endostatin molecules during formation of nanoparticles (Mehrotra et al., 2011). Further, high TPP concentration with a fixed chitosan concentration may increase the solution pH which consequently influences the overall negative charge at the surface of the BSA molecules. This enhances the electrostatic interactions between chitosan chains and BSA molecules and thus results in higher BSA loading and encapsulation efficiency.

Table 4.2: Drug loading capacity and entrapment efficiency

Formulations	Entrapment efficiency	Loading capacity (%)
F1	0.943	31.43
F2	0.953	31.77
F3	0.975	32.50
F4	0.928	30.93
F5	0.984	32.80
F6	0.980	32.67
F7	0.947	31.57
F8	0.973	32.43
F9	0.959	31.97
F10	0.966	32.20
F11	0.963	32.10
F12	0.969	32.30
F13	0.981	32.70
F14	0.971	32.37
F15	0.964	32.13

4.3.4. Nanoparticle Swelling Behaviour and *in vitro* Drug Release

As presented in Figure 4.7, the swelling capacity of BSA-loaded nanoparticles increased with time at the varying CHT concentrations. The degree of swelling was greater at pH 6.8 than at pH 7.4, which would ultimately contribute to an enhanced release of the bioactive at tumoral pH. The effect of PEI and the surface shielding effect of PEG contributed to the swelling behaviour and BSA/endostatin release from the nanoparticles (Mehrotra et al., 2011). Overall, nanoparticle swelling reached equilibrium after 2 hours in the buffer system. RP-HPLC, as presented in Figure 4.8, was employed to quantitate the *in vitro* BSA/endostatin release from the BSA/endostatin loaded nanoparticles as shown in Figure 4.9. BSA elute at 2.216 minutes over a run time of 6 minutes and result corroborates to previous report of Mukhopadhyay and Panja (Mukhopadhyay, 2013; Panja, 2012).

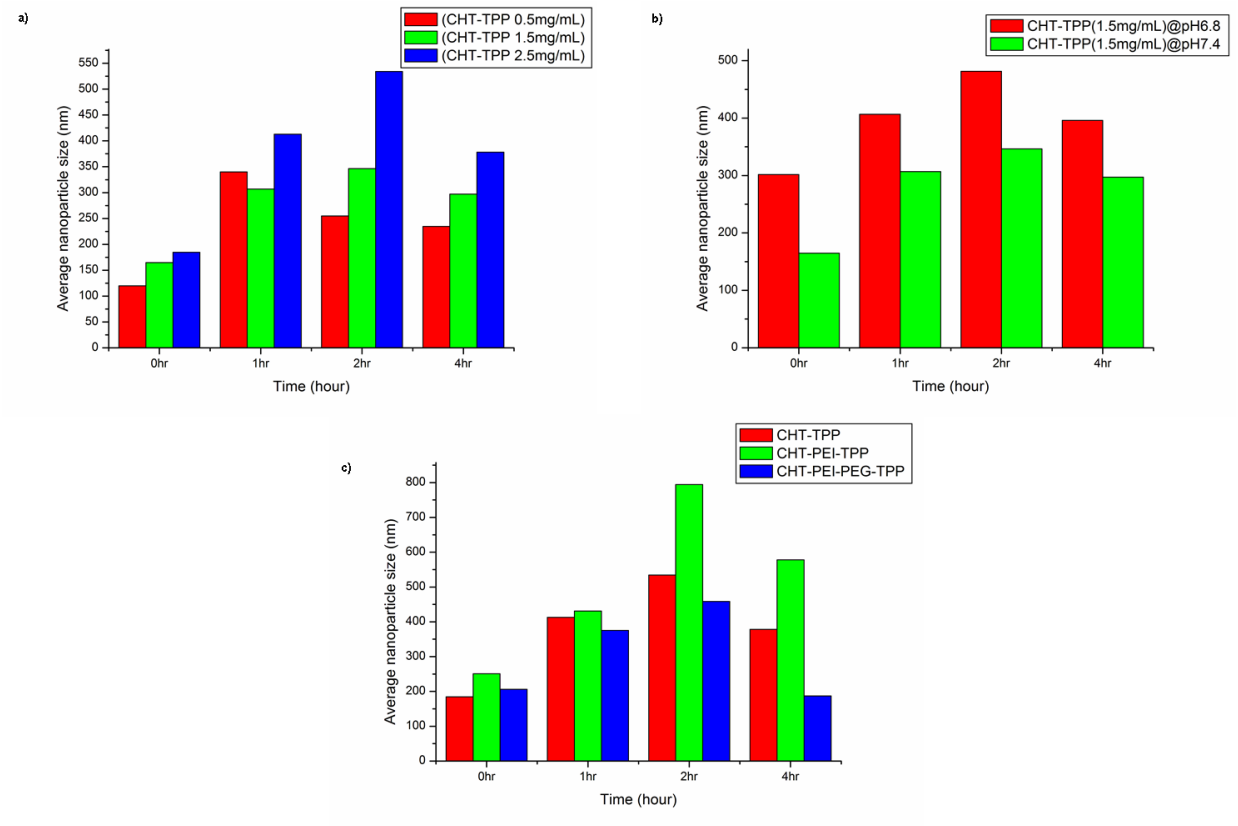


Figure 4.7: Swelling behaviour of drug-loaded nanoparticles. a) Effect of varying CHT concentrations on swelling behaviour of nanoparticles b) effect of varying pH conditions on the swelling behaviour nanoparticles at pH 6.8 and 7.4, respectively c) effect of PEI and PEG grafting on the swelling behaviour of nanoparticles.

4.3.4.1. Effects of chitosan and TPP concentrations on swelling and release kinetics

Chitosan concentration has been reported to play a major role in determining the swelling capacity and drug release kinetics of CHT-based nanoparticles (Seda Tı˘glı Aydın and Pulat, 2012). Formulations with higher CHT concentrations showed a higher swelling ratio with increased BSA release from the nanoparticles. Furthermore, the concentration of the cross linker (TPP) has also been reported to influence the swelling behaviour of CHT-based nanoparticles (Mehrotra et al., 2011). Lower TPP concentrations allow for weak electrostatic interaction with the protonated amines of CHT and thus facilitate mass movement of the buffer solution into the matrix of the nanoparticles. At acidic pH (6.8 as presented in this study), the mass ratio of available protonated amino groups of CHT which can interact with TPP anions

increased at a constant or lower TPP concentration (Figure 4.7a). This in turn results in a more loosely packed nanoparticle matrix which can be easily hydrated by the buffer solution and facilitate the release of the entrapped BSA/endostatin into the system. For instance, F10 has the highest cumulative BSA release at both pH 6.8 (66%) and pH 7.4 (58%) at CHT concentration of 2.5mg/mL and TPP concentration of 0.2%, compared to F8 having cumulative BSA release of 48% at pH 6.8 and 40% BSA release at pH 7.4 at CHT/TPP concentrations of 0.5mg/mL and 0.3%, respectively (Figure 4.9).

4.3.4.2. Effects of pH on nanoparticle swelling and BSA/endostatin release

The tumor microenvironment, including squamous cell carcinoma, and normal cellular physiological condition were both mimicked at pH 6.8 and 7.4, respectively (Gerweck and Seetharaman, 1996) to investigate the swelling behaviour and *in vitro* release kinetics of BSA-loaded nanoparticles. Overall, BSA release from within the nanoparticle matrix was increased at acidic pH 6.8 compared to physiological pH of 7.4 across all formulations over a period of 16 hours (Figure 4.9). Since CHT is the main component of the grafted polymer network forming the nanoparticles, the pH-responsive characteristics of the BSA-loaded nanoparticles should be linked to the hydrolysis of CHT at changing pH conditions. The free amine groups in the CHT moiety within the polymer conjugate become protonated at acidic pH, forming positively charged NH_3^+ groups which are hydrophilic. This further results in an electrostatic repulsion among the protonated amino groups, which weaken both the intra- and intermolecular hydrogen bonding interaction of CHT molecules. This in turn allows the enhanced permeation of the buffer solution into the network therefore causing the equilibrium swelling ratio to increase as opposed to what obtains both at neutral and basic pH conditions. In this study, swelling and shrinking mechanism with regard to swinging pH values has been investigated in terms of CHT-based smart responsive nanoparticulate systems for localized endostatin delivery.

4.3.4.3. Effects of PEI and PEGylation on swelling and drug release

The protonating effects of the amines in PEI at low pH value contributed to the increased swelling of the nanoparticles as presented in Figure 7c. At low pH, the amino groups on both CHT and PEI become protonated and thereby increase the overall NH_3^+ groups, which are hydrophilic. Thus, the buffering system could easily gain access into the nanoparticle network which facilitates an increase in the equilibrium swelling ratio. Meanwhile, the amphiphilic nature of PEG in the grafted polymer network possibly influenced the swelling property as well as the release pattern from the nanoparticles. PEGylation has increased the circulation time of PEG-modified nanosystems as well as prolonging the release of encapsulated drug in nanoparticulate systems (Alexis et al., 2008; Jokerst et al., 2011; Yoo et al., 2010). In our system, the carboxyl group in the bifunctional PEG was used in grafting the amine group of PEI moiety in the CHT-based polymer conjugate. PEG is amphiphilic; its hydrophilic property depends on which part of the polymer is used during covalent reaction. The sheathing effect of PEG on the nanoparticle surface tends to increase the compact nature of the nanoparticulate system and thus, reduce the swelling ratio of the drug-loaded nanoparticle which in turn prolongs the release of the encapsulated drugs within the nanoparticle matrix. As evidenced in Figure 7c, CHT-g-PEI-PEG nanoparticles have a reduced hydrated size as compared to both CHT-PEI and CHT nanoparticle. At equilibrium swelling point after 2 hours, CHT-g-PEI-PEG-NH_2 nanoparticles had an average size of 458.9nm, while both CHT-g-PEI and CHT nanoparticles had sizes of 794.2 and 534.2nm, respectively.

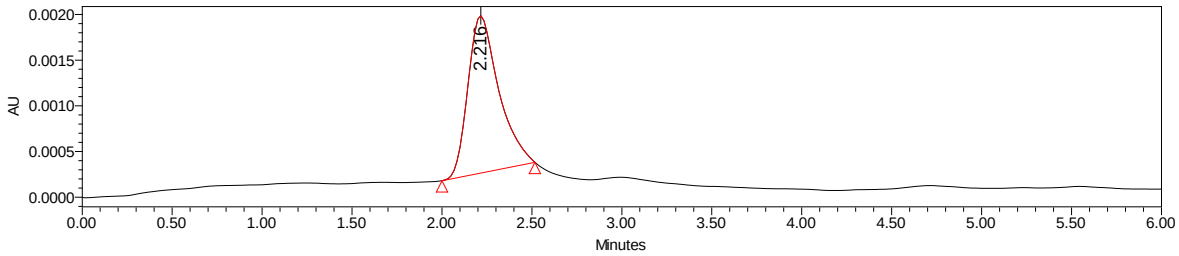


Figure 4.8: Reverse Phase HPLC chromatogram of BSA. Retention time of BSA as a model for endostatin is 2.216 minutes and run time is 6 minutes. No interference was observed for RP-HPLC for blank sample. Elusion was monitored at wavelength of 280 nm to detect BSA as previously reported (Mukhopadhyay, 2013).

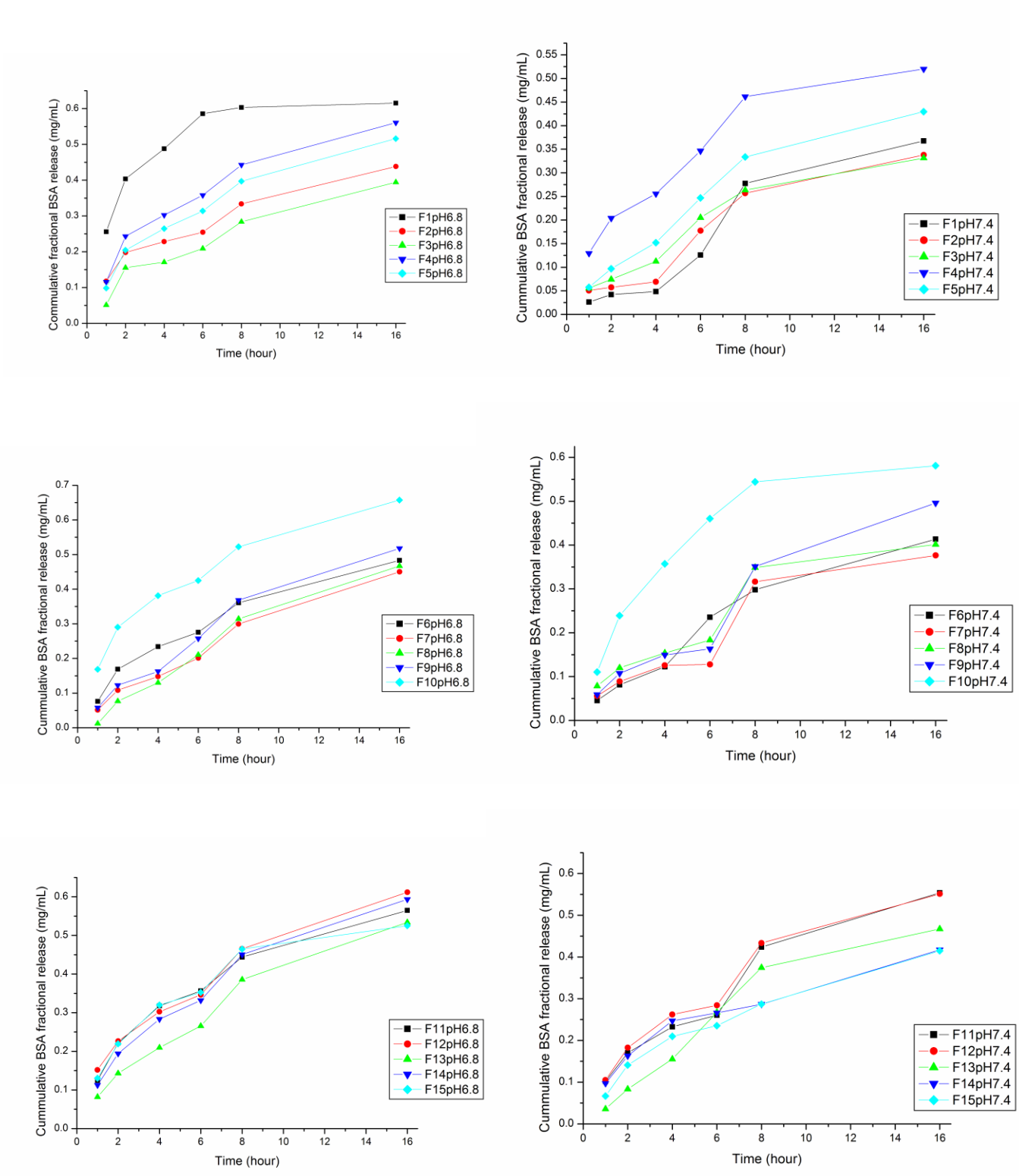


Figure 4.9: Cumulative drug release of the 15 experimental design formulations at pH 6.8 (left panel) and 7.4 (right panel). BSA release is higher at acidic pH of 6.8 than at physiological pH of 7.4 for each corresponding formulation.

4.3.5. Optimization of the experimentally-derived Box–Behnken formulations

The results of the response optimization procedure (MINITAB®, V15, Minitab, USA) showed a direct relationship between the fitted data and the observed response. The surface plot results (Figure 4.10) showed the effects of the polymer complex concentration, the surfactant concentration and TPP concentration on the overall average size of nanoparticles, their surface charge as well as ENT release from the nanoparticle matrix at changing pH conditions of 6.8 and 7.4. Nanoparticle size and ENT release at the lower acidic pH of the tumor microenvironment were maximized while zeta surface potential and ENT release at physiological pH were minimized. These responses were chosen to achieve an optimum desirability in terms of the nanoparticulate system performance in cancer nanomedicines.

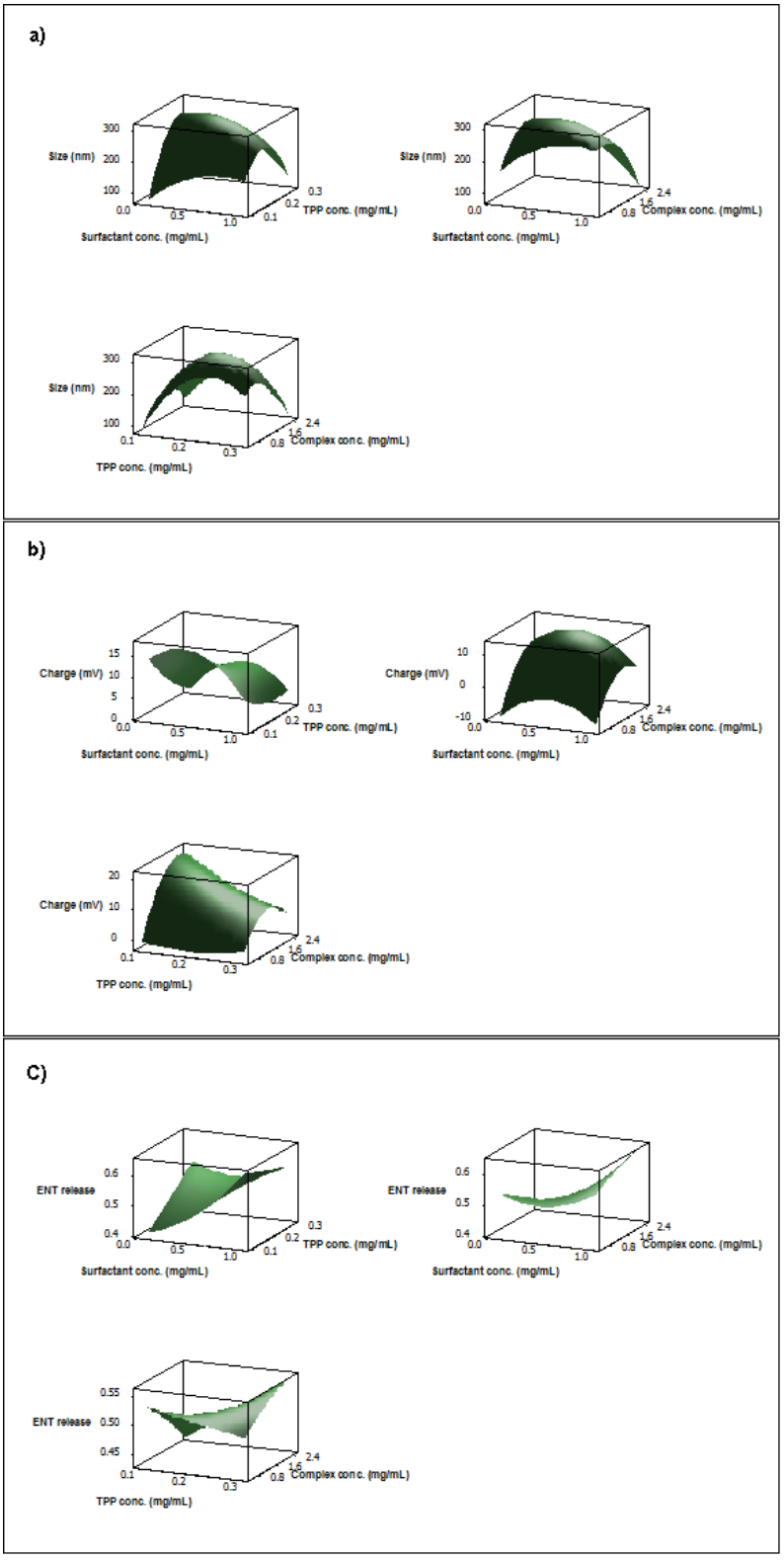


Figure 4.10: Surface plots showing the effects of polymer, TPP and surfactant concentrations on (a) nanoparticle size, (b) surface charge and (c) ENT release.

The optimized levels of the independent variables, the corresponding predicted response, y, as well as both the individual and composite desirability values are presented in Figure 4.11. The optimized formulation variables were 1.22 mg/mL for the grafted polymer conjugate (1.22 mg/mL CHT, 0.25% PEI, 1 mg/mL functionalized PEG), 0.10% PVA and 0.12% TPP for the synthesis of endostatin-loaded nanoparticles. Based on the statistical desirability function, it was found that the composite desirability of the formulation was 0.86. The experimentally-derived values for the nanoparticle size, surface zeta potential and ENT *in vitro* release of the optimized formulation was in close agreement with the predicted values (Size = 100.6 nm, PDI = 0.274, surface zeta potential = 7.95 mV, t_{8h} = 0.39), demonstrating the reliability of the optimization procedure in predicting the unique behaviour of the desired nanoformulation having an average nanoparticulate size and surface charge for efficient cellular binding, uptake and internalization as well as having an improved, sustained and efficient release pattern of ENT at tumor acidic microenvironment, as demonstrated in Figure 4.12.

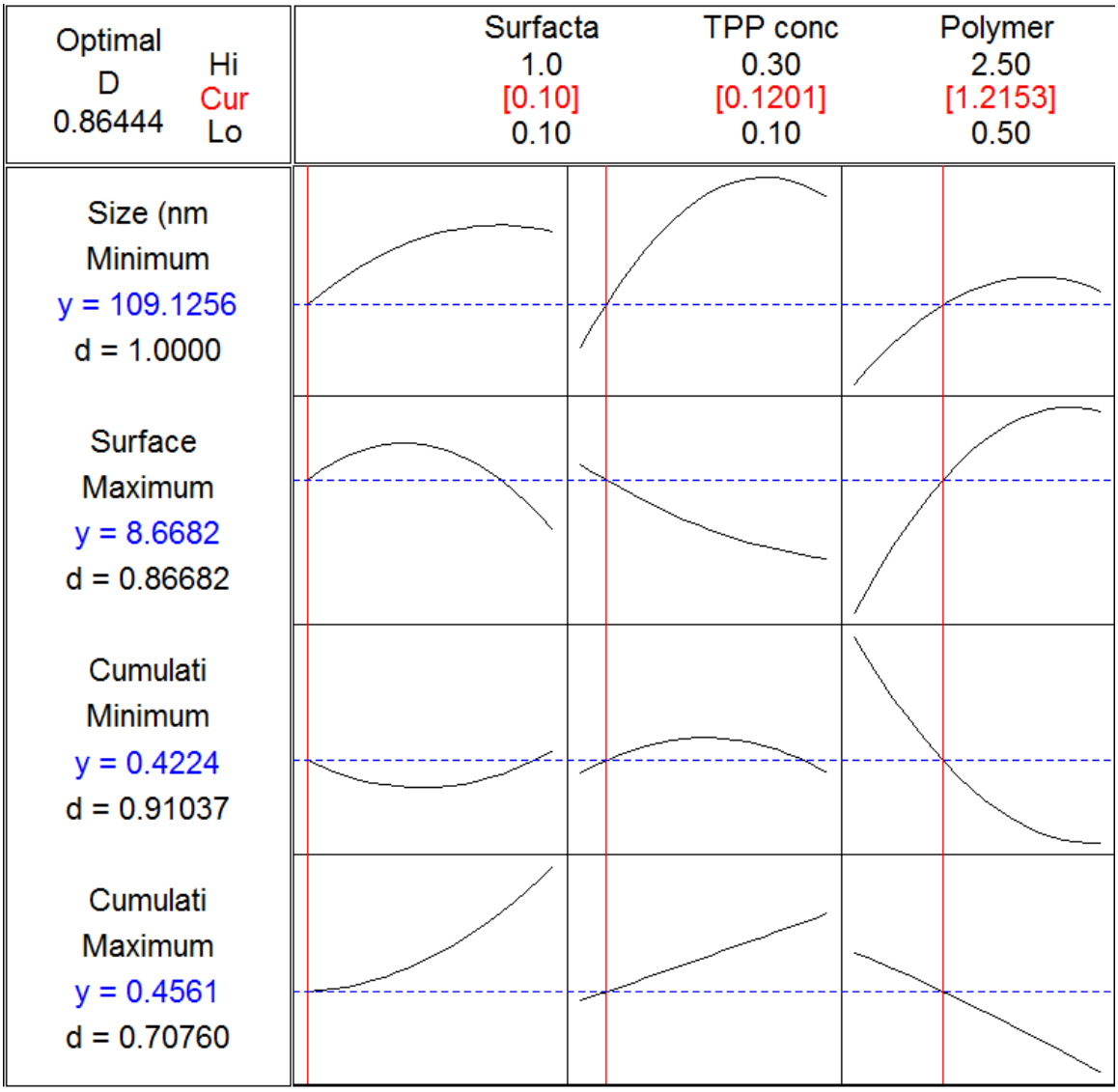


Figure 4.11: Response Optimization plot showing the desirability value, the values of independent variables and predicted values of the optimized nanoparticles.

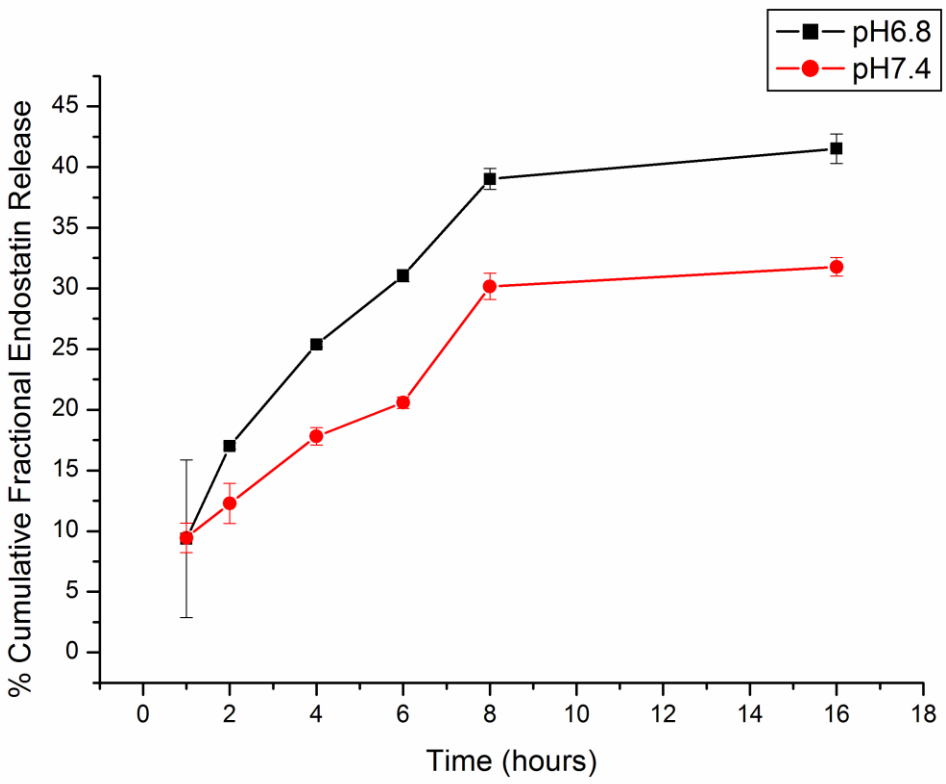


Figure 4.12: *In vitro* drug release kinetics of the optimized endostatin-loaded nanoparticle system at pH conditions of 6.8 and 7.4.

4.3.6. Confirmation of Cytocompatibility and Anti-angiogenic effect of endostatin-loaded nanoparticles

Cytotoxicity of endostatin-loaded and unloaded nanoparticles and their anti-angiogenic effects on Oesophageal squamous cell carcinoma (OSCC) were assessed by treating KYSE-30 cell line with varying concentrations of these nanoformulations. There is no significant difference in cell viability of the native polymer conjugate when compared to the control experiment (untreated cells) at polymer concentrations ranging between 125 – 500 µg/mL (Figure 4.13). Percentage cell viability was above 80%. A major significant difference only occurred at a concentration of 1000µg/mL of the polymer conjugate (63.85% of native polymers conjugate treatment when compared to the control). Thus, this formulation has potential for use in the delivery of cancer therapeutics without toxicity concern since percentage cell viability of 80% or

above shows good cyto-compatibility of tested formulations (Mavuso et al., 2016; Sharma et al., 2012).

Although the polymers employed for nanoparticle synthesis were shown to have good cyto-compactibility and were not toxic, it is possible for nanoparticles to display specific toxicity because of their size, their accumulation and degradation in cells after internalization or due to the addition of other excipients during their preparation (Vega-Villa et al., 2008). Our findings indicate that blank nanoparticles from the polymer will not affect the results from the proliferation assay performed with endostatin-loaded nanoparticles for the same treatment time. As such, oesophageal squamous cell carcinoma (KYSE-30) cells' proliferation was subsequently examined in response to endostatin-loaded nanoparticles.

Reports have shown that endostatin blocks endothelial cycle progression and reduces the expression of proliferation genes (Abdollahi et al., 2004). It induces endothelial cell proliferation (O'Reilly et al., 1997) and apoptosis pathways in the µg/mL range (Dhanabal et al., 1999). The anti-angiogenic efficacy of endostatin-loaded nanoparticles has been well reported (Hammady et al., 2009; Kim et al., 2002; Ling et al., 2007). As presented in our study (Figure 4.13), endostatin-loaded nanoparticles showed a significant reduction in cell viability (38.32%) over a concentration of 1000µg/mL. We observed 5.32% proliferation inhibition in response to nanoparticle concentration of 125µg/mL over 24 hours incubation period. Meanwhile, the proliferation inhibitory effect doubled to 13.36% at 250µg/mL endostatin-loaded nanoparticle concentration over the same treatment period. Interestingly, a dramatic increment in proliferation inhibition, more than four-fold (61.68%), was observed at nanoparticle concentration of 1000µg/mL over the same period of incubation. An unpaired t test, two-tailed P values for native and endostatin-loaded nanoparticles when compared to the control untreated cells showed statistically significant differences at $P = 0.0388$ and $P = 0.0003$ respectively.

Meanwhile, there is no significant difference between native and endostatin-loaded nanoparticles for 125, 250 and 500 µg/mL after 24 hours treatments when compared to the control. However, longer exposure of KYSE-30 cells to longer incubation time may facilitates the inhibition potential of the drug-loaded nanoparticles relative to the native particles when compared to the control.

On a general note, encapsulation with nanocarriers reduces the toxicity of drug as they offer protection against degradation by RES (Zhang and Feng, 2006; Gonzalez-Fajardo et al., 2016). In addition, encapsulation could also enable nanoparticles to target cell membranes by ensuring the release of drug close to the cell surface as well as increase the cellular uptake of nanoparticles in specific targeting studies which could enhance site-specific delivery of the nanocarriers in targeted cells thereby increasing their efficacy (Cho et al., 2001). It is interesting to note that the doses of endostatin-loaded nanoparticles presented in this study, administered to the KYSE-30 cells to achieve the anti-angiogenic drug levels presented in Figure 4.13, were in the range of 125 – 1000µg/mL and were not expected to affect cell proliferation. The positively charged surface of the designed nano-cargo, as presented in Figure 4b, could have facilitated direct binding to the negatively charged surface of KYSE-30 cells having a typical tumor cell surface (Chen et al., 2016). Similarly, the shielding effect of the nanoparticles' surface by PEG could have modulated the release of endostatin within the nanoparticle matrix thereby increasing its anti-angiogenic efficacy on the treated cells.

Formation of new blood vessels and cell proliferation are potent indicators of angiogenesis (Goodwin, 2007; Yokoyama and Ramakrishnan, 2005) which are key for tumor cell survival. Therefore, our novel nanosystem could serve as a potential nano-cargo for the delivery of endostatin and other related anti-angiogenic cancer therapeutics for effective management of SCC.

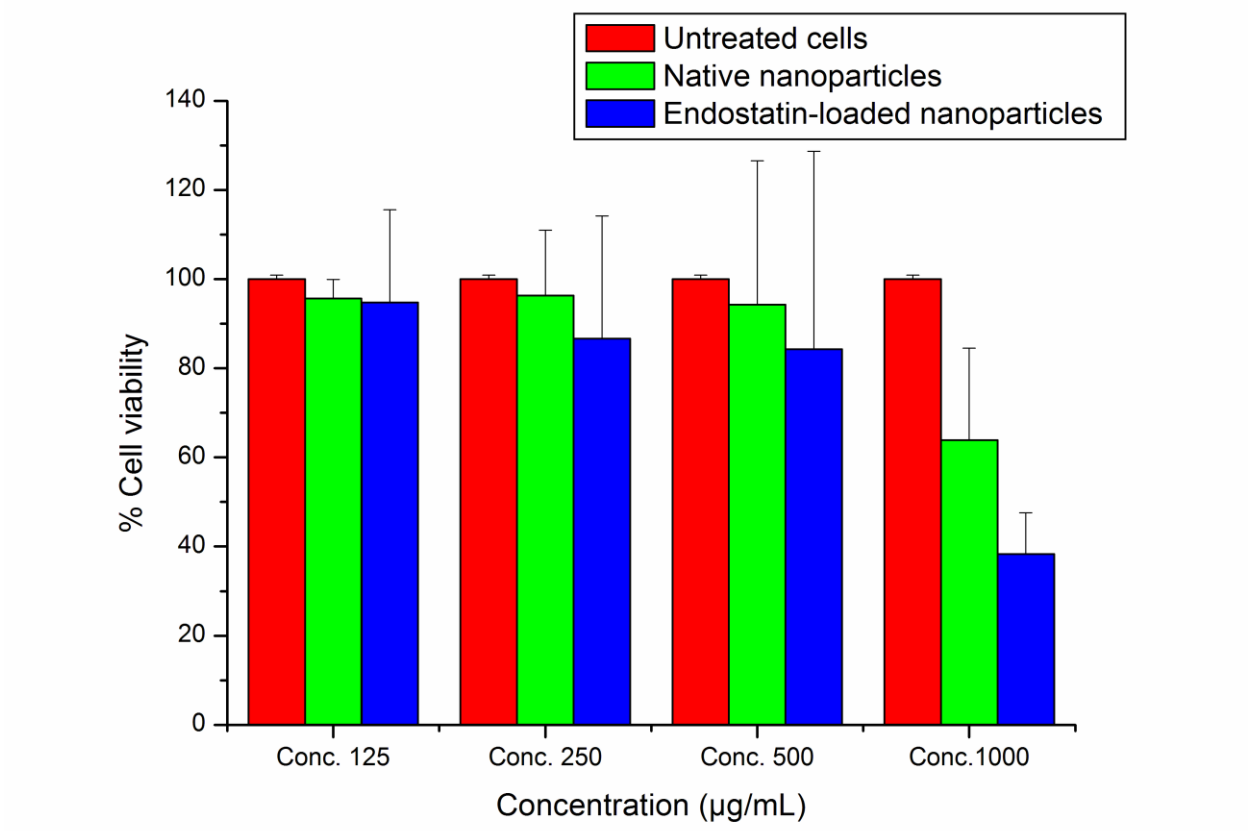


Figure 4.13: Cell viability/proliferation of treated and untreated oesophageal squamous cell carcinoma (KYSE-30) after 24 hour exposure to the nano-formulations at varying polymer concentrations. An unpaired t test, two-tailed P values for native and endostatin-loaded nanoparticles when compared to the control untreated cells showed statistically significant differences at P = 0.0388 and P = 0.0003 respectively. Meanwhile, there is no significant difference between native and endostatin-loaded nanoparticles for 125, 250 and 500 µg/mL after 24 hours treatments.

4.4. Concluding remarks

The study confirmed successful conjugation, formulation and optimization of a PEGylated CHT-g-PEI-based nanosystem loaded with endostatin as a potential delivery vehicle for endostatin. The concentration of CHT as the main polymer as well as the crosslinker concentration was a fundamental factor that modulates the BSA/endostatin encapsulation, release and swelling behavior. More so, addition of PEI onto the CHT moiety increased the overall amine protonation of the grafted polymer network at lower pH value and thus impacted positively on nanoparticle

swelling and *in vitro* BSA/endostatin release. Positively charged spherical nanoparticles were synthesized with a varying BSA/endostatin release profile at tumor pH and normal physiological pH conditions was observed, due to instantaneous swelling and shrinking behaviour of the nanosystem, respectively. The positively charged surface of these nanoparticles could be harnessed for adhesion to the negatively charged surface of many tumor cells including OSCC. The polymer conjugate was validated to be non-toxic to established squamous cell oesophageal carcinoma cell line (KYSE-30). Furthermore, encapsulation of endostatin in the nano-construct showed efficient cytotoxicity against cell proliferation and angiogenesis in a tumor model *in vitro*. This study validates the potential use of endostatin loaded CHT-g-PEI-PEG-NH_2 nanoparticles in OSCC *in vitro*; further *in vivo* experiments are necessary to confirm the preclinical potential of this system. Further, functionalizing this nano-construct with OSCC specific biomarkers could enhance direct targeting of endostatin as a potent endogenous anti-angiogenic inhibitor in OSCC management both *in vitro* and *in vivo*.

4.7. References

AbdElhady, M.M., 2012. Preparation and Characterization of Chitosan/Zinc Oxide Nanoparticles for Imparting Antimicrobial and UV Protection to Cotton Fabric. Int. J. Carbohydr. Chem. 2012, e840591.

Abdollahi, A., Hahnfeldt, P., Maercker, C., Gröne, H.-J., Debus, J., Ansorge, W., Folkman, J., Hlatky, L., Huber, P.E., 2004. Endostatin's antiangiogenic signaling network. Mol. Cell 13, 649–663.

Adebowale, A.S., Choonara, Y.E., Kumar, P., du Toit, L.C., Pillay, V., 2015. Functionalized Nanocarriers for Enhanced Bioactive Delivery to Squamous Cell Carcinomas: Targeting Approaches and Related Biopharmaceutical Aspects. Curr. Pharm. Des. 21, 3167–3180.

Alexis, F., Pridgen, E., Molnar, L.K., Farokhzad, O.C., 2008. Factors Affecting the Clearance and Biodistribution of Polymeric Nanoparticles. Mol. Pharm. 5, 505–515.

Chen, B., Le, W., Wang, Y., Li, Z., Wang, D., Ren, L., Lin, L., Cui, S., Hu, J.J., Hu, Y., Yang, P., Ewing, R.C., Shi, D., Cui, Z., 2016. Targeting Negative Surface Charges of Cancer Cells by Multifunctional Nanoprobes. Theranostics 6, 1887–1898.

Chen, H., Cui, S., Zhao, Y., Zhang, C., Zhang, S., Peng, X., 2015. Grafting Chitosan with Polyethylenimine in an Ionic Liquid for Efficient Gene Delivery. PLoS ONE 10.

Cho, C.S., Cho, K.Y., Park, I.K., Kim, S.H., Sasagawa, T., Uchiyama, M., Akaike, T., 2001. Receptor-mediated delivery of all trans-retinoic acid to hepatocyte using poly(L-lactic acid) nanoparticles coated with galactose-carrying polystyrene. J. Control. Release Off. J. Control. Release Soc. 77, 7–15.

Dhanabal, M., Ramchandran, R., Waterman, M.J., Lu, H., Knebelmann, B., Segal, M., Sukhatme, V.P., 1999. Endostatin induces endothelial cell apoptosis. J. Biol. Chem. 274, 11721–11726.

Dobrzyńska, I., Skrzydlewska, E., Figaszewski, Z.A., 2013. Changes in Electric Properties of Human Breast Cancer Cells. J. Membr. Biol. 246, 161–166.

Dreaden, E.C., Austin, L.A., Mackey, M.A., El-Sayed, M.A., 2012. Size matters: gold nanoparticles in targeted cancer drug delivery. Ther. Deliv. 3, 457–478.

Folkman, J., 1971. Tumor angiogenesis: therapeutic implications. N. Engl. J. Med. 285, 1182–1186.

Folkman, J., 1990. What is the evidence that tumors are angiogenesis dependent? J. Natl. Cancer Inst. 82, 4–6.

Folkman, J., 2006a. Antiangiogenesis in cancer therapy--endostatin and its mechanisms of action. Exp. Cell Res. 312, 594–607.

Folkman, J., 2006b. Antiangiogenesis in cancer therapy--endostatin and its mechanisms of action. Exp. Cell Res. 312, 594–607.

Gao, J.-Q., Zhao, Q.-Q., Lv, T.-F., Shuai, W.-P., Zhou, J., Tang, G.-P., Liang, W.-Q., Tabata, Y., Hu, Y.-L., 2010. Gene-carried chitosan-linked-PEI induced high gene transfection

efficiency with low toxicity and significant tumor-suppressive activity. Int. J. Pharm. 387, 286–294.

Gerweck, L.E., Seetharaman, K., 1996. Cellular pH gradient in tumor versus normal tissue: potential exploitation for the treatment of cancer. Cancer Res. 56, 1194–1198.

Gonzalez-Fajardo, L., Mahajan, L.H., Ndaya, D., Hargrove, D., Manautou, J.E., Liang, B.T., Chen, M.-H., Kasi, R.M., Lu, X., 2016. Reduced in vivo toxicity of doxorubicin by encapsulation in cholesterol-containing self-assembled nanoparticles. Pharmacol. Res. 107, 93–101.

Goodwin, A.M., 2007. In vitro assays of angiogenesis for assessment of angiogenic and anti-angiogenic agents. Microvasc. Res. 74, 172–183.

Hammady, T., Rabanel, J.-M., Dhanikula, R.S., Leclair, G., Hildgen, P., 2009. Functionalized nanospheres loaded with anti-angiogenic drugs: cellular uptake and angiosuppressive efficacy. Eur. J. Pharm. Biopharm. Off. J. Arbeitsgemeinschaft Pharm. Verfahrenstechnik EV 72, 418–427.

He, C., Hu, Y., Yin, L., Tang, C., Yin, C., 2010. Effects of particle size and surface charge on cellular uptake and biodistribution of polymeric nanoparticles. Biomaterials 31, 3657–3666.

Herbst, R.S., Lee, A.T., Tran, H.T., Abbruzzese, J.L., 2001. Clinical studies of angiogenesis inhibitors: the University of Texas MD Anderson Center Trial of Human Endostatin. Curr. Oncol. Rep. 3, 131–140.

Hu, S., Zhang, Y., 2010. Endostar-loaded PEG-PLGA nanoparticles: in vitro and in vivo evaluation. Int. J. Nanomedicine 5, 1039–1048.

Ikomi, F., Hanna, G.K., Schmid-Schönbein, G.W., 1999. Size- and surface-dependent uptake of colloid particles into the lymphatic system. Lymphology 32, 90–102.

Ip, J.C.Y., Ko, J.M.Y., Yu, V.Z., Chan, K.W., Lam, A.K., Law, S., Tong, D.K.H., Lung, M.L., 2015. A Versatile Orthotopic Nude Mouse Model for Study of Esophageal Squamous Cell Carcinoma. BioMed Res. Int. 2015.

Jia, L., Li, Z., Zhang, D., Zhang, Q., Shen, J., Guo, H., Tian, X., Liu, G., Zheng, D., Qi, L., 2013. Redox-responsive catiomer based on PEG-ss-chitosan oligosaccharide-ss-polyethylenimine copolymer for effective gene delivery. Polym Chem 4, 156–165.

Jiang, H.-L., Kim, Y.-K., Arote, R., Nah, J.-W., Cho, M.-H., Choi, Y.-J., Akaike, T., Cho, C.-S., 2007. Chitosan-graft-polyethylenimine as a gene carrier. J. Controlled Release 117, 273–280.

Jiang, H.-L., Kwon, J.-T., Kim, E.-M., Kim, Y.-K., Arote, R., Jere, D., Jeong, H.-J., Jang, M.-K., Nah, J.-W., Xu, C.-X., Park, I.-K., Cho, M.-H., Cho, C.-S., 2008. Galactosylated poly(ethylene glycol)-chitosan-graft-polyethylenimine as a gene carrier for hepatocyte-targeting. J. Control. Release Off. J. Control. Release Soc. 131, 150–157.

Jokerst, J.V., Lobovkina, T., Zare, R.N., Gambhir, S.S., 2011. Nanoparticle PEGylation for imaging and therapy. Nanomed. 6, 715–728.

Kim, Y.-M., Hwang, S., Kim, Y.-M., Pyun, B.-J., Kim, T.-Y., Lee, S.-T., Gho, Y.S., Kwon, Y.-G., 2002. Endostatin Blocks Vascular Endothelial Growth Factor-mediated Signaling via Direct Interaction with KDR/Flk-1. J. Biol. Chem. 277, 27872–27879.

Latha, S., Selvamani, P., Naveenkumar, K., Ayyanar, P., Silambarasi, T., 2012. Formulation and evaluation of capecitabine nanoparticles for cancer therapy. Int. J. Biol. Pharm. Res. 3, 477–487.

Ling, Y., Yang, Y., Lu, N., You, Q., Wang, S., Gao, Y., Chen, Y., Guo, Q.-L., 2007. Endostar, a novel recombinant human endostatin, exerts antiangiogenic effect via blocking VEGF-induced tyrosine phosphorylation of KDR/Flk-1 of endothelial cells. Biochem. Biophys. Res. Commun. 361, 79–84.

Lu, H., Dai, Y., Lv, L., Zhao, H., 2014. Chitosan-Graft-Polyethylenimine/DNA Nanoparticles as Novel Non-Viral Gene Delivery Vectors Targeting Osteoarthritis. PLoS ONE 9.

Mavuso, S., Choonara, Y.E., Marimuthu, T., Kumar, P., du Toit, L.C., Kondiah, P.P.D., Pillay, V., 2016. A dual pH/Redox responsive copper-ligand nanoliposome bioactive complex for the treatment of chronic inflammation. Int. J. Pharm. 509, 348–359.

Mehrotra, A., Nagarwal, R.C., Pandit, J.K., 2011. Fabrication of Lomustine Loaded Chitosan Nanoparticles by Spray Drying and in Vitro Cytostatic Activity on Human Lung Cancer Cell Line L132. J. Nanomedicine Nanotechnol. 2010.

Mukhopadhyay, G., 2013. HPLC analysis on separation of BSA from dilute solution.

Nishiyama, N., Kataoka, K., 2006. Current state, achievements, and future prospects of polymeric micelles as nanocarriers for drug and gene delivery. Pharmacol. Ther. 112, 630–648.

Ogris, M., Walker, G., Blessing, T., Kircheis, R., Wolschek, M., Wagner, E., 2003. Tumor-targeted gene therapy: strategies for the preparation of ligand-polyethylene glycol-polyethylenimine/DNA complexes. J. Control. Release Off. J. Control. Release Soc. 91, 173–181.

O'Reilly, M.S., Boehm, T., Shing, Y., Fukai, N., Vasios, G., Lane, W.S., Flynn, E., Birkhead, J.R., Olsen, B.R., Folkman, J., 1997. Endostatin: an endogenous inhibitor of angiogenesis and tumor growth. Cell 88, 277–285.

Panja, T., 2012. HPLC Analysis on Separation of BSA from Dilute Solution. Int. J. Pharm. Eng. 5–7.

Qiu, B., Ji, M., Song, X., Zhu, Y., Wang, Z., Zhang, X., Wu, S., Chen, H., Mei, L., Zheng, Y., 2012. Co-delivery of docetaxel and endostatin by a biodegradable nanoparticle for the synergistic treatment of cervical cancer. Nanoscale Res. Lett. 7, 666.

Sacchetti, C., Artusi, M., Santi, P., Colombo, P., 2002. Caffeine microparticles for nasal administration obtained by spray drying. Int. J. Pharm. 242, 335–339.

Sarkar, K., Debnath, M., Kundu, P., 2013. Preparation of low toxic fluorescent chitosan-graft-polyethyleneimine copolymer for gene carrier. Carbohydr. Polym. 92, 2048–2057.

Seda Tı˘glı Aydın, R., Pulat, M., 2012. 5-Fluorouracil Encapsulated Chitosan Nanoparticles for pH-Stimulated Drug Delivery: Evaluation of Controlled Release Kinetics. J. Nanomater. 2012, e313961.

Sharma, G., Valenta, D.T., Altman, Y., Harvey, S., Xie, H., Mitragotri, S., Smith, J.W., 2010. Polymer particle shape independently influences binding and internalization by macrophages. J. Controlled Release 147, 408–412.

Sharma, K., Zolotarskaya, O.Y., Wynne, K.J., Yang, H., 2012. Poly (ethylene glycol)-armed hyperbranched polyoxetanes for anticancer drug delivery. J. Bioact. Compat. Polym. 27, 525–539.

Szachowicz-Petelska, B., Dobrzyska, I., Sulkowski, S., A., Z., 2012. Characterization of the Cell Membrane During Cancer Transformation. In: Ettarh, R. (Ed.), Colorectal Cancer Biology - From Genes to Tumor. InTech.

Torchilin, V.P., 2007. Targeted pharmaceutical nanocarriers for cancer therapy and imaging. AAPS J. 9, E128-147.

Vandenberg, G.W., Drolet, C., Scott, S.L., de la Noüe, J., 2001. Factors affecting protein release from alginate-chitosan coacervate microcapsules during production and gastric/intestinal simulation. J. Control. Release Off. J. Control. Release Soc. 77, 297–307.

Vega-Villa, K.R., Takemoto, J.K., Yáñez, J.A., Remsberg, C.M., Forrest, M.L., Davies, N.M., 2008. Clinical toxicities of nanocarrier systems. Adv. Drug Deliv. Rev. 60, 929–938.

Verma, A., Stellacci, F., 2010. Effect of Surface Properties on Nanoparticle–Cell Interactions. Small 6, 12–21.

Yokoyama, Y., Ramakrishnan, S., 2005. Addition of an aminopeptidase N-binding sequence to human endostatin improves inhibition of ovarian carcinoma growth. Cancer 104, 321–331.

Yoo, J.-W., Chambers, E., Mitragotri, S., 2010. Factors that control the circulation time of nanoparticles in blood: challenges, solutions and future prospects. Curr. Pharm. Des. 16, 2298–2307.

Zhang, Z., Feng, S.-S., 2006. The drug encapsulation efficiency, in vitro drug release, cellular uptake and cytotoxicity of paclitaxel-loaded poly(lactide)-tocopheryl polyethylene glycol succinate nanoparticles. Biomaterials 27, 4025–4033.

Zheng, M., 2009. Endostatin derivative angiogenesis inhibitors. Chin. Med. J. (Engl.) 122, 1947–1951.

Zhou, B., Shen, M., Bányai, I., Shi, X., 2016. Structural characterization of PEGylated polyethylenimine-entrapped gold nanoparticles: an NMR study. The Analyst 141, 5390–5397.

Zou, S.M., Erbacher, P., Remy, J.S., Behr, J.P., 2000. Systemic linear polyethylenimine (L-PEI)-mediated gene delivery in the mouse. J. Gene Med. 2, 128–134.

Zou, X., Zhao, X., Ye, L., Wang, Q., Li, H., 2015. Preparation and drug release behavior of pH-responsive bovine serum albumin-loaded chitosan microspheres. J. Ind. Eng. Chem. 21, 1389–1397.

CHAPTER 5

ANTI-PROLIFERATIVE ACTIVITIES OF FOLATE-TARGETED ENDOSTATIN-LOADED NANOPARTICLES ON OESOPHAGEAL SQUAMOUS CELL CARCINOMA

5.1. Introduction

Oesophageal Squamous cell carcinoma (OSCC) is ranked 8th as the most common cancer type and 6th major cause of cancer death worldwide (Hendricks and Parker, 2002). Chemotherapy is the main therapeutic option for treating people living with OSCC. However, drug resistance and lack of specificity have rendered it ineffective in combating the disease even after combination chemotherapy (Wang and Thanou, 2010). Oesophageal cancer remains deadly due to poor early detection with advanced stage prognosis while optimal therapy for patients with resectable tumors remains unclear. The 5-year survival rate for all patients with oesophageal cancer is only 17% (Wu et al., 2012).

A major drawback for cancer therapeutics is the lack of specific delivery to disease sites which in turn accounts for adverse effects on healthy cells. Surface functionalization of smart nanosystems is a preferred strategy to circumvent this limitation and to achieve optimal targeted delivery of anti-cancer drugs (De Jong and Borm, 2008; Jain et al., 2015). Cancer cells overexpress certain proteins as opposed to normal cells which can be exploited for targeted formulation design (Ramesh et al., 2015). Folate receptors, as unique molecular signatures, are overexpressed on the cellular membrane of different tumor cells including Squamous Cell Carcinoma (SCC) (Das and Sahoo, 2012; Lee and Low, 1995a). Folic acid binds to the folate receptors on cell surfaces with high affinity and is internalized through receptor-mediated endocytosis. In a previous report, Wu and colleagues attached folate to a triblock copolymer of

[MPEG-b-P (LA-co-DHP)] while paclitaxel was conjugated with MPEG-b-P (LA-co-MCC), and the two micelles were coassembled into composite micelles containing folic acid and paclitaxel. FA-linked paclitaxel-loaded nanomicelles showed improved anti-tumoral activity against human oesophageal EC9706 cancer cell line *in vitro* and inhibits tumor growth in infected mice than both paclitaxel micelles and native paclitaxel (Wu et al., 2012).

Angiogenesis, the formation of new blood vessels, is fundamental to the survival and growth of tumor cells (Folkman, 1971). Recent focus has been on the use of natural and synthetic inhibitors of angiogenesis that can prevent or slow down the growth of tumor cells by blocking the formation of new blood vessels as a promising strategy for tumor therapy (Folkman, 2006). Peptide inhibitors of angiogenesis such as endostatin are under various stages of clinical trials and development with promising prospective as anti-cancer drugs (Torchilin and Lukyanov, 2003). Endostatin is a proteolytic C-terminal fragment of collagen XVIII with a molecular weight of approximately 20 kDa. Among other angiogenic inhibitors, endostatin has received the greatest attention for its broad-spectrum and low toxicity (Folkman, 2006). These advantages speed up the investigation process of endostatin into the clinical trial. Endostatin has been shown to inhibit endothelial cell proliferation, migration, and formation of new blood vessels (Kim et al., 2002). However, as any other protein, endostatin has many clinical challenges in its application such as high dosage to maintain its efficacy, high price, short circulation half-life and instability (Qiu et al., 2012). As such, incorporation into biodegradable polymers as delivery cargos could be employed to overcome these challenges and improves its therapeutic effects.

The development of nanoparticles with both passive and active targeting has been shown to aggravate the intracellular concentration of drugs in cancer cells without harm to normal cells (Cho et al., 2008). Specific binding of nanoparticles to targeted receptors such as folate receptors allow easy entrance into the core cell through receptor-mediated endocytosis (Wu et

al., 2012). Therefore, they can easily escape recognition by P-glycoprotein and the reticuloendothelial system (RES) which are the main drug resistance mechanisms (Cho et al., 2008). Similarly, the acidic pH condition of the tumor microenvironments as opposed to the physiological pH of healthy cells could be exploited in the delivery of cancer therapeutics (Gerweck and Seetharaman, 1996; Kato et al., 2013). Chitosan (CHT) based nanoparticles have been investigated and employed as carriers for genes and cancer therapeutics with different levels of effectiveness and limitations in cancer therapy (K and Kw, 2006; Yao et al., 2015). CHT's exceptional biological properties including biocompatibility, biodegradability and non-toxicity makes it of prime target in pharmaceutical and biomedical applications but with low transfection efficiency (Seda Tı˘glı Aydın and Pulat, 2012). The addition of polyethylenimine (PEI) with high buffering potential and transfection efficiency to CHT moiety have been explored for the delivery of DNA and other anti-cancer therapeutics in the management of cancer diseases (Ogris et al., 2003; Zou et al., 2000). Meanwhile, surface modification of nanoparticles with polyethylene glycol (PEG) through covalent attachment prolongs *in vivo* circulation half-life of encapsulated chemotherapeutics, protects the surface of nanoparticles from cellular uptake by the RES, and reduced carrier's cytotoxicity with improved colloidal stability (Jia et al., 2013).

In this study, we designed and employed a pH responsive, folate-decorated PEG-PEI-g-CHT nano-cargo to deliver endostatin via a folate receptor-mediated pathway into OSCC cells and facilitate anti-proliferation of KYSE-30 cells for an improved anti-tumoral therapeutic efficacy in SCC management.

5.2. Materials and Methods

5.2.1. Materials

Low molecular weight chitosan (LMW, DE=75-85%), branched polyethylenimine (PEI) (Molecular weight Mw=25KDa), Human recombinant Endostatin (MW=22kDa), 1-ethyl-3-(3-

dimethylaminopropyl) carbodiimide hydrochloride (EDC), N-hydroxysuccinimide (NHS), Sodium tripolyphosphate (TPP) (MW=367.86g/mol), poly(vinyl alcohol) (PVA) (MW=85,000g/mol) and Follic acid (MW=441.40g/mol) were purchased from Sigma-Aldrich Co., Ltd. (St. Louis, MO, USA). Functionalized poly (ethylene) glycol (NH2-PEG-COOH, Mw=2100g/mol) was from NANOCS (New York, NY, USA). KYSE-30, RPMI, HAM's F12, Fetal Bovine Serum (FBS), Pentamycin/streptomycin were from Life Bioscience (Oakleigh, VIC, Australia). All other solvents and reagents were of analytical grade unless stated otherwise.

5.2.2. Methods

5.2.2.1. Preparation of FA-PEG-PEI-g-CHT Endostatin loaded nanoparticles

5.2.2.1.1. Synthesis of CHI-g-PEI FITC labelled conjugates

CHT was grafted to PEI using a modified method described by Gao and colleagues (Gao et al., 2010) by employing 1-Carbonyldiimidazole (CDI) as a cross linker. Briefly, 2.5mg/mL CHT concentration was prepared in 0.5% acetic overnight and the pH adjusted to 4.97 using 0.2M sodium acetate buffer. 50mL (0.000834M) CDI solution was added to the CHT solution and stirred for 1 hour at room temperature to activate the amine group in the CHT solution. Thereafter, 0.25% v/v of branched PEI was dropwisely added at a molar ratio of CHT amine and PEI concentration of 2:1. The reaction mixture was left to polymerized for 24 hours and dialysed using a dialysis membrane (MW=12 000kDa) over double distilled water (DDW) for 24 hours. Meanwhile, 0.1mM Fluorescein Isothiocyanate (FITC) dissolved in dimethyl sulfoxide (DMSO) was mixed with the reaction mixture of CHT-g-PEI solution at room temperature on a shaker for 12 hours for complete conjugation with the amine of PEI as previously described (Feng et al., 2006). Unbound FITC was removed by dialysis over DDW for 24 hours. The final FITC labelled CHT-g-PEI conjugate was then collected by lyophilization over 24 hours.

5.2.2.1.2. Synthesis of Folate-decorated PEG-PEI-CHT FITC labelled conjugates

Prior to the synthesis of the FA-PEG-PEI-CHT conjugates, FA was grafted onto the free amine component of a bifunctional PEG (NH_2-PEG-COOH) using the NHS/EDC chemistry. The carboxyl group of 25mg FA dissolved in 2.5mL DMSO was activated using 35mg EDC and 20mg NHS under stirring for 4 hours. The mixture was then dialysed against DDW for 24 hours to remove any unbound FA while the synthesised FA-PEG-COOH conjugate was collected for further experiment. Amidation reaction, following the method previously described by Jiang and co-workers (Jiang et al., 2008) was employed to conjugate the carboxyl group of FA-PEG-COOH and the amine group of the FITC labelled CHT-g-PEI conjugates. The reaction was allowed to polymerize at 4^0C and 25^0C for 12 hours respectively. The synthesized FA-PEG-PEI-CHT FITC labelled conjugates were then dialysed over DDW for 48 hours and the dried power was collected by lyophilization over 24 hours.

5.2.2.1.3. Endostatin Entrapment and synthesis of FA decorated nanoparticles

Ionotropic gelation technique was employed for the synthesis of FA decorated Endostatin loaded nanoparticles. Briefly, 0.5 mg/mL ENT solution was mixed with the solution mixture of FA-PEG-PEI-CHT conjugates under mild stirring for 5 minutes. 0.1% w/v TPP as a polyanionic agent was drop-wisely added to the endostatin loaded mixture. The formation of an opaque and turbid solution confirmed the formation of endostatin loaded nanoparticles while 1% w/v polyvinyl alcohol (PVA) was added as surfactant. The synthesized FA decorated nanoparticles were then allowed to gelate for 1 hour under mild stirring and the resultant mixture was centrifuged at 5000 rpm for 1 hour to collect the FITC-labelled, ENT-loaded FA-PEG-PEI-CHT nanoparticles in the pellet re-suspended in DDW. Dried powder ENT-loaded FA decorated nanoparticles were then collected by lyophilization over 24 hours and stored at -20^0C until further analysis.

5.2.2.2. Characterization of Conjugated FA-PEG-PEI-CHT Nanoparticles

5.2.2.2.1. Determination of Chemical and Functional Transformations using Fourier Transform Infrared Spectroscopy

The vibrational transitions in the chemical structures of CHT-g-PEI, FA-PEG-COOH, FA-PEG-PEI-CHT and ENT-loaded FA-PEG-PEI-CHT were evaluated using Fourier transform infrared (FTIR) spectroscopy (PerkinElmer Inc., Waltham, Massachusetts, USA). Samples were placed on a single bounce diamond crystal and processed by a universal attenuated total reflectance (ATR) polarization accessory, at a resolution of $4cm^{-1}$, with the spectrum ranging from 4000 to 650 cm^{-1}.

5.2.2.2.2. Structural Modifications using Nuclear Magnetic Resonance Spectroscopy

Nuclear Magnetic Resonance (NMR) spectra were recorded for FA-PEG-COOH and PEG-PEI-g-CHT and FA-PEG-PEI-g-CHT conjugates. ^{1}H NMR chemical shifts, expressed in ppm and analyzed in deuterated water (D2O) doped with deuterated acetic acid (CD3COOD) in a ratio of 5:1 were recorded on a Bruker 500MHz (NMR spectrometer Billerica, MA, USA) instrument at room temperature.

5.2.2.2.3. Size, Zeta potential and Structural Morphology ENT-loaded Nanoparticles

Malvern Zetasizer Nano ZS (Malvern Instruments, Worcestershire, UK) was employed to evaluate the hydrodynamic size and zeta potential of the FA decorated endostatin-loaded nanoparticles. Known sample weights were dispersed in DDW and sonicated for 30 seconds. 2mL of dispersed sample solution was placed in disposable polystyrene cuvettes and the dynamic scatter intensity was recorded at room temperature.

The size and shape of the nanoparticles were also confirmed using Transmission Electron Microscopy (TEM) (FEI Tecnai T12 TEM, 60-120kV, Hillsboro, OR, USA). Small amount of the nanoparticle was dispersed in DDW, ultra-sonicated for 15 minutes and a single drop of the

nanoparticle suspension was dropped on a Form Var® coated 200-mesh copper grip (TAAB Laboratories Equipment Ltd., Aldermaston, England), and allowed to air dry at room temperature prior to TEM analyses.

The morphology of the nanoparticles was also examined using Scanning Electron Microscopy (SEM). Powdered sample of the nanoparticles was placed onto an aluminium specimen stub covered with a double-sided carbon adhesive disc and sputter-coated with both palladium and gold for 4 minutes at 20KV. SEM images of FA decorated ENT-loaded nanoparticles were then viewed by a Scanning Electron Microscope (SIGMA VP, ZEISS Electron Microscopy, Carl Zeiss Microscopy Ltd; Cambridge, UK).

5.2.2.2.4. *In vitro* Endostatin Release

To investigate the *in vitro* release of encapsulated ENT, 5mg each of ENT-loaded nanoparticles and FA decorated ENT-loaded nanoparticles (n = 3) were incubated in 2mL of PBS buffer in a microcentrifuge tubes in an orbital shaker incubator at 37°C for 24 hours. Nanoparticle dissolution was tested at varying pH conditions of 4.6, 6.8 and 7.4 to mimic the endolysosomal acidication of cell, the tumor microenvironment and the physiological pH respectively. Samples were taken at specified time interval (1, 2, 4, 8, 16 and 24) after centrifugation at 5000 rpm for 10 minutes to allow nanoparticles settled into pellets. 200 µL of supernatants were removed in triplicates and replaced with fresh buffer to maintain sink condition. Samples were then analysed for UV absorption of endostatin at 562 nm using a microplate reader (FilterMaxTM F5 Multi-Mode Microplate Reader, Molecular Devices, USA).

5.2.2.3. Analysis of the Endostatin-loaded Nanoparticles is an OSCC Cell Line

Human oesophageal Squamous Cell carcinoma cell line (KYSE-30) (Life Bioscience, Oakleigh, VIC, Australia) were seeded in complete media comprising of RPMI and Ham's F12 (1:1),

supplemented with 10% Fetal Bovine Serum, 2mM glutamine, sodium bicarbonate and 100µL penicillin/streptomycin (Sigma- Aldrich; St. Louise, MO, USA). The cells were maintained in an incubator (RS Biotech Galaxy, Irvine, UK), with a humidified atmosphere of 5% CO_2 at 37 ^{0}C.

5.2.2.3.1. Polymer Cyto-compatibility and Cell Proliferation Assay

In vitro cell cytotoxicity was determined using Alamar blue assay. KYSE-30 cells were diluted in a complete medium at a final concentration of 1 × 10^4 cells/mL and seeded (25µL/well) and incubated for 24 hours prior to cell proliferation evaluation using Alamar blue assay according to the manufacturer's procedures. Native polymer conjugates, ENT-loaded nanoparticles and FA decorated ENT-loaded nanoparticles were dissolved in the serum free culture medium at varying concentrations of ENT (125µg/mL, 250µg/mL, 500µg/mL and 1000µg/mL). Attached cells in the wells were treated with the various nano-formulations in triplicates for 24 hours and cell viability was quantified at maximum emission/excitation wavelengths of 535nm and 595nm respectively on a microplate reader (FilterMaxTM F5 Multi-Mode Microplate Reader, Molecular Devices, USA). Attached cells treated only with serum free media, without the nano-formulation, were used as control. Results are presented as percentage cell viability (%CV) (mean standard deviation), with the percentage of viable cells calculated using the following Equation.

$$CV = \frac{Fluorescence\ reading\ in\ treated\ cells}{Fluorescence\ reading\ in\ control\ (untreated)\ cells} * 100 \ \ldots\ldots Eq..5.1$$

5.2.2.3.2. Cellular uptake, internalization and sub-cellular localization of nanoparticles

KYSE-30 cells (1×10^5 cells/well) were cultured on cover slips in a six-well culture plate for 24 hours in 2mL of RPMI and Ham's F-12 medium (1:1) supplemented with 10% fetal bovine serum (FBS) under a humidified atmosphere of 5% CO_2 in air. Attached cells were washed three times with PBS solution. The medium was then replaced with 2 mL (0.1 mg/mL) fresh

medium without FBS containing FITC-labelled FA-PEG-PEI-CHT ENT-loaded nanoparticles. The cells were then incubated at 37 ^{0}C for 24 hours, followed by removal of the medium and washing the cells twice with PBS solution. Subsequently, the nucleus of cells treated with/without nanoformulations were stained with 10 µl/mL DAPI (4′,6-diamidino-2-phenylindole) solution (Thermo Fisher Scientific, Waltham, MA, USA) for 5 minutes under incubation following the manufacturer's protocol. Stained cells on the coverslips were rinsed three times in PBS prior to image capture.

The intracellular entry of FITC-labelled FA-PEG-PEI-CHT ENT-loaded nanoparticles was monitored using Confocal Laser Scanning Microscope (LSM 780, ZEISS) (Baden-Württemberg, Germany). Treated cells were fixed with 4% paraformaldehyde in PBS for 30 minutes at room temperature. Thereafter, coverslips containing fixed cells were rinsed with PBS and placed in 0.1% Triton-X100 solution to permeate the cells for 5 minutes. The coverslips were then mounted on glass microscope slides by using a drop of 80% v/v cooled glycerol. Cell samples were observed under CLSM at 495 nm excitation to induce the green fluorescence of FITC and their emission was observed at 517 nm. Blue fluorescence of DAPI was induced by 358 nm excitation and detected at 461 nm wavelength excitation spectrum.

5.2.2.3.3. Endothelial cell migration assay using a modified Boyden Chamber

Migration of KYSE-30 cells was assessed using the modified Boyden Chambers (Corning incorporated, NY, USA). Gelatinized polycarbonate filters (pore size, 8.0 µm) with 6.5mm diameter inserts were employed. Briefly, 200 µL solution of native ENT-loaded PEG-PEI-CHT conjugates, FA-PEG-PEI-CHT ENT-loaded nanoparticles or control (untreated cells), and 6.48 × 10^4 KYSE-30 cells in 200 µL serum-free medium were added to the upper chamber. A volume of 0.4 mL of 10% FBS-containing medium was then added to the lower chamber as a chemoattractant. Cells were incubated for 8 hours at 37°C, and non-migrating cells (dead cells

due to treatments with nanoformulations) on the upper surface of the membrane, were then scraped off with cotton swabs. 1 mL Alamar blue reagent was added to cells that migrated to the bottom of the membrane for 4 hours and quantified at maximum emission/excitation wavelengths of 535 nm and 595 nm respectively on a microplate reader (FilterMaxTM F5 Multi-Mode Microplate Reader, Molecular Devices, USA). Thereafter, migrated cells at the bottom side of the membrane were washed twice in PBS and stained with trypan blue. Stained cells were visualised under an Olympus BX 63 optical fluorescence microscopy (OFM) (Olympus DP 80) (Tokyo, Japan).

5.3. Results and Discussion

5.3.1. Biofunctionalization of Polymer Conjugates and ENT-loaded Nanoparticles

Chemical and Structural Modification

CHT was conjugated to PEI using CDI as a cross linker. The imidazoles of CDI linked the amine groups in CHT and that of PEI as shown in Figure 5.1 to form CHT-g-PEI copolymer. In a subsequent experiment, the carboxyl group of FA was immobilized using EDC/NHS chemistry and conjugated to the amine of a bifunctional PEG (NH_2-PEG-COOH) to yield FA-PEG-COOH. The terminal carboxyl group of FA-PEG-COOH was thereafter activated using EDC and NHS prior to its conjugation with the free amines in CHT-g-PEI to produce FA-PEG-PEI-CHT nanocontruct loaded with ENT.

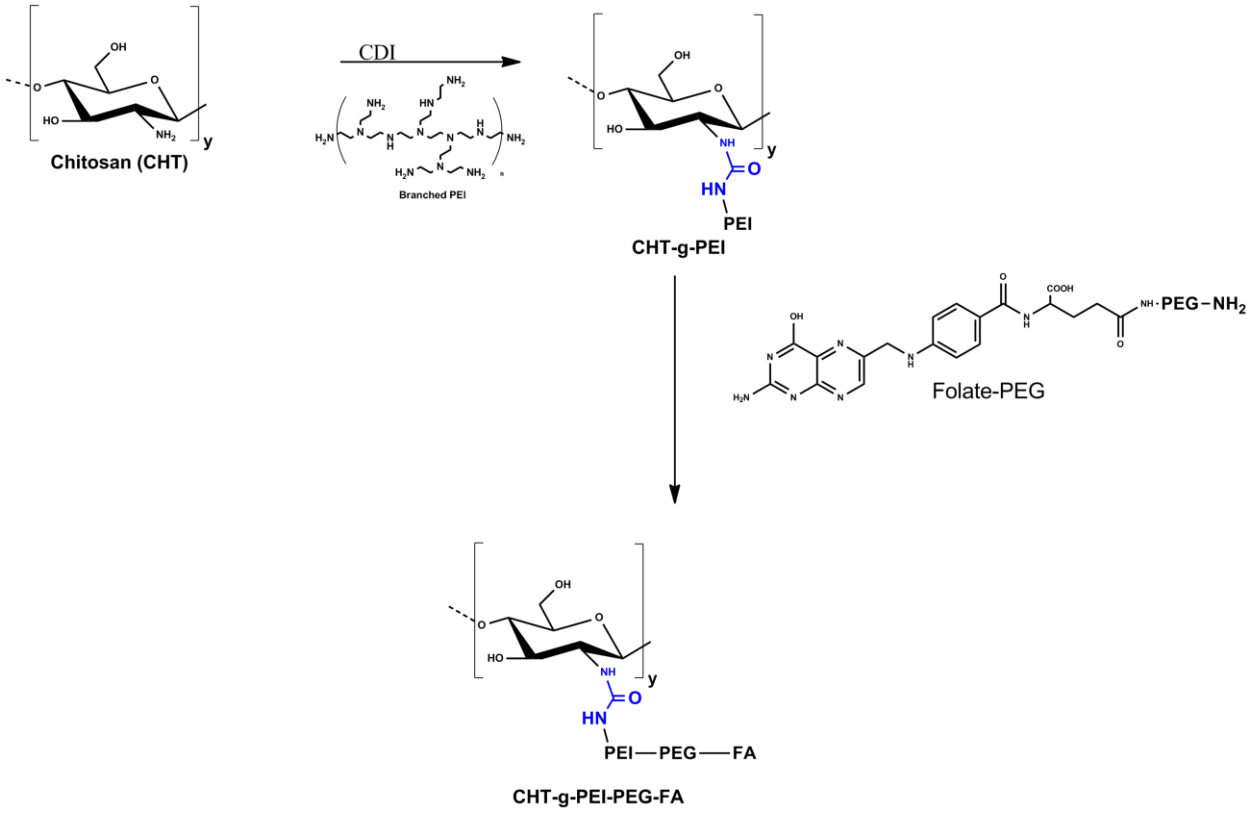


Figure 5.1: Schematic diagram showing the preparation of Folate decorated nanoparticulate system.

The FTIR spectra of the native polymers and the corresponding conjugates are presented in Figure 5.2. Absorption peaks at 3312 cm^{-1} and 3376 cm^{-1} were assigned to the C-H and N-H stretching of the imidazole bonds between the amines of CHT and PEI in the grafted CHT-g-PEI conjugate Figure 5.2a (ii) (Ramasamy, 2015). The characteristic peak of CHT (Figure 5.2a (i)), assigned at 871.15 cm^{-1}, was due to the C-O stretching in the pyranose ring while the peak at 822.14 cm^{-1} (Figure 5.2a (iii)) assigned to the $NHCH_2CH_2$ moiety in PEI were both retained in the CHT-g-PEI conjugate (Figure 5.2a (ii)). Similarly, the characteristic absorption peak of the phenyl ring of FA appeared at 1480.32 cm^{-1} in FA spectrum (Figure 5.2b (vi)) and shifted to a lower frequency at 1463 cm^{-1} in Figure 5.2b (v) when FA is conjugated to the bifunctional PEG. Meanwhile, the frequency of the O-H stretching of the carboxylic group in NH_2-PEG-COOH assigned at 2879 cm^{-1} (Figure 5.2b (iv)) increase slightly at 2882 cm^{-1} in FA-PEG-COOH (Figure

5.2b (v)). The appearance of the peak at 3399.2 cm^{-1} due to the N-H stretch of secondary amide and the peak at 1639.6 cm^{-1} due to C=O stretching in amide bond II (Figure 5.2b (v)) confirmed the formation of amide bond between the carboxyl group of FA and the terminal amine in NH_2-PEG-COOH. Successful conjugation of the carboxyl group in FA-PEG-COOH and the free amine in CHT-g-PEI is confirmed by interpreting the FTIR spectrum FA-PEG-PEI-CHT conjugate in Figure 5.2c (viii), which shows the characteristic absorption bands of the individual components and the formation of amide bond. The peak due to the deformation vibration N-H amide II of the amide bond in FA-PEG-COOH (Figure 5.2c (vii)) at 1597 cm^{-1} shifted to a higher frequency at 1605 cm^{-1} in FA-PEG-PEI-g-CHT (Figure 5.2c (viii)) conjugates signifying the existence of chemical interaction between the carboxyl group in FA-PEG-COOH and the amine in CHT-g-PEI. Further, the corresponding peaks due to N-H bend in plane and C-N stretching in amide bond III assigned at 1178.78 cm^{-1} and 1119.92 cm^{-1} respectively (Figure 5.2c (vii)) were shifted to 1176.0 cm^{-1} and 1115.06 cm^{-1} respectively in Figure 5.2c (viii) suggesting the possibility of a strong interaction between the amine of CHT-g-PEI (Figure 5.2c (ix)) and the carboxyl group in FA-PEG-COOH (Figure 5.2c (vii)).

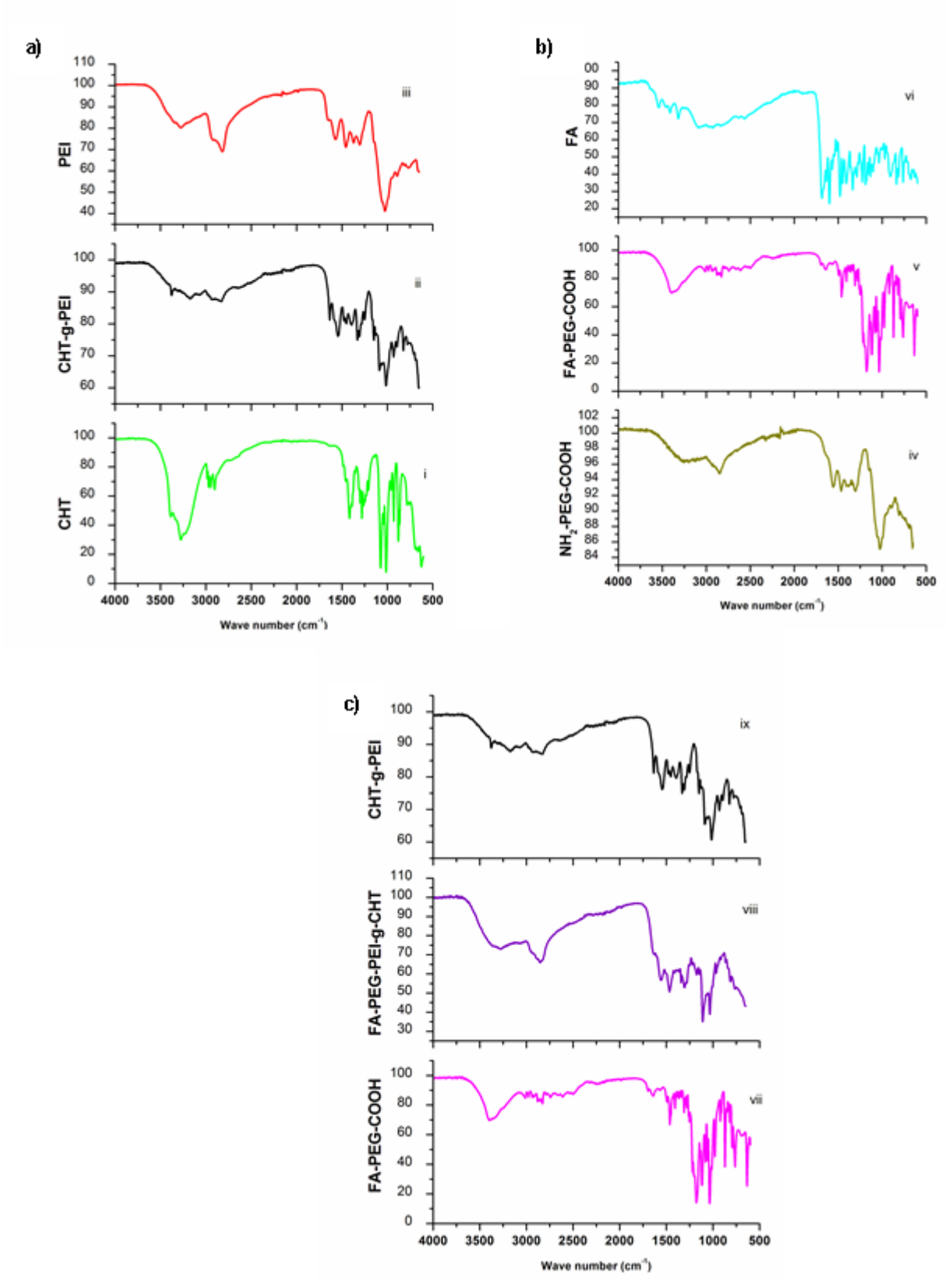


Figure 5.2: FTIR spectra showing conjugation of native polymers and FA decorated nanoparticles.

Figure 5.3 show the ^{1}H NMR spectra of PEG-CHT-g-PEI, FA-PEG-PEI-g-CHT and FA-PEG-COOH copolymer conjugates. From Figure 5.3 (a), the characteristic peaks at δ = 1.9 ppm is indicative of the methyl protons of N-acetyl group of CHT. The presence of peaks between δ = 2.5–3.2 ppm were assigned to methylene protons of PEI (–$NHCH_2CH_2$–). The peak at δ = 3.6 ppm belonged to the methylene protons of PEG (–OCH_2CH_2–). Meanwhile, there was a slight highfield increase in the signals of the characteristic protons of CHT and PEI (Figure 5.3 (b)) after FA is grafted unto PEG-CHT-g-PEI conjugate in Figure 5.3 (a) which possibly indicates a chemical interaction between FA and the polymer conjugates. The characteristic peak of FA was assigned at 8.0 ppm (Figure 5.3 (b)). The appearance of the phenyl protons of FA between 6.6-8.6 ppm and the methylene protons of PEG between 3.2-3.8 ppm (Figure 5.3 (c)) confirmed the successful conjugation of FA unto the carboxyl group of bifunctional PEG. Similar results were reported by Sakar and co-workers (2013) for fluorescent chitosan-graft-polyethyleneimine, Lu and colleagues (Lu et al., 2014) for Chitosan-Graft-Polyethylenimine/DNA Nanoparticles and Li et al (Li et al., 2014) for Folatepolyethylene glycol conjugated carboxymethyl chitosan for tumortargeted delivery of 5fluorouracil. Thus, both the FTIR and the proton NMR results confirmed the successful synthesis of FA decorated PEG-PEI-g-CHT nanoconstructs for ENT encapsulation in subsequent experiments.

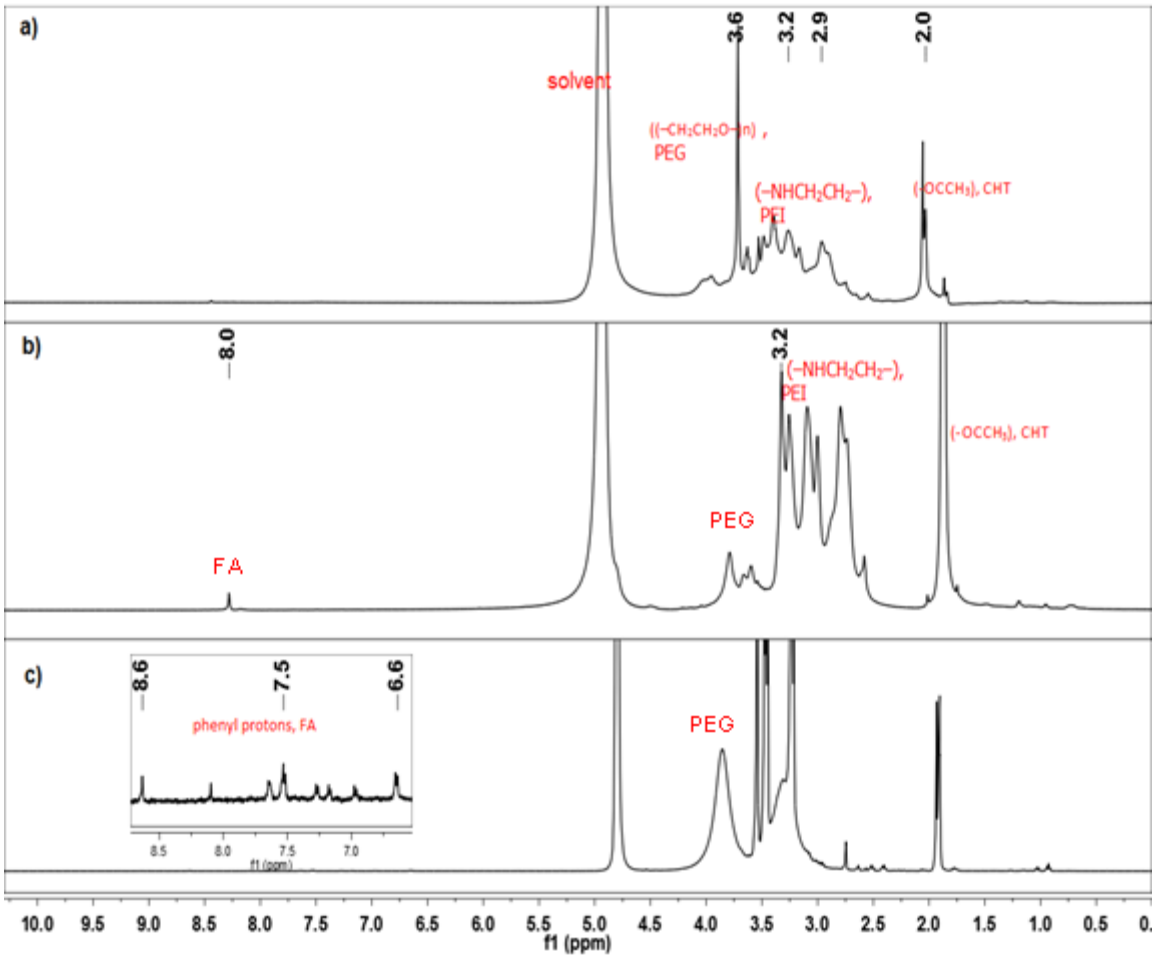


Figure 5.3: ^{1}H NMR of grafted copolymers in D_2O:CH_3COOD (5:1) a) PEG-PEI-g-CHT conjugate b) FA-PEG-PEI-g-CHT conjugate c) FA-PEG-COOH.

5.3.2. *In vitro* Release Kinetics of ENT from FA-decorated Nanoparticles

Endostatin release within the FA-linked nanoparticles was in two phases with a burst release up to about 10% within the first 1 hour and a continuous cumulative fractional release over 24 hours across tested pHs as presented in Figure 5.4. A cumulative fractional release of 66.67% was reached within 24 hours at endosomal pH of 6.8 and 64.79% at pH 6.8 for acidic tumour microenvironment. Interestingly, lower ENT release of about 58.73% was recorded at normal cell physiological pH of 7.4. This could be partly explained due to the swelling behaviour of the CHT backbone of the nanoparticles at acidic pH (Seda Tı˘glı Aydın and Pulat, 2012). This pH-

dependent release pattern might enhance the selectivity of tumour targeting because the acidic conditions of the tumour microenvironment may trigger the release of ENT from the FA functionalized nanoparticles *in vivo*. Similarly, the lower release rate at pH 7.4 would protect the stability of the PEG-PEI-g-CHT nano-cargo in the blood circulation and normal tissues (Ruan et al., 2015).

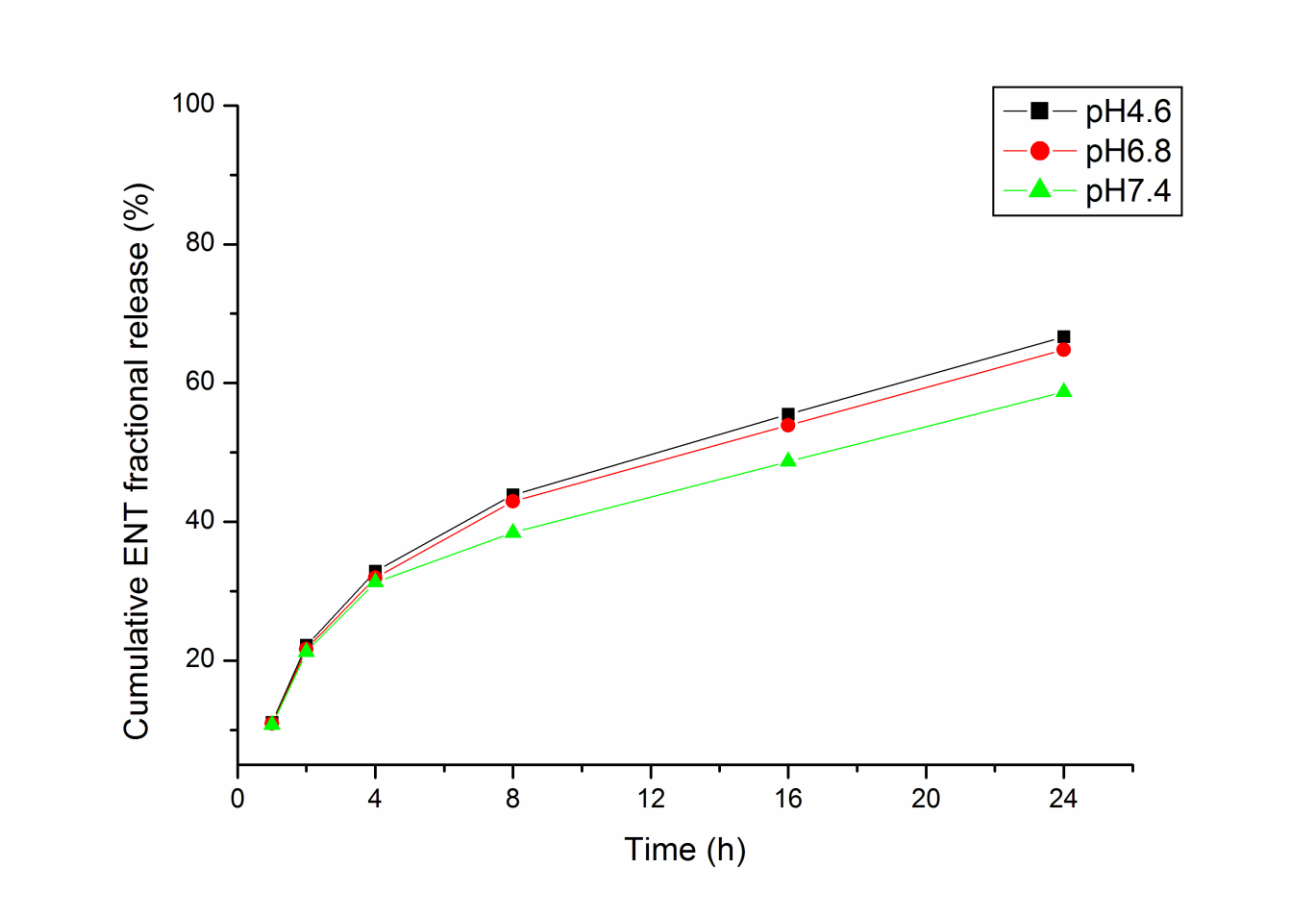


Figure 5.4: *In vitro* release of ENT from FA-functionalized nanoparticles. The release profile was in two phase, with an initial burst release followed by continuous release. Release was higher and more rapid at acidic endosomal and cancer microenvironment pH (4.6 and 6.8 respectively) than at physiological pH of 7.4 of healthy cells.

5.3.3. *In vitro* Cellular Uptake and Intracellular Trafficking of Nanoparticles

Physicochemical characteristics of nanoparticles will significantly affect their cellular uptake, internalization, circulation, biodistribution, and trafficking in biological systems (Duan and Li, 2013). Cellular uptake, internalization and prolong retention of drug loaded nanoparticles by diseased cells determine their therapeutic efficacy in disease management (Hattori and Maitani, 2004). While *in vitro* and *in vivo* biologic processes could vary in their experimental outcomes, *in vitro* investigation could provide important preliminary findings to show the therapeutic advantages of nanoparticles (Wu et al., 2012).

Nanoparticle shape and size have been reported to influenced internal cellular binding and uptake of drug loaded nanoparticles (Favi et al., 2015a, 2015b). Importantly, spherical shape nanoparticles possess more cellular binding effect, internalization and toxicity than nanoparticles with other shape configurations (Favi et al., 2015a; Verma and Stellacci, 2010). As presented in Figure 5.5 and 5.6, the TEM and SEM micrographs show that spherical shaped FA-decorated nanoparticles, having an average size below 250 nm were synthesized.



Figure 5.5: TEM micrograph of the FA-decorated endostatin-loaded nanoparticles. Nanoparticles showed spherical shape with an average size < 200 nm with a hollow centre pore assumed to be encapsulated particles of ENT within the nanoparticle matrix.

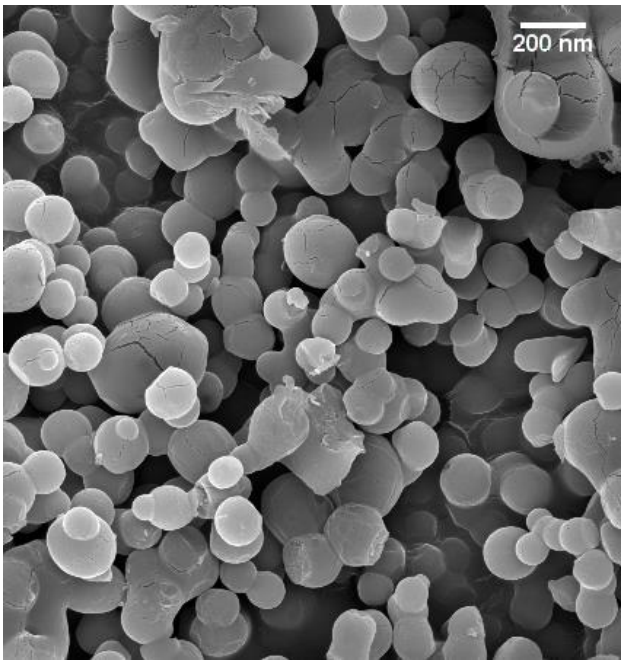


Figure 5.6: Gold-platinum sputtered SEM Micrograph of FA-decorated ENT-loaded nanoparticles. Magnification = 10.07 KX; Voltage = 10.00 kV. Particle showed spherical shape morphology with rough surfaces at high magnification assumed to be folate particles attached to the nanoparticles' surfaces. To check the surface morphology of the particles, SEM was conducted on larger sized particles.

The hydrodynamic size as shown in Figure 5.7 is 207.3 nm. This nano-sized and spherical morphology could probably accounts for the effective cellular uptake and internalization of the FA-functionalized nanoparticles.

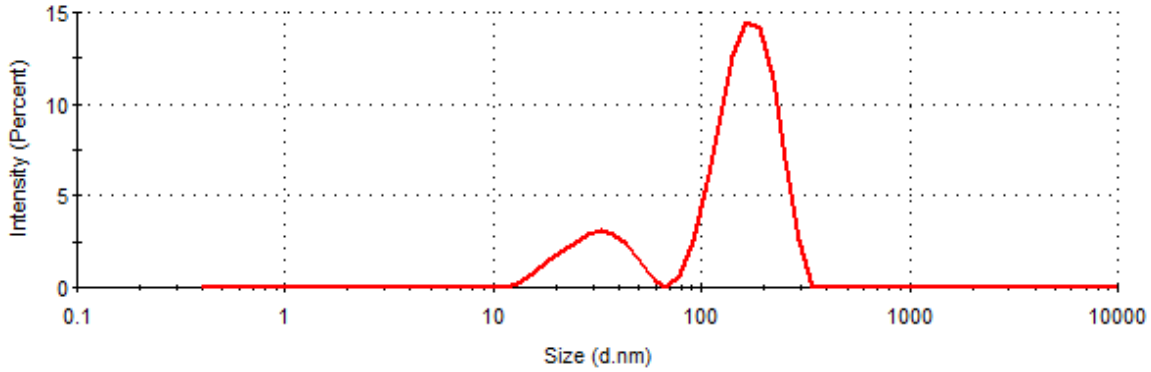


Figure 5.7: Average zeta size of FA decorated ENT-loaded nanoparticle using dynamic light scattering. Average hydrodynamic size of nanoparticles was recorded was less than 250 nm in line with both the TEM and SEM average sizes.

In addition to size effect, the type of charged ions present on the surface nanoparticles plays an important role on the interactions between nanoparticles and cell (Verma and Stellacci, 2010; Xiao et al., 2015). Studies have shown that nanoparticles with positively charged surfaces are more easily internalized by cells than the neutral or negatively charged nanoparticles (Alkilany et al., 2009; Arvizo et al., 2010; Hauck et al., 2008; Murugan et al., 2015; Thorek and Tsourkas, 2008). Cellular uptake and cytotoxicity seemed to depend more on surface charge than size at many instances (Fröhlich, 2012). Xia and colleagues have examined the role of surface charge in internalization of gold nanoparticles by using an I2/KI etchant approach which allows a quantitative differentiation of surface adsorbed nanoparticles versus internalized nanoparticles. Their report revealed positively charged nanoparticles bound and internalized to the negatively charged surface of cell membrane than both neutral and negatively charged nanoparticles (Cho et al., 2009). As presented in Figure 5.8, FA-decorated nanoparticles have an overall positively charged surface, having a zeta potential charge of 12.9 mV. This partly contributes to the direct

targeting, binding to the folate receptors on KYSE-30 cells (as later discussed in this study) and internalization by receptor-mediated endocytosis of FA-PEG-PEI-g-CHT ENT-loaded nanoparticles aside the specific affinity binding of FA to the folate receptors on the surfaces of oesophageal squamous cell carcinoma including KYSE-30 cells (Wu et al., 2012).

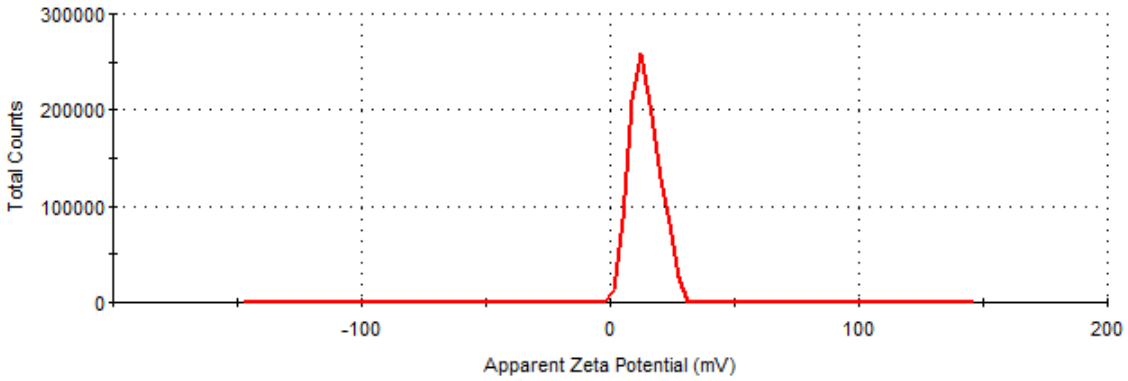


Figure 5.8: Average zeta surface potential of FA decorated endostatin-loaded nanoparticles. An average positively charged surface was recorded at 12.9 mV.

Quite often, the mode of nanoparticle trafficking through various subcellular compartments dictates the channel of drug distribution (Zeng et al., 2014). As shown in Figure 5.9, the green fluorescence is the FITC labelled FA decorated nanoparticles, and the blue fluorescence represents DAPI stained cell nucleus. The green fluorescence was clearly observed within the various sub-cellular compartments of the cell, indicating cellular uptake and internalization of the FA decorated nanoparticles (Figure 5.9 (ii)). It was probably because the positively charged surface of FA-modified nanoparticles provides good interaction with KYSE-30 cells which had negative charge on their surfaces (Chen et al., 2016). This corroborates Liu and colleagues findings that cell type is also a determining factor influencing nanoparticle binding, uptake and internalization aside particle surface and side (Liu et al., 2013).

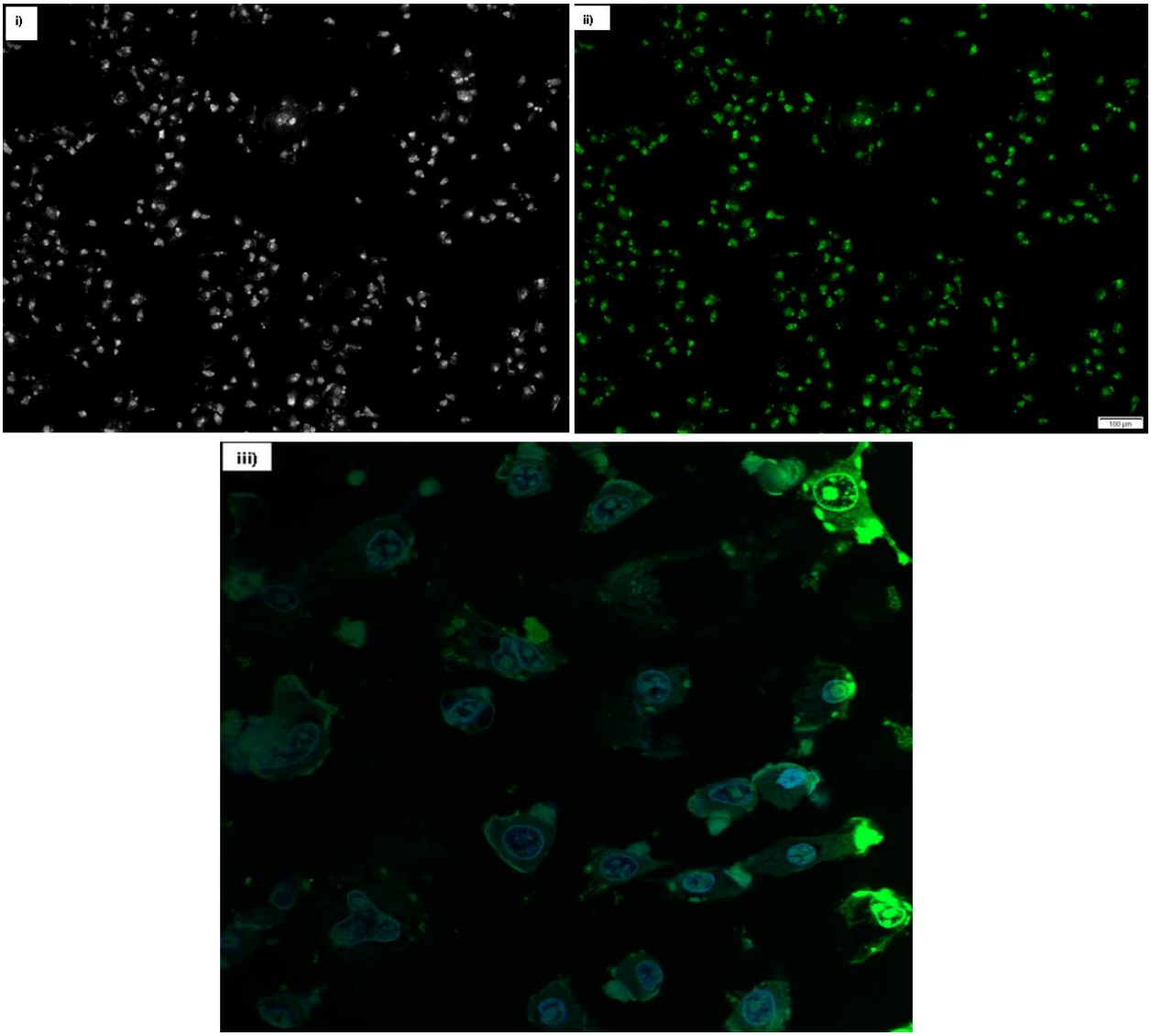


Figure 5.9: Cellular uptake and internalization of FA-decorated endostatin-loaded nanoparticles in KYSE-30 cells. This is after the incubation with FITC labelled endostatin-loaded FA-PEG-PEI-g-CHT nanoparticles; (i) from transmitted light channel, (ii) from FITC channel, (iii) from overlaid channel upon staining the nucleus with DAPI (blue).

More importantly, FA specifically targets the over-expressed folate receptors on the surface of KYSE-30 cells and facilitates cellular internalization of nanoparticles via receptor-mediated endocytosis (Figure 5.10) (Lee and Low, 1995b; Wu et al., 2012). Interestingly, the green fluorescence was found within the nucleus which showed preferential endocytosis of FA conjugated nanoparticles by KYSE-30 cells (Figure 9(iii)). The cellular internalization potential of

this FA enhanced nanoparticles could account for their necrotic and apoptotic effects on nucleus of KYSE-30 cells are presented later in the study.

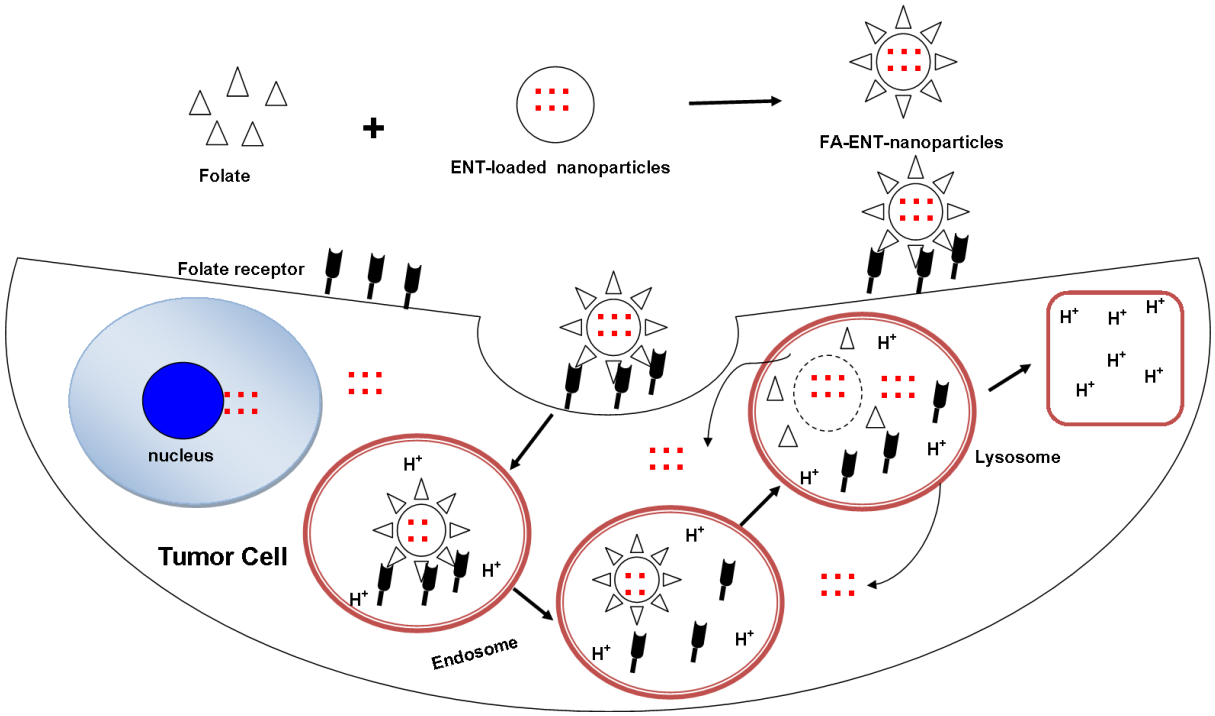


Figure 5.10: Proposed mechanisms for the cellular uptake and internalization of Folate-decorated endostatin-loaded nanoparticles.

While the red fluorescence is due to rhodamine 123 specific staining of the mitochondrial (Figure 5.11(i)), green fluorescence was also seen within the merged image (Figure 5.11(iv)) confirming the sub-cellular trafficking of FA-linked nanoparticles into the mitochondrial. It has been well established that inhibition of mitochondrial respiration induces reactive oxygen related cell death. These reactive oxygen species, generated within the mitochondria, can damage mitochondrial components (Koizumi et al., 1996) and become cytotoxic. As such, any damage to the mitochondrial could inhibit cell proliferation and results in cell death. As presented in Figure 5.11(i), rhodamine 123 staining of the mitochondrial revealed a disruption in its architecture. The convectional elongated morphology of the mitochondrial was changed to rounded shaped structure (as indicated by the white arrows). This corroborates previous report by Lovrić and collegues (Lovrić et al., 2005a) that stressful conditions disintegrate and transform

the network of elongated mitochondria into vesicular punctiform mitochondria having a short and rounded architecture. This shows that FA functionalized nanoparticles target the mitochondrial and allow ENT to affect the mitochondrial. Previous report by Yuan and co-worker showed that ENT promotes the mitochondrial permeability transition pore (mPTP) opening via voltage-dependent anion channel 1 (VDAC1), a major component of mitochondrial outer membrane which induced endothelial cell apoptosis (Yuan et al., 2008). Meanwhile, further assays to quantify mitochondrial activity including specific enzyme like cytochrome c and reactive oxygen species (ROS) involved in apoptosis signalling and cell death should be investigated to authenticate the effects of this nanosystem on the mitochondrial and angiogenesis in squamous cell carcinoma.

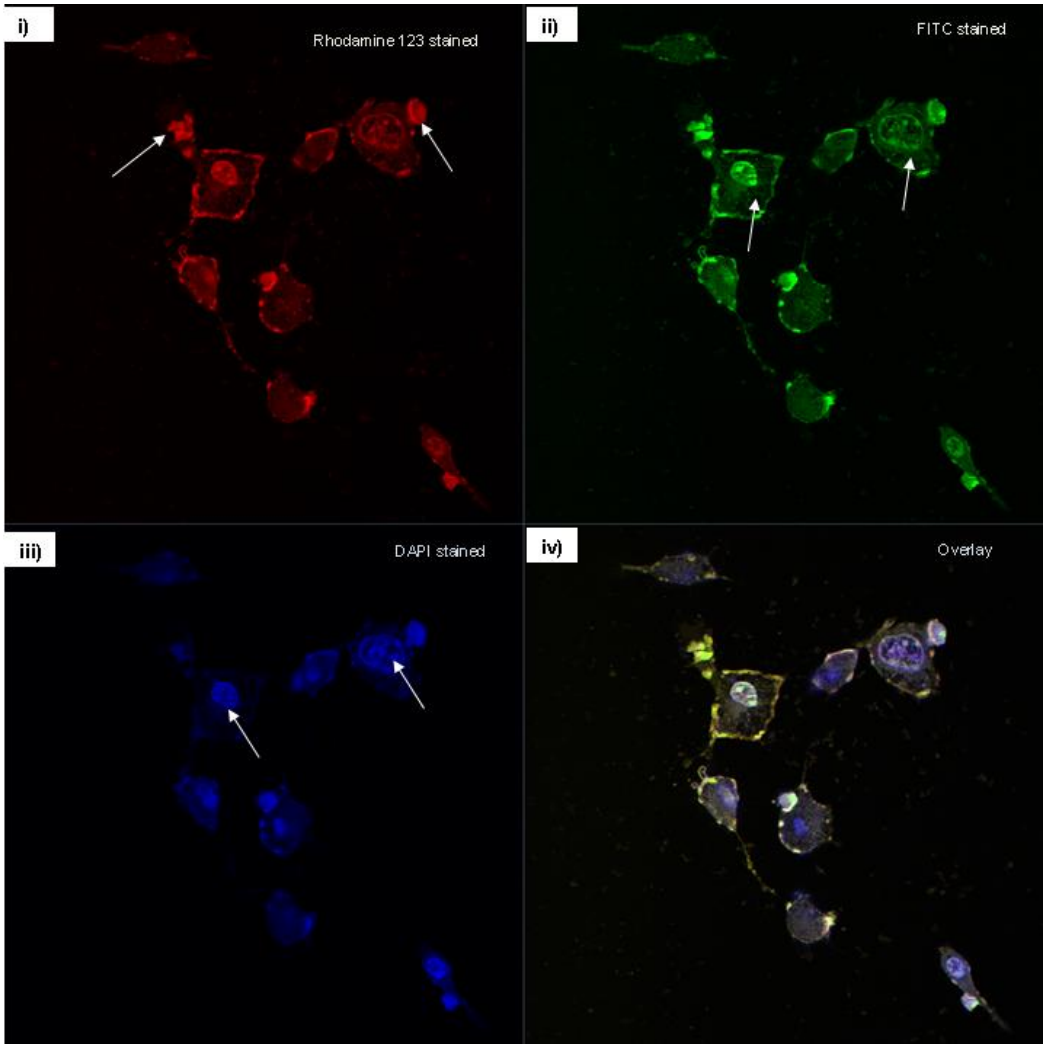


Figure 5.11: Sub-cellular Colocalization of FA decorated nanoparticles. (i) KYSE-30 cells treated with nanoformulation and stained with mitochondrial specific dye rhodamine 123 (ii) treated cells stained with FITC-labelled FA-decorated nanoparticles (iii) treated cells' nucleus stained with DAPI and (iv) merged confocal image of i – iii showing co-localization of the FA-decorated nanoparticles in both the nucleus and the mitochondrial in KYSE-30 cells.

5.3.4. Polymer Cyto-compactibility and Anti-proliferation Effects of FA-linked Nanoparticles

Within the sprouting process of angiogenesis, endothelial cells undergo proliferation. Proliferation assay are highly reproducible, easy to perform and generates precise, accurate and quantifiable data *in vitro* (Staton et al., 2009). Alamar blue assay was performed to evaluate the cyto-compactibility of native nanoparticles and the anti-angiogenic efficacy of ENT-loaded

nanoparticles as well as the FA functionalized ENT-loaded nanoparticles as presented in Figure 5.12. Across the tested formulations, the grafted polymer show cell viability above 80% which is an indices for good cellular biocompatibility (Mavuso et al., 2016). Meanwhile, at a higher concentration of 1000 µg/mL, cell viability reduced to about 63% when compared to the control (untreated cells). This could possibly due to the overall partial positive charge of the conjugated polymer network (Vega-Villa et al., 2008), an effect that can be harnessed in cancer nanomedicines. Interestingly, both ENT-loaded and FA functionalized nanoparticles showed high toxicity to KYSE-30 cells when compared to the control particularly at concentration above 250 µg/mL. At nanoparticles concentration of 500 µg/mL, ENT-loaded nanoparticles show 26.87% inhibition as opposed to 36.69% inhibition when functionalized with FA. Similarly, ENT-loaded nanoparticles have proliferation inhibition of 61.68% at 1000 µg/mL while FA functionalized ENT-loaded nanoparticles show an inhibition of 64.71%. Therefore, our results show that the conjugated polymers are cytocompactible as efficient delivery cargo for ENT in KYSE-30 cells and functionalization with FA aggravates the anti-proliferating effects of ENT when loaded into PEG-PEI-g-CHT nano-carriers.

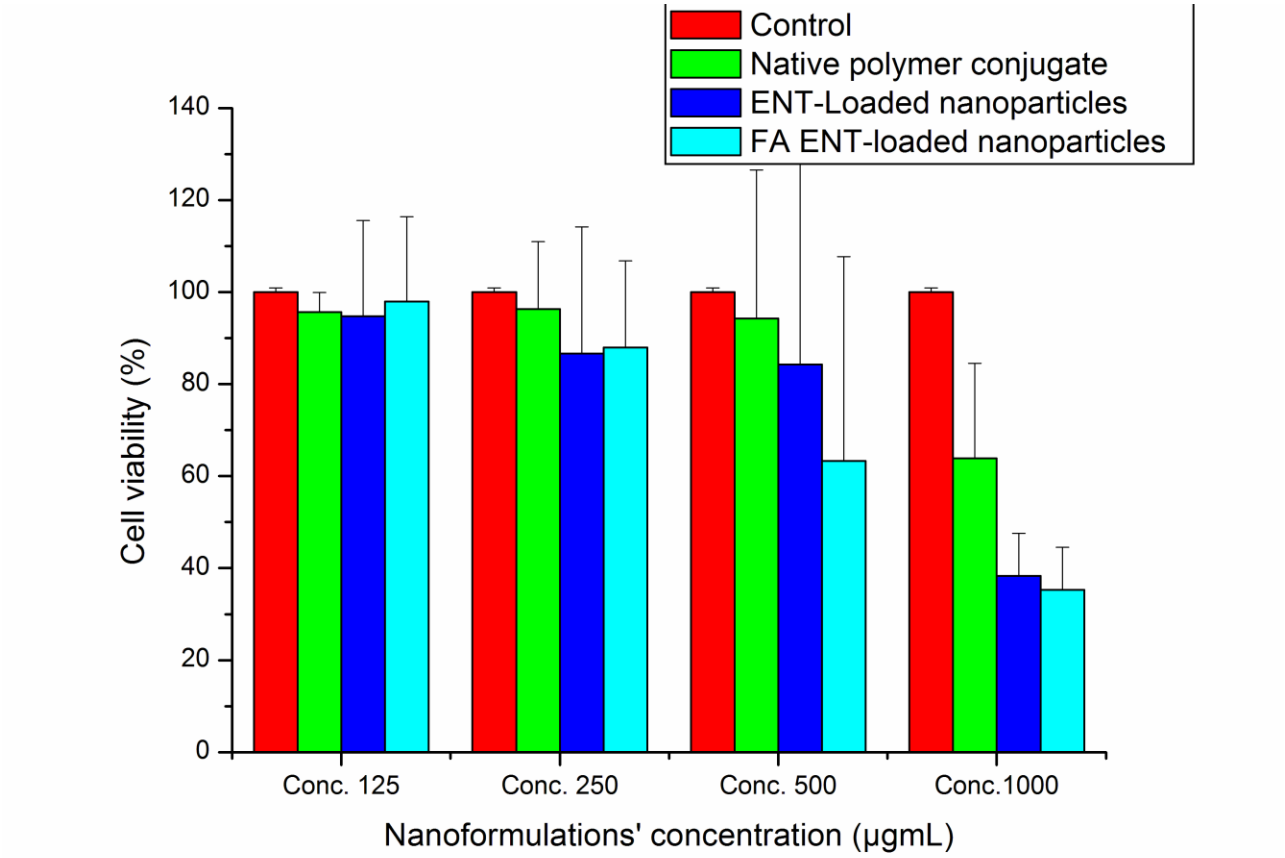


Figure 5.12: Cell viability/proliferation of treated and untreated oesophageal squamous cell carcinoma (KYSE-30) after exposure to 24 hours of the nanoformulations at varying concentrations. (i) Red column is the control without treatment (ii) pink column are cells treated with the native polymer conjugate (iii) the blue column represents cells treated with ENT-loaded nanoparticles and (iv) cyan column represents FA-decorated ENT-loaded nanoparticles.

Intact nuclear morphology is an indicator of the health status of the cell (Leist and Jäättelä, 2001). Chromatin and nuclear condensation, DNA fragmentation with intact plasma membrane are marks of apoptotic cell death, whereas, in necrosis, nuclei are swollen and leaky with early degradation and erosion of the plasma membrane (Lovrić et al., 2005b). To further investigative the anti-angiogenic potential of the FA functionalised nanoparticles, the nucleus of KYSE-30 cells were stained with DAPI as a marker of angiogenesis. As a positive control, cells stained with DAPI but untreated with nanoparticles were employed. As shown in Figure 5.13, stained nuclei with DAPI revealed shrinkage and deformation of nuclei with chromatin aggregation, indicating nuclear damage induced by FA-linked nanoparticles after 24 hours pre-incubation

(Figure 5.13 (ii)) compared to the nucleus of untreated KYSE-30 cells (Figure 5.13 (i)). The plasma membrane of cells treated with FA-decorated ENT-loaded nanoparticles was mostly degraded, an indication of necrosis as compared to the control. Thus, FA-decorated ENT-loaded nanoparticles showed apoptotic and necrotic potential which are indicators of proliferation inhibition thereby anti-angiogenic on KYSE-30 cells. Meanwhile, biochemical indicators of nuclear damage and cell death, such as caspases' activities, should be monitored to justify the findings of this report.

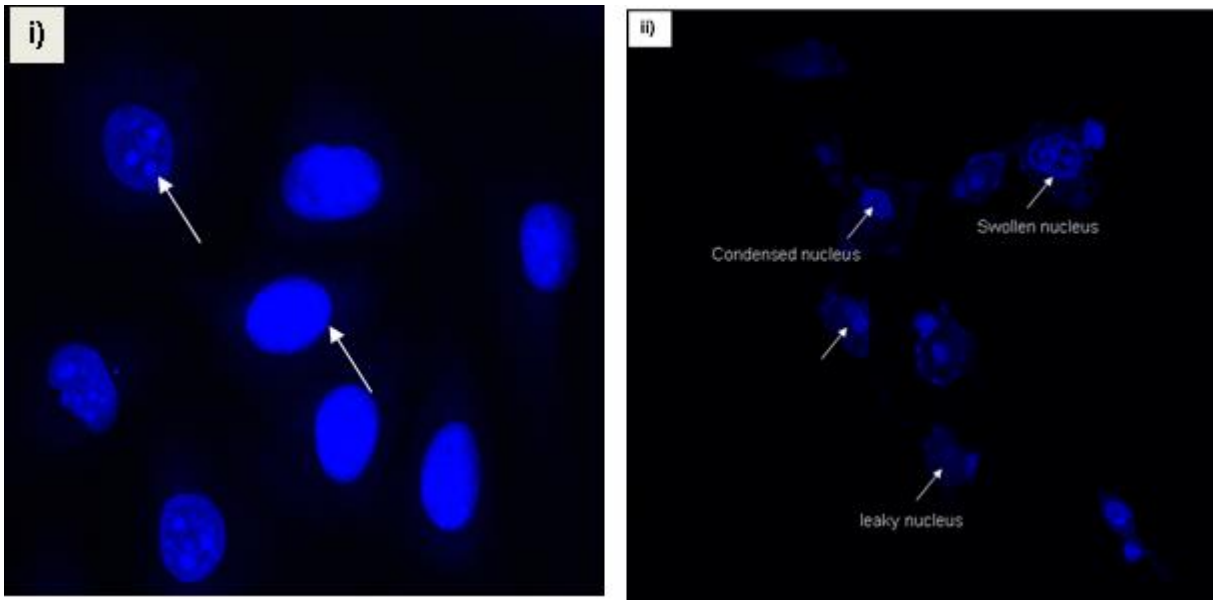


Figure 5.13: Confocal microscopic image of KYSE-30 nucleus. (i) Untreated KYSE-30 nucleus showing the intact morphology and chromatin materials within the nucleus. (ii) Necrotic and apoptotic effects of FA decorated nanoparticles on the nucleus of KYSE-30 cells. Apoptotic nuclei were swollen while necrotic nuclei were condensed and lysed with leaky nuclear materials.

5.3.5. FA-decorated ENT-loaded Nanoparticles Inhibit KYSE-30 Cells' Motility *In vitro*

During the process of angiogenesis, endothelial cells are stimulated to degrade the basement membrane and migrate into the perivascular stroma in response to a gradient of angiogenesis inducing factors including bFGF and VEGF. Thus, an increase in overall endothelial cell motility can also be a measure of an angiogenic response (Staton et al., 2009). Cell motility is of

particular interest in the design of anti-cancer therapeutics, as cell migration is required for both tumor invasion and tumor angiogenesis (Goodwin, 2007). As presented in Figure 5.14, FA-decorated ENT-loaded nanoparticles show an increased migration inhibition of KYSE-30 cells than cells treated with ENT-loaded nanoparticles when compared to the control group. These could be due to the targeted and specific binding of FA to the folate-receptors on the surface of KYSE-30 cells which in turn influenced the intake and internalization of the ENT-loaded nanoparticles thereby influences the anti-angiogenic potential of ENT on KYSE-30 cells. FA-functionalized nanoparticles showed up to 74.12% inhibition to KYSE-30 cells motility while about 71.72% inhibition was recorded pre-incubation with the un-functionalized nanoparticles (Figure 5.14(a)). To further validates the inhibitory efficacy of ENT-loaded nanoparticles as well the FA functionalised nanoparticles, migrated KYSE-30 cells after pre-incubation with the nanoformulations were imaged and the number of migrated cells were counted using imageJ (data not presented). As shown in Figure 5.14(b), the numbers of migrated KYSE-30 cells were reduced when treated with FA-functionalized nanoparticles than the unfunctionalized ENT-loaded nanoparticles in comparison to the control cells. Thus, FA played an important role in facilitating the direct target of ENT-loaded nanoparticles thereby enhancing its anti-angiogenic response in curtailing the migration of KYSE-30 cells.

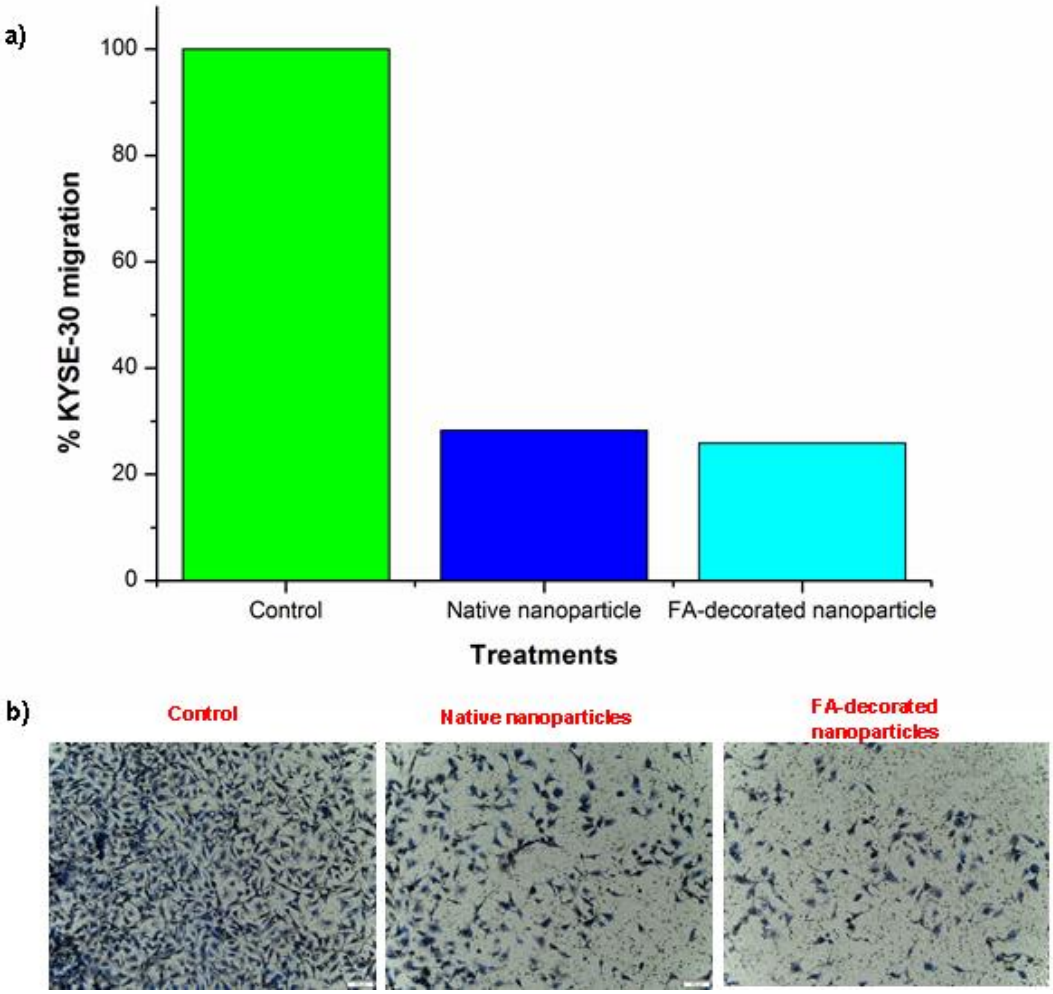


Figure 5.14: The result of migration assay of KYSE-30 cells with 1000 µg/mL pre-incubation with native ENT-loaded thenanoparticles and Folate-decorated ENT-loaded nanoparticles. Untreated KYSE-30 cells containing FBS free culture media only serve as the control. (a) Both treatments showed inhibition to KYSE-30 migration at about 74.12% and 71.72% for FA-decorated nanoparticles and unfunctionalized ENT-loaded nanoparticles respectively. (b) migrated KYSE-30 cells were fixed with 4% paraformaldehyde and stained with trypan blue and subsequently imaged using fluorescent microscopy.

5.4. Concluding remarks

In summary, our findings showed the targeting potential of FA functionalized nanoparticles on an established oesophageal squamous cell carcinoma (KYSE-30). FA-decorated nanoparticles were successfully internalized into the cellular compartments and localized within the nucleus and mitochondrial. While shape, size and overall surface charge of nanoparticles could enhance

cellular uptake and internalization, FA-decorated nanoparticles probably bind preferentially to the over-expressed folate receptor on KYSE-30 cells and are internalized through receptor-mediated endocytosis. Changing pH conditions facilitates the release of ENT within the nanoparticulate network with more ENT release at lower acidic pH. FA-decorated ENT-loaded nanoparticles showed apoptotic and necrotic potential which are key indicators of proliferation inhibition thereby anti-angiogenic on KYSE-30 cells. Migrations of KYSE-30 cells were inhibited after pre-incubation with FA functionalized nanoparticles in comparison to the control and the unfunctionalized ENT-loaded nanoparticles. Thus, FA played an important role in facilitating the direct targeting of ENT-loaded nanoparticles thereby enhances the delivery of endostatin and improves its anti-angiogenic response *in vitro*. Meanwhile, further research is needed to fully understand and ascertain the mechanism of the anti-proliferation potential of both FA decorated and unfunctionalized ENT-loaded nanoparticles on oesophageal squamous cell carcinoma.

5.7. References

Alkilany, A.M., Nagaria, P.K., Hexel, C.R., Shaw, T.J., Murphy, C.J., Wyatt, M.D., 2009. Cellular uptake and cytotoxicity of gold nanorods: molecular origin of cytotoxicity and surface effects. Small Weinh. Bergstr. Ger. 5, 701–708.

Arvizo, R.R., Miranda, O.R., Thompson, M.A., Pabelick, C.M., Bhattacharya, R., Robertson, J.D., Rotello, V.M., Prakash, Y.S., Mukherjee, P., 2010. Effect of nanoparticle surface charge at the plasma membrane and beyond. Nano Lett. 10, 2543–2548.

Chen, B., Le, W., Wang, Y., Li, Z., Wang, D., Ren, L., Lin, L., Cui, S., Hu, J.J., Hu, Y., Yang, P., Ewing, R.C., Shi, D., Cui, Z., 2016. Targeting Negative Surface Charges of Cancer Cells by Multifunctional Nanoprobes. Theranostics 6, 1887–1898.

Cho, E.C., Xie, J., Wurm, P.A., Xia, Y., 2009. Understanding the role of surface charges in cellular adsorption versus internalization by selectively removing gold nanoparticles on the cell surface with a I2/KI etchant. Nano Lett. 9, 1080–1084.

Cho, K., Wang, X., Nie, S., Chen, Z. (Georgia), Shin, D.M., 2008. Therapeutic Nanoparticles for Drug Delivery in Cancer. Clin. Cancer Res. 14, 1310–1316.

Das, M., Sahoo, S.K., 2012. Folate decorated dual drug loaded nanoparticle: role of curcumin in enhancing therapeutic potential of nutlin-3a by reversing multidrug resistance. PloS One 7, e32920.

De Jong, W.H., Borm, P.J., 2008. Drug delivery and nanoparticles: Applications and hazards. Int. J. Nanomedicine 3, 133–149.

Duan, X., Li, Y., 2013. Physicochemical Characteristics of Nanoparticles Affect Circulation, Biodistribution, Cellular Internalization, and Trafficking. Small 9, 1521–1532.

Favi, P.M., Gao, M., Johana Sepúlveda Arango, L., Ospina, S.P., Morales, M., Pavon, J.J., Webster, T.J., 2015a. Shape and surface effects on the cytotoxicity of nanoparticles: Gold nanospheres versus gold nanostars. J. Biomed. Mater. Res. A 103, 3449–3462.

Favi, P.M., Valencia, M.M., Elliott, P.R., Restrepo, A., Gao, M., Huang, H., Pavon, J.J., Webster, T.J., 2015b. Shape and surface chemistry effects on the cytotoxicity and cellular uptake of metallic nanorods and nanospheres. J. Biomed. Mater. Res. A 103, 3940–3955.

Feng, M., Lee, D., Li, P., 2006. Intracellular uptake and release of poly(ethyleneimine)-co-poly(methyl methacrylate) nanoparticle/pDNA complexes for gene delivery. Int. J. Pharm. 311, 209–214.

Folkman, J., 1971. Tumor angiogenesis: therapeutic implications. N. Engl. J. Med. 285, 1182–1186.

Folkman, J., 2006. Antiangiogenesis in cancer therapy--endostatin and its mechanisms of action. Exp. Cell Res. 312, 594–607.

Fröhlich, E., 2012. The role of surface charge in cellular uptake and cytotoxicity of medical nanoparticles. Int. J. Nanomedicine 7, 5577–5591.

Gao, J.-Q., Zhao, Q.-Q., Lv, T.-F., Shuai, W.-P., Zhou, J., Tang, G.-P., Liang, W.-Q., Tabata, Y., Hu, Y.-L., 2010. Gene-carried chitosan-linked-PEI induced high gene transfection

efficiency with low toxicity and significant tumor-suppressive activity. Int. J. Pharm. 387, 286–294.

Gerweck, L.E., Seetharaman, K., 1996. Cellular pH gradient in tumor versus normal tissue: potential exploitation for the treatment of cancer. Cancer Res. 56, 1194–1198.

Goodwin, A.M., 2007. In vitro assays of angiogenesis for assessment of angiogenic and anti-angiogenic agents. Microvasc. Res. 74, 172–183.

Hattori, Y., Maitani, Y., 2004. Enhanced in vitro DNA transfection efficiency by novel folate-linked nanoparticles in human prostate cancer and oral cancer. J. Control. Release Soc. 97, 173–183.

Hauck, T.S., Ghazani, A.A., Chan, W.C.W., 2008. Assessing the effect of surface chemistry on gold nanorod uptake, toxicity, and gene expression in mammalian cells. Small Weinh. Bergstr. Ger. 4, 153–159.

Hendricks, D., Parker, M.I., 2002. Oesophageal cancer in Africa. IUBMB Life 53, 263–268.

Jain, A., Jain, A., Garg, N.K., Tyagi, R.K., Singh, B., Katare, O.P., Webster, T.J., Soni, V., 2015. Surface engineered polymeric nanocarriers mediate the delivery of transferrin-methotrexate conjugates for an improved understanding of brain cancer. Acta Biomater. 24, 140–151.

Jia, L., Li, Z., Zhang, D., Zhang, Q., Shen, J., Guo, H., Tian, X., Liu, G., Zheng, D., Qi, L., 2013. Redox-responsive catiomer based on PEG-ss-chitosan oligosaccharide-ss-polyethylenimine copolymer for effective gene delivery. Polym Chem 4, 156–165.

Jiang, H.-L., Kwon, J.-T., Kim, E.-M., Kim, Y.-K., Arote, R., Jere, D., Jeong, H.-J., Jang, M.-K., Nah, J.-W., Xu, C.-X., Park, I.-K., Cho, M.-H., Cho, C.-S., 2008. Galactosylated poly(ethylene glycol)-chitosan-graft-polyethylenimine as a gene carrier for hepatocyte-targeting. J. Controlled Release 131, 150–157.

K, B., Kw, L., 2006. Chitosan nanoparticles for oral drug and gene delivery. Int. J. Nanomedicine 1, 117–128.

Kato, Y., Ozawa, S., Miyamoto, C., Maehata, Y., Suzuki, A., Maeda, T., Baba, Y., 2013. Acidic extracellular microenvironment and cancer. Cancer Cell Int. 13, 89.

Kim, Y.-M., Hwang, S., Kim, Y.-M., Pyun, B.-J., Kim, T.-Y., Lee, S.-T., Gho, Y.S., Kwon, Y.-G., 2002. Endostatin Blocks Vascular Endothelial Growth Factor-mediated Signaling via Direct Interaction with KDR/Flk-1. J. Biol. Chem. 277, 27872–27879.

Koizumi, T., Shirakura, H., Kumagai, H., Tatsumoto, H., Suzuki, K.T., 1996. Mechanism of cadmium-induced cytotoxicity in rat hepatocytes: Cadmium-induced active oxygen-related permeability changes of the plasma membrane. Toxicology 114, 125–134.

Lee, R.J., Low, P.S., 1995a. Folate-mediated tumor cell targeting of liposome-entrapped doxorubicin in vitro. Biochim. Biophys. Acta BBA - Biomembr. 1233, 134–144.

Lee, R.J., Low, P.S., 1995b. Folate-mediated tumor cell targeting of liposome-entrapped doxorubicin in vitro. Biochim. Biophys. Acta BBA - Biomembr. 1233, 134–144.

Leist, M., Jäättelä, M., 2001. Four deaths and a funeral: From caspases to alternative mechanisms. Nat. Rev. Mol. Cell Biol. 2, 589–598.

Li, H.-L., He, Y.-X., Gao, Q.-H., Wu, G.-Z., 2014. Folate‐polyethylene glycol conjugated carboxymethyl chitosan for tumor‐targeted delivery of 5‐fluorouracil. Mol. Med. Rep. 9, 786–792.

Liu, X., Huang, N., Li, H., Jin, Q., Ji, J., 2013. Surface and Size Effects on Cell Interaction of Gold Nanoparticles with Both Phagocytic and Nonphagocytic Cells. Langmuir 29, 9138–9148.

Lovrić, J., Cho, S.J., Winnik, F.M., Maysinger, D., 2005. Unmodified cadmium telluride quantum dots induce reactive oxygen species formation leading to multiple organelle damage and cell death. Chem. Biol. 12, 1227–1234.

Lu, H., Dai, Y., Lv, L., Zhao, H., 2014. Chitosan-Graft-Polyethylenimine/DNA Nanoparticles as Novel Non-Viral Gene Delivery Vectors Targeting Osteoarthritis. PLoS ONE 9.

Mavuso, S., Choonara, Y.E., Marimuthu, T., Kumar, P., du Toit, L.C., Kondiah, P.P.D., Pillay, V., 2016. A dual pH/Redox responsive copper-ligand nanoliposome bioactive complex for the treatment of chronic inflammation. Int. J. Pharm. 509, 348–359.

Murugan, K., Choonara, Y.E., Kumar, P., Bijukumar, D., du Toit, L.C., Pillay, V., 2015. Parameters and characteristics governing cellular internalization and trans-barrier trafficking of nanostructures. Int. J. Nanomedicine 10, 2191–2206.

Ogris, M., Walker, G., Blessing, T., Kircheis, R., Wolschek, M., Wagner, E., 2003. Tumor-targeted gene therapy: strategies for the preparation of ligand-polyethylene glycol-polyethylenimine/DNA complexes. J. Control. Release Soc. 91, 173–181.

Qiu, B., Ji, M., Song, X., Zhu, Y., Wang, Z., Zhang, X., Wu, S., Chen, H., Mei, L., Zheng, Y., 2012. Co-delivery of docetaxel and endostatin by a biodegradable nanoparticle for the synergistic treatment of cervical cancer. Nanoscale Res. Lett. 7, 666.

Ramasamy, R., 2015. Vibrational Spectroscopic Studies of Imidazole. Armen. J. Phys. 8, 51–55.

Ramesh, R., Amreddy, N., Muralidharan, R., Babu, A., Mehta, M., Johnson, E., Munshi, A., Zhao, Y., 2015. Tumor-targeted and pH-controlled delivery of doxorubicin using gold nanorods for lung cancer therapy. Int. J. Nanomedicine 6773.

Ruan, S., Yuan, M., Zhang, L., Hu, G., Chen, J., Cun, X., Zhang, Q., Yang, Y., He, Q., Gao, H., 2015. Tumor microenvironment sensitive doxorubicin delivery and release to glioma using angiopep-2 decorated gold nanoparticles. Biomaterials 37, 425–435.

Sarkar, K., Debnath, M., Kundu, P., 2013. Preparation of low toxic fluorescent chitosan-graft-polyethyleneimine copolymer for gene carrier. Carbohydr. Polym. 92, 2048–2057.

Seda Tı˘glı Aydın, R., Pulat, M., 2012. 5-Fluorouracil Encapsulated Chitosan Nanoparticles for pH-Stimulated Drug Delivery: Evaluation of Controlled Release Kinetics. J. Nanomater. 2012, e313961.

Staton, C.A., Reed, M.W.R., Brown, N.J., 2009. A critical analysis of current in vitro and in vivo angiogenesis assays. Int. J. Exp. Pathol. 90, 195–221.

Thorek, D.L.J., Tsourkas, A., 2008. Size, charge and concentration dependent uptake of iron oxide particles by non-phagocytic cells. Biomaterials 29, 3583–3590.

Torchilin, V.P., Lukyanov, A.N., 2003. Peptide and protein drug delivery to and into tumors: challenges and solutions. Drug Discov. Today 8, 259–266.

Vega-Villa, K.R., Takemoto, J.K., Yáñez, J.A., Remsberg, C.M., Forrest, M.L., Davies, N.M., 2008. Clinical toxicities of nanocarrier systems. Adv. Drug Deliv. Rev. 60, 929–938.

Verma, A., Stellacci, F., 2010. Effect of Surface Properties on Nanoparticle–Cell Interactions. Small 6, 12–21.

Wang, M., Thanou, M., 2010. Targeting nanoparticles to cancer. Pharmacol. Res., 62, 90–99.

Wu, W., Zheng, Y., Wang, R., Huang, W., Liu, L., Hu, X., Liu, S., Yue, J., Tong, T., Jing, X., 2012. Antitumor activity of folate-targeted, paclitaxelloaded polymeric micelles on a human esophageal EC9706 cancer cell line. Int. J. Nanomedicine 7, 3487–3502.

Xiao, K., Liu, Q., Li, H., Xia, Q., Liu, Y., 2015. Role of surface charge in determining the biological effects of CdSe/ZnS quantum dots. Int. J. Nanomedicine 7073.

Yao, X., Wang, Y., Qin, F., Lu, M., Zhang, Y., Jiang, M., Tan, H., 2015. pH-responsive glycol chitosan-cross-linked carboxymethyl-β-cyclodextrin nanoparticles for controlled release of anticancer drugs. Int. J. Nanomedicine 7359.

Yuan, S., Fu, Y., Wang, X., Shi, H., Huang, Y., Song, X., Li, L., Song, N., Luo, Y., 2008. Voltage-dependent anion channel 1 is involved in endostatin-induced endothelial cell apoptosis. Am. Soc. Exp. Biol. 22, 2809–2820.

Zeng, X., Morgenstern, R., Nyström, A.M., 2014. Nanoparticle-directed sub-cellular localization of doxorubicin and the sensitization breast cancer cells by circumventing GST-Mediated drug resistance. Biomaterials 35, 1227–1239.

Zou, S.M., Erbacher, P., Remy, J.S., Behr, J.P., 2000. Systemic linear polyethylenimine (L-PEI)-mediated gene delivery in the mouse. J. Gene Med. 2, 128–134.

CHAPTER 6

A NOVEL DUAL PEPTIDE-ENHANCED ENDOSTATIN-LOADED NANO-CONSTRUCT FOR TARGETED ANTI-ANGIOGENIC EFFECTS IN SQUAMOUS CELL CARCINOMA

6.1. Introduction

Cancer often has specific molecular alterations of signal transduction pathway or of other molecules linked to the proliferation and wide spreading of tumour cells. Peptides as targeting ligands of nanoparticles are becoming even more relevant in cancer research and many are developed from different larger proteins or ligands. Most often, targeting peptides are conjugated with other functional peptides or conjugated with other nanoparticles to augment drug delivery both *in vitro and in vivo* (Zhang et al., 2012). The current identification of tumor homing peptides through phage display technology has opened a new strategy for targeted therapy of SCC diseases. The use of homing peptides in targeted SCC therapy is due to the fact that their properties are readily combined with that of a toxin or a pro-drug molecule. Targeted therapy restricts the toxic effects of a drug to the malignant tissues, thereby increasing its efficacy and decreasing the undesired side-effects of the drug to normal cells or tissues (Enbäck and Laakkonen, 2007).

Two cellular targets that are often exploited in cancer nanomedicine include the cancer cells and the endothelial cells of the tumor. Specific receptors identified for targeting the endothelial cells of the tumor that have been researched to date are the vascular endothelial growth factor receptors (VEGFR), the integrins (α4β3, α5β1), the vascular cell adhesion molecule-1 (VCAM-1), and the matrix metalloproteinase (MMPs). Using these strategies, targeted nanosystems are

designed to specifically target and eliminate angiogenic blood vessels and thereby kill tumor cells indirectly (Danhier et al., 2012; Sznol and Davis, 2002).

The use of small peptides as targeting moieties has gained enormous considerations due to their smaller size than antibodies, low immunogenicity, their large scale synthesis by chemical methods, ability to be incorporated into certain delivery cargos and their ability to achieve high specificity (Pan et al., 2013; Wu et al., 2004). LyP-1 is a nine-amino-acid cyclic peptide (CGNKRTRGC) and was identified and isolated from human MDA-MB-435 breast cancer xenografts using the phage display biopanning technique (Wigle et al., 2002). Aside from the recognition of tumor-associated lymphatic vessels, LyP-1 identifies a marker that is shared by both the tumor cells and the tumor endothelial cells similar to other vascular homing peptides (Enbäck and Laakkonen, 2007; Wigle et al., 2002). It is often found to accumulate in the nucleus of both the primary tumor cell as well as their metastatic lesions after intravenous injection. LyP-1, binds specifically to the lymphatic vessels in certain tumors, but not to the lymphatics of normal tissues (Wigle et al., 2002). Its uniqueness as a homing peptide lies in its ability to cause the apoptosis of the cells to which it binds in addition to its homing and internalization by the lymphatic endothelial cells and tumor cells. LyP-1 binds to a cell surface form of mitochondrial protein, p32 which serves as its receptor (Sugahara et al., 2009).

The screening of all peptides homing to a mouse model of SCC resulted in the identification of CGKRK (designated as PENT in this study). It is a pentapeptide that can home to all types of tumor tested during the experiment and it is capable of penetrating the nucleus of the targeted cell. Its internalization has been proposed to be as a result of its binding to heparan sulphates at the surface of the cell (Laakkonen et al., 2004). Both LyP-1 and CGKRK have been shown to inhibit tumor growth in a tumor-bearing mouse when conjugated with fluorescein and doxorubicin as well as serve as tumor imaging tools (Enbäck and Laakkonen, 2007).

Endostatin (ENT) as a potent peptide inhibitor of angiogenesis is under clinical trials and development with promising prospective as an anti-cancer drug (Torchilin and Lukyanov, 2003). ENT is a proteolytic C-terminal fragment of collagen XVIII with a molecular weight of approximately 20 kDa. ENT has received the greatest attention for its broad-spectrum and low toxicity relative to other angiogenic inhibitors (Folkman, 2006). Previous reports have shown that ENT inhibit endothelial cell proliferation, migration, and angiogenesis (Kim et al., 2002; Zheng, 2009). Meanwhile, there are a number of clinical challenges that mitigate its application including high dosage form to obtain a therapeutic effect, high price, short circulation half-life and instability (Qiu et al., 2012). Thus, strategic intervention through the incorporation of ENT into biodegradable polymers as delivery nano-constructs could be employed to overcome these challenges and improve its therapeutic effects. More so, surface functionalization of such ENT-loaded nanoparticles will enhance the targeted and optimum delivery of their payloads at the disease site.

In this study, both LyP-1 and PENT were employed as homing peptides to facilitate specific and direct targeting of ENT to the nucleus and mitochondrial of KYSE-30 cells for anti-angiogenic effects. Similarly, VEFG-C as a potent marker of lymphatic angiogenesis and MMP2 which is critical for cell invasion and metastasis in tumorigenesis, were targeted using our designed peptide-enhanced ENT-loaded nanosystem for anti-angiogenic therapy in SCC nanomedicine.

6.2. Materials and Methods

6.2.1. Materials

LyP-1 [CC(Acm)GNKRTRGC(Acm)] and lysine rich pentapeptide (CGKRK) were purchased from Peptron, Inc. Yuseong-gu, Daejeon, South Korea having 98% HPLC purity. Low molecular weight chitosan (LMW, DE=75-85%), branched polyethylenimine (PEI) (Mw=25KDa), human

recombinant endostatin (MW=22kDa), 1-ethyl-3-(3-dimethylaminopropyl) carbodiimide hydrochloride (EDC), N-hydroxysuccinimide (NHS), sodium tripolyphosphate (TPP) (MW=367.86 g/mol), poly(vinyl alcohol) (PVA) (MW=85,000 g/mol), triethylamine, dimethylformamide (DMF) and Fluorescein isothiocyanate (FITC) (MW=389.382 g/mol) were purchased from Sigma-Aldrich Co., Ltd. (St. Louis, MO, USA). Functionalized poly (ethylene) glycol (NH_2-PEG-COOH, Mw=2100 g/mol) was from NANOCS (New York, NY, USA). KYSE-30, RPMI, HAM's F12, Fetal Bovine Serum (FBS), pentamycin/streptomycin were from Life Bioscience (Oakleigh, VIC, Australia). All other solvents and reagents were of analytical grade unless stated otherwise.

6.2.2. Methods

6.2.2.1. Preparation of Peptide-PEG-PEI-g-CHT Endostatin loaded nanoparticles

Following our preliminary findings (Chapters 3, 4 and 5), optimized LyP-1/PENT functionalized ENT-loaded nanoparticles was synthesized.

6.2.2.1.1. Synthesis of CHI-g-PEI conjugates

CHT was grafted to PEI using a modified method described by Gao and co-workers (Gao et al., 2010) by employing 1-carbonyldiimidazole (CDI) as a cross linker. Briefly, 1.2153 mg/mL CHT concentration was prepared in 0.5% acetic and the pH adjusted to 4.97 using 0.2 M sodium acetate buffer. 50 mL (0.000834 M) CDI solution was added to the CHT solution and stirred for 1 hour at room temperature to activate the amine group in the CHT solution. Thereafter, 0.25 %v/v of branched PEI was dropwisely added at a molar ratio of CHT amine and PEI concentration of 2:1. The reaction mixture was left to polymerized for 24 hours and dialysed using a dialysis membrane (MW=12 000 kDa) over double distilled water (DDW) for 24 hours. Meanwhile, 0.1mM fluorescein isothiocyanate (FITC) dissolved in dimethyl sulfoxide (DMSO) was mixed with the reaction mixture of CHT-g-PEI solution at room temperature on a shaker for

12 hours for complete conjugation with the amine of PEI as previously described (Feng et al., 2006). Unbound FITC was removed by dialysis over DDW for 24 hours. The final FITC labelled CHT-g-PEI conjugate was then collected by lyophilization over 24 hours.

6.2.2.1.2. Synthesis of Peptide-Enhanced PEG-PEI-CHT FITC labelled conjugates

Prior to the synthesis of the LyP-1-PEG-PEI-CHT and PENT- PEG-PEI-CHT conjugates, LyP-1 and PENT were grafted onto the free amine component of a bifunctional PEG (NH_2-PEG-COOH) using the NHS/EDC. Briefly, the carboxyl group of 20 mg NH_2-PEG-COOH dissolved in 20 mL 0.1 M MES buffer was activated using 5 mg EDC and 5 mg NHS under stirring for 15 minutes. Subsequently, 1.3 mg/mL LyP-1 or PENT in PBS, pH 7.0, was added into the activated solution and the reaction mixture was left overnight.

6.2.2.1.2.1. Cyclization of conjugated LyP-1-PEG-NH_2 conjugates

In order to form cyclic peptide after being conjugated to NH_2-PEG-COOH, the thiol of Cys^2 and Cys^{10} was protected with acetamidomethyl (Acm), which could conjugate with each other during deprotection process. Thus, cyclic LyP-1 modified construct (LyP-1-PEG- NH_2) was synthesized by Acm deprotection at Cys^2 and Cys^{10} using iodine reagent (Luo et al., 2010a). Briefly, LyP-1-PEG-NH_2 construct was mixed with 0.2 mol/L citric acid at a concentration of 1 mg/mL. 0.1 mL of 1 mol/L hydrazine hydrochloride was added to the mixture. To the resulting mixture 4 mL iodic methanol solution (5mmol/L) was immediately added and stirred for 1 hour at room temperature. Thereafter 1mol/L ascorbic acid was added dropwise to the solution until the colour of mixture became clear. Cyclic LyP-1-PEG- NH_2 particles were collected by centrifugation at 14,000 rpm at 4°C for 45 minutes.

6.2.2.1.2.2. Preparation of FITC labelled LyP-1/PENT-PEG-NH_2 conjugates

3.08 µmol FITC, dissolved in DMF was added onto the conjugated LyP-1-PEG-NH_2 or PENT-PEG-NH_2 conjugates followed by the addition of 100µL trimethylamine under mild stirring for 48 hours at room temperature. The reaction mixture was then dialyzed against double distil water (DDL) for 12 hours respectively and the resultant FITC labelled LyP-1-PEG-NH_2 or PENT-PEG-NH_2 conjugates were kept at 4°C until further use.

6.2.2.1.2.3. Preparation of FITC labelled Peptide Enhanced PEG-PEI-CHT conjugates

The amino group of preformed CHT-PEI was activated using CDI chemistry for 1 hour as previously discussed. Subsequently, either LyP-1-PEG-NH_2 or PENT-PEG-NH_2 conjugates were added onto the amino activated CHT-PEI solution in order to link with the terminal amino group of LyP-1-PEG-NH_2 or PENT-PEG-NH_2 respectively. The mixture was then left to react for 12 hours at 4^0C and 12 hours at 25°C for complete polymerization as previously described (Chen et al., 2015).

6.2.2.2. Endostatin Entrapment and synthesis of Peptide Enhanced ENT-loaded nanoparticles

Ionotropic gelation technique was employed for the synthesis of either LyP-1 or PENT functionalized ENT-loaded nanoparticles. Briefly, 0.5 mg/mL ENT solution was mixed with the solution mixture of FITC labelled LyP-1-PEG-PEI-CHT conjugates under mild stirring for 1 minute. 0.1 %w/v TPP as a polyanionic agent was drop-wisely added to the ENT-loaded mixture and 0.1% w/v polyvinyl alcohol (PVA) was added as surfactant. The formation of an opaque and turbid solution confirmed the formation of endostatin loaded nanoparticles. The synthesized LyP-1 functionalized ENT-loaded PEG-PEI-CHT nanoparticles were then allowed to gelate for 1 hour under mild stirring and the resultant mixture was centrifuged at 5000 rpm for 1 hour.

Nanoparticles in the pellet were re-suspended in DDW and dried powder nanoparticles were collected by lyophilization over 24 hours and stored at -20°C until further analysis. The same procedure was employed for the synthesis of PENT modified FITC labelled PEG-PEI-CHT ENT-loaded nanoparticles.

6.2.2.3. Characterization of Conjugated Peptide-Enhanced PEG-PEI-CHT Nanoparticles

6.2.2.3.1. Determination of Chemical and Functional Transformations using Fourier Transform Infrared Spectroscopy

The vibrational transitions in the chemical structures of CHT-PEI, LyP-1-PEG-NH_2, PENT-PEG-NH_2, ENT-loaded LyP-1/PENT functionalized PEG-PEI-CHT nanoparticles and the native polymers were evaluated using Fourier transform infrared (FTIR) spectroscopy (PerkinElmer Inc., Waltham, Massachusetts, USA). Samples were placed on a single bounce diamond crystal and processed by a universal attenuated total reflectance (ATR) polarization accessory, at a resolution of 4 cm^{-1}, with the spectrum ranging from 4000 to 650 cm^{-1}.

6.2.2.3.2. Structural Modifications using Nuclear Magnetic Resonance Spectroscopy

Nuclear Magnetic Resonance (NMR) spectra were recorded for PEI-CHT, LyP-1-PEG-NH_2, PENT-PEG-NH_2, LyP-1-PEG-PEI-CHT, and PENT-PEG-PEI-CHT conjugates. ^{1}HNMR chemical shifts, expressed in ppm and analyzed in deuterated water (D_2O) doped with deuterated acetic acid (CD_3COOD) in a ratio of 5:1 were recorded on a Bruker Avance III spectrometer operating at 500MHz (Bruker BioSpin GmbH, Germany) at room temperature.

6.2.2.3.3. Size, Zeta potential and Structural Morphology Peptide-Enhanced ENT-loaded Nanoparticles

Malvern Zetasizer Nano ZS (Malvern Instruments, Worcestershire, UK) was employed to evaluate the hydrodynamic size and zeta potential of the LyP-1 or PENT functionalized ENT-

loaded nanoparticles. Known sample weights were dispersed in DDW and sonicated for 30 seconds. Thereafter, 2mL of dispersed sample solution was placed in disposable polystyrene cuvettes and the dynamic scatter intensity was recorded at room temperature.

The size and shape of the nanoparticles were also confirmed using Transmission Electron Microscopy (TEM) (FEI Tecnai T12 TEM, 60-120kV, Hillsboro, OR, USA). Small amount of the nanoparticle was dispersed in DDW, ultra-sonicated for 15 minutes and a single drop of the nanoparticle suspension was dropped on a Form Var® coated 200-mesh copper grip (TAAB Laboratories Equipment Ltd., Aldermaston, England), and allowed to air dry at room temperature prior to TEM analyses.

The morphology of the nanoparticles was also examined using Scanning Electron Microscopy (SEM). Powdered sample of the nanoparticles was placed onto an aluminium specimen stub covered with a double-sided carbon adhesive disc and sputter-coated with both palladium and gold for 4 minutes at 20KV. Images of nanoparticles were then obtained by a Scanning Electron Microscope (SIGMA VP, ZEISS Electron Microscopy, Carl Zeiss Microscopy Ltd; Cambridge, UK).

6.2.2.4. *In vitro* Endostatin Release

To investigate the *in vitro* release of encapsulated ENT, 5 mg each of LyP-1 and PENT ENT-loaded nanoparticles (n = 3) were dispersed in 2mL of PBS buffer in respective microcentrifuge tubes and incubated in the orbital shaker at 37°C for 24 hours. Nanoparticle dissolution was tested at varying pH conditions of 4.6, 6.8 and 7.4 to mimic the endolysosomal acidification of cell, the tumor microenvironment and the physiological pH respectively. Samples were taken at specified time interval (1, 2, 4, 8, 16 and 24) after centrifugation at 5000 rpm for 10 minutes to allow nanoparticles settled into pellets. Supernatants (200µL) were removed in triplicate and

replaced with fresh buffer to maintain sink condition. Samples were then analysed for UV absorption of endostatin at 562 nm using a microplate reader (FilterMaxTM F5 Multi-Mode Microplate Reader, Molecular Devices, USA).

6.2.2.5. Cell Culture Experiments

Human oesophageal squamous cell carcinoma cell line (KYSE-30) (Life Bioscience, Oakleigh, VIC, Australia) were seeded in complete media comprising of RPMI and Ham's F12 (1:1), supplemented with 10% Fetal Bovine Serum, 2mM glutamine, sodium bicarbonate and 100µL penicillin/streptomycin (Sigma- Aldrich; St. Louise, MO, USA). The cells were maintained in an incubator (RS Biotech Galaxy, Irvine, UK), with a humidified atmosphere of 5% CO_2 at 37°C.

6.2.2.5.1. Polymer Cyto-compatibility and Cell Proliferation Assay

In vitro cell cytotoxicity was determined using Alamar blue assay. KYSE-30 cells were diluted in a complete medium at a final concentration of 1×10^4 cells/mL and seeded (25 µL/well) and incubated for 24 hours prior to cell proliferation evaluation using Alamar blue assay according to the manufacturer's procedures. Native polymer conjugates, ENT-loaded nanoparticles, LyP-1 and PENT functionalized ENT-loaded nanoparticles were dissolved in the serum free culture medium at varying concentrations of ENT (125 µg/mL, 250 µg/mL, 500µg/mL and 1000 µg/mL). Attached cells in the wells were treated with the various nano-formulations in triplicates for 24 hours and cell viability was quantified at maximum emission/excitation wavelengths of 535 nm and 595 nm respectively on a microplate reader (FilterMaxTM F5 Multi-Mode Microplate Reader, Molecular Devices, USA). Attached cells treated only with serum free media, without the nano-formulation, were used as control. Results are presented as percentage cell viability (%CV) (mean standard deviation), with the percentage of viable cells calculated using the following Equation.

$$CV = \frac{Fluorescence\ reading\ in\ treated\ cells}{Fluorescence\ reading\ in\ control\ (untreated)\ cells} \ldots\ldots Eq \ldots 6.1$$

6.2.2.5.2. Cellular uptake, Internalization and sub-cellular localization of nanoparticles

KYSE-30 cells (1×10^5 cells/well) were cultured on cover slips in a six-well culture plate for 24 hours in 2 mL of RPMI and Ham's F-12 medium (1:1) supplemented with 10% fetal bovine serum (FBS) under a humidified atmosphere of 5% CO_2 in air. Attached cells were washed three times with PBS solution. The medium was then replaced with 2 mL (0.1 mg/mL) fresh medium without FBS containing FITC-labelled LyP-1 or PENT PEG-PEI-CHT ENT-loaded nanoparticles. The cells were then incubated at 37°C for 24 hours, followed by removal of the medium and washing the cells twice with PBS solution. Subsequently, the nucleus of cells treated with/without nanoformulations were stained with 10 µl/mL DAPI (4′,6-diamidino-2-phenylindole) solution (Thermo Fisher Scientific, Waltham, MA, USA) for 5 minutes under incubation following the manufacturer's protocol. Stained cells on the coverslips were rinsed three times in PBS prior to image capture.

The intracellular entry of FITC-labelled LyP-1 or PENT functionalized PEG-PEI-CHT ENT-loaded nanoparticles was monitored using Confocal Laser Scanning Microscope (LSM 780, ZEISS) (Baden-Württemberg, Germany). Treated cells were fixed with 4% paraformaldehyde in PBS for 30 minutes at room temperature. Thereafter, coverslips containing fixed cells were rinsed with PBS and placed in 0.1% Triton-X100 solution to permeate the cells for 5 minutes. The coverslips were then mounted on glass microscope slides by using a drop of 80 %v/v cooled glycerol. Cell samples were observed under CLSM at 495 nm excitation to induce the green fluorescence of FITC and their emission was observed at 517 nm. Blue fluorescence of DAPI was induced by 358 nm excitation and detected at 461 nm wavelength excitation spectrum.

6.2.2.5.3. Endothelial Cell Migration Assay using Modified Boyden Chamber

Migration of KYSE-30 cells was assessed using the modified Boyden chambers (Corning incorporated, NY, USA). Gelatinized polycarbonate filters (pore size, 8.0µm) with 6.5mm diameter inserts were employed. Briefly, 200 µL solution of native ENT-loaded PEG-PEI-CHT conjugates, LyP-1 or PENT functionalized PEG-PEI-CHT ENT-loaded nanoparticles, control (untreated cells), and 6.48×10^4 KYSE-30 cells in 200 µL serum-free medium were added to the upper chamber. A volume of 0.4mL of 10% FBS-containing medium was then added to the lower chamber as a chemoattractant. Cells were incubated for 8 hours at 37°C, and non-migrating cells (dead cells due to treatments with nanoformulations) on the upper surface of the membrane, were then scraped off with cotton swabs. 1 mL Alamar blue reagent was added to cells that migrated to the bottom of the membrane for 4 hours and quantified at maximum emission/excitation wavelengths of 535 nm and 595 nm respectively on a microplate reader (FilterMaxTM F5 Multi-Mode Microplate Reader, Molecular Devices, USA). Thereafter, migrated cells at the bottom side of the membrane were washed twice in PBS, fixed with 4% formaldehyde for 15 min and stained with trypan blue. Stained cells were visualised under an Olympus BX 63 optical fluorescence microscopy (OFM) (Olympus DP 80) (Tokyo, Japan).

6.2.2.5.4. Anti-VEGF and Anti-MMP2 ELISA assay

For VEGF and MMP2 ELISA assay, each well was normalized to 774000 cells. The conditioned media was collected at 0, 12, 24, and 48 hours after exposure to the nanoformulations including LyP-1 and PENT functionalized nanoparticles, ENT-loaded nanoparticles as well as cells treated only with serum free media as control. The protein in the cell culture supernatant was concentrated at 2000 rpm at 4^0C for 10 minutes by using the Labotech centrifuge (Göttingen, Germany). Samples were assayed by a VEGF ELISA kit from Sigma Aldrich (Minneapolis, MN, USA) and abcam MMP2 Human ELISA kit with normalized protein amounts according to the

manufacturer's instructions. Protein amount was quantified in duplicates at 450 nm on a microplate reader (FilterMaxTM F5 Multi-Mode Microplate Reader, Molecular Devices, USA).

6.3. Results and Discussion

6.3.1. Structural and functional modifications of peptide functionalized nano-conjugates

A multi-step approach using CDI and EDC/NHS as coupling agents was employed for the synthesis of the polymer conjugates as shown in the reaction mechanism in Figure 6.1. The imidazoles of CDI were used to couple the amine groups of CHT and PEI (CHT-PEI conjugates) while the carboxylic group of bifunctional PEG (NH_2-PEG-COOH) was linked to the amine group of LyP-1 to form the LyP-1-PEG-NH_2 conjugate. Acm deprotection of the thiol of Cys^2 and Cys^{10} using iodine reagent was employed to cyclized the attached LyP-1 peptide in order to enhance its stability (Luo et al., 2010b). The free amine of LyP-1-PEG-NH_2 was then linked to the amine of CHT-PEI using the CDI chemistry as previously discussed. The ternary LyP-1-PEG-PEI-CHT conjugate formed was then loaded with ENT for further experiments.

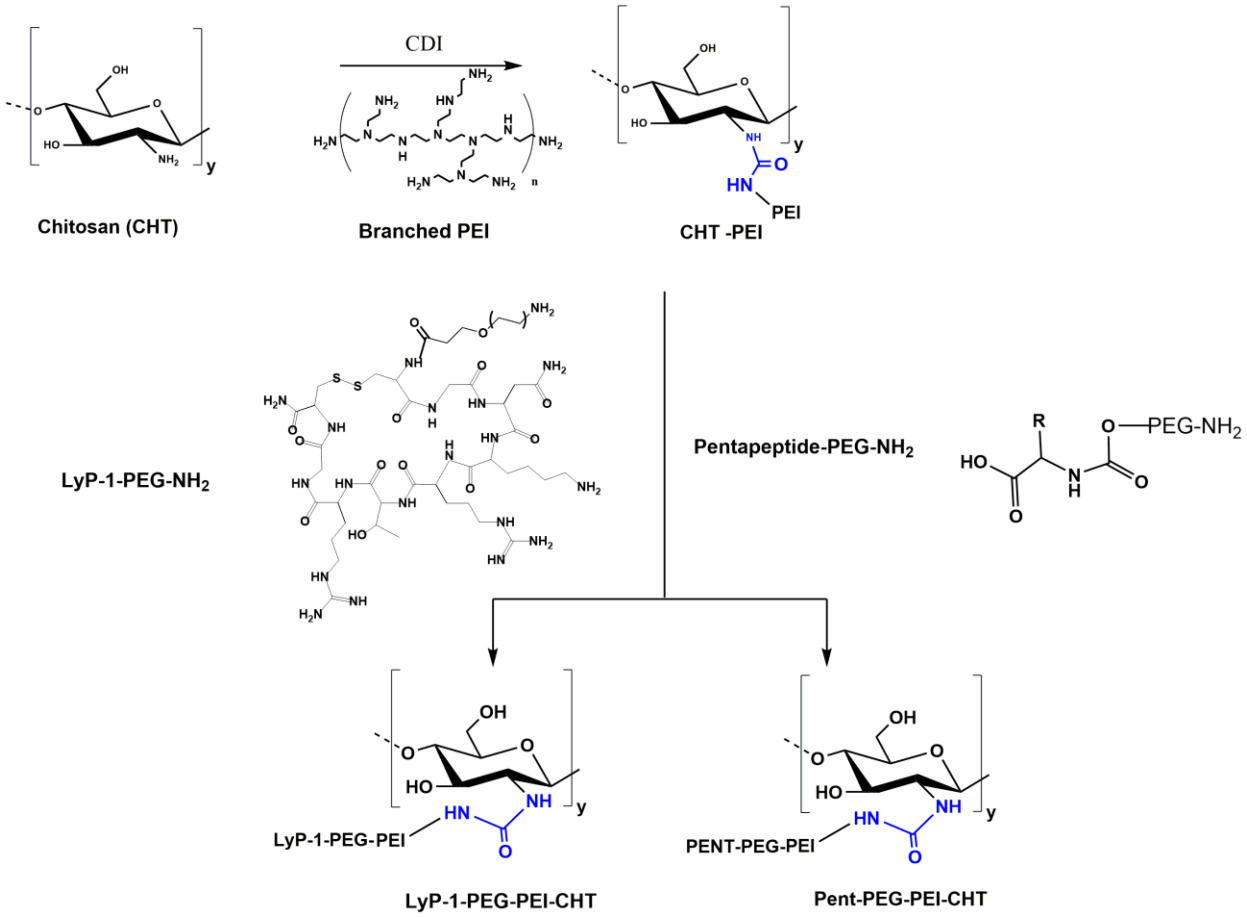


Figure 6.1: Reaction scheme for the synthesis of peptide-enhanced nanoparticulate system.

Figure 6.2 represents the NMR spectra of the conjugated nano-constructs. Characteristic peaks of CHT, assigned at δ = 1.9 ppm, indicates the methyl protons of the N-acetyl group of CHT (Figure 6.2a) while the presence of peaks between δ = 2.5–3.2 ppm were assigned to the methylene protons of PEI (–$NHCH_2CH_2$–) confirming the successful grafting of CHT to PEI using CDI as a cross-linker. Proton NMR spectra for both the linear and cyclic LyP-1 peptides confirmed the cyclization of linear LyP-1 peptide to a more stable cyclic LyP-1 peptide. There is an upfield shift in the methylene signals for cyclic LyP-1 (3.25, 3.48) relative to the linear LyP-1 peptide (3.32, 3.56) (Figure 6.2b & 2c). Interestingly, both spectra confirmed the conjugation of LyP-1 to NH_2-PEG-COOH to yield LyP-1-PEG-NH_2 conjugates. The repeating units of PEG appeared in the range between 3.7 – 3.8 ppm in the ^{1}HNMR spectrum of cyclic LyP-1-PEG-NH_2

conjugate (Yan et al., 2012). Upon the linking of CHT-PEI to LyP-1-PEG-NH_2 conjugates, the appearance of the characteristic peak of PEG protons around 3.6 ppm confirmed the formation of the complex LyP-1-PEG-PEI-CHT as shown in Figure 6.2d. Similarly, the characteristic peaks of both PEI and CHT were retained in the spectrum at 3.1 and 1.9 ppm, respectively

.

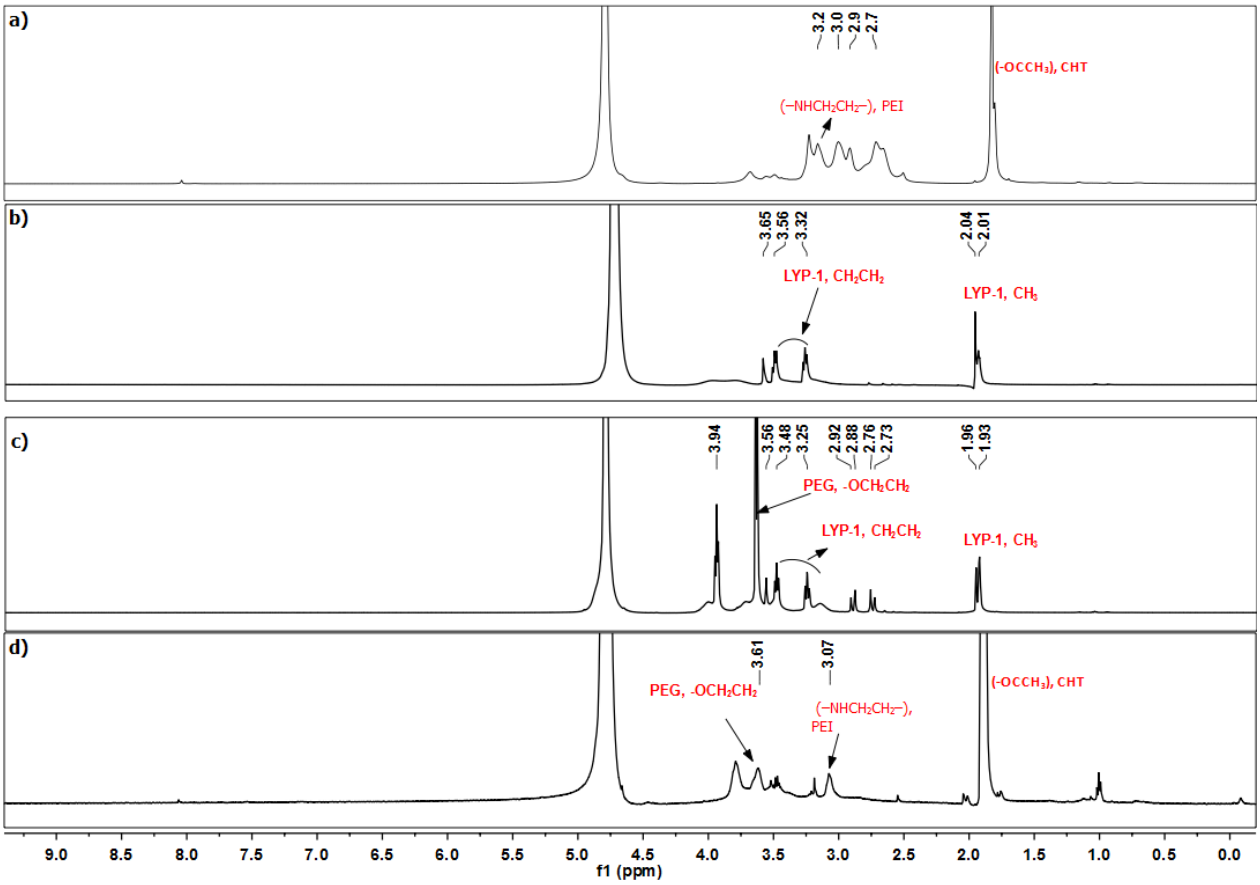


Figure 6.2: ^{1}HNMR of grafted copolymers in D_2O:CH_3COOD (5:1) a) PEI-CHT conjugate b) Linear LyP-1-PEG-NH_2 conjugate c) Cyclic LyP-1-PEG-NH_2 conjugate (d) Cyclic LyP-1-PEG-PEI-CHT conjugate.

FTIR spectra and detailed absorption peaks of the native polymers and the corresponding conjugates are presented in Figure 6.3 and Table 6.1. As presented in Figure 6.3a, characteristic peaks of CHT, due to the C-O bend of pyranose ring was assigned at 887 cm^{-1} (Table 6.1, Figure 6.3a (i)), while the signals at 855 and 1465 cm^{-1} were assigned to –$NHCH_2CH_2$ stretch in PEI (Table 6.1, Figure 6.3a (ii)). Similarly, the peak at 841 cm^{-1},

contributing to the absorption of CH_2 from $[CH_2CH_2O]n$ was assigned to PEG (Table 6.1, Figure 6.3a (iii)). Absorption peaks at 3038 and 3376 cm^{-1} were assigned to the C-H and N-H stretching of the imidazole bonds between the amines of CHT and PEI in the grafted CHT-PEI conjugate Figure 6.3b (iv) (Ramasamy, 2015). Reduction in the frequencies of the characteristic peaks of both CHT at 883 cm^{-1}, and PEI at 829 cm^{-1} confirmed the successful grafting of the two polymers. Of interest are the formations of the amide bonds in LyP-1-PEG-NH_2 conjugate. As seen in Figure 6.3c (v - vi), the characteristics peak at 1697 cm^{-1} was assigned to the absorption from the C=O stretch in amide bond I, 1464 and 1495 cm^{-1} were peaks attributed to the absorptions from both the N-H bend and C-N stretch in amide bond II while the tripartite absorption peaks at 1310, 1283 and 1262 cm^{-1} were attributed to the N-H bend in plane and C-N stretch in amide bond III. Meanwhile, an absorption peak at 3395 cm^{-1} was attributed to the N-H stretch from the free primary amine group attached to the PEG in the conjugate. Upon the conjugation of the LyP-1-functionlaized amino terminal PEG onto CHT-PEI, there seem to be a mild increase in the overall amine density. The absorption peaks the free terminal amine shifted to a higher frequency at 3408 cm^{-1} from 3395 cm^{-1}. Similarly, the frequencies of the amide bonds shifted slightly to 1698 cm^{-1} (amide I), 1464 cm^{-1}, 1497 cm^{-1} (amide II), and 1311, 1280, 1253 cm^{-1} in amide III (Table 6.1, Figure 6.3d (vii)).

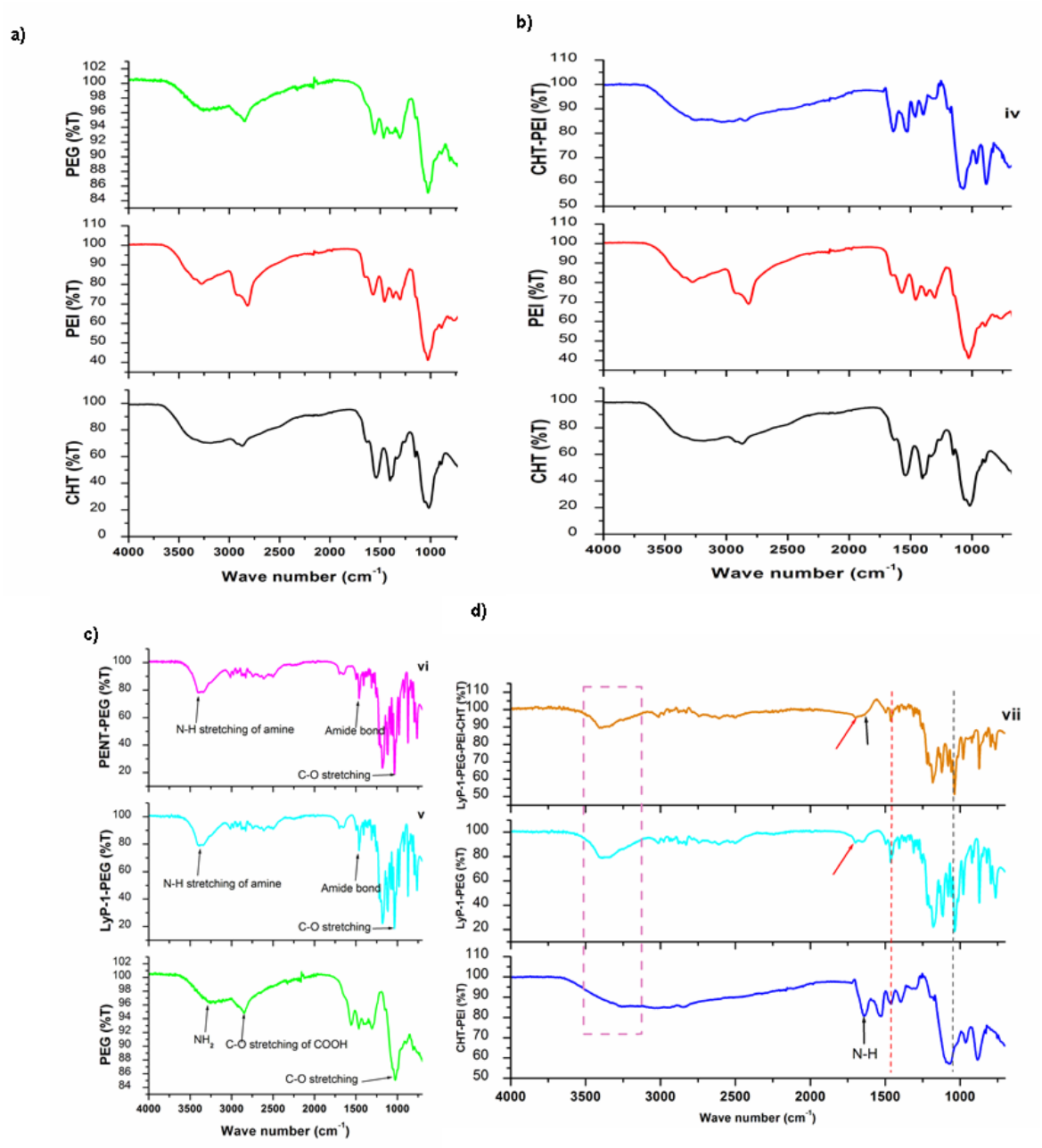


Figure 6.3: FTIR spectra of native and peptide-enhanced nanosystems. (a) spectra of the native polymers including CHT, PEI and PEG (b) spectra showing peaks for CHT, PEI and CHT-g-PEI nano-conjugate (c) spectra of PEG and peptide-PEG conjugates (d) spectra of CHT-g-PEI, LyP-1-PEG and LyP-1-PEG-PEI-CHT nano-conjugates.

Table 6.1: Assignment of FTIR spectra of native polymers, polymer and peptide conjugates presented in Figure 6.3.

Polymer & polymer conjugates	IR absorption bands (cm^{-1})
CHT	3363.69, 2849.95, 2362.23, 1636.15, 1533.82, 1467.33, 1403.27, 1291.59, 1245.70, 1177.65, 1071.30, 964.29, 886.69, 757.67
PEI	3382.49, 2942.31, 2828.00, 2167.17, 1638.25, 1588.50, 1534.79, 1465.07, 1291.62, 1247.22, 1177.84, 1115.17, 1083.88, 958.50, 882.91, 759.30, 854.83
NH_2-PEG-COOH	2882.54, 2741.58, 1965.36, 1621.12, 1588.16, 1532.21, 1588.16, 1414.15, 1456.35, 1359.61, 1340.92, 1280.21, 1240.81, 1177.54, 1146.22, 1088.60, 1059.82, 846.40, 841.33, 784.82, 711.64
CHT-PEI	3038.23, 1640.61, 1525.24, 1461.02, 1395.19, 1174.37, 1070.98, 963.44, 882.85, 828.80, 702.28
LyP-1-PEG-NH_2	3395.04, 3013.30, 2978.79, 2939.03, 2922.49, 2829.68, 2746.93, 2607.91, 2496.41, 1697.46, 1495.23, 1463.54, 1406.77, 1378.75, 1360.88, 1337.95, 1310.28, 1297.95, 1280.16, 1278.89, 1219.39, 1202.88, 1179.49, 1137.35, 1115.00, 1079.57, 1035.92, 1013.96, 979.92, 921.48, 911.10, 848.80, 821.32, 871.83, 838.22, 795.42, 763.25, 635.22, 591.05, 582.92, 567.98
LyP-1-PEG-PEI-CHT	3408.00, 3012.39, 2829.72, 2607.85, 1697.54, 1496.61, 1463.55, 1407.27, 1361.05, 1310.56, 1280.18, 1253.22, 1297.92, 1137.34, 1220.94, 1182.47, 1137.34, 1122.69, 1079.81, 1059.32, 1038.21, 979.53, 921.89, 821.62, 796.04, 764.32, 697.72, 636.21, 584.79, 592.76, 573.12, 560.37

a ^{v} = stretching vibration, v^{s} = symmetric stretching vibration; v^{as} = asymmetric , stretching vibration; δ= bending vibration; ω = wagging.

6.3.2. *In vitro* ENT release from modified ENT-loaded nanoparticles

A direct relationship occurs between how nanoparticles react to their environment and their intricate material composition (Danhier et al., 2010). Nanomaterials can be tailored to release their payload at predetermined rate based on material erosion, or diffusion of the captured payload through the nanoparticulate matrix or pores (Hauert and Bhatia, 2014). Certain external stimulus, such as pH, can influence the release of their payload or alters their physicochemical properties (Jia et al., 2013). Interestingly, the tumor microenvironment exhibits a more acidic pH than the physiological pH of healthy cells (Kato et al., 2013). Thus, nanoparticles can be tailor-made to withhold or release their payload in response to the pH of the cell's micro and macro environments. As presented in Figure 6.4, both LyP-1 and PENT modified nanoparticles release more ENT within the nanoparticulate matrix at lower acidic pH values of 4.6 and 6.8 respectively than at the physiological pH of 7.4. There is no significant difference (data not shown) in the release pattern of ENT between the functionalized and native nanoparticles. As such, functionalizing the nanoparticles surfaces does not influence ENT release but rather enhanced the direct homing of the nanoparticles to their active sites within the cell. In this manner, sub-optimal release of ENT that often accounts for its high dosage form was overcome with optimal release at the disease site with increased therapeutic effect. More importantly, the reduced ENT release at physiological pH will enhance the stability of the peptide functionalized nanoparticles in the blood circulation and healthy tissues (Ruan et al., 2015).

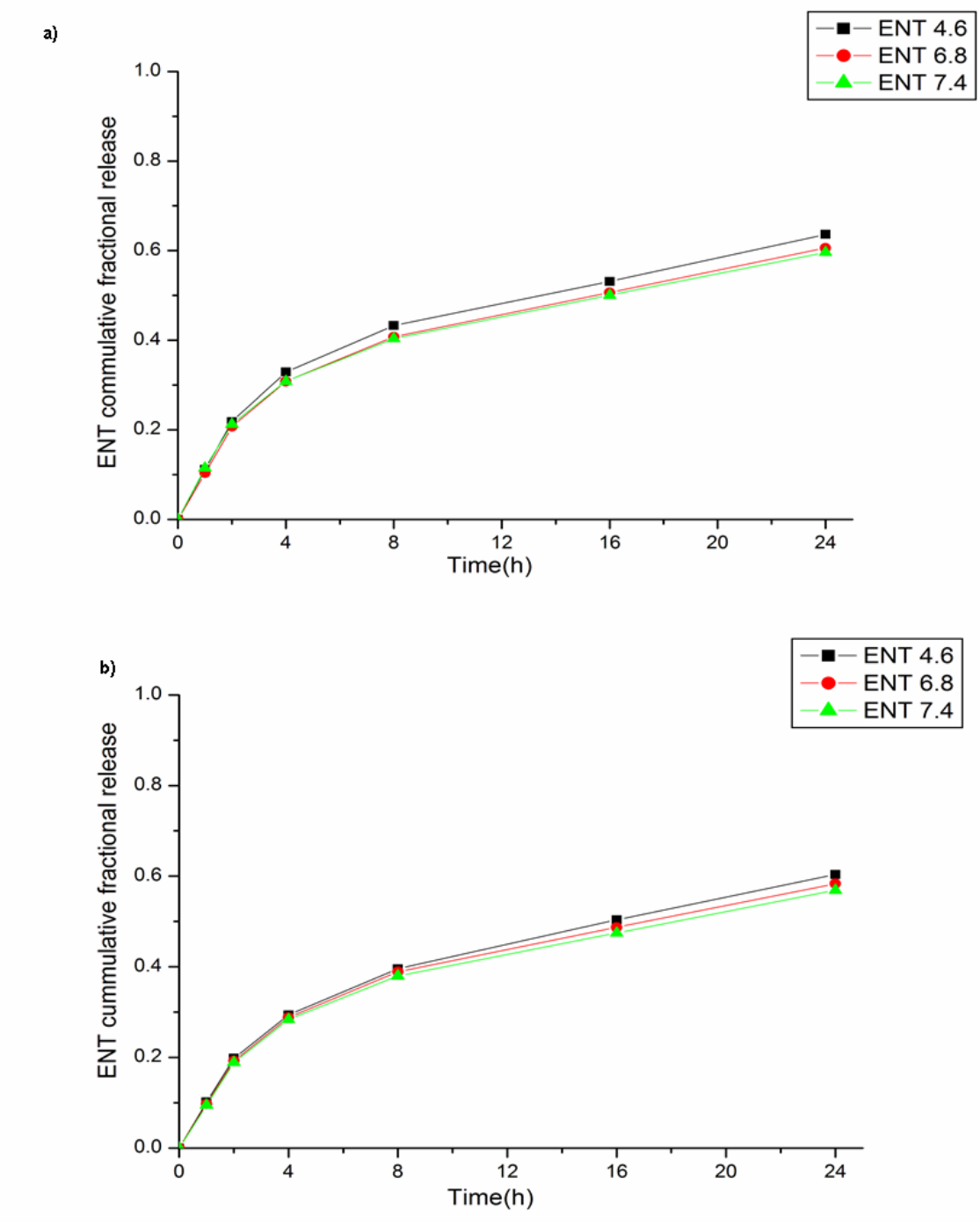


Figure 6.4: *In vitro* ENT release from the peptide-enhanced ENT-loaded nanoparticles (a) LyP-1 functionalized ENT-loaded nanoparticles (b) PENT functionalized ENT-loaded nanoparticles.

6.3.3. Effects of physicochemical properties of peptide functionalized ENT-loaded nanoparticles on cellular uptake, internalization and sub-cellular colocalization

Most often, cellular uptake, internalization, circulation, distribution and intra-cellular trafficking of nanoparticles within the biological system are influenced by their physicochemical properties (Duan and Li, 2013; Murugan et al., 2015). A unique advantage of nanoparticulate systems in cancer therapeutics is their ability to pass through the porous tumor angiogenic endothelium and dys-functional lymphatic drainage through passive transport into the tumor cells (Hauert and Bhatia, 2014).

The size and shape of nanoparticulate systems have been reported to influence their cellular uptake and internalization, circulation time, extravasation and interstitial diffusion within the cell (Adebowale et al., 2015; Erik C Dreaden et al., 2012; Hauert and Bhatia, 2014; Thorek and Tsourkas, 2008). Both TEM and SEM micrographs showed that spherical peptide functionalized ENT-loaded nanoparticles were synthesized with an average size spanning between 30 – 200 nm (Figure 6.5a & b). Large-scaled SEM micrograph of the nanoparticles at 50kx magnification (data not shown), showed that the surfaces of the nanoparticles are rough possibly due to the attachment of the peptide particles on the nanoparticles surfaces. Meanwhile, hydrodynamic size of the nanoparticles ranged between 25 – 106.45 nm as presented in Figure 6.5c. Interestingly, the lymphatic drainage among endothelial cells of cancer disease can allow the passive transport of biomaterials and molecules with sizes up to 150 nm including OSCC (Dreaden et al., 2012; Ikomi et al., 1999; Luo et al., 2010a; Rahman and Mohammed, 2015; Shayan et al., 2006). More so, spherical nanoparticles have proven more efficient for cellular uptake and internalization into tumor microenvironments (Hauert and Bhatia, 2014). Thus, the surfaced-engineered nanoparticles possessed good size and shape parameters for effective internalization into a tumor microenvironment as later presented in the study.

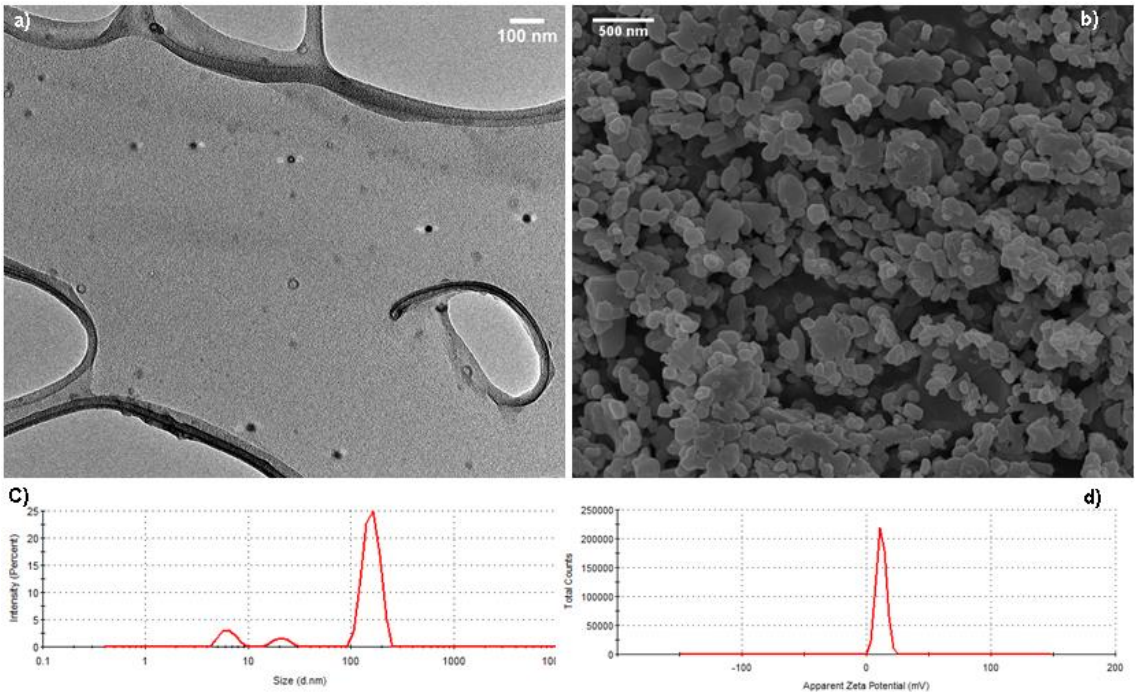


Figure 6.5: Physicochemical characterization of peptide-functionalized ENT-loaded nanoparticles. (a) TEM micrographs of peptide-enhanced ENT-loaded nanoparticles (b) SEM micrographs of peptide-enhanced ENT-loaded nanoparticles (c) Hydrodynamic zeta size of peptide-enhanced ENT-loaded nanoparticles (d) Zeta surface charge of peptide-enhanced ENT-loaded nanoparticles.

The surface zeta potential of nanoparticles influenced their cellular binding, internalization and circulation time frame within the living system. Upon their internalization, charged nanoparticles are targeted by phagocytes within the immune system through opsonization for destruction (Adebowale et al., 2015; Hauert and Bhatia, 2014; Owens III and Peppas, 2006). Based on previous reports, positively charged nanoparticulate surfaces preferentially bind to cells and are internalized compared to nanoparticles having neutral and negatively charged surfaces. More importantly, positively charged nanoparticles are preferentially engulfed by tumor cells relatively to uncharged particles (Alkilany et al., 2009; Arvizo et al., 2010; Hauck et al., 2008; Park et al., 2011; Thorek and Tsourkas, 2008; Verma and Stellacci, 2010). Interestingly, our peptide functionalized ENT-loaded nanoparticles have an average zeta potential surface charge of 17.3 mV as presented in Figure 5d. As such, our synthesized peptide-enhanced nanoparticulate

system could bind more specifically to the negatively charged ions on OSCC cells (Chen et al., 2016) and internalised through receptor-mediated endocytosis.

Beyond size and surface charge, targeting ligands (Brannon-Peppas and Blanchette, 2012; Kanapathipillai et al., 2014) including peptides can be attached to nanoparticle surfaces to facilitate their direct binding and internalization into the cells (Pearce et al., 2012). Specific receptors that are over-expressed on some tumor cells can be explored as molecular signatures that home the direct binding, internalization and delivery of peptide-engineered nanoparticles into cells (Ruoslahti et al., 2010). In this study, cyclic LyP-1 was attached to the surface of ENT-loaded nanoparticles. To account for peptide stability and enhance binding affinity, the Acm thiol protected Cys^{2} and Cys^{10} of the linear peptide were deprotected and cyclized using an iodine protection mechanism as previously discussed. Cyclic peptides have been reported to have higher binding affinity and stability than linear ones (Conibear et al., 2016). As presented in Figure 6.6, green fluorescent particles were found within KYSE-30 cells after pre-incubation with FITC-labelled peptide-enhanced nanoparticles. This is possibly due to their interactions with the negatively charge ions on KYSE-30 cells' surfaces. Similarly, FITC labelled particles selectively co-localized into the nuclear and mitochondrial compartments within KYSE-30 cells (Figure 6.7).

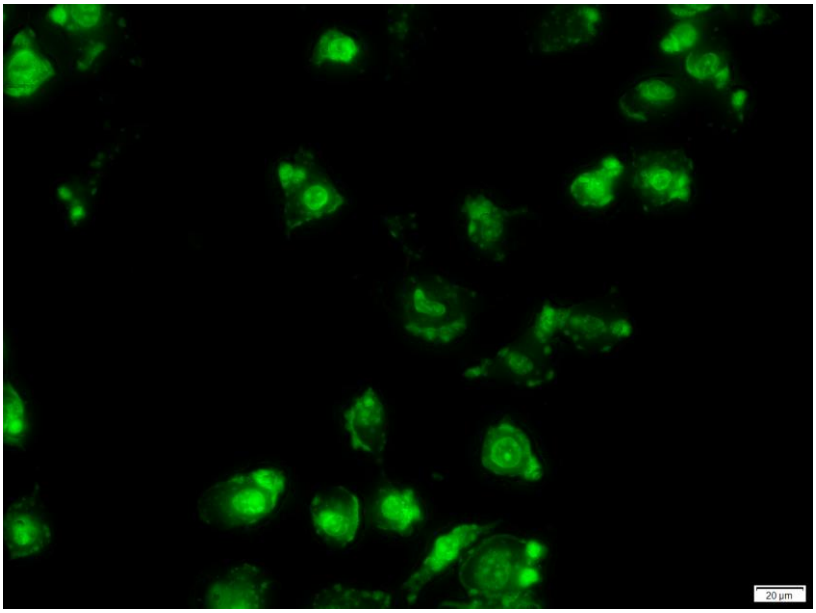


Figure 6.6: CLSM micrograph showing cellular uptake and internalization of peptide-enhanced ENT-loaded nanoparticles. Nanoparticles were labelled with FITC.

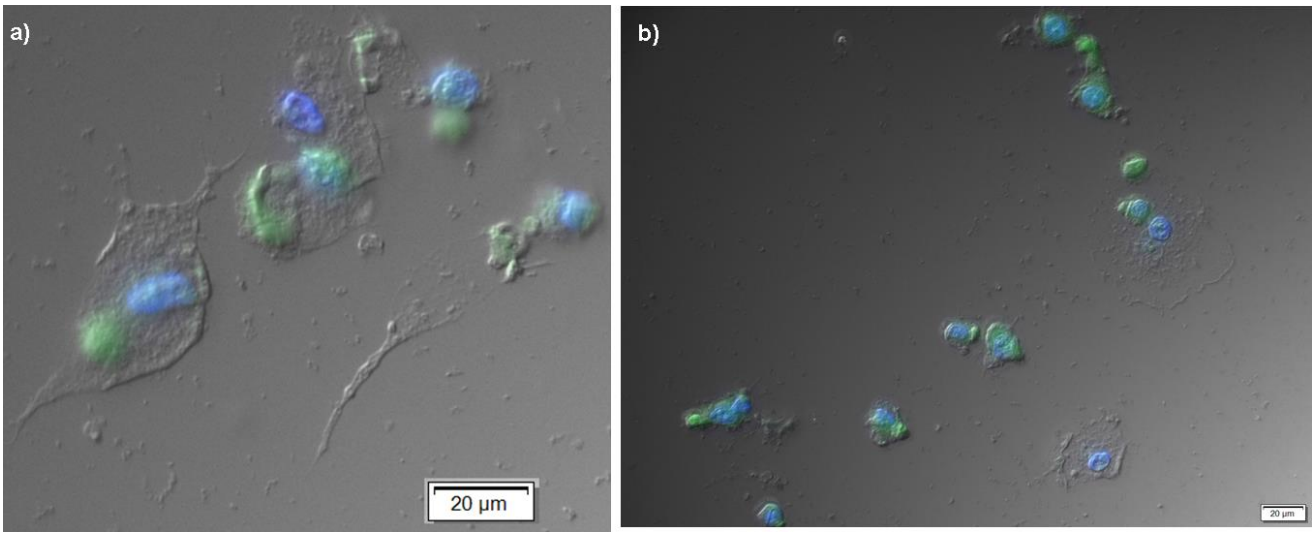


Figure 6.7: DIC micrographs showing subcellular colocalization of peptide-enhanced ENT-loaded nanoparticles in the nucleuses of KYSE-30 cells stained with DAPI. (a) LyP-1 functionalized targeted ENT-loaded nanoparticles (b) PENT functionalized targeted ENT-loaded nanoparticles.

Differential interference contrast (DIC) images of both the nucleus (Figure 6.8) and the mitochondrial (Figure 6.9) of KYSE-30 cells when stained with DAPI and rhodamine 123 fluorophores respectively, showed selective sub-cellular localization of both LyP-1 and PENT

functionalized nanoparticles within their compartments. As can be seen, green fluorescent particles are condensed within the nucleus (blue) indicating the selective targeting of the nucleus probably for nuclear protein such as nucleoline which has been reported as a biomarker for endothelial cells in angiogenesis (Christian et al., 2003; Yao and Yang, 2005).

When combined, peptide-functionalized positively charged spherical nanoparticles, with nano-range sizes, could display selective binding affinity and internalization relative to other forms of surfaced-engineered nanoparticulate systems in cancer nanomedicine. These parameters also influenced their intra-cellular trafficking, localization and therapeutic effects in biological systems (Murugan et al., 2015).

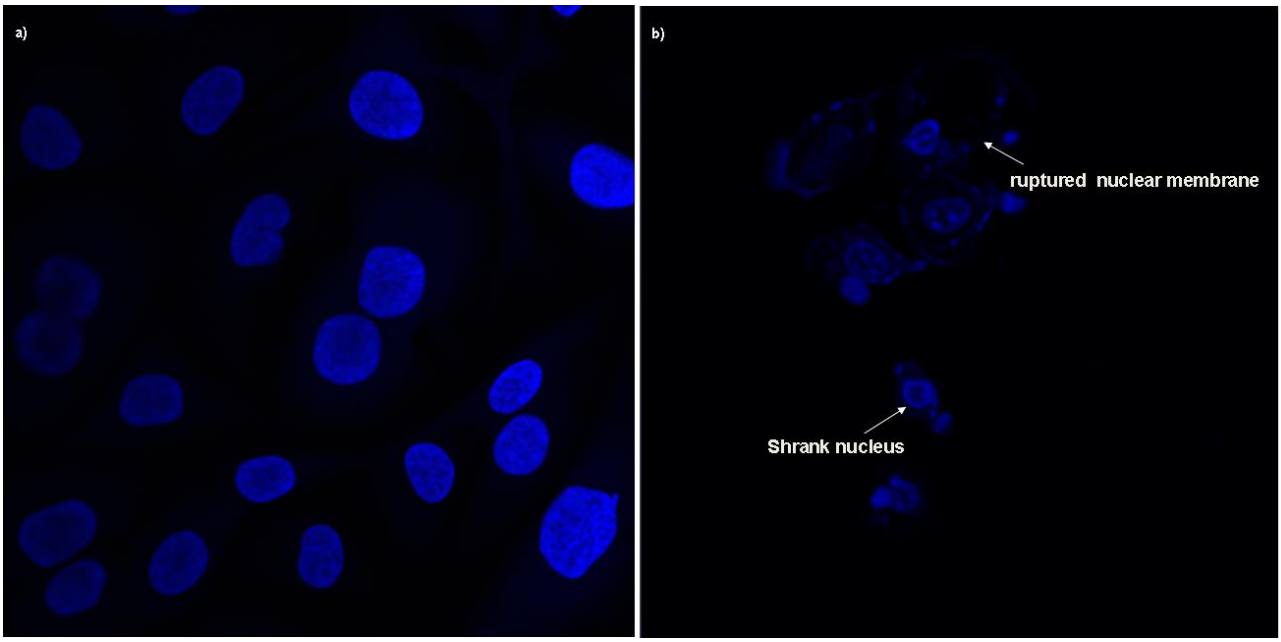


Figure 6.8: CLSM images of the nucleus of KYSE-30 cells stained with DAPI (a) untreated KYSE-30 cells (b) KYSE-30 cells pre-incubated with peptide-functionalized ENT-loaded nanoparticles. Shrank and depleted nuclear membrane showed signs of apoptosis and necrosis.

6.3.4. Specific binding and cytotoxic effects of peptide-enhanced ENT-loaded nanoparticles

The morphological integrity of the nucleus of cells is a clear index of their health status (Leist and Jäättelä, 2001). A leaky and swollen nucleus with early degradation and erosion of the plasma membrane characterized necrotic nuclei whereas apoptotic nucleus showed DNA fragmentation, nuclear and chromatin condensation with intact plasma membrane (Lovrić et al., 2005). KYSE-30 cells nuclei were stained with DAPI to monitor the anti-angiogenic effects of the functionalized ENT-loaded nanosystem as presented in Figure 6.8. As opposed to the nuclei control cells, nuclei of cells treated with both LyP-1 and PENT functionalized ENT-loaded nanoparticles 24 hours pre-incubation showed nuclear plasma degradation, nuclear condensation and the release of nuclear materials into the cytosol of the cells. While the mechanisms of anti-angiogenic effects of LyP-1 and PENT functionalized ENT-loaded nanoparticles are not fully understood at this stage of study, it is clear that both peptides induce cell death by apoptosis. Meanwhile, further investigation of key biochemical indicators of nuclear damage and cell death, such as caspases' activities, should be performed to validate the findings of this report.

The mitochondrial, as an organelle which plays a pivotal role in both cell survival and cell death is implicated in different types of diseases, including cancer. Changes that affect the mitochondrial compartments, particularly its DNA, can result in increased proliferation and avoidance of cell death pathways as seen in cancer cells (ShiDu Yan, 2014). Therefore, specific targeting of the mitochondrial represent a strategic intervention in cancer nanomedicine since cancer cells utilize the mitochondrial to increase disease progression. Interestingly, LyP-1 home specifically to mitochondrial protein p32 over-expressed on cancer cells' surfaces including OSCC (Fogal et al., 2010, 2008; Laakkonen and Vuorinen, 2010). Previous report has shown that rhodamine 123 selectively binds to the mitochondrial of living cells (Johnson et al., 1980).

Its positively charged ions at physiological pH bind preferentially to the abundant negatively charge ions across the mitochondrial membrane. As such, any external damage to the morphology of the mitochondrial of living cells can be easily assessed. As presented in Figure 6.9, both LyP-1 and PENT functionalized ENT-loaded nanoparticles caused a significant change in the mitochondrial configuration of KYSE-30 cells upon pre-incubation with the nanoformulations. Ruptured mitochondrial membrane, distorted mitochondrial morphology and enlarged mitochondrial DNA as seen in Figure 6.9 are indices of apoptosis (ShiDu Yan, 2014), which in turn account for the reduced cell viability presented in Figure 6.10. Results showed that both peptides (LyP-1 and PENT) contribute to the direct targeting of ENT-loaded nanoparticles for enhanced anti-angiogenic effects on KYSE-30 cells *in vitro*.

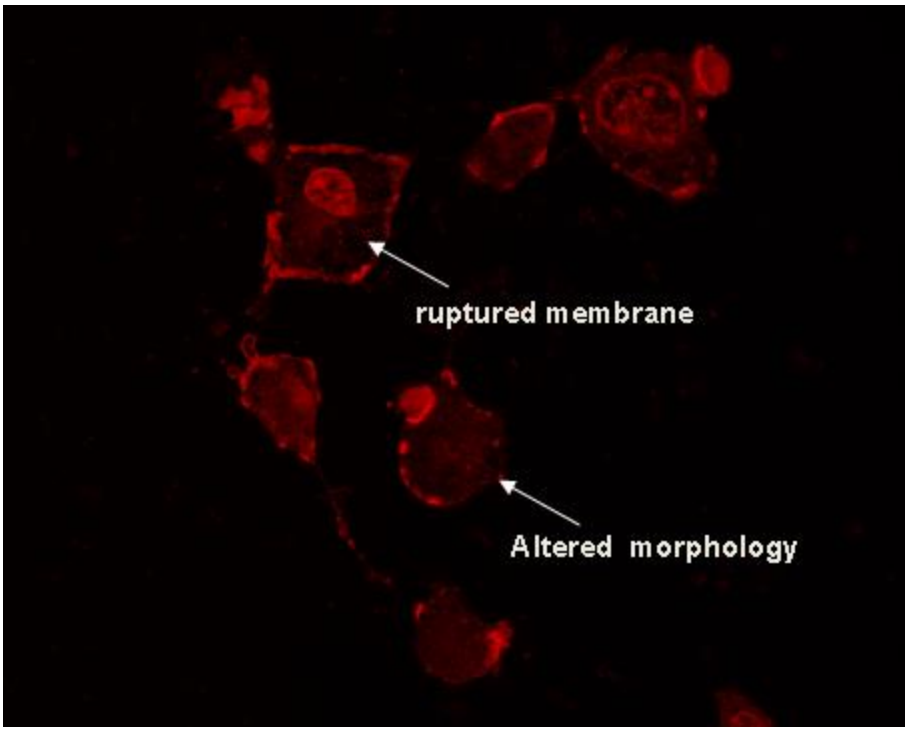


Figure 6.9: CLSM images of mitochondrial stained with rhodamine 123 in live KYSE-30 cells. Altered-configuration of the mitochondrial morphology and disrupted mitochondrial membrane showed apoptosis (Johnson et al., 1980).

6.3.5. Reduced migration and anti-proliferative effects of LyP-1/PENT functionalized nanosystem on KYSE-30 cells

Endothelial cell proliferation and migration are the key features of angiogenesis in tumor cells (Staton et al., 2009). Increased cell survival and endothelial cell proliferation are the major channels by which cells that made up new blood vessels are produced and maintained in living systems. Proliferation assays can be used to measure angiogenic activity when low-serum or low-growth factor conditions are used, or anti-angiogenic activity when the culture medium contains normal levels of serum and/or growth factors (Goodwin, 2007). The Alamar blue assay, an efficient and easy to reproduce cell quantitative method (Al-Nasiry et al., 2007), was employed to evaluate the cytotoxic effects of the synthesized peptide-enhanced nanoformulations on KYSE-30 cells. As presented in Figure 6.10, KYSE-30 cells were pre-incubated over 24 hours with serum-free cell medium containing the native polymer conjugates, ENT-loaded nanoparticles as well as both LyP-1/PENT functionalized ENT-loaded nanoparticles at varying concentrations. Across the tested concentrations, the polymer conjugates showed cell viability above 80%, an indices of good cyto-compactibility when compared to the control (untreated KYSE-30 cells) (Mavuso et al., 2016). Interestingly, cells treated with both LyP-1 and PENT functionalized nanoparticles showed reduced proliferation up to three-fold at concentration of 1000 µg/mL when compared to the control. A possible explanation for this could be the targeting effects of LyP-1 and PENT in homing the ENT-loaded nano-cargo specifically to the over-expressed nuclear and mitochondrial proteins such as p32 on KYSE-30 cells which in turn enhanced ENT anti-angiogenic effects (Agemy et al., 2013).

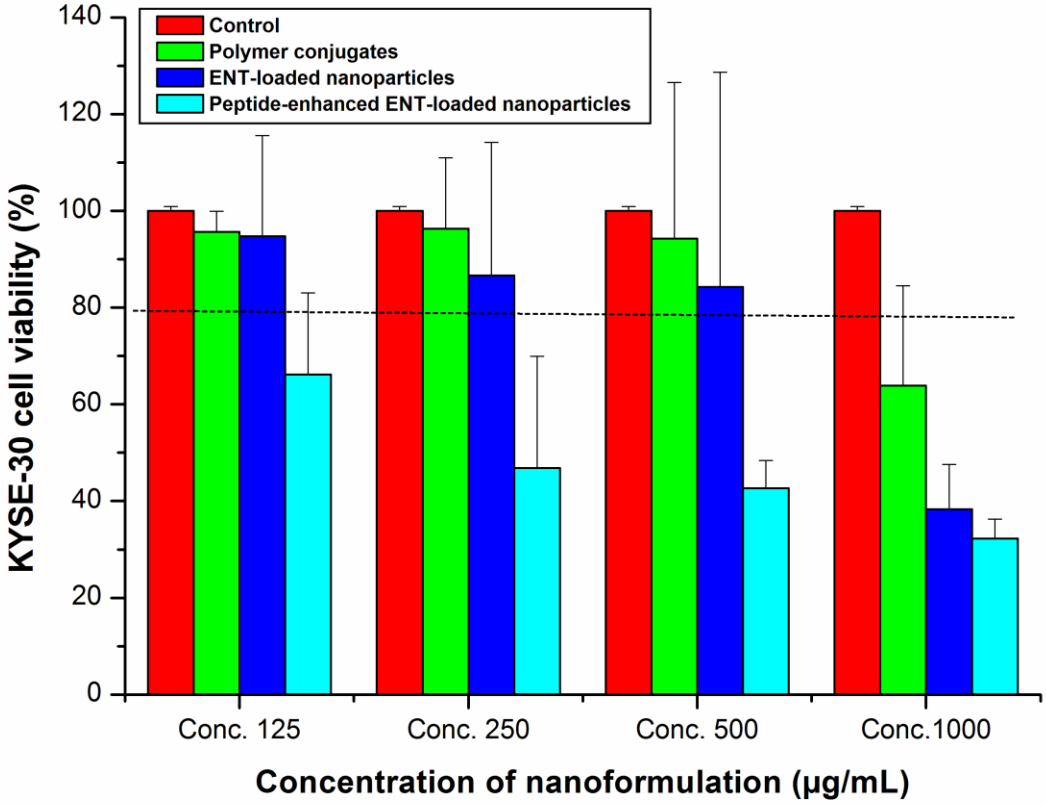


Figure 6.10: KYSE-30 cells viability after pre-incubation with nanoformulations at varying concentrations for 24 hours.

Of particular interest in the design of anti-cancer nanomedicines is cell motility as both tumor invasion and tumor angiogenesis require cell migration as a key determining factor (Goodwin, 2007). The mechanism by which cancer cells spread throughout the body necessitate their migration and invasion across the extracellular matrix (ECM), intravasation into the blood circulation or lymphatic vessel, getting attached to distant site after metastasis and a subsequent extravasation to form foci at another distant position (Justus et al., 2014). As presented in Figure 6.11b, KYSE-30 cells treated with both LyP-1 and PENT functionalized nanoparticles showed migration inhibition of more than 60% when compared to the motility of control cells. Cells pre-incubated with the native polymer conjugates showed a little higher migration than those pre-exposed to ENT-loaded nanoparticles. This however is expected as

ENT released from the nanoparticles matrix accounts for cell death thereby reduces the number of migrated cells across the trans-membrane pores in Boyden chamber as presented in Figure 6.11a.

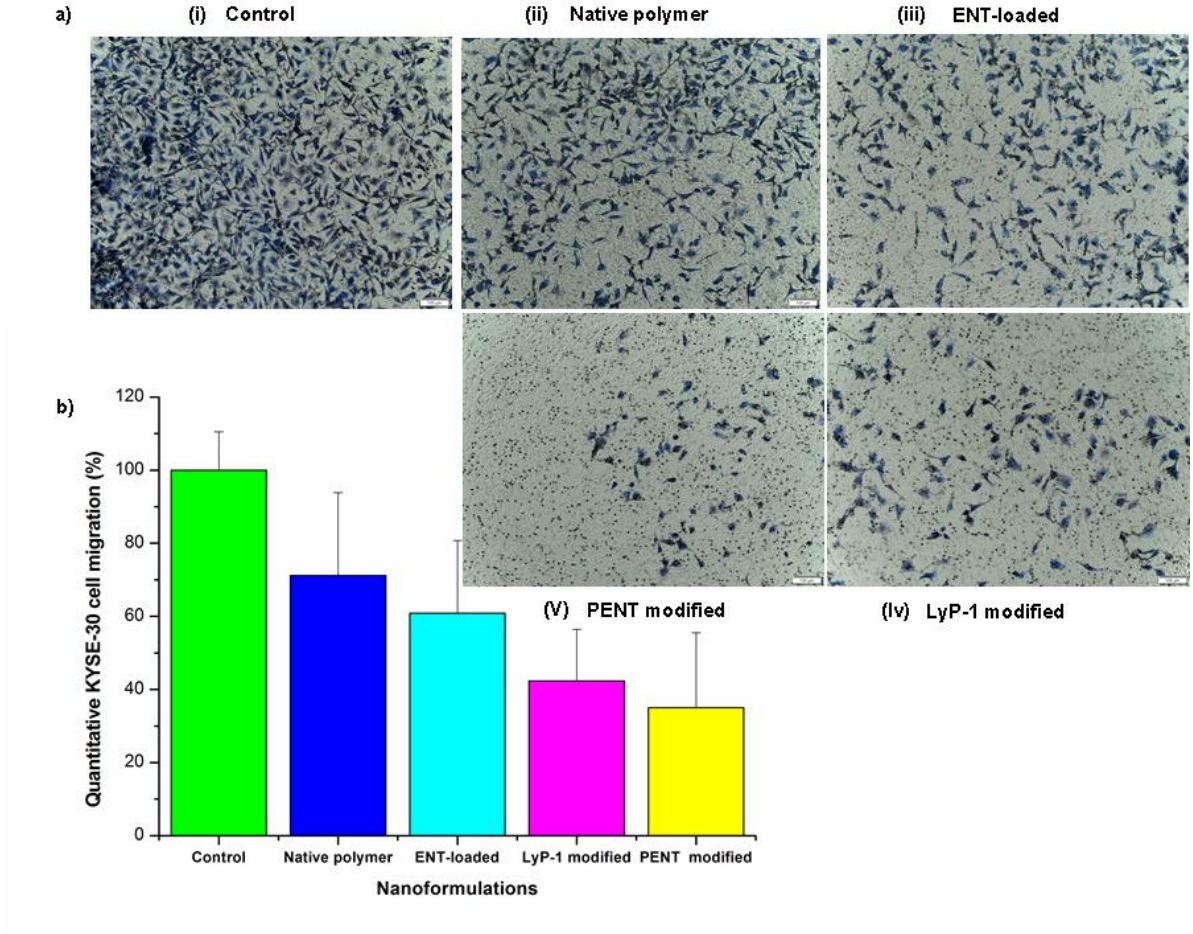


Figure 6.11: Transwell migration assay of KYSE-30 cells pre-treated with native, ENT-loaded and Peptide-functionalized nanoformulations (a) Representative microscopic images of the transwell inserts of KYSE-30 cells after pre-incubation with different nanoformulations (i) control, (ii) native polymer conjugates, (iii) ENT-loaded nanoparticles (iv) LyP-1 functionalized ENT-loaded nanoparticles, (v) PENT functionalized ENT-loaded nanoparticles. The inserts show the macroscopic images of transwell inserts stained by trypan violet. Pores of the membranes could also be observed as the numerous small, round and dark colored dots in the picture. (b) Histogram showing the quantification of the relative migration of KYSE-30 cells toward the chemo-attractant. Relative cell migration was expressed as the percentage of migrated cells with treatment compared to those without treatment (control).

6.3.6. Enzyme linked immunosorbent assay (ELISA) for VEGF-C and MMP2

ENT is known to reduce tumor growth by inhibiting angiogenesis (Folkman, 2006). Tumor cells enhance angiogenic process by producing angiogenic factors, such as basic fibroblast growth factor (bFGF) and vascular endothelial growth factor (VEGF) in particular. Interestingly, ENT is a potent anti-angiogenic protein that blocks VEGF-C (Fukumoto et al., n.d.; Kim et al., 2002; Zheng et al., 2016). Similarly, ENT inhibits endothelial and tumor cellular invasion by binding to the catalytic domain of MMP2 thereby blocking its activation and catalytic activity (Kim et al., 2000; Lee et al., 2002).

VEGF is a key factor that mediates tumor angiogenesis associated with the development of tumor blood supply and the progression of cancer in response to hypoxia (Lai et al., 2012). This present study investigates whether LyP-1/PENT functionalized ENT-loaded nanoparticles regulate VEGF and MMP2 expressions and activity levels *in vitro*. As presented in Figure 6.12, both LyP-1 and PENT functionalized ENT-loaded nanoparticles reduced VEGF-C expression over the incubation period. While there is progressive increase (1.74 fold increase) in the secretion of VEGF-C into the conditioned media by the control (untreated) KYSE-30 cells over 48 hours, VEGF-C expression was reduced up to 2.9 and 2.5 fold in cells pre-incubated with LyP-1 and PENT functionalized ENT-loaded nanoparticles respectively. This phenomena reduction in VEGF-C expression is in agreement with the report of Kim and colleagues (Kim et al., 2002) that ENT inhibits vascular endothelial growth factor-mediated signalling through a direct interaction with KDR/Flk-1 *in vivo.* Interestingly, previous report has shown LyP-1 to block lymphangiogenesis-related receptors, such as VEGF signalling proteins and nucleolin expressed on lymphatic vessels on primary tumors and metastatic lymph nodes (Yan et al., 2011). Therefore, we propose that LyP-1 probably enhances the therapeutic effects of ENT in suppressing VEGF-C expression as presented in this study.

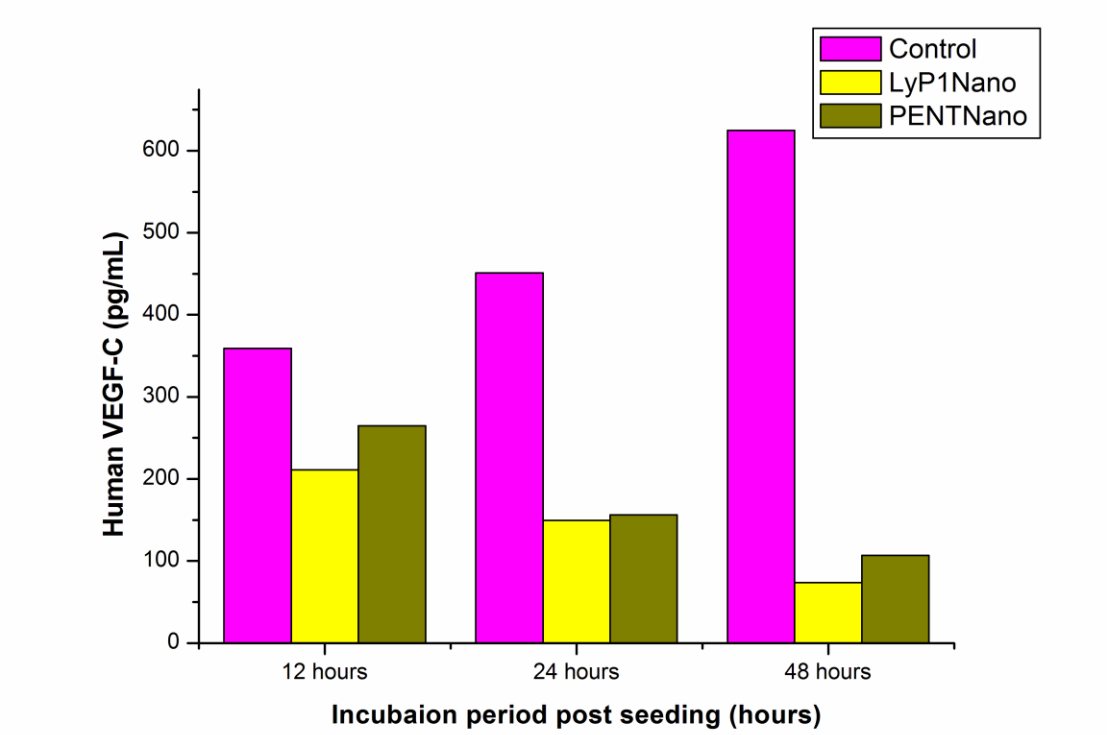


Figure 6.12: VEGF-C expression in Oesophageal squamous cell carcinoma KYSE-30 cells under cell culture conditions. KYSE-30 cells in culture conditions were washed with PBS and cultured in fresh medium without FBS as control. LyP-1 and PENT functionalized ENT-loaded nanoparticles were dissolved in free FBS culture media (2.5 mg/mL) as treatment groups. Culture supernatants were harvested at 12, 24 and 48 hours post-treatment by ELISA assay. Concentration of VEGF in supernatants was represented as pg/mL in duplicates according to the manufacturer's protocol.

Extracellular cell matrix degradation is one of the key factors associated with cancer cells' invasion and metastasis. Meanwhile, MMPs have an important role in this process (Sun and Hemler, 2001), and MMP2 has been proposed to promote the invasion and metastasis of cancer cells to the lymph nodes. The relationship between the inhibitory effects of ENT against MMP-2 secretion on KYSE-30 cells was tested over 48 hour pre-incubation period on conditioned media of KYSE-30 cells exposed to peptide-functionalized ENT-loaded nanoparticles (5mg dissolved in 2mL serum free media). Media supernatant at different time points were collected and quantitated using ELISA assay. As presented in Figure 6.13, ENT effectively suppressed the secretion of MMP-2 relative to untreated KYSE-30 cells. The control cells continuously secret MMP-2 into conditioned media as shown by the gradual increase of

MMP-2 between 12 to 48 hour incubation periods. In relation to the untreated control, cells treated ENT loaded nanoformulation disrupted this pattern of time-dependent increase of MMP-2 secretion. This inhibitory ENT effect on MMP-2 secretion was observed as early as 12 hours post-exposure to both LyP-1 and PENT functionalized ENT-loaded nanoparticles, where its expression was reduced by up to 1.7 folds when compared to the control. Similarly, the inhibition of MMP-2 expression lingered up to 48 hours and resulted in up to 1.5 and 1.8 fold reduction for LyP-1 and PENT functionalized ENT-loaded systems respectively when compared to the untreated control. This corroborates with the findings of Kim and co-workers (Kim et al., 2000) that ENT inhibits endothelial and tumor cellular invasion by blocking the activation and catalytic activity of MMP2. Meanwhile, LyP-1 conjugated nanoparticles have been reported to play a promising role in the direct target of lymphatic metastatic tumors (Luo et al., 2010b). Thus, the anti-MMP2 suppression displayed by ENT could have been aggravated through a complimentary role of LyP-1 peptide in facilitating the direct targeting of ENT-loaded nanoparticles to deliver their optimal payloads at the disease sites.

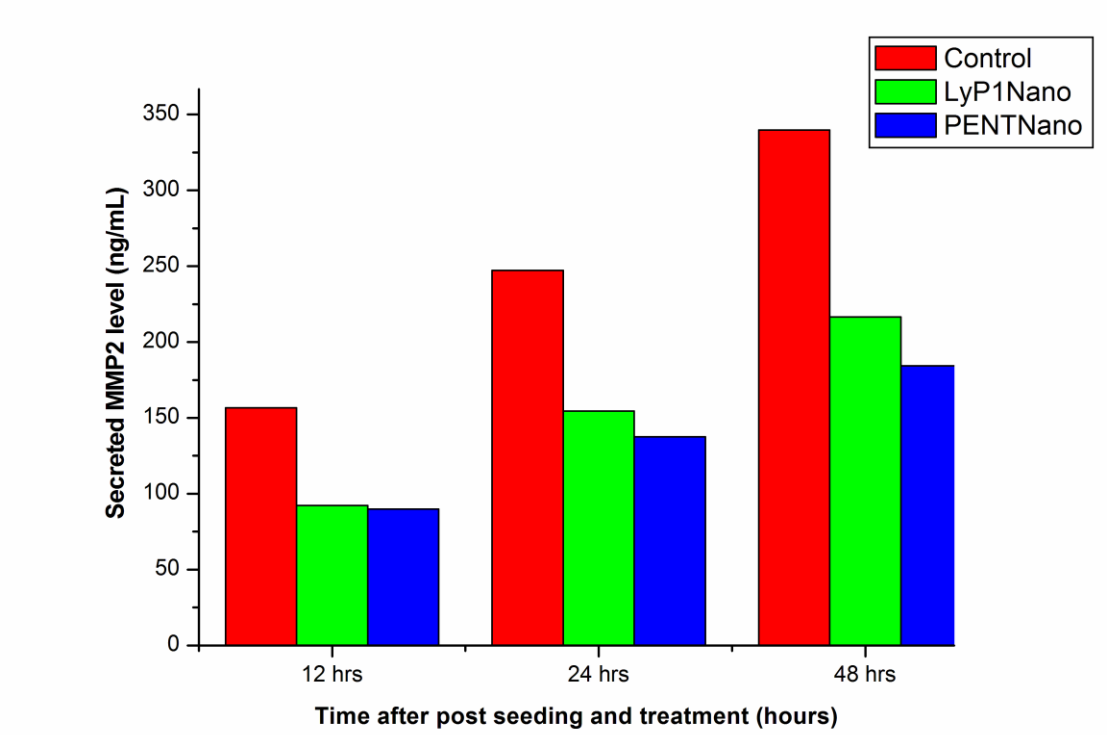


Figure 6.13: Effects of ENT on MMP-2 production by KYSE-30 squamous carcinoma cells. KYSE-30 cells (80% confluent, in a 75 cm^2 flask) were incubated with both LyP-1/PENT functionalized ENT-loaded nanoparticles for 48 hours (each at 2.5 mg/mL). Untreated KYSE-30 cells were used as control. Cell supernatants were harvested for MMP2 assay by ELISA. Samples were prepared in duplicates according to the manufacturer's manual.

Overall, these results demonstrated that both VEGF-C and MMP2 expression and secretion levels were reduced following pre-incubation with LyP-1 and PENT functionalized ENT-loaded nanoformulations suggesting that our designed peptide-enhanced nano-cargo could be a potent delivery vehicle for ENT for improved VEGF-C/MMP2-driven anti-angiogenic therapy in the management of SCC.

6.4. Concluding remarks

Poor delivery, sub-optimal dosage at disease sites and accumulation, low bioavailability, and/or non-specific targeting are major hurdles that confront the clinical efficacy of the vastly discovered new and highly potent therapeutic molecules, specifically in cancer nanomedicine. Meanwhile, targeted delivery still remains the key in the development of enhanced therapeutics.

Design and development of smart nanosystems, such as presented in this study, using homing peptides like LyP-1 and PENT as driver of ENT-loaded nano-cargoes, present promising alternatives for an on-site delivery of ENT for effective anti-tumoral activity in SCC. In all, LyP-1/PENT functionalized ENT-loaded nanoparticles exhibit anti-angiogenic potential against KYSE-30 cells by targeting tumor lymphatics, nucleus and mitochondrial rupture, reduced cell proliferation and migration as well as inhibits VEGF-C and MMP2 expressions as angiogenic makers in SCC management.

6.7. References

Agemy, L., Kotamraju, V.R., Friedmann-Morvinski, D., Sharma, S., Sugahara, K.N., Ruoslahti, E., 2013. Proapoptotic Peptide-Mediated Cancer Therapy Targeted to Cell Surface p32. Mol. Ther. 21, 2195–2204.

Alkilany, A.M., Nagaria, P.K., Hexel, C.R., Shaw, T.J., Murphy, C.J., Wyatt, M.D., 2009. Cellular uptake and cytotoxicity of gold nanorods: molecular origin of cytotoxicity and surface effects. Small Weinh. Bergstr. Ger. 5, 701–708.

Al-Nasiry, S., Geusens, N., Hanssens, M., Luyten, C., Pijnenborg, R., 2007. The use of Alamar Blue assay for quantitative analysis of viability, migration and invasion of choriocarcinoma cells. Hum. Reprod. 22, 1304–1309.

Arvizo, R.R., Miranda, O.R., Thompson, M.A., Pabelick, C.M., Bhattacharya, R., Robertson, J.D., Rotello, V.M., Prakash, Y.S., Mukherjee, P., 2010. Effect of nanoparticle surface charge at the plasma membrane and beyond. Nano Lett. 10, 2543–2548.

Barzi, A., Lenz, H.-J., 2012. Angiogenesis-related agents in esophageal cancer. Expert Opin. Biol. Ther. 12, 1335–1345.

Brannon-Peppas, L., Blanchette, J.O., 2012. Nanoparticle and targeted systems for cancer therapy. Adv. Drug Deliv. Rev., Most Cited Papers In The History Of Advanced Drug

Delivery Reviews: A Tribute to The 25th Anniversary of The Journal 64, Supplement, 206–212.

Chang, D.-K., Chiu, C.-Y., Kuo, S.-Y., Lin, W.-C., Lo, A., Wang, Y.-P., Li, P.-C., Wu, H.-C., 2009. Antiangiogenic Targeting Liposomes Increase Therapeutic Efficacy for Solid Tumors. J. Biol. Chem. 284, 12905–12916.

Chen, B., Le, W., Wang, Y., Li, Z., Wang, D., Ren, L., Lin, L., Cui, S., Hu, J.J., Hu, Y., Yang, P., Ewing, R.C., Shi, D., Cui, Z., 2016. Targeting Negative Surface Charges of Cancer Cells by Multifunctional Nanoprobes. Theranostics 6, 1887–1898.

Chen, H., Cui, S., Zhao, Y., Zhang, C., Zhang, S., Peng, X., 2015. Grafting Chitosan with Polyethylenimine in an Ionic Liquid for Efficient Gene Delivery. PLoS ONE 10.

Christian, S., Pilch, J., Akerman, M.E., Porkka, K., Laakkonen, P., Ruoslahti, E., 2003. Nucleolin expressed at the cell surface is a marker of endothelial cells in angiogenic blood vessels. J. Cell Biol. 163, 871–878.

Conibear, A.C., Chaousis, S., Durek, T., Johan Rosengren, K., Craik, D.J., Schroeder, C.I., 2016. Approaches to the stabilization of bioactive epitopes by grafting and peptide cyclization. Pept. Sci. 106, 89–100.

Danhier, F., Ansorena, E., Silva, J.M., Coco, R., Le Breton, A., Préat, V., 2012. PLGA-based nanoparticles: An overview of biomedical applications. J. Controlled Release, Drug Delivery Research in Europe 161, 505–522.

Danhier, F., Feron, O., Préat, V., 2010. To exploit the tumor microenvironment: Passive and active tumor targeting of nanocarriers for anti-cancer drug delivery. J. Controlled Release 148, 135–146.

Dreaden, E.C., Austin, L.A., Mackey, M.A., El-Sayed, M.A., 2012. Size matters: gold nanoparticles in targeted cancer drug delivery. Ther. Deliv. 3, 457–478.

Dreikhausen, L., Blank, S., Sisic, L., Heger, U., Weichert, W., Jäger, D., Bruckner, T., Giese, N., Grenacher, L., Falk, C., Ott, K., Schmidt, T., 2015. Association of angiogenic factors with prognosis in esophageal cancer. BMC Cancer 15, 121.

Duan, X., Li, Y., 2013. Physicochemical Characteristics of Nanoparticles Affect Circulation, Biodistribution, Cellular Internalization, and Trafficking. Small 9, 1521–1532.

Enbäck, J., Laakkonen, P., 2007. Tumour-homing peptides: tools for targeting, imaging and destruction. Biochem. Soc. Trans. 35, 780–783.

Feng, M., Lee, D., Li, P., 2006. Intracellular uptake and release of poly(ethyleneimine)-co-poly(methyl methacrylate) nanoparticle/pDNA complexes for gene delivery. Int. J. Pharm. 311, 209–214.

Fogal, V., Richardson, A.D., Karmali, P.P., Scheffler, I.E., Smith, J.W., Ruoslahti, E., 2010. Mitochondrial p32 protein is a critical regulator of tumor metabolism via maintenance of oxidative phosphorylation. Mol. Cell. Biol. 30, 1303–1318.

Fogal, V., Zhang, L., Krajewski, S., Ruoslahti, E., 2008. Mitochondrial/cell surface protein p32/gC1qR as a molecular target in tumor cells and tumor stroma. Cancer Res. 68, 7210–7218.

Folkman, J., 1971. Tumor angiogenesis: therapeutic implications. N. Engl. J. Med. 285, 1182–1186.

Folkman, J., 1990. What is the evidence that tumors are angiogenesis dependent? J. Natl. Cancer Inst. 82, 4–6.

Folkman, J., 2006. Antiangiogenesis in cancer therapy--endostatin and its mechanisms of action. Exp. Cell Res. 312, 594–607.

Fukumoto, S., Morifuji, M., Katakura, Y., Ohishi, M., Nakamura, S., n.d. Endostatin inhibits lymph node metastasis by a down-regulation of the vascular endothelial growth factor C expression in tumor cells. Clin. Exp. Metastasis 22, 31–38.

Gao, J.-Q., Zhao, Q.-Q., Lv, T.-F., Shuai, W.-P., Zhou, J., Tang, G.-P., Liang, W.-Q., Tabata, Y., Hu, Y.-L., 2010. Gene-carried chitosan-linked-PEI induced high gene transfection efficiency with low toxicity and significant tumor-suppressive activity. Int. J. Pharm. 387, 286–294.

Goodwin, A.M., 2007. In vitro assays of angiogenesis for assessment of angiogenic and anti-angiogenic agents. Microvasc. Res. 74, 172–183.

Han, Y., Wang, X., Wang, B., Jiang, G., 2016. The progress of angiogenic factors in the development of leukemias. Intractable Rare Dis. Res. 5, 6–16.

Hauck, T.S., Ghazani, A.A., Chan, W.C.W., 2008. Assessing the effect of surface chemistry on gold nanorod uptake, toxicity, and gene expression in mammalian cells. Small Weinh. Bergstr. Ger. 4, 153–159.

Hauert, S., Bhatia, S.N., 2014. Mechanisms of cooperation in cancer nanomedicine: towards systems nanotechnology. Trends Biotechnol., Special Issue: Next Generation Therapeutics 32, 448–455.

Ikomi, F., Hanna, G.K., Schmid-Schönbein, G.W., 1999. Size- and surface-dependent uptake of colloid particles into the lymphatic system. Lymphology 32, 90–102.

Jia, L., Li, Z., Zhang, D., Zhang, Q., Shen, J., Guo, H., Tian, X., Liu, G., Zheng, D., Qi, L., 2013. Redox-responsive catiomer based on PEG-ss-chitosan oligosaccharide-ss-polyethylenimine copolymer for effective gene delivery. Polym Chem 4, 156–165.

Johnson, L.V., Walsh, M.L., Chen, L.B., 1980. Localization of mitochondria in living cells with rhodamine 123. Proc. Natl. Acad. Sci. U. S. A. 77, 990–994.

Justus, C.R., Leffler, N., Ruiz-Echevarria, M., Yang, L.V., 2014. In vitro Cell Migration and Invasion Assays. J. Vis. Exp. JoVE.

Kanapathipillai, M., Brock, A., Ingber, D.E., 2014. Nanoparticle targeting of anti-cancer drugs that alter intracellular signaling or influence the tumor microenvironment. Adv. Drug Deliv. Rev., Engineering of tumor microenvironments 79–80, 107–118.

Kato, Y., Ozawa, S., Miyamoto, C., Maehata, Y., Suzuki, A., Maeda, T., Baba, Y., 2013. Acidic extracellular microenvironment and cancer. Cancer Cell Int. 13, 89.

Kim, Y.-M., Hwang, S., Kim, Y.-M., Pyun, B.-J., Kim, T.-Y., Lee, S.-T., Gho, Y.S., Kwon, Y.-G., 2002. Endostatin Blocks Vascular Endothelial Growth Factor-mediated Signaling via Direct Interaction with KDR/Flk-1. J. Biol. Chem. 277, 27872–27879.

Kim, Y.-M., Jang, J.-W., Lee, O.-H., Yeon, J., Choi, E.-Y., Kim, K.-W., Lee, S.-T., Kwon, Y.-G., 2000. Endostatin Inhibits Endothelial and Tumor Cellular Invasion by Blocking the Activation and Catalytic Activity of Matrix Metalloproteinase 2. Cancer Res. 60, 5410–5413.

Kleespies, A., Guba, M., Jauch, K.-W., Bruns, C.J., 2004. Vascular endothelial growth factor in esophageal cancer. J. Surg. Oncol. 87, 95–104.

Laakkonen, P., Åkerman, M.E., Biliran, H., Yang, M., Ferrer, F., Karpanen, T., Hoffman, R.M., Ruoslahti, E., 2004. Antitumor activity of a homing peptide that targets tumor lymphatics and tumor cells. Proc. Natl. Acad. Sci. U. S. A. 101, 9381–9386.

Laakkonen, P., Vuorinen, K., 2010. Homing peptides as targeted delivery vehicles. Integr. Biol. 2, 326–337.

Lai, S.-L., Cheah, S.-C., Wong, P.-F., Noor, S.M., Mustafa, M.R., 2012. In Vitro and In Vivo Anti-Angiogenic Activities of Panduratin A. PLOS ONE 7, e38103.

Lee, S.J., Jang, J.W., Kim, Y.M., Lee, H.I., Jeon, J.Y., Kwon, Y.G., Lee, S.T., 2002. Endostatin binds to the catalytic domain of matrix metalloproteinase-2. FEBS Lett. 519, 147–152.

Leist, M., Jäättelä, M., 2001. Four deaths and a funeral: From caspases to alternative mechanisms. Nat. Rev. Mol. Cell Biol. 2, 589–598.

Lovrić, J., Cho, S.J., Winnik, F.M., Maysinger, D., 2005. Unmodified cadmium telluride quantum dots induce reactive oxygen species formation leading to multiple organelle damage and cell death. Chem. Biol. 12, 1227–1234.

Luo, G., Yu, X., Jin, C., Yang, F., Fu, D., Long, J., Xu, J., Zhan, C., Lu, W., 2010a. LyP-1-conjugated nanoparticles for targeting drug delivery to lymphatic metastatic tumors. Int. J. Pharm. 385, 150–156.

Luo, G., Yu, X., Jin, C., Yang, F., Fu, D., Long, J., Xu, J., Zhan, C., Lu, W., 2010b. LyP-1-conjugated nanoparticles for targeting drug delivery to lymphatic metastatic tumors. Int. J. Pharm. 385, 150–156.

Mavuso, S., Choonara, Y.E., Marimuthu, T., Kumar, P., du Toit, L.C., Kondiah, P.P.D., Pillay, V., 2016. A dual pH/Redox responsive copper-ligand nanoliposome bioactive complex for the treatment of chronic inflammation. Int. J. Pharm. 509, 348–359.

Murugan, K., Choonara, Y.E., Kumar, P., Bijukumar, D., du Toit, L.C., Pillay, V., 2015. Parameters and characteristics governing cellular internalization and trans-barrier trafficking of nanostructures. Int. J. Nanomedicine 10, 2191–2206.

Owens III, D.E., Peppas, N.A., 2006. Opsonization, biodistribution, and pharmacokinetics of polymeric nanoparticles. Int. J. Pharm. 307, 93–102.

Pan, W.-S., Han, C., Yue, L., Tai, L., Li Zhou, Li, X., Xing, G., Yang, X., Sun, 2013. A novel small peptide as an epidermal growth factor receptor targeting ligand for nanodelivery in vitro. Int. J. Nanomedicine 1541.

Park, J., Nam, J., Won, N., Jin, H., Jung, S., Jung, S., Cho, S.-H., Kim, S., 2011. Compact and Stable Quantum Dots with Positive, Negative, or Zwitterionic Surface: Specific Cell Interactions and Non-Specific Adsorptions by the Surface Charges. Adv. Funct. Mater. 21, 1558–1566.

Pearce, T.R., Shroff, K., Kokkoli, E., 2012. Peptide Targeted Lipid Nanoparticles for Anticancer Drug Delivery. Adv. Mater. 24, 3803–3822.

Qiu, B., Ji, M., Song, X., Zhu, Y., Wang, Z., Zhang, X., Wu, S., Chen, H., Mei, L., Zheng, Y., 2012. Co-delivery of docetaxel and endostatin by a biodegradable nanoparticle for the synergistic treatment of cervical cancer. Nanoscale Res. Lett. 7, 666.

Raman, M., Mohammed, S., 2015. Breast cancer metastasis and the lymphatic system. Oncol. Lett. 10, 1233–1239.

Ramasamy, R., 2015. Vibrational Spectroscopic Studies of Imidazole. Armen. J. Phys. 8, 51–55.

Ruan, S., Yuan, M., Zhang, L., Hu, G., Chen, J., Cun, X., Zhang, Q., Yang, Y., He, Q., Gao, H., 2015. Tumor microenvironment sensitive doxorubicin delivery and release to glioma using angiopep-2 decorated gold nanoparticles. Biomaterials 37, 425–435.

Ruoslahti, E., Bhatia, S.N., Sailor, M.J., 2010. Targeting of drugs and nanoparticles to tumors. J. Cell Biol. 188, 759–768.

Shayan, R., Achen, M.G., Stacker, S.A., 2006. Lymphatic vessels in cancer metastasis: bridging the gaps. Carcinogenesis 27, 1729–1738.

ShiDu Yan, S., 2014. Disrupting cancer cell function by targeting mitochondria. Integr. Cancer Sci. Ther. 1.

Staton, C.A., Reed, M.W.R., Brown, N.J., 2009. A critical analysis of current in vitro and in vivo angiogenesis assays. Int. J. Exp. Pathol. 90, 195–221.

Sugahara, K.N., Teesalu, T., Karmali, P.P., Kotamraju, V.R., Agemy, L., Girard, O.M., Hanahan, D., Mattrey, R.F., Ruoslahti, E., 2009. Tissue-penetrating delivery of compounds and nanoparticles into tumors. Cancer Cell 16, 510–520.

Sun, J., Hemler, M.E., 2001. Regulation of MMP-1 and MMP-2 Production through CD147/Extracellular Matrix Metalloproteinase Inducer Interactions. Cancer Res. 61, 2276–2281.

Sznol, M., Davis, T., 2002. Tumor antigens as targets for anticancer drug development. In: Kerr, B.C.B.J. (Ed.), Anticancer Drug Development. Academic Press, San Diego, pp. 157–170.

Thorek, D.L.J., Tsourkas, A., 2008. Size, charge and concentration dependent uptake of iron oxide particles by non-phagocytic cells. Biomaterials 29, 3583–3590.

Torchilin, V.P., Lukyanov, A.N., 2003. Peptide and protein drug delivery to and into tumors: challenges and solutions. Drug Discov. Today 8, 259–266.

Verma, A., Stellacci, F., 2010. Effect of Surface Properties on Nanoparticle–Cell Interactions. Small 6, 12–21.

Wigle, J.T., Harvey, N., Detmar, M., Lagutina, I., Grosveld, G., Gunn, M.D., Jackson, D.G., Oliver, G., 2002. An essential role for Prox1 in the induction of the lymphatic endothelial cell phenotype. EMBO J. 21, 1505–1513.

Wu, X., Zhao, R., Li, Z., Yao, M., Wang, H., Han, J., Qu, S., Chen, X., Qian, L., Sun, Y., Xu, Y., Gu, J., 2004. A novel small peptide as a targeting ligand for receptor tyrosine kinase Tie2. Biochem. Biophys. Res. Commun. 315, 1004–1010.

Yan, Z., Wang, F., Wen, Z., Zhan, C., Feng, L., Liu, Y., Wei, X., Xie, C., Lu, W., 2012. LyP-1-conjugated PEGylated liposomes: A carrier system for targeted therapy of lymphatic metastatic tumor. J. Controlled Release 157, 118–125.

Yan, Z., Zhan, C., Wen, Z., Feng, L., Wang, F., Liu, Y., Yang, X., Dong, Q., Min Liu, Lu, W., 2011. LyP-1-conjugated doxorubicin-loaded liposomes suppress lymphatic metastasis by inhibiting lymph node metastases and destroying tumor lymphatics. Nanotechnology 22, 415103.

Yao, Y.-L., Yang, W.-M., 2005. Nuclear proteins: promising targets for cancer drugs. Curr. Cancer Drug Targets 5, 595–610.

Zhang, X.-X., Eden, H.S., Chen, X., 2012. Peptides in cancer nanomedicine: Drug carriers, targeting ligands and protease substrates. J. Controlled Release 159, 2–13.

Zheng, M., 2009. Endostatin derivative angiogenesis inhibitors. Chin. Med. J. (Engl.) 122, 1947–1951.

Zheng, Y., Sun, M., Chen, J., He, L., Zhao, N., Chen, K., 2016. Effect of VEGF-C siRNA and endostatin on ring formation and proliferation of esophageal squamous cell carcinoma lymphatic endothelial cells. OncoTargets Ther. 9, 6727–6732.

CHAPTER 7

IN VIVO SUBCUTANEOUS DELIVERY OF AN INJECTABLE PEPTIDE-ENHANCED ENDOSTATIN LOADED NANO-SYSTEM FOR OESOPHAGEAL SQUAMOUS CELL CARCINOMA TREATMENT IN ATHYMIC MICE MODEL

This study had received the approval of the Animal Ethics Screening Committee of the University of the Witwatersrand with ethics clearance number 2016/01/04/D (Appendix 9.4.1*). Ethics clearance was granted for the in vivo studies.*

7.1 Introduction

Cancer remains a fatal disease with features of abnormal cell proliferation due to genetic mutation (Nair and Reddy, 2016). Oesophageal Squamous cell carcinoma (OSCC) is ranked 8th as the most common cancer type and 6th major cause of cancer death worldwide (Adebowale et al., 2015; Higuchi et al., 2009). Chemotherapy is the main therapeutic option for treating people living with OSCC. However, drug resistance and lack of specificity are major obstacles that limit its efficacy in combating the disease even after combination chemotherapy (Wang and Thanou, 2010). Thus, a paradigm shift in cancer nanomedicines is the design of smart nanoparticulate systems functionalized with specialized targeting moieties, such as small homing peptides and ligands: LyP-1, Pentapeptide, FA referred to as PEL nanosystem in this study, to enhance the direct delivery of anti-cancer drugs with optimum therapeutic effects on tumor cells and vasculature without or with minimum side effects on healthy cells.

In vitro design, optimization and *ex-vivo* testing of the PEL nanosystem have been examined in Chapters 3, 4, 5 and 6. However, an *in vivo* study is required in order to validate the efficiency of the designed PEL delivery system. *In vitro* experimental data is not sufficient to represent *in vivo*

conditions and the use of computer models would not provide a holistic correlation between *in vitro and in vivo* parameters needed to determine the effectiveness of the delivery system. Further, the application of *in vivo* analysis allows for a better and accurate pharmacokinetic and pharmacodynamic evaluation of the therapeutic agent as well as providing more realistic clinical results (Crawford et al., 1998; Gong et al., 2012). It is important to first carry out *in vivo* experiments in animal models prior to testing it in humans due to ethical considerations.

The role of animal models in cancer research is vital due to their ability to give better insights about the molecular mechanisms underlying metastasis and tumor host interactions (Hibberd et al., 2013; Nair and Reddy, 2016; Saxena and Christofori, 2013 - order of references). Additionally, the use of animal models is crucial in understanding the pathophysiology of various diseases thereby contributing indirectly to the development of novel interventions in cancer nanomedicines (Ruggeri et al., 2014). As opposed to several other animal models that have been used in oesophageal cancer *in vivo* research including the rat (*Rattus norvegicus*) (Hashimoto, 2012; Hori et al., 2001), mouse (*Mus musculus*) (Crescenzi et al., 2011a; Nakagawa et al., 1997), rabbit (*Oryctolagus cuniculus*) (Liu et al., 2013), guinea pig (*Cavia porcellus*) (Cheng et al., 2014) and hamster (*Mesocricetus auratus*) (Dunham and Sheets, 1974), athymic (nude) mice are considered suitable candidates for this project due to their partially compromised immune system and susceptibility to OSCC cancer cell lines (Liu et al., 2008).

The goal of this study is to elucidate the necessary optimum parameters for delivey of the PEL endostatin-loaded nanosystem in the athymic nude mice model prior to pilot human biostudies. Furthermore, this study also served as a platform to investigate the safety and tolerance of the PEL nanosystem *in vivo*.

7.2. Materials and Methods

7.2.1. Cell lines and establishment of xenografts

KYSE-30 is an established OSCC cell line (Li et al., 2015; Shimada et al., 1992). Human oesophageal cancer cell line (KYSE-30) were purchased from Life Bioscience (Oakleigh, VIC, Australia) and used within six month of resuscitation. KYSE-30 cells were grown in RPMI 1640 medium + Ham's F-12 media (1:1) supplemented with 10% FBS and 2mM glutamine. The culture was maintained at 37°C in a humidified 5% CO_2 and 95% air atmosphere.

7.2.2. Animal welfare, housing and habituation prior to drug study experiment

Mice were housed in a cage maintained under a 12 hour light and dark cycle and fed a commercial diet. Figure 7.1 represents a digital photograph showing the mice in their cages and the daily habituation process. Habituation is an important process before tumor inoculation into the mice and prior to subsequent dosage form administration so as to foster conducive working conditions with improved animal handling and reduce the challenges that could impede the administration of formulations. The habituation process involved visiting the animals twice daily for routine check-up, ensuring their feed and water was intact, and weight measurement.

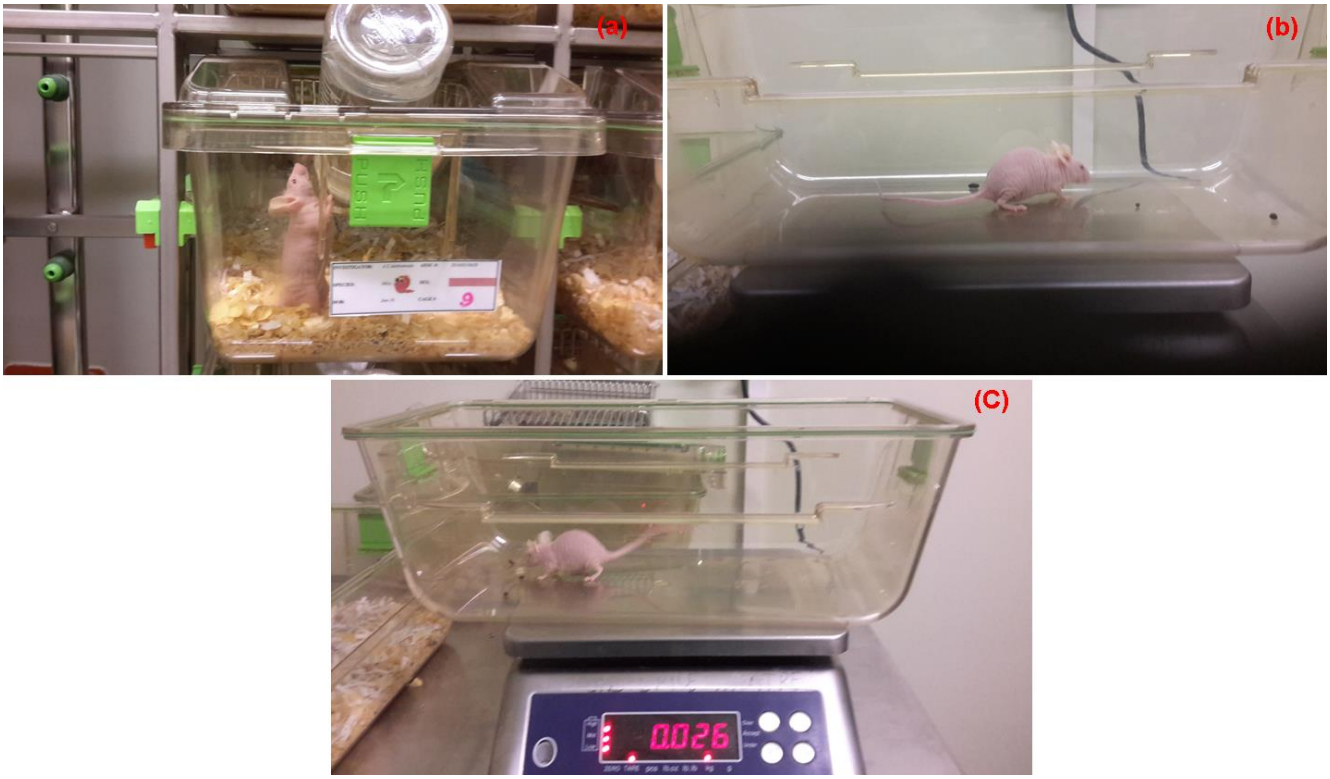


Figure 7.1: Photographic evidence of (a) Housing of the nude mice (b - c) daily measurement of mouse weight using the weighing balance.

7.2.3. Administration of KYSE-30 cells and development of tumor xenograft in mice

All athymic nude mice were anesthetized with intramuscular ketamine HCl (60mg/kg) and xylazine HCL (10mg/kg). The mice were then injected subcutaneously with 1 x 10^6 KYSE-30 cancer cells in the FBS free culture medium at the right flank. As presented in Figure 7.2, a solid tumor developed in the infected mice 31 days post-inoculation with KYSE-30 cells. Nair and Reddy (2016) reported the growth of solid tumor at a minimum time interval of 4 weeks post inoculation (Crescenzi et al., 2011a; Nair and Reddy, 2016). The solid tumor was measured using a digital calliper upon its visibility 31 days post inoculation as shown in Figure 7.4.



Figure 7.2: Photographic image of solid tumor. Mice developed tumor after 35 days post-KYSE-30 cells inoculation.

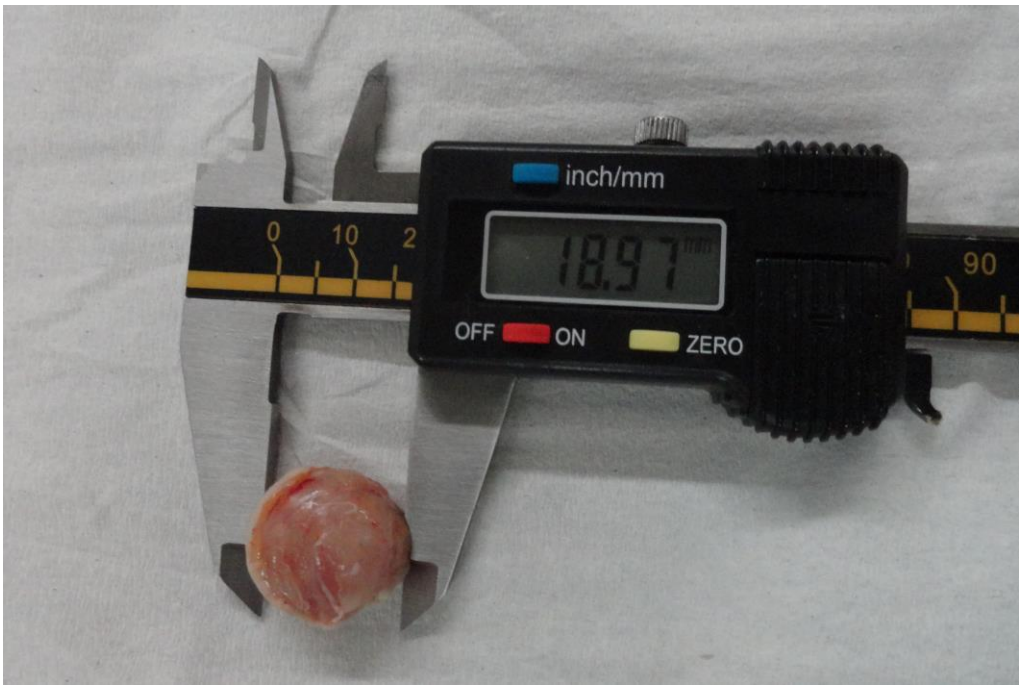


Figure 7.3: Representative photographic image showing excised tumor measurement using a digital caliper from an infected mouse among the control group.

7.2.4. Preparation of endostatin-loaded PEL nanosystem components

The PEL nanosystems loaded with endostatin (comprising of Folate-functionalized and Peptide-enhanced ENT-loaded nanoparticles), were prepared as discussed in Chapter 5 and 6 under sub-sections 5.2.2.1 and 6.2.2.1 respectively.

7.2.5. Administration of the PEL nanosystem loaded with endostatin

The PEL nanosystems loaded with endostatin were subcutaneously injected around the peri-tumoral region of infected mice to target folate receptors and nuclear/mitochondrial proteins expressed on the surface of OSCC cells (Antony, 1996; Christian et al., 2003; Hilgenbrink and Low, 2005; Yao and Yang, 2005; Yan et al., 2011). The PEL nanosystems loaded with endostatin were administered to the experimental groups when the tumor was visible approximately 31 days after inoculation (Crescenzi et al., 2011a). Meanwhile, mice in the control group were treated with PBS without endostatin. Mice were anesthetized with ketamine HCL

(60mg/kg) and xylazine HCL (10mg/kg) and then received 1mL of the PEL nanosystems at an endostatin dosage of 20mg/kg. This was administered subcutaneously (S.C.) with an 18G needle and a 1mL syringe.

7.2.6. *In vivo* study design

16 weeks old athymic nude mice were imported for this study. The study design comprised of 4 experimental groups (1, 2, 3, and 4), and a control/comparison group of mice each with a sample size n=3. Different formulations were evaluated in each group. In the experimental groups, PEL nanosystem-loaded endostatin nanoparticles were utilized for the targeted treatment of OSCC.

Ex vivo toxicity studies of the various formulations as delivery systems were investigated prior to the *in vivo* experimental animal study. Meanwhile, cellular cytotoxicity of these formulations, with or without the targeting ligands (folate) and homing peptides (LyP-1/PENT), at relevant dose levels was determined. Additionally, the cellular uptake of the nanoparticles to determine the selectivity of these particles for the targeted cells was investigated. Cell death was assessed by mitochondrial/nuclear function using the tetrazolium salt MTT/Alamar blue assay. Studies examining the cytotoxicity of the polymers without endostatin were also conducted as presented in previous chapters.

15 athymic nude mice were randomly assigned to 5 groups of 3 mice each per group:

- **Group 1** (Control/Comparison group 1, n=3): OSCC cell line (KYSE-30) was injected subcutaneously into the right flank of the mice. This group also received a subcutaneous injection containing PBS.

- **Group 2** (experimental group 1, n=3): OSCC cell line (KYSE-30) was injected subcutaneously into the right flank of the mice. This group also received a subcutaneous injection containing endostatin alone in order to compare the synthesized PEL nanosystem with what is currently obtained in the market.

- **Group 3** (Experimental group 2, n=3): OSCC cell line (KYSE-30) was injected subcutaneously into the right flank of the mice. This group also received a subcutaneous injection of the PEL nanosystem containing PEG-CHI-PEI endostatin-loaded nanoparticles without the ligands.

- **Group 4** (Experimental group 3, n=3): OSCC cell line (KYSE-30) was injected subcutaneously into the right flank of the mice. This group also received a subcutaneous injection containing of the PEL nanosystem containing FA-conjugated PEG-CHI-PEI endostatin-loaded nanoparticles without the homing peptide.

- **Group 5** (Experimental group 4, n=3): OSCC cell line (KYSE-30) was injected subcutaneously into the right flank of the mice. This group also received a subcutaneous injection of the PEL nanosystem containing LyP-1/PENT- conjugated PEG-CHI-PEI endostatin-loaded nanoparticles.

Previous research performed on athymic nude mice has indicated an intraperitoneal administration of murine recombinant endostatin with a concentration of 2.5 mg/kg/day, 5 times a week for two weeks (Hanna et al., 2000). Meanwhile, Yokoyama and Ramakrishnan (2005) reported a subcutaneous administration of 20 mg/kg/day endostatin in a phosphate buffer saline (PBS) solution in athymic nude mice for 12 consecutive days. All injections were administered

subcutaneously - 2cm away from the growing tumor mass. These dosages were employed in this study and the confidence level was set at 95% as outlined in Table 7.1. Further illustration for the model highlighted above is shown using flow diagram in Figure 7.4.

Table 7.1: Drugs and recommended dosages as administered to mice

Drug/Substance	Route (e.g., S.C, I.V., I.M.)	Dose	Frequency
Endostatin	subcutaneous	4 mg/kg	once daily for 5 consecutive days.
PEL nanosystems loaded with endostatin	Subcutaneous	20mg/kg	twice weekly (four injections in all)
Xylazine	Intramuscular injection	10mg/kg	Administered for anaesthesia before injection of cancer cells, drug loaded PEL nanosystems and prior to euthanasia.
Ketamine	Intramuscular injection	60mg/kg	Administered for anaesthesia before injection of cancer cells, drug loaded PEL nanosystems. Isofor was administered as anaesthesia prior to euthanasia.
Sodium Pentobarbitone	Intracardiac injection	200mg/kg	Administered once off for euthanasia.
Isoflurane	Inhalation	1.5% in oxygen	Used as anaesthesia before ultrasonic vevo imaging

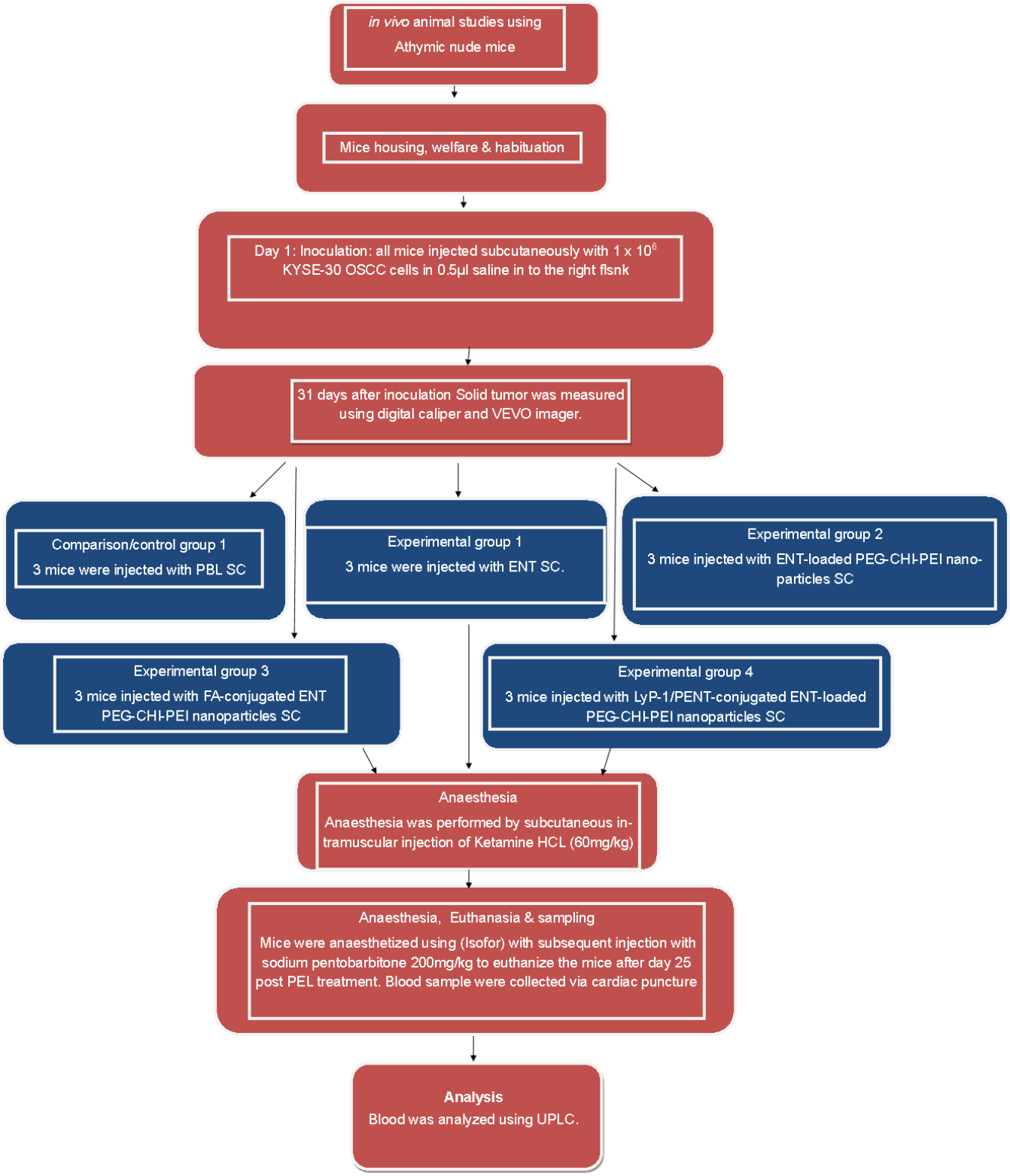


Figure 7.4: Schematic showing the in vivo studies model for the PEL nanosystem containing peptide/ligand-PEG-CHI-PEI nanoparticles loaded with/without endostatin as preclinical studies for targeting OSCC.

The mice were randomly assigned to five groups. All the groups were injected with OSCC cell line (KYSE-30) subcutaneously and the tumors were allowed to develop over 31 days (Crescenzi et al., 2011b). When the tumors have become visible approximately 31 days post inoculation, the mice in each group received different treatment as shown in Figure 7.4.

7.2.7. Ultrasound imaging of solid tumor in athymic nude mice

Athymic mice that have developed solid tumor were exposed to ultrasound experiment to visualize and measure solid tumor (Figure 7.5). Tumor bearing mice were imaged using a Vevo 2100® treatment (Visual sonics Inc, Toronto, Canada) imager. Once the tumors have developed, the imager was used to detect the effectiveness and course of the treatment. High-Frequency Ultrasound Preclinical Imaging using the Vevo 2100 High-Frequency Ultrasound System capable of both 2D and 3D *in vivo* imaging in small animals was used to calculate the lesion size. For ultrasound imaging, the Vevo 2100 high frequency ultrasound system (VisualSonics, Inc., Toronto, Ontario, Canada) was also employed. The Vevo 2100 ultrasound probe has a 40MHz center frequency with a 6-mm focal depth and enables high-resolution imaging down to 30 microns. The spatial resolution at the focus is 40 x 80 x 80 μm^3.

7.2.7.1. Protocol for microultrasound imaging

- Mice were anaesthetised and anaesthesia was maintained in a chamber with 2% isoflurane gas in oxygen. Body temperature was constantly monitored and maintained at 37°C.
- Mice were then placed supine on the imaging stage. Their fore- and hind legs were extended and taped to the stage to enable monitoring of respiration and minimisation of respiration motion.
- Ultrasound imaging gel (EcoGel 100™ imaging ultrasound gel) was applied on the site of interest.
- Solid tumor was visualised with a moveable transducer using the B-mode for general imaging.

- Images were acquired as frames and video loops.

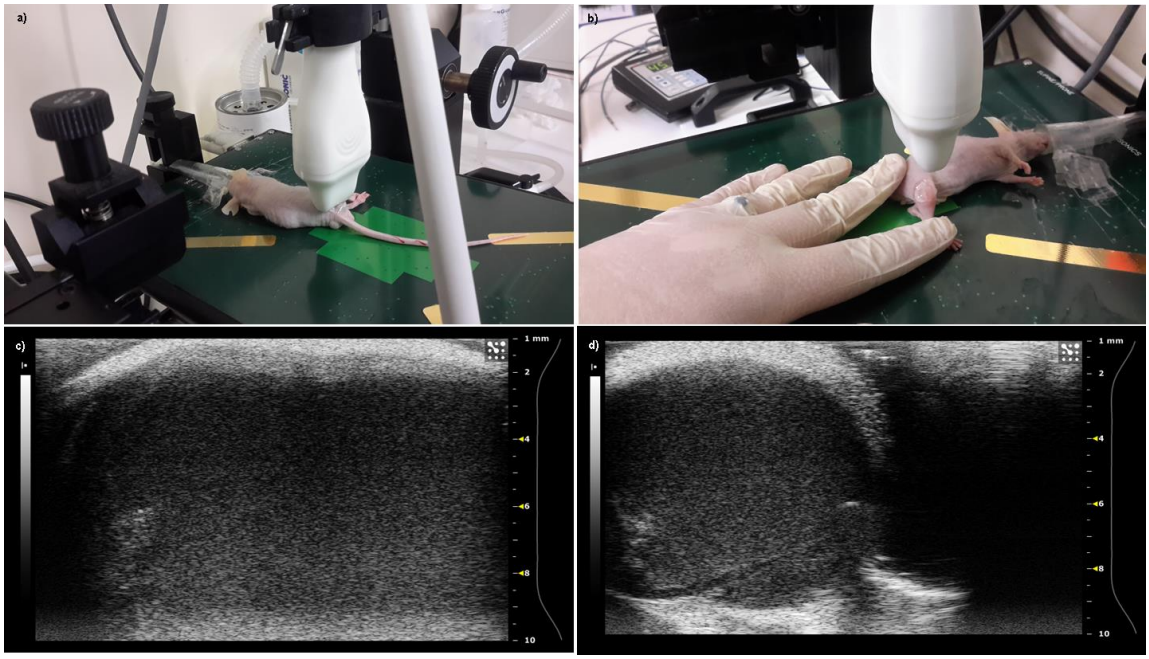


Figure 7.5: Ultrasound imaging experiment using Vevo ultrasound imager. (a) Mice were anaesthezied with isoflurane (b) ultrasound imaging gel was applied onto the tumor and visualized employing a transducer (c) – (d) ultrasound images of solid tumor.

7.2.8. Blood collection and tissue sampling for histological analyses

As outlined in the model in Figure 7.4, infected mice were anaesthetized using isoflurane with subsequent injection with sodium pentobarbitone to euthanize the mice after day 25 post PBS, endostatin and endostatin-loaded PEL treatments. Blood samples were collected via cardiac puncture as shown in Figure 7.6. Solid tumor was excised and tissue samples including the heart, liver, kidney, lungs, spleen and the oesophagus were collected through surgery and stored in 10%$^{v}/_{v}$ neutral buffered formaldehyde for subsequent histological studies (Figure 7.7).



Figure 7.6: Blood collection from euthanized mouse using cardiac puncture.



Figure 7.7: Tissue sample collection. Solid tumor, the heart, lung, kidney, liver, spleen, and the oesophagus were surgically collected and stored in 10%v/v neutral buffered formaldehyde.

7.2.9. Preparation of calibration standards and generation of corresponding *in vivo* and *in vitro* endostatin release samples

Calibration standards were prepared for generating a standard curve of endostatin and for method validation; 10µL aliquots the internal standard solution of diclofenac sodium, were added to 50µL endostatin concentrations (0.1 – 0.5mg/mL, stock concentration of 1mg/mL) in an inert polypropylene tubes and diluted up to 500µL. Aliquots (300µL) of the supernatants were filtered through a 0.22µm Millipore® filter and transferred to UPLC injection vials. Thereafter, 10µL of the filtered solution was injected onto the UPLC column to measure the amount of endostatin released. Calibration curves were generated by the ratio of the peak areas (between diclofenac sodium: as the internal standard, and endostatin) against the concentration data for the calibration standards. A linear regression analysis was applied to the calibration curves. Five calibration standards were generated with concentrations spanning from 0.05 to 0.5mg/mL of endostatin PBS. A standard linear curve was constructed from the five calibration standards.

In order to generate corresponding *in vitro* endostatin release samples, release studies were conducted on 5mg of the optimal PEL formulation (containing 0.5mg/mL endostatin) in 2mL PBS at pH 7.4 in an oscillating laboratory incubator. Samples were withdrawn at 0.5, 1, 2, 4 and 8 hours and filtered (0.22µm PVDF, Millipore Corporation, USA). Filtered samples were subsequently analysed via UPLC as described for the calibration standards for endostatin determination.

7.2.10. Quantification of *in vivo* endostatin concentrations released from the PEL nanosystem into the plasma of nude mice with solid tumor

Frozen plasma samples collected from the blood of euthanized mice were allowed to thaw at room temperature (±25°C) and plasma containing endostatin: aliquot of plasma (500µL) was transferred to polypropylene tubes for the validation of endostatin release *in vivo*. An ultra-

performance liquid chromatographic (UPLC) method (Waters® ACQUITY™LC system (Waters®, Milford, MA, USA) coupled 258 with a photodiode array detector (PDA), and Empower® Pro Software (Waters®, Milford, MA, USA)) was developed to evaluate the amount of ENT released from the nanoparticulate systems into the blood of infected mice treated with the native ENT and the PEL nanosystem loaded with ENT. The UPLC was fitted with an Aquity UPLC® Bridged Ethyl Hybrid (BEH) Shield RP18 column, with a pore size of 1.7µm. A gradient method with a run time of 2 minutes was developed using acetonitrile and double deionized water as the mobile phase (Table 7.2). UPLC analysis enabled accurate simultaneous detection of micro-levels of endostatin. A solvent flow rate of 0.25mL/min was maintained with an average initial pressure of 6500psi. The pre-filtered samples (10µL) were injected onto the column. The column and sample manager temperature was maintained at 21±0.5ºC. Prior to use, the column was equilibrated by passing 45mL of mobile phase solvent through the system. The eluent was monitored at analytical wavelength set at 280nm and the entire assay procedure was performed at room temperature (25±0.5ºC).

Table 7.2: UPLC parameters employed for the determination of ENT concentration *in vitro* and *in vivo*

Parameters	**Conditions**
Mobile phase	ACN and Water (50:50) isocratic gradient
Flow rate	0.25mL/min
Injection volume	10µL
Wavelength	280nm
Column temperature	21ºC
Sample temperature	25ºC

Diclofenac sodium was identified via preliminary screening assays as an appropriate internal standard for endostatin. Diclofenac sodium has a separate retention time of 1.46 minutes, as opposed to ENT having a retention time of 0.76 mins for quality analysis of peak areas. A standard linear curve was generated, as subsequently described to evaluate the respective ENT concentrations released from the PEL nanosystem at various time points both *in vitro* and *in*

vivo.

7.3. Results and Discussions

7.3.1. Effects of ENT-loaded PEL nanosystems on tumor volume and mice weight

Angiogenesis, as a recruitment process for new blood vessels, is generally upregulated in tumor growth and metastasis and evidence abounds in support of the activation of angiogenesis in esophageal cancer (Inoue et al., 1997; Karpanen et al., 2001; Kitadai et al., 1998). Importantly, vascular endothelial growth factor (VEGF) is highly expressed in esophageal cancer as evidenced in surgical samples in patients undergoing curative surgery (Kleespies et al., 2004; Shih et al., 2000). Meanwhile, studies have shown that increase in microvessel density (MVD) varies proportionately to disease progression, tumor size and stage, and depth of invasion in esophageal carcinoma (Crescenzi et al., 2011b). Current strategies that target angiogenesis and reduce tumor growth and metastasis are being explored in cancer nanomedicines. Endogenous inhibitors of angiogenesis, including endostatin, present potent alternatives in the management of cancer disease including OSCC. As evidenced in the previous chapters (Chapter 4, 5 and 6), the endostatin-loaded PEL nanosystem served as a potential nano-cargo for endostatin delivery for direct and specific targeting of tumor vasculature with enhanced anti-tumoral activities. Meanwhile, *in vivo* testing of PEL nanosystems is essential to validate its possible clinical significance in OSCC management.

As presented in Figure 7.11, PEL nanosystems loaded with endostatin showed higher anti-tumoral effects on tumor mass relative to the control. Meanwhile, mice treated with ENT and ENT-loaded nanoparticles showed increased therapeutic efficacies on tumor volume as opposed to the control group that received only PBS. Overall, after 31 days post inoculation with KYSE-30 cells and appearance of solid tumor, tumor mass increased up to 5505.54mm^3 in the control group while a substantial reduction occurred in the treatment group down to 128.23 mm^3

(97.67%). Tumor volume reduced from 1000.2 mm^3 to 567.64 mm^3 (43.25%) in the ENT group, from 324.43 mm^3 to 190.25 mm^3 (41.36%) in ENT-Nano group, from 1374.21 mm^3 to 998.67 mm^3 (27.33%) in FA-ENT-Nano group, and from 328.86 mm^3 to 128.23 mm^3 (61.01%) in peptide-ENT-Nano group after treatment. There is no significant difference in the reduction in tumor mass between mice treated with FA-ENT-loaded nanoparticles and those that received peptide-ENT-loaded nanoparticles. However, ENT-loaded nanoparticles showed a two-fold reduction in tumor volume relative to the pure ENT treated group. Overall, the PEG-PEI-CHT nano-construct contributes to the effective delivery of endostatin for an enhanced anti-tumoral activity. More importantly, surface modification using both folate (FA) and short homing peptides (LyP-1 and Pentapeptide) in PEL nanosystems, contributes immensely in facilitating the direct and targeted delivery of endostatin for anti-tumoral activity in OSCC therapy.

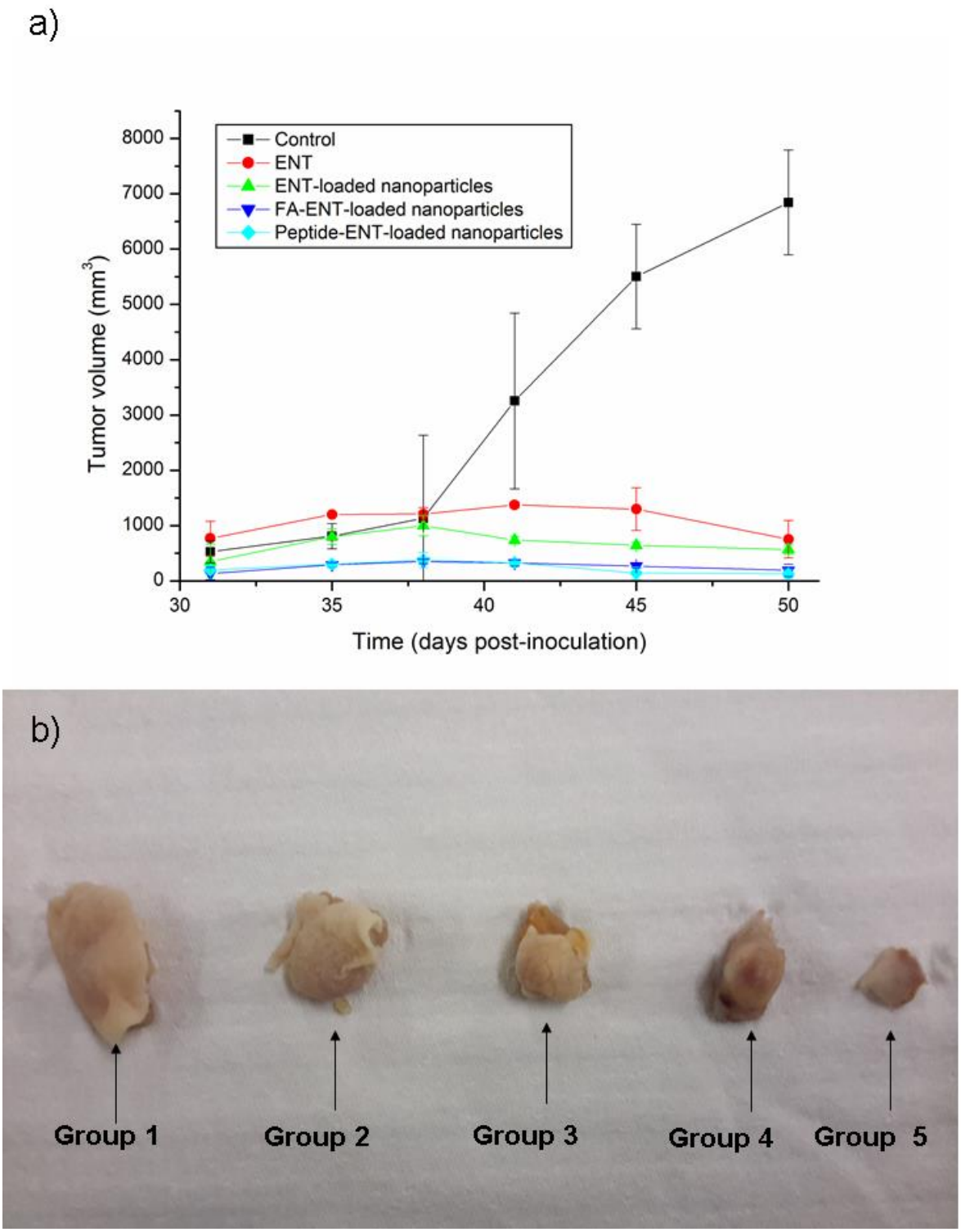


Figure 7.8: Therapeutic effects of PEL nanosystem treatment in KYSE-30 xenografts. (a) Kinetics of tumor growth. Athymic nude mice were implanted with KYSE-30 cells (n=3 mice/group) and treated or not treated with native ENT, ENT-loaded nanoparticles, FA-functionalized ENT-loaded nanoparticles and peptide-enhanced ENT-loaded nanoparticles (20 mg/kg/d). Mice were sacrificed on the 25 days post-treatment (b) selected macroscopic images

of excised solid tumors. Group 1 = Control, group 2 = ENT treated, group 3 = ENT-loaded nanoparticles, group 4 = FA-ENT-loaded nanoparticles, and group 5 = peptide-ENT-loaded nanoparticles.

Endostatin has been shown to be a potent anti-angiogenic factor and inhibits tumor growth and metastasis (O'Reilly et al., 1997). Increased tumor volume should result in reduction in the total body weight of the mice (Murray et al., 1997). As such, the control mice that received only PBS, with increasing tumor mass, showed a dramatic reduction in total body weight (29.20g – 22.96g) as opposed to the treatment groups after the development of tumor 31 days post inoculation as presented in Figure 7.11. Interestingly, mice within the treatment groups showed little or no reduction in body weight over 24 days post treatment either with native endostatin or the PEL nanosystems loaded with endostatin. The body weight of mice treatment groups changed from 28.05g – 27.53g for ENT group, 27.01g – 28.03g for the ENT-Nano group, 28.16g – 26.42g for the FA-ENT-Nano group, and 26.72g – 25.12g for the peptide-ENT-Nano group. Therefore, findings from this study showed that endostatin inhibits tumor growth and thus minimizes total body weight loss in athymic nude mice with a tumor xenograft. More importantly, the novel PEL nanosystems showed immense potential as a delivery vehicle for enhanced and targeted anti-tumoral effects for endostatin in OSCC therapy.

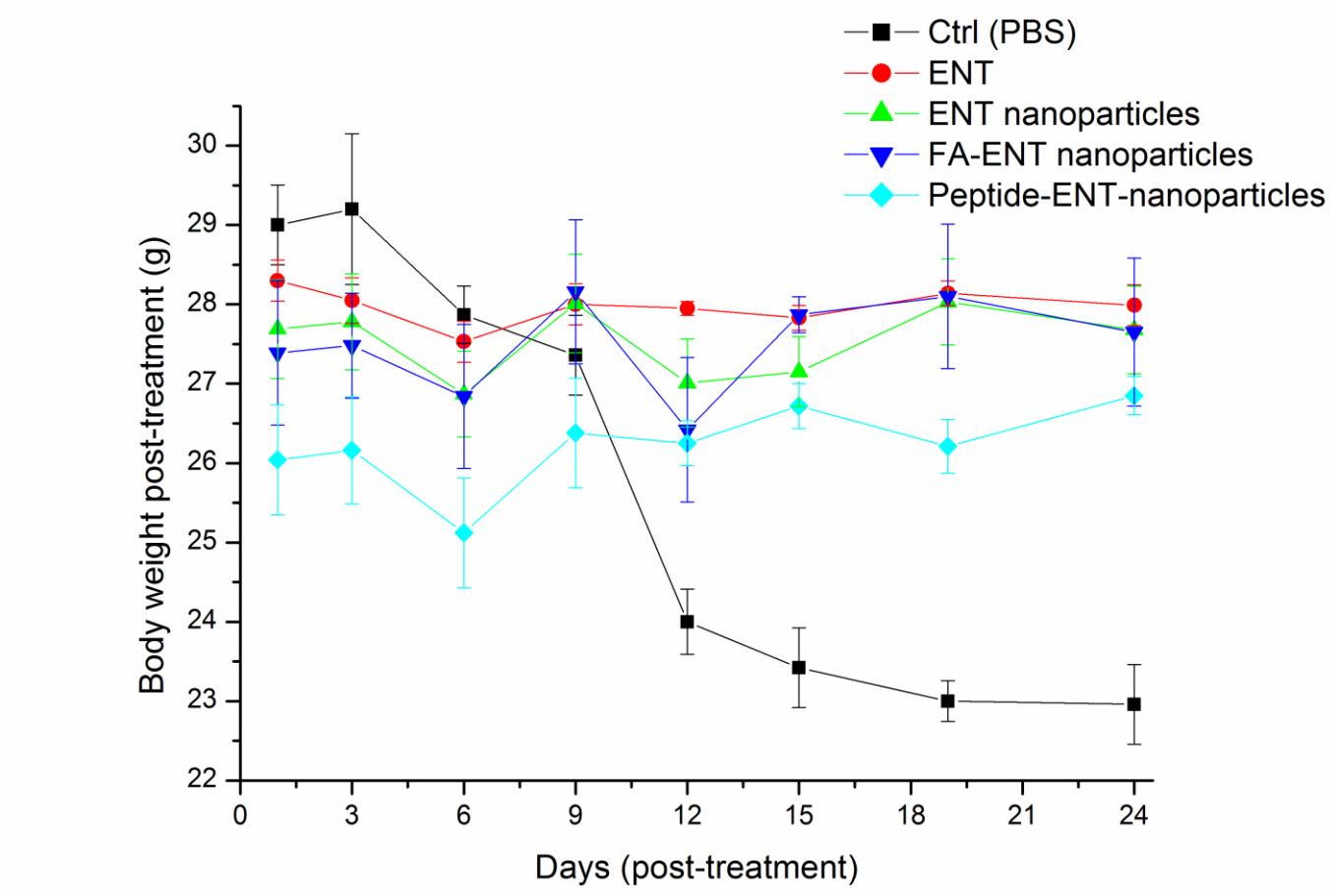


Figure 7.9: Change in body mass of athymic mass for the control and treatment groups over the study period. Human OSCC cells (KYSE-30) (5×10^6) were implanted in the right flank of athymic mice (*n* = 3). Equimolar injections were administered every day (for a total of 5 times) of Control (PBS), ENT (4mg/kg), ENT-Nano (20mg/kg), FA-ENT-Nano (20mg/kg), and Peptide-ENT-Nano (20mg/kg). No significant difference was observed in the body weight of treated mice. Meanwhile, there is a dramtic reduction in mice body weight of control (untreated) from 29g – 22.96g before termination. Error bars indicate ± SD.

7.3.2. In vivo quantification of plasma concentration of endostatin released from the PEL nanosystem in mice bearing KYSE-30 cells xenograft

Chromatographic analysis as presented in Figure 7.10 showed two distinct and defined peaks at 280nm with respective retention times of 0.76 minutes (endostatin), and 1.46 minutes (diclofenac sodium), respectively. The amount of endostatin released from the PEL nanosystems as well as native endostatin into the serum after S.C. administration into infected mice were extrapolated from the standard endostatin graph in Figure 7.11. *In vivo* release

kinetics demonstrated controlled and prolonged permeation of endostatin through the PEL nanosystem into the blood circulation. As presented in Figure 7.12, 30 minutes after administration, the amount of endostatin released was 0.13, 0.09 and 0.10 mg/mL for ENT, ENT-loaded nanoparticles, and the PEL enabled nanosystem, respectively. Similarly, 0.16mg/mL equimolar amount of endostatin was released after 2 hours post-administration from ENT-loaded nanoparticles and the PEL nanosystem while 0.19mg/mL of endostatin was released from the native ENT administration. Interestingly, both ENT nanoparticles and PEL nanosystems showed a controlled endostatin release of 0.28mg/mL and 0.31mg/mL 8 hours post-administration, respectively, as opposed to 0.44mg/mL endostatin released when native endostatin was administered. A possible explanation for this sustained release kinetics from the PEL enabled nanosystem could be owing to the enhanced targeting of ENT facilitated by the ligand moieties attached to the surface of the nanoparticles. Released endostatin probably concentrates around the tumor mass before diffusion into the blood circulation. Un-encapsulated endostatin diffuses more rapidly into the systemic circulation thus facilitating its rapid clearance from the blood. Similarly, previous reports have shown that nanoparticles increased drug *in vivo* circulation time and controlled release of their payloads for enhanced therapeutic effects in relation to native drugs (Davis et al., 2008; Mohanraj and Chen, 2007; Wang et al., 2012). Thus, the PEL nanosystem, as presented in this study, could serve as a potential vector for enhanced and targeted delivery of endostatin or other anti-cancer drugs in cancer nanomedicine.

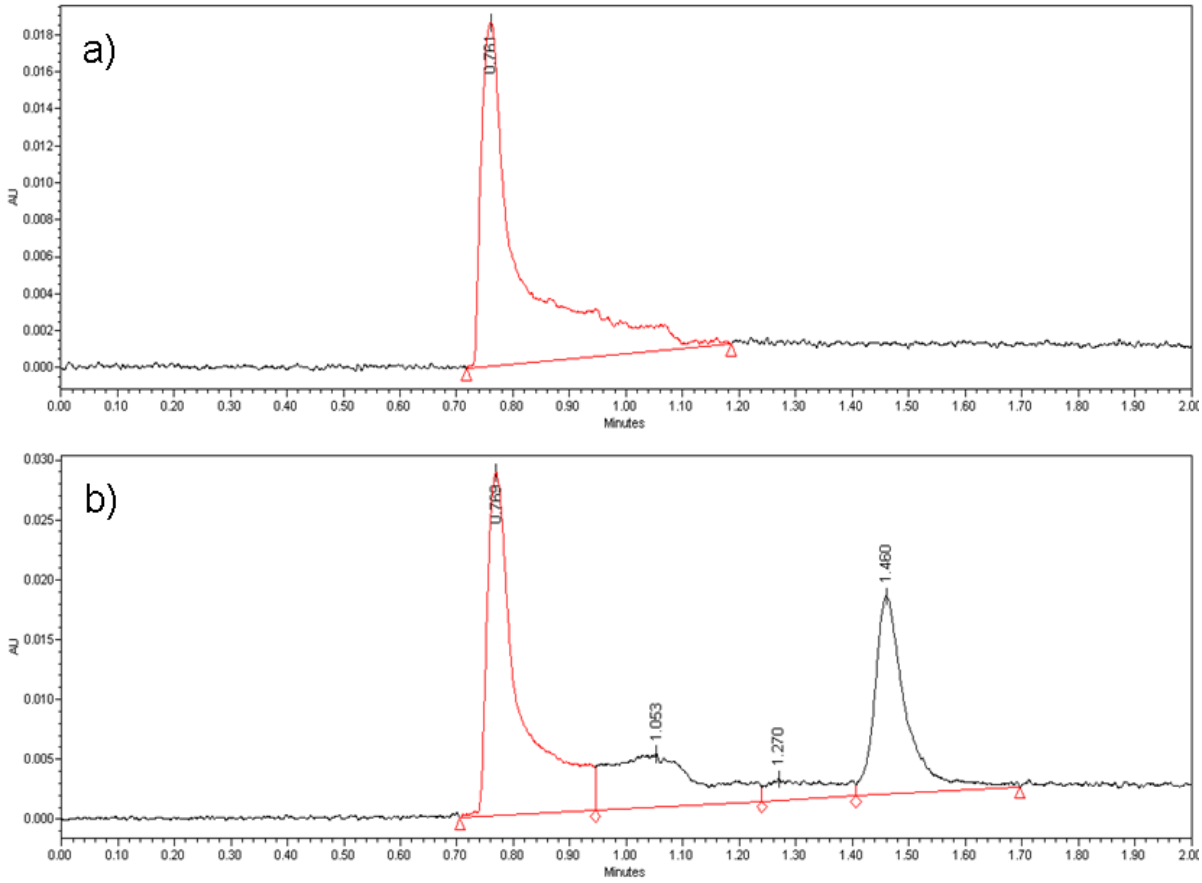


Figure 7.10: Typical chromatogram depicting a) ENT and b) the separation of both ENT and diclofenac sodium after spiking. 10 µL 0.00625 mg/mL solution of diclofenac sodium was used as internal standard to spike extracted plasma samples of ENT and *in vitro* ENT release samples from the nanoparticles.

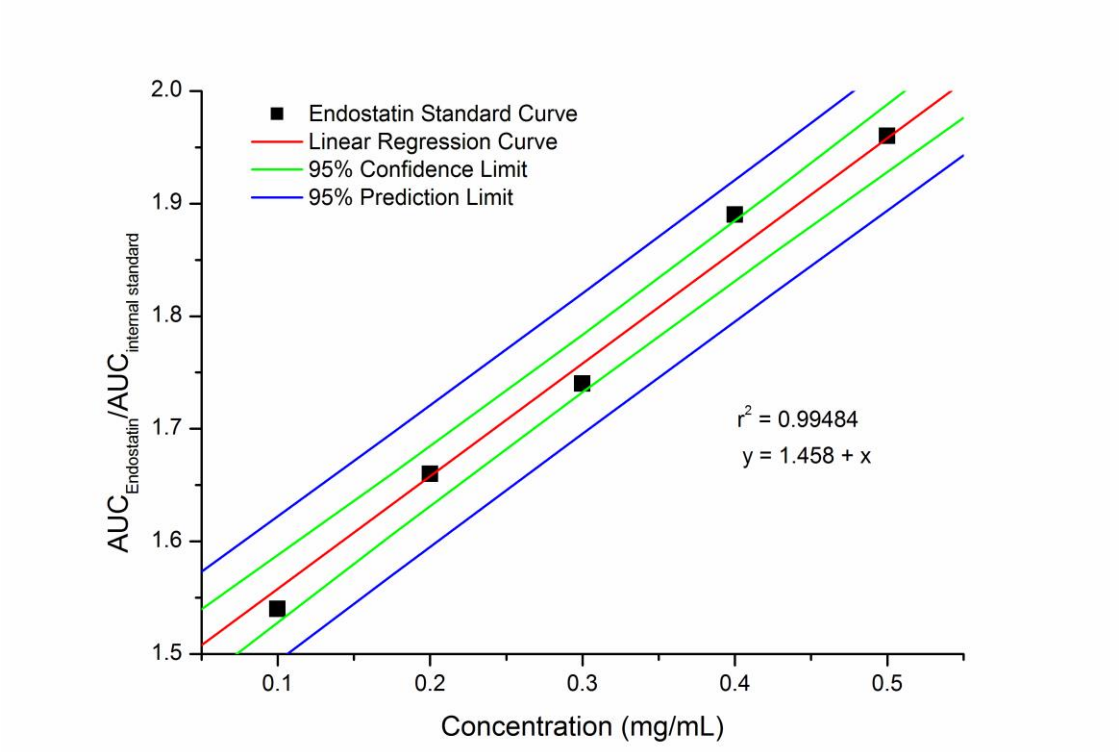


Figure 7.11: Calibration curves generated for endostatin at 280 nm, SD ≤ 0.02049, N = 5.

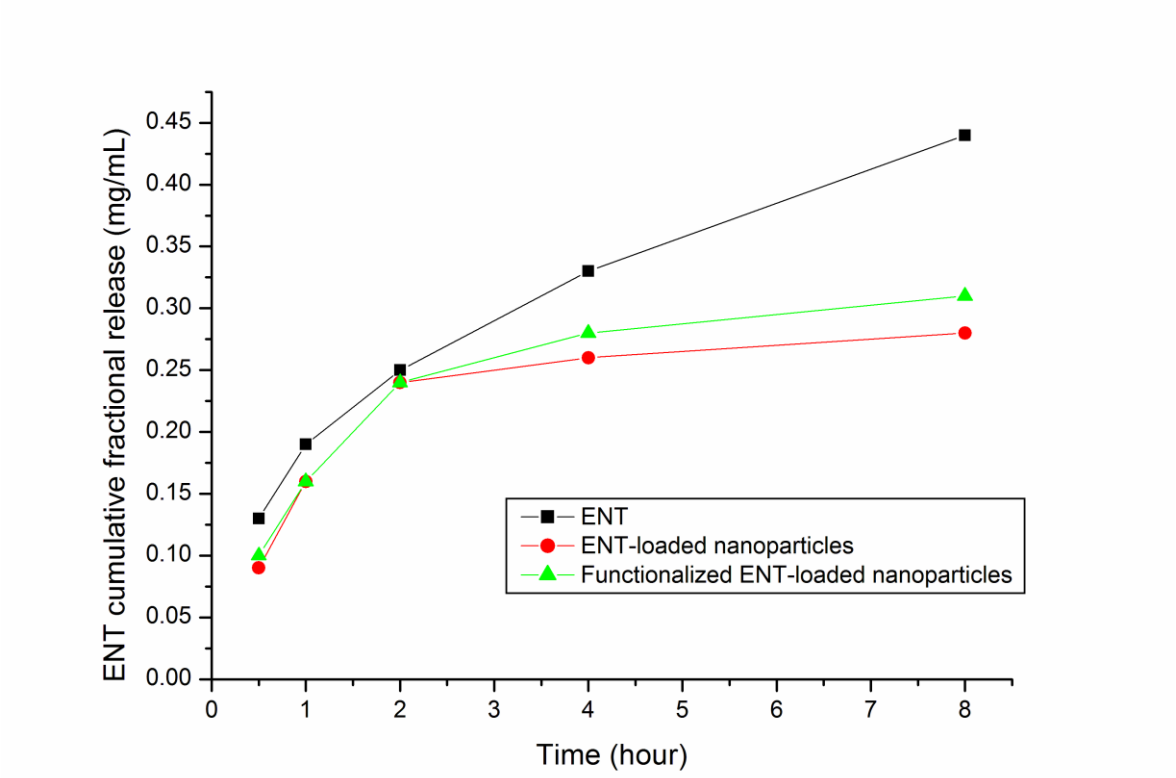


Figure 7.12: Plasma endostatin concentration profile depicting the release behaviour over 8 hours of native endostatin relative to encapsulated endostatin nanoparticles, and functionalized endostatin-loaded nanoparticles. SD = 0.021

7.3.3. Necrotic and anti-angiogenic effects of endostatin-loaded PEL nanosystem in KYSE-30 xenografts

Tumor necrosis is a condition that characterizes a tumor mass with one or more dead tissues in its surrounding environment associated with hypoxia, angiogenesis and inflammation response (Bredholt et al., 2015). Most often, this is due to increased growth beyond the tumor's blood supply. As opposed to apoptosis, necrosis often accounts for a powerful inflammatory response, which may be involved in tumor regression during anticancer therapy (Wang and Lin, 2008). Necrosis-like caspase-independent programmed cell death (PCD), induced by tumor necrotic factor (TNF), are usually characterized by absent or marginal chromatin condensation, lack of nuclear fragmentation and disruption of membrane integrity (Leist and Jäättelä, 2001; Mocellin et al., 2005). Necrosis-like caspase-independent PCD is the most characterized type of TNF-

driven PCD. Meanwhile, ENT is a potent antiangiogenic agent characterized with minimal toxicity and drug resistance with ability to induce endothelial cell apoptosis in tumor cells (Dhanabal et al., 1999; Liang et al., 2016).

As presented in Figure 7.13, mice bearing established *S.C.* KYSE-30 xenografts treated with ENT and PEL nanosystem loaded with ENT showed large necrotic areas compared with the control. Treatments increased the extent of tumor necrosis in tumors of mice that received FA-functionalized and peptide-enhanced PEL nanosystems relative to the ENT treated tumor. These findings corroborate the results of Crescenzi and collegues (2011b) that L19mTNFα induced acute anti-tumoral effects in xenografts of esophageal cancer with increased necrotic areas when compared to the control tumor. Meanwhile, the necrosis found in the control group could partly due to the larger volume of the xenograft with respect to the short-term experimental period as there is a possibility of rapid recovery of oesophageal tumors (Crescenzi et al., 2011b). Similarly, as seen in Figure 7.13, there appeared to be some distortions in the structural morphology of the tumor stroma with partial loss of extracellular matrix and disruption of grandular-like structures in the treated tumors relative to the control. This further validates the anti-angiogenic therapeutic effects of ENT and more importantly, the enhanced role of the targeting moieties (FA, LyP-1 and Pentapeptide (PENT)) in facilitating the direct delivery and targeting of tumor vasculatures by ENT-loaded PEL nanosystems as discussed in previous chapters.

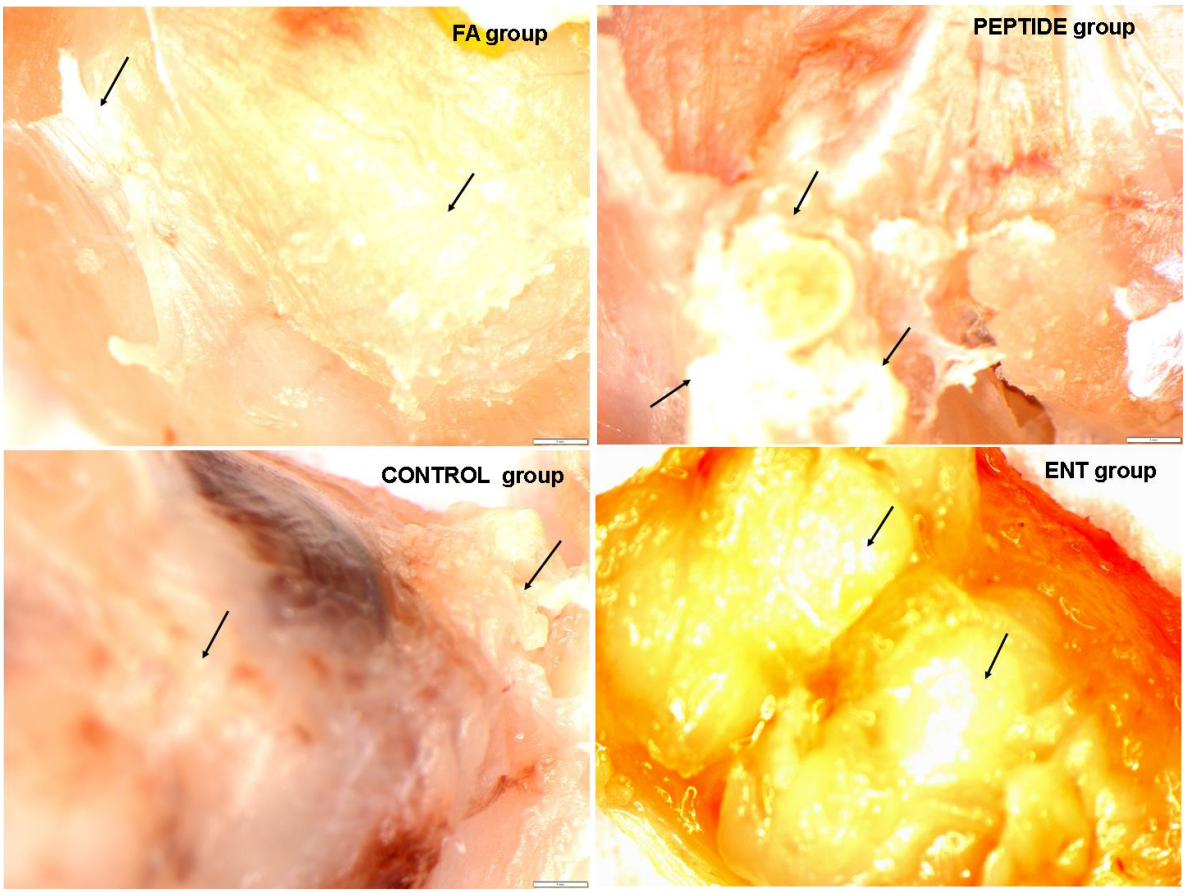


Figure 7.13: Representative cross-sectional images of tumor samples showing the necrotic areas after treatment with PEL nanosystem or no treatment in the control group. Images were viewed and captured under a light microscopy at high magnification (100x).

7.4. Concluding remarks

KYSE-30 xenografts were successfully induced after 31 days post-inoculation. Treatments of KYSE-30 xenografts with PEL nanosystems loaded with ENT could serve as a therapeutic alternative for the targeted delivery of anti-cancer chemotherapeutics in cancer nanomedicine. A major finding in this study is the marked reduction in tumor volume and increased necrotic areas in tumors observed following treatment of squamous cell oesophageal carcinoma with the functionalized ENT-loaded nanoparticles. Thus, the enhanced targeting abilities of both FA and the short homing peptides in the PEL nanosystems facilitate ENT release for optimum anti-tumoral effects *in vivo*.

7.5. References

Adebowale, A.S., Choonara, Y.E., Kumar, P., du Toit, L.C., Pillay, V., 2015. Functionalized Nanocarriers for Enhanced Bioactive Delivery to Squamous Cell Carcinomas: Targeting Approaches and Related Biopharmaceutical Aspects. Curr. Pharm. Des. 21, 3167–3180.

Antony, A.C., 1996. Folate Receptors. Annu. Rev. Nutr. 16, 501–521.

Bredholt, G., Mannelqvist, M., Stefansson, I.M., Birkeland, E., Bø, T.H., Øyan, A.M., Trovik, J., Kalland, K.-H., Jonassen, I., Salvesen, H.B., Wik, E., Akslen, L.A., 2015. Tumor necrosis is an important hallmark of aggressive endometrial cancer and associates with hypoxia, angiogenesis and inflammation responses. Oncotarget 6, 39676–39691.

Cheng, Y.-M., Cao, A.-L., Zheng, J.-P., Wang, H.-W., Sun, Y.-S., Liu, C.-F., Zhang, B.-B., Wang, Y., Zhu, S.-L., Wu, D.-Z., 2014. Airway hyperresponsiveness induced by repeated esophageal infusion of HCl in guinea pigs. Am. J. Respir. Cell Mol. Biol. 51, 701–708.

Christian, S., Pilch, J., Akerman, M.E., Porkka, K., Laakkonen, P., Ruoslahti, E., 2003. Nucleolin expressed at the cell surface is a marker of endothelial cells in angiogenic blood vessels. J. Cell Biol. 163, 871–878.

Crawford, H.C., Matrisian, L.M., Liaw, L., 1998. Distinct Roles of Osteopontin in Host Defense Activity and Tumor Survival during Squamous Cell Carcinoma Progression in Vivo. Cancer Res. 58, 5206–5215.

Crescenzi, M., Persano, L., Esposito, G., Zulato, E., Borsi, L., Balza, E., Ruol, A., Ancona, E., Indraccolo, S., Amadori, A., 2011a. Vandetanib improves anti-tumor effects of L19mTNFalpha in xenograft models of esophageal cancer. Clin. Cancer Res. Off. J. Am. Assoc. Cancer Res. 17, 447–458.

Crescenzi, M., Persano, L., Esposito, G., Zulato, E., Borsi, L., Balza, E., Ruol, A., Ancona, E., Indraccolo, S., Amadori, A., 2011b. Vandetanib improves anti-tumor effects of L19mTNFalpha in xenograft models of esophageal cancer. Clin. Cancer Res. Off. J. Am.

Assoc. Cancer Res. 17, 447–458.

Davis, M.E., Chen, Z. (Georgia), Shin, D.M., 2008. Nanoparticle therapeutics: an emerging treatment modality for cancer. Nat. Rev. Drug Discov. 7, 771–782.

Dhanabal, M., Ramchandran, R., Waterman, M.J., Lu, H., Knebelmann, B., Segal, M., Sukhatme, V.P., 1999. Endostatin induces endothelial cell apoptosis. J. Biol. Chem. 274, 11721–11726.

Dunham, L.J., Sheets, R.H., 1974. Effects of esophageal constriction on benzo(alpha)pyrene carcinogenesis in hamster esophagus and forestomach. J. Natl. Cancer Inst. 53, 875–881.

Gong, J., Liu, X., Li, Y., Zhen, Y., 2012. Pingyangmycin downregulates the expression of EGFR and enhances the effects of cetuximab on esophageal cancer cells and the xenograft in athymic mice. Cancer Chemother. Pharmacol. 69, 1323–1332.

Hanna, N.N., Seetharam, S., Mauceri, H.J., Beckett, M.A., Jaskowiak, N.T., Salloum, R.M., Hari, D., Dhanabal, M., Ramchandran, R., Kalluri, R., Sukhatme, V.P., Kufe, D.W., Weichselbaum, R.R., 2000. Antitumor interaction of short-course endostatin and ionizing radiation. Cancer J. Sudbury Mass 6, 287–293.

Hashimoto, N., 2012. Expression of COX2 and p53 in Rat Esophageal Cancer Induced by Reflux of Duodenal Contents. ISRN Gastroenterol. 2012, 914824.

Hibberd, C., Cossigny, D.A.F., Quan, G.M.Y., 2013. Animal cancer models of skeletal metastasis. Cancer Growth Metastasis 6, 23–34.

Higuchi, K., Koizumi, W., Tanabe, S., Sasaki, T., Katada, C., Azuma, M., Nakatani, K., Ishido, K., Naruke, A., Ryu, T., 2009. Current Management of Esophageal Squamous-Cell Carcinoma in Japan and Other Countries. Gastrointest. Cancer Res. GCR 3, 153–161.

Hilgenbrink, A.R., Low, P.S., 2005. Folate receptor-mediated drug targeting: From therapeutics to diagnostics. J. Pharm. Sci. 94, 2135–2146.

Hori, T., Yamashita, Y., Ohira, M., Matsumura, Y., Muguruma, K., Hirakawa, K., 2001. A novel

orthotopic implantation model of human esophageal carcinoma in nude rats: CD44H mediates cancer cell invasion in vitro and in vivo. Int. J. Cancer 92, 489–496.

Inoue, K., Ozeki, Y., Suganuma, T., Sugiura, Y., Tanaka, S., 1997. Vascular endothelial growth factor expression in primary esophageal squamous cell carcinoma. Cancer 79, 206–213.

Karpanen, T., Egeblad, M., Karkkainen, M.J., Kubo, H., Ylä-Herttuala, S., Jäättelä, M., Alitalo, K., 2001. Vascular endothelial growth factor C promotes tumor lymphangiogenesis and intralymphatic tumor growth. Cancer Res. 61, 1786–1790.

Kitadai, Y., Haruma, K., Tokutomi, T., Tanaka, S., Sumii, K., Carvalho, M., Kuwabara, M., Yoshida, K., Hirai, T., Kajiyama, G., Tahara, E., 1998. Significance of vessel count and vascular endothelial growth factor in human esophageal carcinomas. Clin. Cancer Res. Off. J. Am. Assoc. Cancer Res. 4, 2195–2200.

Kleespies, A., Guba, M., Jauch, K.-W., Bruns, C.J., 2004. Vascular endothelial growth factor in esophageal cancer. J. Surg. Oncol. 87, 95–104.

Leist, M., Jäättelä, M., 2001. Four deaths and a funeral: From caspases to alternative mechanisms. Nat. Rev. Mol. Cell Biol. 2, 589–598.

Li, S., Jiang, S., Jiang, W., Zhou, Y., Shen, X.-Y., Luo, T., Kong, L.-P., Wang, H.-Q., 2015. Anticancer effects of crocetin in human esophageal squamous cell carcinoma KYSE-150 cells. Oncol. Lett. 9, 1254–1260.

Liang, J., Liu, X., Xie, Q., Chen, G., Li, X., Jia, Y., Yin, B., Qu, X., Li, Y., 2016. Endostatin enhances antitumor effect of tumor antigen-pulsed dendritic cell therapy in mouse xenograft model of lung carcinoma. Chin. J. Cancer Res. 28, 452–460.

Liu, J., Li, N., Li, L., Li, D., Liu, K., Zhao, L., Tang, J., Li, L., 2013. Local hyperthermia for esophageal cancer in a rabbit tumor model: Magnetic stent hyperthermia versus magnetic fluid hyperthermia. Oncol. Lett. 6, 1550–1558.

Liu, Y., Xiao, H., Tian, Y., Nekrasova, T., Hao, X., Lee, H.J., Suh, N., Yang, C.S., Minden, A., 2008. The Pak4 Protein Kinase Plays a Key Role in Cell Survival and Tumorigenesis in

Athymic Mice. Mol. Cancer Res. 6, 1215–1224.

Mocellin, S., Rossi, C.R., Pilati, P., Nitti, D., 2005. Tumor necrosis factor, cancer and anticancer therapy. Cytokine Growth Factor Rev. 16, 35–53.

Mohanraj, V.J., Chen, Y., 2007. Nanoparticles - A review. Trop. J. Pharm. Res. 5, 561–573.

Murray, S., Schell, K., McCarthy, D.O., Albertini, M.R., 1997. Tumor growth, weight loss and cytokines in SCID mice. Cancer Lett. 111, 111–115.

Nair, D.V., Reddy, A.G., 2016. Laboratory animal models for esophageal cancer. Vet. World 9, 1229–1232.

Nakagawa, H., Wang, T.C., Zukerberg, L., Odze, R., Togawa, K., May, G.H., Wilson, J., Rustgi, A.K., 1997. The targeting of the cyclin D1 oncogene by an Epstein-Barr virus promoter in transgenic mice causes dysplasia in the tongue, esophagus and forestomach. Oncogene 14, 1185–1190.

O'Reilly, M.S., Boehm, T., Shing, Y., Fukai, N., Vasios, G., Lane, W.S., Flynn, E., Birkhead, J.R., Olsen, B.R., Folkman, J., 1997. Endostatin: an endogenous inhibitor of angiogenesis and tumor growth. Cell 88, 277–285.

Ruggeri, B.A., Camp, F., Miknyoczki, S., 2014. Animal models of disease: pre-clinical animal models of cancer and their applications and utility in drug discovery. Biochem. Pharmacol. 87, 150–161.

Saxena, M., Christofori, G., 2013. Rebuilding cancer metastasis in the mouse. Mol. Oncol. 7, 283–296.

Shih, C.H., Ozawa, S., Ando, N., Ueda, M., Kitajima, M., 2000. Vascular endothelial growth factor expression predicts outcome and lymph node metastasis in squamous cell carcinoma of the esophagus. Clin. Cancer Res. Off. J. Am. Assoc. Cancer Res. 6, 1161–1168.

Shimada, Y., Imamura, M., Wagata, T., Yamaguchi, N., Tobe, T., 1992. Characterization of 21 newly established esophageal cancer cell lines. Cancer 69, 277–284.

Wang, A.Z., Langer, R., Farokhzad, O.C., 2012. Nanoparticle Delivery of Cancer Drugs. Annu. Rev. Med. 63, 185–198.

Wang, M., Thanou, M., 2010. Targeting nanoparticles to cancer. Pharmacol. Res., Towards clinical applications of nanoscale medicines 62, 90–99.

Wang, X., Lin, Y., 2008. Tumor necrosis factor and cancer, buddies or foes? Acta Pharmacol. Sin. 29, 1275–1288.

Yan, Z., Zhan, C., Wen, Z., Feng, L., Wang, F., Liu, Y., Yang, X., Dong, Q., Min Liu, Lu, W., 2011. LyP-1-conjugated doxorubicin-loaded liposomes suppress lymphatic metastasis by inhibiting lymph node metastases and destroying tumor lymphatics. Nanotechnology 22, 415103.

Yao, Y.-L., Yang, W.-M., 2005. Nuclear proteins: promising targets for cancer drugs. Curr. Cancer Drug Targets 5, 595–610.

Yokoyama, Y., Ramakrishnan, S., 2005. Addition of an aminopeptidase N-binding sequence to human endostatin improves inhibition of ovarian carcinoma growth. Cancer 104, 321–331.

CHAPTER 8

CONCLUSIONS AND RECOMMENDATIONS

"And further, by these, my son, be admonished: of making many books ***there is no end****; and much study is a weariness of the flesh. Let us hear* ***the conclusion of the whole matter:*** *Fear God, and keep his commandments: for this is the whole duty of man"* ***Eccl. 12:12-13***

8.1. Conclusions

Cancer remains the most deadly chronic disease after cardiovascular disease that threatened the survival of people across race, colour, age groups and gender in the history of human existence. Worse still, the huge biotechnological breakthroughs through cutting edge nanotechnological advances in drug discovery have not made much impact in salvaging its victims. Chemotherapeutics, as promising alternative for the management of people living with cancer disease, have been hampered ineffective owning to challenging side effects due to multi-resistance within the biological system and non-specific targeting, toxicity to healthy cells, high dosage form and sub-optimal accumulation at the disease site. Thus, targeted delivery of potent cancer therapeutics using smart and intelligent nanosystems remain a proactive and promising treatment alternative to circumvent these anomalies and enhance the delivery of these treatment regimen for optimal anti-tumoral effects.

Based on these modalities, the conceptualization, design, optimization and characterization of a smart nano-construct capable of encapsulating vis-a-vis release of potent cancer drugs was fabricated in this study. Current cutting edge convectional technologies for the design of functionalized nanoconstructs for targeted delivery of therapeutics for OSCC was reviewed. Thereafter, a novel pH responsive PEG-PEI-CHT nano-construct was optimised for endostatin

(ENT) release and characterized particularly to explore the higher acidic tumor microenvironment as opposed to healthy cells. The optimized nano-formulation was then enhanced for direct targeting of characteristics molecular biomarkers uniquely expressed on tumor cells including folate receptors and mitochondrial/nuclear proteins. Surface functionalization of optimized PEG-PEI-CHT nano-cargo, using Lyp-1, PENT and folate (termed - PEL nanosystems), as targeting ligands, with ability to facilitate the specific homing of ENT-loaded nanoparticles to cancer cells, was successfully investigated during the course of this study.

Detailed *in vitro* cellular and *in vivo* experiments validate the fabricated PEL nanoparticulate systems as efficient delivery cargo of ENT with an enhanced anti-tumoral activity in OSCC, as a model cancer type, by targeting the angiogenic pathway in KYSE-30 cells. The PEL nanosystem loaded with ENT showed a pragmatic inhibition of potent angiogenic factors including cell proliferation, nuclear apoptosis and necrosis, cell migration and invasion as well as reduced expressions of both VEGF-C and MMP2 proteins as molecular makers for anti-angiogenesis. Athymic nude mice induced with OSSC cells showed a dramatic reduction in tumor volume after treatments with the PEL ENT-loaded nanoparticles.

In summary, this study focussed on the design and fabrication through to preclinical analyses of a novel smart nanoparticulate system for direct targeting and release of ENT for an enhanced anti-tumoral activity in oesophageal squamous cell carcinoma. In concise terms, a novel nano-construct, loaded with ENT, surface-engineered with short homing peptides (LyP-1 and PENT) and folic acid, with promising targeting capability has been developed and extensively characterized. This novel PEL nanosystem could clinically enhanced the delivery of chemotherapeutics for robust therapeutic outcomes in OSSC management.

8.2. Recommendations

While the therapeutic efficacy and anti-tumoral effects of the ENT-loaded PEL nanosystem have been well established up till a preclinical standpoint, other factors will have to be considered to advance its applicability as an alternative regimen in cancer nanomedicines. Despites the outstanding discoveries made in this study on the ENT-loaded PEL nanoparticulate system, to gain a wider attention for therapeutic application, product scale-up and production, other biochemical assays that serve as indicators for nuclear damage and cell death including caspases' activities, TUNEL assay among others should be validated. Similarly, biochemical markers for mitochondrial degradation such as reactive oxygen species (ROS) quantification should be evaluated to justify the findings of this study. Also, *in silico* modelling of the nanosystem can provide a more robust design for an improved conjugation strategy between the independent components of the PEL nanosystem. For instance, a unique surface modification strategy, using both folic acid and LyP-1, for targeting the folate receptors and the nuclear/mitochondrial proteins (e.g, p32) distinctively over-expressed on cancer cells, could provide a broader active targeting spectrum in OSCC management. Interestingly, folate receptors are surface proteins expressed on the surface of cancer cells while p32 protein is expressed in the mitochondrial and localized in the nucleus. As such, a novel combinatorial strategy of using both folic acid and LyP-1 as active targeting moieties on pH-sensitive nano-construct as designed in this study (PEG-PEI-CHT), could serve a potent delivery alternative for site-specific targeting of tumor cells both at the surface level for receptor-mediated endocytosis as well as direct intra-cellular trafficking of the internalized nanoparticles to the nucleus and mitochondrial of tumor cells to facilitate programmed cell death upon the release of their encapsulated payloads such as ENT.

Finally, while ENT was selected as a peptide-based model drug in this study due to its broad spectrum anti-angiogenic activities and limitations, the novel PEL nanosystem can be employed

to incorporate alternative cancer chemotherapeutics for enhance on-site delivery for optimum therapeutic response in cancer therapy.

APPENDICES

9.1. APPENDIX A

9.1.1. Research Publications

9.1.1.1. Review paper

Current Pharmaceutical Design, 2015, *21*, 3167-3180

Functionalized Nanocarriers for Enhanced Bioactive Delivery to Squamous Cell Carcinomas: Targeting Approaches and Related Biopharmaceutical Aspects

Adeyemi S. Adebowale, Yahya E. Choonara, Pradeep Kumar, Lisa C. du Toit and Viness Pillay*

Wits Advanced Drug Delivery Platform Research Unit, Department of Pharmacy and Pharmacology, School of Therapeutic Science, Faculty of Health Sciences, University of the Witwatersrand, Johannesburg, 7 York Road, Parktown, 2193, South Africa



Viness Pillay

Abstract: Cancer has been described as one of the major and leading causes of death worldwide. By the year 2030, it has been postulated that over 21.4 million new cases of cancer could be expected, 17 million cancer deaths yearly and a total of 75 million people will be living with cancer within five years of diagnosis. Chemotherapy is the main therapeutic intervention for treating people living with SCC. However, drug resistance has rendered it inefficient and ineffective in combating the disease even after combination chemotherapy. Many peptides and proteins have been investigated to possess biological activities that mark them as potential anti-cancer agents. Targeting peptides are conjugated with other functional peptides or nanoparticles to augment drug delivery both *in vitro* and *in vivo* assays. The current identification of tumor-homing peptides through phage display technology has opened a new strategy for targeted therapy in SCC diseases. Despite the advances in cancer nanomedicine, targeted approaches in the delivery of therapeutics for the treatment of squamous cell carcinoma related tumours have not been well established. In this review, current drugs employed in cancer nanomedicine are highlighted, possible rate limiting factors for the application of polymeric materials in cancer nanomedicine are elucidated and functionalized nano-constructs using receptor ligands and homing peptides as targeted moieties are discussed. The combinatorial strategy of attaching both homing peptides and receptor ligands as dual moieties on nano-cargos should further strengthen the advantages of each technology in cancer targeted therapy.

Keywords: Cancer, chemotherapy, homing peptides, nanoparticles, receptor ligands, squamous cell carcinoma.

9.1.1.2. Research paper I

SYNTHESIS AND IN VITRO CHARACTERIZATION OF A pH-SENSITIVE CHITOSAN-POLYETHYLENIMINE NANOSYSTEM FOR THE POTENTIAL DELIVERY OF THERAPEUTIC PROTEINS

Samson A. Adeyemi, Yahya E. Choonara, Pradeep Kumar, Lisa C. du Toit and Viness Pillay*

Wits Advanced Drug Delivery Platform Research Unit, Department of Pharmacy and Pharmacology, School of Therapeutic Science, Faculty of Health Sciences, University of the Witwatersrand, Johannesburg, 7 York Road, Parktown, 2193, South Africa

ABSTRACT

This study aimed to design and characterize novel chitosan-based nanoparticles with potential applications as delivery cargos for protein therapeutics in cancer nanomedicine. Bovine Serum Albumin (BSA) loaded Chitosan-based nanosystem using tripolyphosphate (TPP) as a polyanionic agent was synthesized. The synthesized nano-construct was characterized for structural and functional modifications, particle size, morphology, zeta potential, thermal stability, protein loading efficiency and subsequent release kinetics. H^1 NMR and FT-IR experiments confirmed the successful grafting of the co-polymers to chitosan moiety. The average size and morphology of the BSA loaded nanoparticles as confirmed by TEM, Dynamic Light Scattering (DLS) and SEM results showed that the nanoparticles exhibited a spherical shape and had a narrow particle size distribution with polydispersity index (PDI) of 0.232 with an average of size of 63.14±31.31nm. Both the TGA and DSC results confirmed the thermal stability of BSA loaded nanoparticles compared to the native polymers. Protein loading efficiency was evaluated to be 77.2% with an initial burst release probably due to surface protein desorption and subsequent prolong release through diffusion from sublayers only after 2hrs up to 30hrs at changing pH conditions. Meanwhile, the release kinetics at pH 6.8 is higher than that observed at pH 7.4. Conclusively, this novel nanosystem could be explored as vehicles for targeting therapeutic proteins in cancer nanomedicines.

Key words: Chitosan-based nanoparticles, Protein therapeutics, Cancer nanomedicine, BSA, Tripolyphosphate (TPP), Squamous Cell Carcinoma

9.1.1.3. Research paper II

Design and Characterization of Endostatin Loaded Nanoparticles for *In Vitro* Anti-angiogenesis in Squamous Cell Carcinoma

Samson A. Adeyemi, Yahya E. Choonara, Pradeep Kumar, Lisa C. du Toit, Thashree Marimuthu and Viness Pillay*

Wits Advanced Drug Delivery Platform Research Unit, Department of Pharmacy and Pharmacology, School of Therapeutic Science, Faculty of Health Sciences, University of the Witwatersrand, Johannesburg, 7 York Road, Parktown, 2193, South Africa

Abstract

The aim of this study is to effectively enhance antitumor activities of endostatin by preparing polymeric nano-carriers. NMR and FTIR spectra confirmed the successful grafting of the CHT-g-PEI and CHT-g-PEI-PEG-NH_2 conjugates. SEM micrographs confirmed the shape of endostatin-loaded nanoparticles to be spherical while both TEM and zeta size results showed nanoparticle's average size to be 100.6nm having a positively charged surface with zeta potential of 7.95mV. The concentrations of CHT and TPP as well as the changing pH conditions account for the increased swelling pattern of endostatin-loaded nanoparticles and influenced endostatin release *in vitro*. PEI increased the overall amine protonation while PEG aggravated endostatin encapsulation and release. Nanoparticles swell and release endostatin at acidic tumour pH of 6.8 than at physiological pH of 7.4. The native CHT-g-PEI-PEG-NH_2 conjugate showed high cyto-compactibility above 80% cell viability across tested formulations. Endostatin-loaded nanoparticles showed a significant reduction in cell viability across tested formulations, with 5.32% cell death at 125µg/mL and 13.36% at 250µg/mL following 24 hours incubation period. Interestingly, more than a four-fold (61.68%) increment in cytotoxicity was observed at nanoparticle concentration of 1000µg/mL. It was concluded that CHT-g-PEI-PEG-NH_2 is an effective cargo for endostatin delivery with anti-angiogenic effect in Squamous cell carcinoma.

Keywords: Antitumor, nano-carriers, nanoparticles, endostatin, cyto-compactibility, Anti-angiogenic, Squamous cell carcinoma.

9.1.1.4. Research paper III

Anti-proliferative Activities of Folate-targeted Endostatin-loaded Nanoparticles on Oesophageal Squamous Cell Carcinoma

Samson A. Adeyemi, Yahya E. Choonara, Pradeep Kumar, Lisa C. du Toit, Thashree Marimuthu and Viness Pillay*

Wits Advanced Drug Delivery Platform Research Unit, Department of Pharmacy and Pharmacology, School of Therapeutic Science, Faculty of Health Sciences, University of the Witwatersrand, Johannesburg, 7 York Road, Parktown, 2193, South Africa

Abstract

Angiogenesis, the formation of new blood vessels, is fundamental to the survival and growth of tumor cells. Smart nanosystems designed to specifically deliver cancer therapeutics and facilitate optimal dosage form at disease sites with potent anti-proliferative effects is the paradigm shift in anti-angiogenic research. Endostatin (ENT), as an endogenous inhibitor of angiogenesis targeting tumor vasculature, has been clinically proven to be promising as an anti-cancer drug. Meanwhile, endostatin has many clinical challenges in its application including high dosage form to maintain its efficacy, short circulation half-life and instability. Thus, incorporation into biodegradable polymers as delivery cargos has been proposed to overcome these challenges and improves its therapeutic effects. Cancer cells overexpress certain proteins as opposed to normal cells which can be exploited for targeted formulation design. Folate receptors, as unique molecular signatures, are overexpressed on the cellular membrane of different tumor cells including Oesophageal Squamous Cell Carcinoma (OSCC). In this study, we employed folic acid (FA); having a high affinity for folate receptors, as a driver for direct targeting of endostatin-loaded nanoparticles in OSCC management. Spherical nanoparticles, having an overall positively charged surface, were synthesized with selective pH response for ENT release *in vitro*. Our results confirmed successful internalization of folate-decorated nanoparticles into OSCC cells with preferential binging to the nucleus and the mitochondrial for necrotic and apoptotic effects. Moreover, FA-linked ENT-loaded nanoparticles showed increased proliferation inhibition of 64.71% and reduced KYSE-30 cells migration up to 74.12% *in vitro* when compared to the control. In summary, our findings demonstrate the potential use of FA-decorated nanoparticles as delivery vectors for active transport of ENT into tumor cells with an enhanced anti-proliferative efficacy in OSCC management.

Keywords: Angiogenesis; Endostatin; Folate receptors; Folic acid; Nanoparticles; Necrotic; Apoptotic; Proliferation inhibition.

9.1.1.5. Research paper IV

A Novel Dual Peptide-Enhanced Endostatin-Loaded Nano-construct for Targeted Anti-Angiogenic Effects in Squamous Cell Carcinoma

Samson A. Adeyemi, Yahya E. Choonara, Pradeep Kumar, Lisa C. du Toit, Thashree Marimuthu and Viness Pillay*

Wits Advanced Drug Delivery Platform Research Unit, Department of Pharmacy and Pharmacology, School of Therapeutic Science, Faculty of Health Sciences, University of the Witwatersrand, Johannesburg, 7 York Road, Parktown, 2193, South Africa

Abstract

Targeted delivery of smart nanosystems is a prospective and proactive alternative to circumvent the draw backs encountered with many conventional cancer chemotherapeutics with non-specific targeting, sub-optimal dosage and adverse effects on healthy cells. Short peptides, with strategic homing ability, could be employed to functionalize the surface of novel nano constructs since cancer cells over-express certain proteins on their cellular membrane as opposed to normal cells. This study aimed to design and characterize novel LyP-1 and CGKRK (PENT) enhanced nanoparticles with promising applications as targeted delivery cargoes for the delivery of endostatin (ENT) in the management of Squamous Cell Carcinoma (SCC). ENT-loaded nanoparticles were successfully synthesized using an ionic gelation procedure. The synthesized nano constructs were characterized for structural and functional modifications, particle size, morphology, zeta potential, drug loading efficiency and release kinetics. The cytotoxic effects of LyP-1/PENT functionalized ENT-loaded nanoparticles were examined using Alamar blue assay on an established SCC cell line (KYSE-30). ^{1}H NMR and FT-IR experiments confirmed the successful conjugation of native polymers. The average size and morphology of the ENT-loaded nanoparticles as confirmed by TEM, dynamic light scattering (DLS) and SEM results showed that the nanoparticles exhibited a spherical shape with an average size below 100nm having zeta potential of +17.3mV. The release kinetics of ENT from the nanoparticles is optimal at pH 4.6 than at the physiological pH. The cell proliferation assay showed that the peptide-enhanced ENT-loaded nano constructs exhibited increased cytotoxic effects on the KYSE-30 cells than the native nanoparticles. Interestingly, both peptides facilitate the uptake, intra-cellular trafficking and site specific binding of nanoparticles to nuclear and mitochondrial proteins to enhance the

anti-angiogenic efficacy of ENT *in vitro*. Migration of KYSE-30 cells was impeded and both VEGF-C and MMP-2 expressions, as potent angiogenic makers, were significantly reduced.

Key words: Targeted delivery, Smart nanosystems, Lyp-1, CGKRK, Squamous cell carcinoma, endostatin, anti-angiogenic, VEGF-C and MMP2

9.2. APPENDIX B

9.2.1. Abstracts of Research Outputs at Conference Proceedings

9.2.1.1. 6th Cross-Faculty Graduate Symposium, University of the Witwatersrand, Johannesburg, South Africa, October 27th-31st, 2014.

A Novel Chitosan-based Nano-construct for Sustained Subcutaneous Delivery of Proteins via the Lymphatic System in Squamous Cell Carcinoma

Samson .A. Adeyemi, Yahya .E. Choonara, Pradeep Kumar, Lisa .C. du Toit and Viness Pillay

Wits Advanced Drug Delivery Platform Research Unit, Department of Pharmacy and Pharmacology, School of Therapeutic Science, Faculty of Health Sciences, University of the Witwatersrand, Johannesburg, 7 York Road, Parktown, 2193, South Africa

Email: Samson.Adeyemi@students.wits.ac.za

The significance of both peptides and proteins, as potent therapeutics has increased drastically. Chitosan based nanoparticles have been employed as carriers for genes and therapeutic proteins with different levels of effectiveness and set-backs in cancer therapy. This study aimed to design and characterize novel chitosan-based nanoparticles with potential applications as delivery cargos for protein therapeutics in cancer nanomedicine. Bovine Serum Albumin (BSA) loaded Chitosan-based nano-constructs using tripolyphosphate (TPP) as a polyanionic agent was synthesized. The synthesized nano-construct was characterized for structural and functional modifications, particle size, morphology, zeta potential, thermal stability, protein loading efficiency and subsequent release kinetics. H^1 NMR and FT-IR experiments confirmed the successful grafting of the co-polymers to chitosan moiety. The average size and morphology of the BSA loaded nanoparticles as confirmed by TEM, dynamic light scattering (DLS) and SEM results showed that the nanoparticles exhibited a spherical shape and had a narrow particle size distribution with polydispersity index (PDI) of 0.496 with size range between 80 – 260nm. A Zeta potential value of +19.8mV was obtained for the nanoparticles with possible mucoadhesive properties. Both the TGA and DSC results confirmed the thermal stability of BSA loaded nanoparticles compared to the native polymers. Protein loading efficiency was evaluated to be 77.2% with an initial burst release probably due to surface protein desorption and subsequent

prolong release through diffusion from sublayers only after 6 hours up to 48 hours. Conclusively, these nano-constructs could be employed as vehicles for therapeutic proteins for subcutaneous delivery via the lymphatics in SCC treatments.

9.2.1.2. Academy of Pharmaceutical Sciences of South Africa, Johannesburg, South Africa, September 17th -19th, 2015.

Preparation and Characterization of a Novel PEGylated Chitosan-grafted-Polyethylineimine Nanospheres for Targeted Subcutaneous Delivery of Proteins via the Lymphatic System in Squamous Cell Carcinoma

Samson .A. Adeyemi, Yahya .E. Choonara, Pradeep Kumar, Lisa .C. du Toit and Viness Pillay

Wits Advanced Drug Delivery Platform Research Unit, Department of Pharmacy and Pharmacology, School of Therapeutic Science, Faculty of Health Sciences, University of the Witwatersrand, Johannesburg, 7 York Road, Parktown, 2193, South Africa

Purpose: The significance of both peptides and proteins, as potent therapeutics has increased drastically and administered through the parental route as injectables. Meanwhile, subcutaneous administration has been reported as a robust means for the delivery of many of the approved protein therapeutics. Chitosan based nanoparticles have been investigated and employed as carriers for genes and therapeutic proteins with different levels of effectiveness and set-backs in cancer therapy. This study aimed to design and characterize novel chitosan-based nanoparticles with potential and promising applications as delivery cargos for protein therapeutics in cancer nanomedicine.

Methods: Using BSA as a model protein, we have synthesized and characterized a protein loaded PEGYlated chitosan-based polyethyleimine nano-constructs using tripolyphosphate (TPP) as a polyanionic agent. The BSA-loaded chitosan-based nano-construct was characterized for structural and functional modifications, particle size, morphology, zeta potential, thermal stability, protein loading efficiency and subsequent release kinetics.

Results: H^1 NMR and FT-IR experiments both confirmed the successful grafting of the co-polymers to chitosan moiety as presented. The average size and morphology of the BSA loaded nanoparticles as confirmed by TEM, dynamic light scattering (DLS) and SEM results showed that the nanoparticles exhibited a spherical shape and had a narrow particle size distribution with polydispersity index (PDI) of 0.496 and size ranging between 80 – 260nm. A positive value zeta potential of 19.8mV was obtained for the nanoparticles with minimal stability with possible mucoadhesive properties. Both the TGA and DSC results showed the synthesized BSA loaded nanoparticles were more stable than the single polymers. The protein loading efficiency was evaluated to be 77.2% with an initial burst release probably due to surface protein desorption and subsequent prolong slow release through diffusion from sublayers only after 6 hours up to 48 hours.

Conclusions: In general, this study demonstrated that grafting other biopolymers such as PEI and PEG to chitosan improved its thermal stability and could as well enhances its protein encapsulation and possible release kinetics. However, the initial burst release effect, in releasing large amount of protein molecules remained a major drawback of chitosan-based nanoparticles and its application as potent carrier of protein therapeutics.

9.2.1.3. 10th World Biomaterials Congress, Montreal, Canada , 17th – 22nd May, 2016.

A Novel Functionalized Chitosan-based Nanoconstruct for Targeted Subcutaneous Delivery of Protein therapeutics in Squamous Cell Carcinoma

Samson .A. Adeyemi, Yahya .E. Choonara, Pradeep Kumar, Lisa .C. du Toit and Viness Pillay

Wits Advanced Drug Delivery Platform Research Unit, Department of Pharmacy and Pharmacology, School of Therapeutic Science, Faculty of Health Sciences, University of the Witwatersrand, Johannesburg, 7 York Road, Parktown, 2193, South Africa

Introduction: The significance of both peptides and proteins, as potent therapeutics has increased drastically and administered through the parental route as injectables. Meanwhile, subcutaneous administration has been reported as a robust means for the delivery of many of the approved protein therapeutics. Chitosan based nanoparticles have been investigated and employed as carriers for genes and therapeutic proteins with different levels of effectiveness and set-backs in cancer therapy. Non-targeted delivery and sub-optimal dosage at disease sites are major limitations of most conventional chemotherapeutics. This study aimed to design and characterize novel ligand-enhanced chitosan-based nanoparticles with potential and promising applications as targeted delivery cargos for protein therapeutics in the management of Squamous Cell Carcinoma (SCC).

Methods and Methods: Using BSA as a model protein, we have synthesized and characterized a protein loaded PEGYlated chitosan-based polyethyleimine nano-constructs using tripolyphosphate (TPP) as a polyanionic agent. The BSA-loaded chitosan-based nano-construct was characterized for structural and functional modifications, particle size, morphology, zeta potential, thermal stability, protein loading efficiency and subsequent release kinetics. Surface modification of the synthesized nanoconstructs will be achieved using LyP-1 as a homing ligand for targeted delivery. MTT assay will be performed to access the cytotoxic efficacy of the functionalized nanoconstructs loaded with endostatin in place of BSA.

Results and Discussion: H^1 NMR and FT-IR experiments both confirmed the successful grafting of the co-polymers to chitosan moiety as presented. The average size and morphology of the BSA loaded nanoparticles as confirmed by TEM, dynamic light scattering (DLS) and SEM results showed that the nanoparticles exhibited a spherical shape and had a narrow particle size distribution with polydispersity index (PDI) of 0.496 with an average size less than 100nm. A positive value zeta potential of 19.8mV was obtained for the nanoparticles with minimal stability with possible mucoadhesive properties. Both the TGA and DSC results showed the synthesized BSA loaded nanoparticles were more stable than the single polymers. The protein loading efficiency was evaluated to be 77.2% with an initial burst release probably due to surface protein desorption and subsequent prolong slow release through diffusion from sublayers only after 6 hours up to 48 hours.

Conclusions: In general, this study demonstrated that grafting other biopolymers such as PEI and PEG to chitosan improved its thermal stability and could as well enhances its protein encapsulation and possible release kinetics. However, the initial burst release effect, in

releasing large amount of protein molecules remained a major drawback of chitosan-based nanoparticles and its application as potent carrier of protein therapeutics but could be harnessed for cytotoxic effect in tumor cells. Meanwhile, our designed nanoconstruct is intended for targeted delivery of endostatin upon its functionalization for enhanced therapeutic effects in SCC management and represent the first prototype for protein delivery when these polymers are complexed as a single system.

References

Gan, Q., Wang, T., 2007. Chitosan nanoparticle as protein delivery carrier—Systematic examination of fabrication conditions for efficient loading and release. Colloids Surf. B Biointerfaces 59, 24–34.
Gao, J.-Q., Zhao, Q.-Q., Lv, T.-F., Shuai, W.-P., Zhou, J., Tang, G.-P., Liang, W.-Q., Tabata, Y., Hu, Y.-L., 2010a. Gene-carried chitosan-linked-PEI induced high gene transfection efficiency with low toxicity and significant tumor-suppressive activity. Int. J. Pharm. 387, 286–294.
Ruoslahti E, Bhatia SN, Sailor MJ. Targeting of drugs and nanoparticles to tumors. J Cell Biol 2010;188:759–68
Fosgerau, K., Hoffmann, T., 2015. Peptide therapeutics: current status and future directions. Drug Discov. Today 20, 122–128.
McDonald, T.A., Zepeda, M.L., Tomlinson, M.J., Bee, W.H., Ivens, I.A., 2010. Subcutaneous administration of biotherapeutics: current experience in animal models. Curr. Opin. Mol. Ther. 12, 461–470

9.2.1.4. Faculty of Health Sciences Research Day, University of the Witwatersrand, Johannesburg, South Africa, September 1, 2016

A Novel Peptide-Enhanced Endostatin-Loaded Nano-construct for Targeted Anti-Angiogenic Effect in Squamous Cell Carcinoma

Samson .A. Adeyemi, Yahya .E. Choonara, Pradeep Kumar, Lisa .C. du Toit and Viness Pillay

Wits Advanced Drug Delivery Platform Research Unit, Department of Pharmacy and Pharmacology, School of Therapeutic Science, Faculty of Health Sciences, University of the Witwatersrand, Johannesburg, 7 York Road, Parktown, 2193, South Africa

Email: Samson.Adeyemi@students.wits.ac.za

Abstract

Targeted delivery of smart nanosystems is a prospective alternative to circumvent the draw backs encountered with many conventional cancer chemotherapeutics with non-specific targeting, sub-optimal dosage and adverse effects on healthy cells. Short peptides could be employed to functionalize the surface of novel nano constructs since cancer cells over-express certain proteins on their cellular membrane as opposed to normal cells. This study aimed to design and characterize novel pentapeptide-enhanced nanoparticles as targeted delivery cargo for the delivery of endostatin in Squamous Cell Carcinoma (SCC) management. Endostatin-

loaded nanoparticles were successfully synthesized using an ionic gelation procedure and characterized for structural and functional modifications, particle size, morphology, zeta potential, drug loading efficiency and release kinetics. Surface modification of the synthesized endostatin-loaded nanoparticles was achieved using CGKRK as a homing peptide. The cytotoxic effects of the CGKRK functionalized endostatin-loaded nanoparticles were examined using MTT assay on an established SCC cell line (KYSE-30). H1 NMR and FT-IR experiments showed that the native polymers were successfully grafted. The average size and morphology of the endostatin-loaded nanoparticles as confirmed by TEM, and SEM results showed that the nanoparticles exhibited a spherical shape and had a narrow particle size distribution with polydispersity index (PDI) less than 0.5 with an average size below 100nm. A positive value zeta potential of 17.3mV was obtained for the nanoparticles. The drug release kinetics was optimal at pH 6.8 than at the physiological pH. The cell proliferation assay showed that the peptide-enhanced endostatin-loaded nano constructs exhibited increased cytotoxic effects on the KYSE-30 cell lines than the non-targeted endostatin loaded nanoparticles

9.2.1.5. APA International Conference on Advanced Polymers, Biomaterials, Bioengineering & Nano Drug Delivery, Flic-En-Flac, Mauritius, September 5th -7th , 2016.

A Novel Folate-Decorated Nano-Cargo For Targeted Endostatin Delivery in Squamous Cell Carcinoma

Samson .A. Adeyemi, Yahya .E. Choonara, Pradeep Kumar, Lisa .C. du Toit and Viness Pillay

Wits Advanced Drug Delivery Platform Research Unit, Department of Pharmacy and Pharmacology, School of Therapeutic Science, Faculty of Health Sciences, University of the Witwatersrand, Johannesburg,
7 York Road, Parktown, 2193, South Africa

Email: samson.adeyemi@students.wits.ac.za

Abstract

A major drawback for cancer therapeutics is the lack of specificity which in turn accounts for adverse effects on healthy cells. Surface functionalization of smart nanosystems is a preferred strategy to circumvent this limitation and to achieve optimal targeted delivery of anti-cancer drugs. Cancer cells overexpress certain proteins as opposed to normal cells which can be exploited for targeted formulation design. Folate receptors, as unique molecular targets, are overexpressed on the cellular membrane of different tumor cells including Squamous Cell Carcinoma (SCC). Chitosan (CHT) based nanoparticles have been investigated and employed as carriers for genes and therapeutic proteins with different levels of effectiveness and limitations in cancer therapy. This study aimed to design and characterize novel folate-enhanced chitosan-based nanoparticles for application as a targeted delivery vector to deliver endostatin in the management of SCC.

Using BSA as a model protein, a CHT-PEI nanoconstruct enveloped with an amino PEG acid derivative using sodium TPP as a polyanionic agent was synthesized. The BSA-loaded chitosan-based nanoconstruct was characterized for structural and functional modifications, particle size, morphology, zeta potential, thermal stability, protein loading efficiency and bioactive release kinetics.

Successful grafting of the PEI onto the chitosan moiety and the conjugation of PEG to the resultant graft polymer was verified using H^1 NMR and ATR-FTIR analyses. The average size and morphology of the BSA-loaded nanoparticles as confirmed by TEM, dynamic light scattering (DLS) and SEM results showed that the nanoparticles exhibited a spherical shape with a narrow particle size distribution (PDI 0.454) with an average size <100nm. A zeta potential value of +36.7mV was obtained for the nanoparticles. The thermal analyses results showed the synthesized BSA-loaded nanoparticles were more stable than the native polymers. The protein loading efficiency was evaluated to be 77.25% with approximately 80.42% of the loaded BSA released after 8 hours at pH 6.8.

This study demonstrated that grafting biopolymers such as PEI and PEG to chitosan improved its thermal stability and enhanced its protein encapsulation and release kinetics. The high positive surface charge of the nanoconstruct could enhanced its interaction and binding particularly with cancer cells having a negatively charged surface. Surface modification of the nanoconstruct will be achieved using Folate as a homing ligand for targeted delivery. Furthermore, MTT assay will be performed to access the cytotoxic efficacy of the functionalized nanoconstructs loaded with endostatin instead of BSA on an established SCC cell line (KYSE-30). Meanwhile, the designed nanoconstruct is intended for targeted delivery of endostatin once functionalized for an enhanced therapeutic effect in SCC management and represents the first prototype for the delivery of protein therapeutics where these polymers are complexed as a single system.

References

1. Q. Gan, T. Wang, Colloids Surf B Biointerfaces, 2007, 59, 24–34.

2. J.Q. Gao, Q.Q. Zhao, T.F. Lv, W.P. Shuai, J. Zhou, G.P. Tang, W.Q. Liang, Y. Tabata, Y.L. Hu, Int J Pharm, 2010, 387, 286–294.

3. E. Ruoslahti, S.N. Bhatia, M.J. Sailor, J Cell Biol, 2010,188, 759–68.

4. K. Fosgerau, T. Hoffmann, Drug Discov Today, 2015, 20, 122–128.

9.3.1. APPENDIX C

9.3.2. Certificate of research presentation



9.3.3. Certificate of research presentation



WBC2016

10th World Biomaterials Congress
May 17-22, 2016 | Montréal, Canada

Certificate of Attendance

This is to certify that

Samson A Adeyemi

attended the 10th World Biomaterials Congress
held on May 17-22, 2016
in Montreal, Canada

Gaétan Laroche	Diego Mantovani	J. Paul Santerre	Hasan Uludag
Congress Co-chair	Congress Co-chair	Congress Co-chair	Congress Co-chair

9.3.4. Certificate of research presentation

APA International Conference on

Advanced Polymers, Biomaterials, Bioengineering & Nano Drug Delivery

September 5-7, 2016 | Flic-En-Flac, Mauritius

Certificate of Participation

This is to certify that

Mr. Samson Adebowale Adeyemi

(Reg Id: 4)

participated as Delegate

and presented an Oral Paper

Titled: A Novel Folate-Decorated Nano-Cargo For Targeted Endostatin Delivery in Squamous Cell Carcinoma

Organized by

Asian Polymer Association

Centre for Biomedical and Biomaterials Research, University of Mauritius

CBBR

In Collaboration with

Indo-Italian Forum on Biomaterials & Tissue Engineering

Bhuvanesh Gupta
Chair, APA 2016

Dhanjay Jhurry
Co-Chair, APA 2016

Archana Bhaw-Luximon
Conference Secretary, APA 2016

9.4. APPENDIX D

9.4.1. Animal ethics approval

STRICTLY CONFIDENTIAL

ANIMAL ETHICS SCREENING COMMITTEE (AESC)

CLEARANCE CERTIFICATE NO. 2016/01/04/D

APPLICANT: Mr S Adeyemi

SCHOOL: Pharmacy and Pharmacology
DEPARTMENT:
LOCATION:

PROJECT TITLE: In vivo subcutaneous delivery of an injectable peptide-enhanced endostatin loaded nano-system for oesophageal squamous cell carcinoma treatment in an athymic nude mice model

Number and Species

192 Athymic nude mice (12 for the pilot study and 180 for the main study)

Approval was given for the use of animals for the project described above at an AESC meeting held on 2016/01/26. This approval remains valid until 29 February 2018.
Unreported changes to the application may invalidate the clearance given by the AESC

The use of these animals is subject to AESC guidelines for the use and care of animals, is limited to the procedures described in the application form and is subject to any additional conditions listed below:

A pilot study is to be performed first with up to 12 mice and a report on the outcomes must be submitted to the AESC before proceeding to the main study

Signed: _____ (Chairperson, AESC) Date: 7 December 2016

I am satisfied that the persons listed in this application are competent to perform the procedures therein, in terms of Section 23 (1) (c) of the Veterinary and Para-Veterinary Professions Act (19 of 1982)

Signed: _____ (Registered Veterinarian) Date: 7 December 2016

cc: Supervisor: Professor V Pillay
Director: CAS

Works 2000/lain0015/AESCCert.wps